The Aperiodic Nature of Mullite
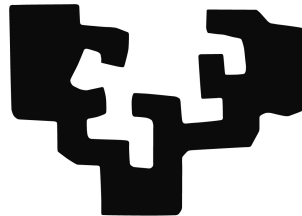
A dissertation by

Paul Klar

supervised by

Gotzon Madariaga

eman ta zabal zazu

Department of Condensed Matter Physics
Faculty of Science and Technology
University of the Basque Country UPV/EHU

2018

This dissertation was submitted in partial fulfilment of the requirements for the degree of **Doctor of Philosophy** in **Physics**. Further requirements include some signatures, several bureaucratic steps and the public thesis defence in front of a doctorate committee of three or five scientists.

tl;dr

A unified superspace model for the crystal structure of mullite is developed based on diffraction and computational methods.

AUTHORISATION OF THE THESIS SUPERVISOR
FOR THE PRESENTATION OF THE THESIS

Dr. **Gotzon Madariaga Menéndez** with National ID Card number 14946688T in his capacity as Supervisor of the Doctoral Thesis *The Aperiodic Nature of Mullite* completed within the *Doctoral Programme of Physics* by the PhD student Mr **Paul Benjamin Klar**, hereby authorises the presentation of the mentioned Doctoral Thesis, given that it fulfils the conditions necessary for its viva.

Leioa, 24th October, 2018

THE THESIS SUPERVISOR

Signed: Gotzon Madariaga Menéndez

AUTHORISATION OF THE DOCTORAL PROGRAMME'S
ACADEMIC COMMISSION

The *Academic Commission of the Doctoral Programme in Physics* during its meeting held on 24th October, 2018, agreed to authorise the presentation of the Doctoral Thesis entitled *The Aperiodic Nature of Mullite* supervised by Dr. **Gotzon Madariaga** and presented by Mr. **Paul Benjamin Klar** and registered with the *Department of Condensed Matter Physics.*

Leioa, 24th October, 2018

THE COORDINATOR OF THE DOCTORAL PROGRAMME

Signed: Francisco Javier Zúñiga Lagares

DEPARTMENT AUTHORISATION

The Board of the *Department of Condensed Matter Physics* during its meeting held on 24th October, 2018, agreed to authorise the processing of the Doctoral Thesis entitled *The Aperiodic Nature of Mullite* supervised by Dr. **Gotzon Madariaga** and presented by Mr. **Paul Benjamin Klar** to this Department.

Leioa, 24th October, 2018

DIRECTOR OF THE DEPARTMENT

SECRETARY OF THE DEPARTMENT

Signed: Gotzon Madariaga Menéndez

Signed: César Luis Folcia Basa

PHD DEGREE CERTIFICATE

DOCTORAL THESIS VIVA CERTIFICATE

PhD Student: Mr. Paul Benjamin Klar (born 18th February, 1988, in Munich, Germany)

Title of the Thesis: The Aperiodic Nature of Mullite

After having witnessed the completion of the viva by the PhD student and his response to any objections and/or suggestions made, the Panel appointed by the Postgraduate Commission of the University of the Basque Country to examine the Doctoral Thesis, meeting on the indicated date, agreed *unanimously / by majority vote* to award the following grade:

(*distinction / merit / pass / fail*)

Viva languages: ☐ Spanish ____%   ☐ Basque ____%   ☐ English ____%

Leioa, _____

CHAIRPERSON   SECRETARY

Signed: Dr.   Signed: Dr.

MEMBER 1   MEMBER 2   MEMBER 3

Signed: Dr.   Signed: Dr.   Signed: Dr.

PHD STUDENT

Signed: Paul Benjamin Klar

This thesis is dedicated to my parents Walter and Gönke.

Abstract

Mullites ($Al_{4+2\delta}Si_{2-2\delta}O_{10-\delta}$) are one of the most important components of ceramic materials including traditional porcelain, furnace windows and heat shields for space vehicles. Despite the broad interest of the ceramic industry and a large record of research on the crystalline state and applications, the crystal structure of mullite is not well understood from a fundamental point of view. The presence of a composition dependent structural modulation alongside diffuse scattering indicates that ordering mechanisms of different length scales are present. The objective of this thesis is to understand these phenomena by developing a unified superspace model to characterise and understand the aperiodic nature of mullite.

Different methods were applied to investigate the vacancy and Al/Si order in mullite. At first the symmetry was analysed thoroughly to derive constraints on the vacancy distribution based on crystal chemical premises. On this basis a superspace model was developed that defines the polyhedra network consisting of octahedra, tetrahedral tricluster units and tetrahedral dicluster units as a function of the modulation wave vector $\mathbf{q}$ and the vacancy concentration δ. Refinements of superspace models based on synchrotron single crystal X-ray diffraction measurements indicate that in the real structure the identified pattern is present, but with a decreased degree of order. Different samples exhibit different degrees of order suggesting that mainly disordered and fully ordered mullite crystals exist. The Al/Si ordering could not be derived from symmetry constraints and the occupancy of Si could not be refined. Nevertheless, an Al/Si ordering pattern could be identified from the analysis of the displacive modulation.

The dependence of the satellite reflections on the chemical composition was studied with two complementary methods. Electron diffraction measurements were carried out on a broad range of different samples to investigate the dependence of the modulation wave vector $\mathbf{q} = (\alpha\,0\,\gamma)$ on the vacancy concentration δ. The dependence could be explained based on the symmetry analysis by implementing additional constraints on the tricluster distribution leading to the relationship $\alpha = \frac{1-\delta}{2}$, which defines a unified superspace model for the composition range $0 \leq \delta \leq 0.5$. Commensurate superstructures based on the superspace model were investigated with a set of pioneering atomistic simulations applying density functional theory. This allowed to characterise the structural modulation on a new level and reveal the fundamental ordering patterns that define the crystal structure of mullite in terms of vacancy and Al/Si order. The understanding of the crystal structure forms a new basis for future research on the properties of mullite and related applications.

I

Resumen

At the University of the Basque Country is is obligatory to present a summary of the thesis in Spanish or in Basque if the thesis is not written or defended in one of the two languages (Article 13 of the Academic Regulations for Doctoral Studies). It is my pleasure to present this Spanish summary on the following pages.

Contenido de la tesis

El Capítulo 1 da una introducción a varios aspectos de las mullita. El Capítulo 2 introduce los fundamentos relevantes de cristalografía, difracción, superespacio y métodos computacionales. Las muestras, los experimentos y los parámetros de las simulaciones se describen en el Capítulo 3. Nuevos modelos de la estructura cristalina de las mullitas se presentan en el Capítulo 4, incluyendo el análisis de la simetría. Los modelos se extienden a un rango de composición más amplio basado en la difracción de electrones. En el capítulo 5 los resultados se presentan en un contexto más amplio comparando modelos diferentes entre si con modelos anteriores para aumentar la comprensión de los fenómenos de ordenamiento. El capítulo 6 resume el trabajo de tesis. En las siguientes páginas se presentan los aspectos más relevantes de la tesis.

Introducción

Las mullitas son minerales con composición flexible ($Al_{4+2\delta}Si_{2-2\delta}O_{10-\delta}$), que forman el componente principal en porcelana tradicional o cerámicas de alta tecnología como, por ejemplo, ventanas para hornos o ladrillos refractarios, que se emplean, entre otros, como escudos en recubrimiento de transbordadores espaciales [1]. La mayor parte del trabajo realizado en los últimos siglos concierne más a las aplicaciones tecnológicas de estos materiales que a la explicación, desde un punto de vista más fundamental, de sus propiedades y la relación de éstas con aspectos estructurales. La estructura cristalina consiste en columnas de octaedros interconectadas por tetraedros de AlO_4 y SiO_4. Los tetraedros forman unidades de dos tetraedros (dicluster) o de tres tetraedros (tricluster). Las componentes claves de la estructura son la presencia de vacantes de oxígeno que determinan la distribución de diclusters y triclusters y la distribución de los tetraedros de SiO_4. Entonces, la definición de la estructura requiere el conocimiento de la distribución de vacantes y los átomos de sílice. La concentración de vacantes δ y obviamente también la concentración de sílice depende de la composición. Reflexiones satélites en el patrón de difracción de las mullitas indican claramente una modulación estructural, lo cual es un orden de largo alcance. El orden máximo de las reflexiones satélites es entre uno y siete, pero en la gran mayoría de las muestras satélites de bajo orden y diffuse scattering indican la presencia de desordenamiento estructural. Cameron (1977) ha observado que el vector de modu-

lación depende de la composición [2]. Además, se indica una reducción de simetría para mullitas más aluminosas. Aunque las mullitas constituyen una familia de compuestos extensamente estudiados que se descubrieron hace casi 100 años, todavía no se ha encontrado un modelo estructural que permite entender y describir fundamentalmente la modulación y el ordenamiento de las vacantes y Al/Si. Objetivos El objetivo de esta tesis doctoral es desarrollar un modelo superespacial unificado que describe cuantitativa y cualitativamente los fenómenos de ordenamiento en las mullitas para comprender la naturaleza de la modulación en función de la composición. Se requiere el desarrollo de modelos ordenados y desordenados a cara del diffuse scattering y las reflexiones satélites de alto orden observadas en algunas muestras con difracción de electrones. Antecedentes En las últimas décadas se ha investigado la estructura de la mullite por varias maneras diferentes. Modelos desordenados han determinado la distribución de vacantes que es capaz reproducir muchos detalles del diffuse scattering, pero no se ha establecido una relación con ordenamiento de largo alcance y por lo tanto no reproducen la intensidad de las reflexiones satélites [3, 4]. Medidas resonancia magnética nuclear indican que en las mullitas átomos de sílice prefieren un entorno de átomos de aluminio, pero que es necesario implementar entornos diferentes. De todas formas, estos resultados no permiten analizar una relación entre el ordenamiento de sílice y el ordenamiento de vacantes [5]. Birkenstock et al. (2015) ha publicado el primer modelo estructural usando el formalismo del superespacio [6]. Los autores concluyen que los modelos establecidos por Freimann & Rahman (2001) son básicamente correctos, es decir que las vacantes casi no muestran orden de largo alcance. Aunque también se han incluido medidas de difracción de neutrones, no se he revelado un ordenamiento de sílice [6]. Una investigación basada en el análisis de la simetría aplicando la teoría de grupos ha identificado dos celdas estructurales. La superposición de estas celdas con una contribución modulada forma cuantitativamente un modelo estructural que incluye una descripción de la distribución de vacantes y sílice, y también del desplazamiento de ciertos átomos [7]. Sin embargo, el estudio no refina los parámetros del modelo en base de medidas de difracción y ciertos presupuestos sobre la simetría no son válidos porque están en conflicto con la simetría superespacial.

Metodología

Para proporcionar una visión unificada de la familia de las mullitas, se requiere la investigación de la modulación y su dependencia de la composición e igualmente su implicación para la estructura, sobre todo la distribución de vacantes. El modelo superespacial constituye, en este caso, la herramienta más apropiada para el análisis estructural de estos compuestos permitiendo modelos sencillos que contemplen distribuciones uniformes de vacantes. Algunos resultados claves de la tesis están basados en el análisis de la simetría usando el formalismo superespacial y requisitos de la naturaleza química [8]. Predicciones

del análisis se han verificado medidas de difracción y con simulaciones computacionales. Para la tesis se han analizado muestras industriales, muestras sol-gel y muestras de quenching. Se han medido cuatro muestras monocristalinas con radiación de sincrotrón con los instrumentos de BM01 e ID28 de la European Synchrotron Radiation Facility en Grenoble, Francia. Es un sitio muy bonito y adecuado para realizar medidas revolucionarias. Se han realizado algunas cien medidas de un gran número de muestras distintas con difracción de electrones en colaboración con el Dr. Lukáš Palatinus en su 'Laboratorio de difracción de electrones' en Praga, Chequia. Es un sitio muy bonito y adecuado para realizar medidas revolucionarias. Experimentos de difracción de polvo, microscopía de electrones y espectroscopía de rayos X amplían la caracterización de las muestras. Además, se han ejecutado cálculos de fuerza [9] y cálculos basados en la teoría del funcional de la densidad (DFT) para analizar detalles de la modulación como el ordenamiento de sílice, el desplazamiento de los átomos y la dependencia en la concentración de vacantes. La disponibilidad de un propio cluster moderno ha permitido realizar simulaciones de superestructuras muy grandes (hasta 500 átomos por celda unidad) con el código 'Vienna Ab Initio Simulation Package' (VASP) [10, 11]. Análisis de la simetría superespacial Actualmente el formalismo del superespacio en cuatro dimensiones es un concepto estándar y necesario para la investigación, descripción y análisis de estructuras moduladas [12]. Con las medidas de difracción de monocristales se ha determinado que el grupo superespacial $Pbam(\alpha 0\frac{1}{2})0ss$ describe la estructura de las mullitas con una concentración de vacantes $\delta \leq 0.5$. Esto conduce a un pequeño conjunto de posibles distribuciones de vacantes para una composición química determinada y un vector de onda de modulación respectivo. A partir de esto se han derivado las restricciones para la descripción de la estructura cristalina de mullita en el superespacio.

Modelo desordenado

En base de las medidas de monocristal con difracción de rayos X y las restricciones derivadas de la simetría se han desarrollado modelos estructurales con funciones harmónicas de modulación que describe el ordenamiento de diclusters, triclusters y vacantes. El análisis cuantitativo de las medidas en el superespacio se ha realizado mediante el programa Jana2006, destinado al refinamiento de modelos de estructuras moduladas en 4 dimensiones [13, 14]. Se han analizado aspectos cristaloquímocos como la geometría de la red de poliedros y la distancia modulada entre los átomos. Todos los refinamientos describen básicamente el mismo modelo, pero las amplitudes de modulación de los refinamientos cambian notablemente en función de la muestra analizada. Entonces, las vacantes siguen el mismo patrón de ordenamiento, pero el grado de ordenamiento de largo alcance es diferente en cada muestra. Según estos resultados las mullitas existen no solo en un rango amplio de composiciones químicos, sino también con un rango amplio de grados

de ordenamiento. La distribución de sílice no se ha podido implementar en el refinamiento porque experimentos con difracción de rayos X no son capaces de distinguir bien entre Si^{4+} y Al^{3+}. Para la tesis se ha desarrollado un nuevo método con el fin de determinar la distribución de sílice mediante la combinación de la teoría de la densidad funcional con los volúmenes modulados de los tetraedros. Con este enfoque se ha identificado la presencia de diclusters de Si_2O_7 y $AlSiO_7$. La presencia de Si_2O_7 propone una revisión de la clasificación de mullita como mineral, porque en la actualidad está clasificado como mineral sin unidades diclusters del tipo Si_2O_7.

Modelo ordenado

El modelo ordenado derivado de la simetría y en acuerdo con una interpolación del patrón de ordenamiento del modelo desordenado consiste en una estructura definida por una distribución de dicluster, tricluster y vacantes. Los diclusters forman bloques denominadas 'bloques sin vacantes' (vacancy-free blocks) y los triclusters juntos con las vacantes forman bloques denominadas 'bloques de vacantes' (vacancy blocks). El ordenamiento de sílice en los tetraedros no se puede determinar a partir del análisis de simetría. Por eso la distribución de sílice se ha investigado sistemáticamente con cálculos de fuerza. A partir de un modelo ordenado de la mullita 2/1 ($\delta = 0.4$) se han generado 38760 estructuras que representan todas las distribuciones de sílice permitidos por la simetría. Con las simulaciones computacionales se han identificado los candidatos más estables para cálculos más precisos aplicando la teoría del funcional de la densidad. Los resultados, por un lado, han confirmado que los modelos derivados a partir de la simetría superespacial son estables y, por otro, también han relevado patrones generales del ordenamiento de sílice. El model final representa el ordenamiento ideal en la mullita 2/1.

Modelo unificado

El tamaño de las muestras de sol-gel y de quenching no es adecuado para investigaciones estructurales con difracción de Rayos X. Para establecer una relación experimental entre el vector de onda de modulación y la composición se han refinado modelos estructurales en base de las medidas de difracción de electrones. El análisis propone que la relación es $\alpha = \frac{1-\delta}{2}$. La misma relación resulta si en las restricciones derivada de la simetría se implementa un patrón que prohíbe la formación de pilas de *triclusters*. Esta relación describe precisamente la distribución de diclusters, triclusters, y vacantes para mullitas con composición $0 \leq \delta \leq 0.5$, pero no está uncluido el ordenamiento de los átomos sílice.

Cálculos de fuerza

Los modelos desarrollados se han usado para generar varias estructuras que representan caso comensurables del modelo unificado. Los cálculos han relevado el ordenamiento de los átomos sílice para un rango largo de composiciones. La comparación de los resultados de composiciones diferentes indica que hay un patrón del ordenamiento de a aluminio y sílice, que también se ha incluido en el modelo unificado. Este modelo describe precisamente la distribución de los átomos de oxígeno, aluminio y sílice en la mullita ordenada de cualquiera composición con $\delta \leq 0.5$. Además, un análisis más profundo indica que también se puede describir la modulación del desplazamiento con un modelo unificado. Eso es una idea para un trabajo en el futuro. Si lo conseguimos, sería la hostia.

Simulación de *diffuse scattering*

Se han analizado varios modelos en base de los resultados de los últimos párrafos. El modelo desordenado explica bien el patrón difuso en la sección $hk0$, pero no es capaz de reproducir la forma básica que se observa en las secciones $0k\ell$ y $h0\ell$. Resulta que es necesario excluir, como en el modelo unificado, la formación de pilas de *triclusters*. El modelo todavía requiere el refinamiento de algunos detalles. Estamos trabajando con Prof. Reinhard Neder y Ella Schmidt del 'Instituto de Física de la Materia Condensada' en la Universidad de Erlangen, Alemania. Es un sitio muy bonito y adecuado para realizar simulaciones revolucionarias.

Conclusión

Todas las investigaciones computacionales sobre la mullita han usado una distribución aleatoria de vacantes para investigar aspectos diferentes de la mullita y su dinámica. Parece que los modelos estructurales anteriores no han convencido a la comunidad científica o se ha asumido que la diferencia entre una distribución aleatoria y la distribución verdadera es despreciable. Los resultados de esta tesis ofrecen un modelo que está exactamente definido y que sirve como base para investigaciones tanto para una mejor comprensión de sus propiedades, como para la mejora de sus actuales y futuras aplicaciones. Todos los modelos de las últimas décadas se han concentrado en las interacciones entre las vacantes, pero resulta que la interacción entre los triclusters es la clave para entender y describir la naturaleza aperiódica de la mullita.

Figuras claves

Las figuras claves de esta tésis son las siguientes (la primera cifra indica el número del capítulo en la que se encuentra la figura): 1.2, 4.1, 4.4, 4.5, 4.7, 4.14, 4.18, 4.19, 4.22, 5.2, 5.6, CD4.P2.18, 5.10.

Publicaciones y actividades científicas

He presentado los resultados de este trabajo en varios congresos, por ejemplo, en la '9th Conference on Aperiodic Crystals' en Ames, Estados Unidos, y en el '24th Congress and General Assembly of the International Union of Crystallography'. Además, se han publicado dos artículos: (1) 'Ordered vacancy distribution in mullite: A superspace model'. *Acta Cryst.* B**73**, 377–388. (2) 'Exploiting superspace to clarify vacancy and Al/Si ordering in mullite'. *IUCrJ* **5**, 497–509.

Preface

This PhD thesis on the crystal structure of mullite was written between winter 2014 and autumn 2018 under the supervision of Professor Gotzon Madariaga at the 'Department of Condensed Matter Physics', Faculty of Science and Technology, University of the Basque Country UPV/EHU at the campus of Leioa close to Bilbao, Spain. This document is composed of an introduction to mullite and its structural aspects (Chapter 1), a chapter on selected foundations of crystallography and diffraction (Chapter 2), the experimental and computational part (Chapter 3) and chapters presenting the results, discussion and a summary (Chapters 4–6). A more detailed overview of the scheme of this thesis is given in § 1.4.2. In this preface I want to describe the environment in which this thesis was written.

First of all, I had the privilege to work in an exceptional research group. Any question in my mind was quickly answered by one of the great minds in this department, usually my supervisor, and for any kind of problem there was someone around with a hint. Modern experimental equipment with the appropriate software allowed to easily perform measurements by pushing a few buttons. Apart from the resources of the Department of Condensed Matter Physics I had the opportunity to work with other research groups. In November 2015 I visited the 'Glass and Ceramics Institute' (ICV-CSIC) of the Spanish National Research Council in Madrid, Spain, to get insights into the synthesis of mullite under the supervision of Doctor Luis Sanchez Muñoz. In 2017 I spent 5 months at the 'Institute of Physics' (FZU), Czech Academy of Sciences in Prague, Czechia, under the supervision of Doctor Lukáš Palatinus to carry out electron diffraction measurements. In March 2018 I visited the 'Chair of Crystallography and Structural Physics', Friedrich-Alexander University in Erlangen, Germany, under the supervision of Professor Reinhard Neder and his amazing PhD student Ella Schmidt to work on diffuse scattering. Furthermore, I participated in several summer schools, courses and conferences. All this was possible due to the generous funding of the Basque Government (PhD Grant, support of my stay in Prague, project IT-779-13) and the Spanish Government (FEDER funds, project MAT2015-66441-P). The University of the Basque Country, the Spanish Crystallographic Association (GE3C), the European Crystallographic Association (ECA) and the International Union of Crystallography (IUCr) supported many of the different meetings with travel grants and accommodation grants. In many occasions I had the opportunity to present ideas and results of my research as poster, oral presentation or both. A list of scientific activities and publications is given on page 163.

I want to highlight one peculiarity: Pedro Miguel Echenique emphasised in his talk 'Consejos a un(a) joven científico(a)' at a PhD symposium ('I Jornadas Doctorales de la UPV/EHU', July 2016) that young scientists should be conscious about the opportunities of modern computers. Back then I did not understand what he meant, but maybe

I do so now. About a year later the department bought a new computer cluster which allowed to carry out sophisticated calculations that took between a few hours and a few weeks. The obtained results are very important for this thesis, but such a super computer did not exist until a few years ago. Hence, the results could not have been obtained without the available computational power. Apart from the hardware, also the software is very important because modern programs allow to generate a lot of valuable data in very little time using a simple input file. Many programs I wrote for the thesis were mainly analysing a batch of output files because the manual analysis would have taken too long. Considering that two decades ago my laptop would have been among the 100 most powerful computers in the world and that I used many sophisticated programs written by others, I am not exaggerating when I claim, that this thesis could have never achieved the current state without the hardware and programs of this decade. One might ask the question, if *Moore's law* also holds for the scope of a PhD thesis. Independent of the computational power, the power of *human resources* that supported the thesis may not be underestimated.

Paul Klar in Bilbao, 8th October 2018

Acknowledgements

Contents

List of selected Acronyms

Acronym	Description
AS1, AS2, AS3	labels of Al/Si ordering schemes
BM01	Swiss-Norwegian beamline at the ESRF
CN	coordination number
DFT	density functional theory
ED	electron diffraction
EDX	energy dispersive X-ray spectroscopy
ESRF	European Synchrotron Radiation Facility
FF	force field
PBE, PBEsol	functionals used in DFT calculations
PBEsol-D	dispersion corrected DFT calculations
PEDT	precession electron diffraction tomography
pXRD	powder X-ray diffraction
SSM	superspace model
sXRD	single crystal X-ray diffraction
TEM	transmission electron microscopy
VB	vacancy block
VFB	vacancy-free block
XRD	X-ray diffraction

Chapter 1

Introduction to mullite

> "The crystalline phase, which causes the X-ray pattern of mullite,
> cannot have the composition $3\,Al_2O_3 \cdot 2\,SiO_2$"
> Hermann Franz Mark & Paul Rosbaud (1926)[1]

> "Yes, it can."
> Paul Klar (2018)

---

[1]Translated from German by the author of the thesis [15].

1.1 Mullite research: history and overview

1.1.1 Mullite: more applied than understood

"Phases of the SiO_2–Al_2O_3 [...] system have had, and will continue to have, a
significant role in the development of traditional and advanced ceramics."
İlhan A. Aksay, Daniel M. Dabbs & Mehmet Sarikaya (1991)

"Mullite has achieved outstanding importance as a material for both
traditional and advanced ceramics [...]"
Hartmut Schneider, Jürgen Schreuer & Bernd Hildmann (2008)

The authors quoted are convinced, that mullite is a unique material, that satisfies many
needs of the ceramics industry and bears the potential for new technologies and applica-
tions [16, 17]. Many ceramics requiring structural stability at elevated temperatures and
chemical resistance, like furnace windows or heat shields for space vehicles, are based on
mullite [18].

"[It] stresses the need of a deeper understanding of the relationships between
crystal structure and properties of mullite."
Hartmut Schneider, Reinhard Fischer & Jürgen Schreuer (2015)

Despite its highly praised status in the world of ceramics [1], from a fundamental point
of view, the structural details of mullite are only little understood. The aim of this thesis
is to develop crystal structure models of mullite as a basis for a better understanding of
the properties on a fundamental level. This chapter outlines the relevant research on the
mullite structure from its discovery to the most recent models.

1.1.2 The discovery of mullite

The investigation of mullite has a long history of ambiguity, which began 100 years before
the actual discovery of mullite. In 1824 the rock-forming mineral sillimanite (Al_2SiO_5) was
discovered [19] and subsequently identified as one of the main components in porcelain
[20, 21, 22]. It was stated that sillimanite exhibits congruent melting behaviour [23],
but exactly 100 years after the first description of sillimanite[2], the phase diagram of
the system SiO_2–Al_2O_3 was reinvestigated by Bowen & Greig in 1924. The melting of
sillimanite crystals and subsequent slow cooling led to the initial formation of α-Al_2O_3
corresponding to incongruent melting behaviour, although the formation of Al_2O_3 could be
avoided by changing the growth conditions [24]. Nevertheless, there was no way to obtain

---

[2]Interestingly, sillimanite was discovered in 1824 by G. T. Bowen, and mullite in 1924 by N. L. Bowen.

a sample consisting of a single phase with composition Al_2SiO_5 as there was always a glassy phase forming alongside needle shaped crystals. The glass phase formation decreased by enriching the synthesis with Al_2O_3 until a single crystalline phase resulted for a nominal composition of $3\,Al_2O_3 \cdot 2\,SiO_2$. The name 'mullite' was suggested based on the discovery of a new mineral on the Isle of Mull, Scotland, with the same properties as the artificial samples of $3\,Al_2O_3 \cdot 2\,SiO_2$ [24]. Two years before it was reported that at the same location "well-crystallised minerals, such as [...] sillimanite" [25] were found. Therefore, the discovery of mullite required to verify carefully the classification of other 'sillimanite' samples. Needle shaped crystals in porcelain, glass pots, tank blocks, refractories and many other ceramics turned out to be mullite and not sillimanite as anticipated earlier [26, 27, 28].

X-ray diffraction patterns of mullite and sillimanite appeared to be virtually identical with tiny differences in the lattice parameters close to the experimental error [29]. Only few reflections showed different intensities, which was difficult to quantify in the early days of X-ray crystallography. The determination of the lattice parameters and the chemical composition led to the conclusion that the unit cell contains a non-integer number of atoms. As such a case had never been observed before, other researchers brought the existence of mullite into question. For example, Mark & Rosbaud (1926) stated that mullite must necessarily have an integer number of atoms in the unit cell and therefore the composition must be identical to that of sillimanite [15]. Wyckoff (1926) concluded that the determined non-integer number of atoms is correct and that the true cell must be larger [29].

1.1.3 Structural elements of sillimanite and mullite

Taylor (1928) solved the crystal structure of sillimanite (Tab. 1.1) in the orthorhombic space group *Pbnm* with lattice parameters $a = 7.43\,(3)\,\text{Å}$, $b = 7.58\,(4)\,\text{Å}$, $c = 5.74\,(2)\,\text{Å}$ [30]. The model consists of octahedra chains extending along the c direction interlinked by chains of $AlSiO_7$ double tetrahedra named diclusters (Fig. 1.1).

The crystal structure of mullite was solved at a much later stage, and initially the structure of sillimanite was taken as a basis to derive the structural elements of mullite. Due to the chemical composition, oxygen vacancies must be present in the crystal structure of mullite [31]. It was suspected that with respect to sillimanite, oxygen atoms are removed from the O_C site and the cations of the broken dicluster shift apart to form triclusters as shown in Figure 1.1. The prediction of this vacancy position and environment was based on considerations on the coordination numbers (CN). In sillimanite there are four different oxygen sites: O_A and O_B with $CN = 3$ are each bonded to two octahedral sites and one tetrahedral site. O_D also with $CN = 3$ is bonded to one octahedral and two tetrahedral sites. O_C is bonded to two tetrahedral sites ($CN = 2$). Removing an oxygen atom from

Site label (Sillimanite)	Respective label in mullite	CN	Wyckoff site	x	y	z
Al$_\mathrm{I}$	Al1	6	4a	0	0	0
Al$_\mathrm{II}$	Al2	4	4c	-0.14	0.33	0.25
Si	Si2	4	4c	0.18	-0.35	0.25
O$_\mathrm{A}$	O1	3	4c	0.11	0.12	0.25
O$_\mathrm{B}$	O1	3	4c	-0.10	-0.16	0.25
O$_\mathrm{C}$	O3	2	4c	0.08	0.46	0.25
O$_\mathrm{D}$	O2	3	8d	0.15	-0.18	0

Table 1.1: Fractional coordinates of initial crystal structure solution of sillimanite in space group *Pbnm*. All sites have a structurally similar site in the mullite crystal structure with a different label. CN is the number of atoms coordinating the respective site.

Site label	Obsolete labels	CN	Wyckoff site	Description
Al1	Al	6	2a	Cation at the origin of the unit cell coordinated by four O1 and two O2 atoms.
Al2 or T	Al, M_I	4	4h	Al2 and Si2 are statistically distributed on the T site.
Si2 or T	Si, M_I	4	4h	
Al3 or T*	Al*, M_II	4	4h	Two T sites and a T* site form a tricluster with O4 at the central corner.
Si3 or T*	Si*	4	4h	Si on the T* site is not considered in the majority of models.
O1	Oab, O$_\mathrm{I}$	3	4h	O1 is bonded to two octahedral sites and one tetrahedral site.
O2	Od, O$_\mathrm{II}$	3	4g	O2 is bonded to one octahedral site and two tetrahedral sites.
O3	Oc, O$_\mathrm{III}$	2	2c	O3 links two corner-sharing T sites forming a dicluster.
O4	Oc*, O*, O$_\mathrm{IV}$	3	4h	O4 links two T sites and one T* site.
Vacancy		14	2c	The void of a vacancy is a distorted tetrakis hexahedron.

Table 1.2: Description and labels of atom sites in the average structure of mullite. Obsolete labels refer to labels that were used in the (less recent) literature.
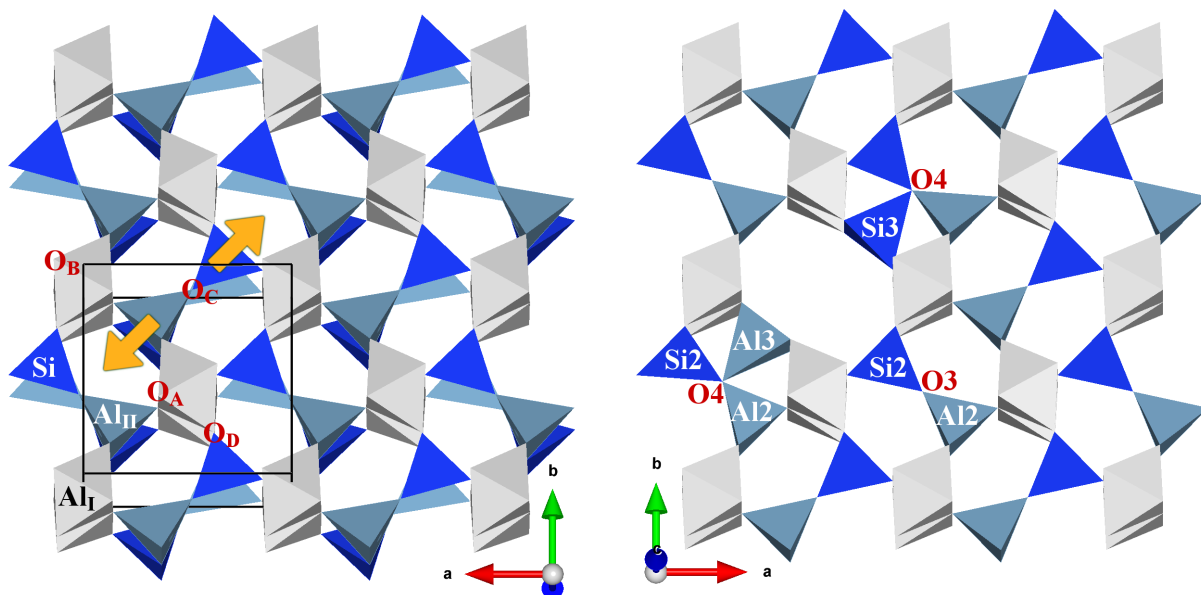
Figure 1.1: Crystal structure model of sillimanite (left) and mullite with one vacancy (right). The removal of an Oc atom alongside a shift of two cations as indicated by the orange arrows introduces a vacancy into the sillimanite structure. The Si distribution on the right is preserved and thus the shown model is not charge balanced. Al tetrahedra in grey blue, Si tetrahedra in dark blue.

the octahedra, i.e. O_A, O_B or O_D, requires the rearrangement of two tetrahedral sites and one octahedral site. Removing an oxygen atom from the O_C site, in contrast, requires that only two tetrahedral sites adapt and that the overall CN of the anion substructure increases by two. In that case, two cations have to find a new environment to retain the tetrahedral coordination. If both cations bond to the same O_A, O_B or O_D oxygen that oxygen is the coordinated by five cations and is strongly overbonded. Similarly, bonding both cations to the same O_C leads to CN = 4. The least increase of the CN is achieved by bonding the two cations to two different O_C sites, which thus become three-fold coordinated oxygen atoms [31]. The structural unit consisting of three connected tetrahedra is denominated 'tricluster'. In total, the introduction of a vacancy affects two oxygen sites and two cation sites, apart from the oxygen that is removed. From crystal chemical considerations it is easy to see, that the triclusters must be located directly next to the vacancy. Otherwise one tetrahedron of the tricluster would necessarily share a face with a tetrahedron of a neighbouring dicluster. This is only avoided if the third tetrahedron of each tricluster 'shares' a face with the void of the vacancy (Fig. 1.1).

Atom site labels of mullite are based on the initial structure solution of sillimanite but using numbers instead of letters. In the average structure of mullite Al2 and Si2 are disordered on a common tetrahedral site labelled 'T site'. The presence of triclusters introduces two additional sites, Al3 and O4, with respect to the structure of sillimanite. The Al3 site is also labelled T^* because it can be considered as a split site of T. The

central oxygen atom of triclusters is labelled O4 and is slightly displaced towards the bonding atom on the *T** site. Thus, in the average structure O4 appears as a split site of O3. The coordinates of the geometric centre of the void around the vacancy are the same as the coordinates of the O3 site, which is therefore also called 'vacancy site'. The terminology will be further clarified in § 1.1.5. A description of all sites and labels is given in Table 1.2.

1.1.4 Chemical formula

The removal of an O^{2-} from a model sillimanite structure requires the replacement of two Si^{4+} by two Al^{3+}. In the literature, this replacement scheme with a focus on the charge balance is often expressed as $2Si^{4+} + O^{2-} \rightleftharpoons 2Al^{3+} + \square$ [16, 17]. The square symbols $\square$ represents a vacancy. The chemical formula of mullite as a solid solution is expressed correspondingly as $Al_{4+2\delta}Si_{2-2\delta}O_{10-\delta}$ with δ being the vacancy concentration. The replacement scheme can be extended to account for the coordination number indicated by superscript Roman numbers: $2Si^{IV} + 3O^{II} \rightleftharpoons 2Al^{IV} + 2O^{III} + \square^{XIV}$. The respective chemical formula, separating the octahedra backbone and the interconnecting tetrahedra is $(Al_2^{VI}O_8^{III})(Al_{2+2\delta}^{IV}Si_{2-2\delta}^{IV}O_{2-3\delta}^{II}O_{2\delta}^{III})$. Due to the term $2 - 3\delta\, O^{II}$ this chemical formula and replacement scheme are only valid in the range $0 \leq \delta \leq \frac{2}{3}$ because higher vacancy concentrations would correspond to a negative concentration of diclusters. The replacement schemes are useful to describe how a structural model of mullite is obtained starting from a structural model of sillimanite, but they should not be regarded as a chemical reaction or a process which takes place during the formation of mullite.

In few cases the chemical formula was expressed as $Al_{4+2\delta}Si_{2-2\delta}O_{10-\delta}\square_\delta$, which specifically accounts for the presence of vacancies represented by the square symbol $\square$ [32, 33]. However, in a void of a vacancy two *T*, two *T**, one O3 and two O4 sites are vacant and can also be described as vacancy sites. To avoid ambiguity with the assignment of the vacancy site in this thesis the chemical formula is expressed as $Al_{4+2\delta}Si_{2-2\delta}O_{10-\delta}$ without the square symbol. The vast majority of studies on mullite expresses the chemical formula in this way. In the literature the vacancy concentration is represented by the symbol x. Throughout this thesis the symbol δ is used to avoid confusion with coordinate parameters.

1.1.5 Vacancies, voids and defects

> "The crystal structure of mullite is a modified defect structure of sillimanite"
>
> İlhan A. Aksay, Daniel M. Dabbs & Mehmet Sarikaya (1991)

Vacancies play a crucial role for the characterisation of the crystal structure of mullite [16]. This section defines the terms 'vacancy' and 'void' and a few other terms are discussed.
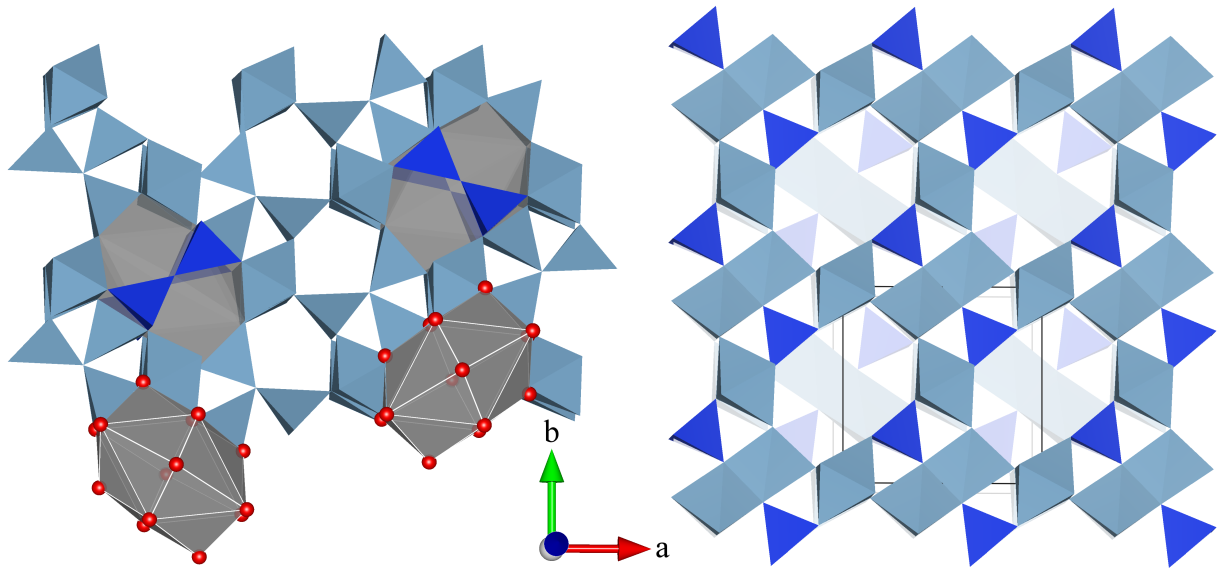
Figure 1.2: Geometric shape of of voids in mullite (left) and in andalusite (right). The coordination sphere of vacancies in mullite is a strongly distorted tetrakis hexahedron. The subsequent layer in the andalusite (Al_2SiO_5) model is shown with decreased opacity.

In mullite there are voids in the crystal structure with a diameter of about 5 to 6 Å that are completely surrounded by a tetrahedra network (Fig. 1.2). According to Michele Catti a vacancy is a point defect described by "the absence of an atom from its expected position" (Chapter 9 in [34]). According to this definition every absent T, T^*, O3 or O4 atom is a vacancy, which makes the description of the vacancy distribution unnecessarily complicated. For example, the simple description of a dicluster requires to describe two T^* vacancies and two O4 vacancies. According to Gary Gladysz a void with a size between 10^{-10} m to 10^{-8} m is a 'free volume' [35]. Hence, the voids in mullite should rather be termed 'free volume' instead of 'vacancy'. Nevertheless, the scientific community silently agreed on using the term 'vacancy' to refer to the void or free volume in the polyhedra network. Therefore, the following definitions will be used throughout this thesis:

- 'Vacancy' refers to a crystallographic site characterised by the simultaneous absence of one O3, two O4, two T and two T^* site atoms in mullite. The position of the vacancy is at the vacant O3 site with site symmetry $\frac{2}{m}$ in the average structure.

- 'Void' refers to the unoccupied volume of approximately 80 Å^3 in the vicinity of the vacancy.

Are these voids defects? The andalusite crystal structure consists of the same octahedra backbone like mullite and sillimanite, but in andalusite voids are regularly placed on well defined crystallographic sites and the geometry of the voids is very similar to the voids in mullite (Fig. 1.2). It was reported that in highly ordered mullite samples the vacancies are also perfectly ordered [36]. In these cases, the term 'defect' is clearly not appropriate.

On the other hand, the majority of mullite samples show characteristic diffuse scattering indicating that correlated disorder is present. As the diffuse scattering seems to be independent of the temperature an *in situ* single crystal X-ray diffraction study concluded, that the vacancy distribution in mullite is independent of the temperature [37]. Taking into account that the quantity of voids is uniquely determined by the chemical composition and not by other parameters like the temperature, the term 'defect' might be misleading because in many materials the concentration and distribution of defects is highly temperature dependent [38]. Nevertheless, the voids may be regarded as volume defects and thus the term defect is not wrong, but in certain cases not suitable. Throughout this thesis the term defect is avoided to describe the crystal structure of mullite.

1.1.6 Nomenclature of mullite compounds

Mullite forms a solid solution range [39, 16, 1]. The chemical composition can be expressed in different ways and depending on the focus of the study, one way or the other is preferred. For the description of phase diagrams and synthesis experiments the mullite composition is mainly expressed as the concentration $[Al_2O_3]$ in units of mol% or wt%. The sample composition is also defined by the molar ratio $R_{AS} = [Al_2O_3] : [SiO_2]$. Mullite with an Al_2O_3:SiO_2 ratio of 3:2 is named 3/2-mullite and the ratio 2:1 corresponds to 2/1-mullite. However, in the literature these labels are often used with an undefined flexibility, i.e. the terms often refer to a composition close to the theoretical composition but not necessarily to the exact composition. A more abstract way is to represent the chemical composition by the vacancy concentration δ. The chemical composition can be exactly calculated with $\delta = (R_{AS}-1)/(R_{AS}+\frac{1}{2})$ or $\delta = (4 \cdot [Al_2O_3]-2)/([Al_2O_3]+1)$. Table 1.3 lists some members of the solid solution range with the ideal composition expressed in different ways. Here, only rational values of δ and R_{AS} are mentioned, but intermediate compositions with irrational δ are possible as well. However, in experiments rational and irrational numbers cannot be distinguished due to the experimental uncertainty.

The term 'mullite' is part of a large family of compounds that are structurally derived from a tetragonal aristotype with space group $P4/mbm$ and a characteristic backbone of edge-sharing octahedra chains. This family of so-called 'mullite-type' structures includes many different groups that are classified by different symmetries and subgroup relationships [18]. In this thesis the term mullite exclusively refers to compounds with chemical composition $Al_{4+2\delta}Si_{2-2\delta}O_{10-\delta}$. This mullite corresponds to the mullite group II.3 according to Schneider & Komarneni (2005) [18].

Label	vacancy concentration δ	Al_2O_3:SiO_2 ratio	[Al_2O_3] in mol%	[Al_2O_3] in wt%
	$0.20 = \frac{1}{5}$	11:8	57.89	70.00
3/2-mullite	$0.25 = \frac{1}{4}$	3:2	60.00	71.79
7/4-mullite	$0.33 \approx \frac{1}{3}$	7:4	63.64	74.81
2/1-mullite	$0.40 = \frac{2}{5}$	2:1	66.67	77.24
9/4-mullite	$0.45 \approx \frac{5}{11}$	9:4	69.23	79.24
7/3-mullite	$0.47 \approx \frac{8}{17}$	7:3	70.00	79.83
5/2-mullite	$0.50 = \frac{1}{2}$	5:2	71.43	80.92
3/1-mullite	$0.57 \approx \frac{4}{7}$	3:1	75.00	83.58
4/1-mullite	$0.67 \approx \frac{2}{3}$	4:1	80.00	87.16
9/1-mullite	$0.84 \approx \frac{16}{19}$	9:1	90.00	93.85

Table 1.3: Labels of selected members of the mullite solid solution and the respective composition. The concentration [Al_2O_3] is given in weight% and in mol%.

1.1.7 Phase diagram(s) of the system SiO_2–Al_2O_3

Mullite is made of the three most abundant elements of the earth crust, which are oxygen, silicon and aluminium [40]. The binary phase diagram of the oxide components silica SiO_2 and alumina Al_2O_3 was a matter of controversy for several decades as contradicting findings on the solid solution range and melting behaviour were reported. The first noteworthy phase diagram was published by Bowen & Greig (1924) with the discovery of mullite and included 3/2-mullite as the only stable intermediate phase with incongruent melting behaviour [24]. In 1959 a phase diagram was published, based on a study with a series of quenching experiments, which included a solid solution range from 60 mol% < [Al_2O_3] < 63 mol% (71.8 wt% < [Al_2O_3] < 74.3 wt%, corresponds to $0.25 < \delta < 0.32$) and congruent melting behaviour [41, 42]. In 1974 a phase diagram with incongruent melting behaviour and with a solid solution range from 58.5 mol% < [Al_2O_3] < 62.7 mol% (70.5 wt% < [Al_2O_3] < 74.0 wt%, corresponds to $0.21 < \delta < 0.32$) was published based on experiments applying the diffusion couple technique [43] at temperatures below the melting point between 1678 °C and 1813 °C [44]. Additional quenching experiments revealed a metastable extension of the solid solution range to about 74.5 mol% Al_2O_3 [45]. These findings were mostly confirmed by another extensive study (Fig. 1.3), which also reported incongruent melting behaviour but a different solid solution range [46]. Differences between the studies from 1974 and 1987 were attributed to the different experimental approaches, i.e. both studies are considered to be valid with respect to the experimental conditions [16]. Especially the presence and absence of alumina nuclei has a crucial influence on the phases that crystallise and the observed borders of the solid solution range of
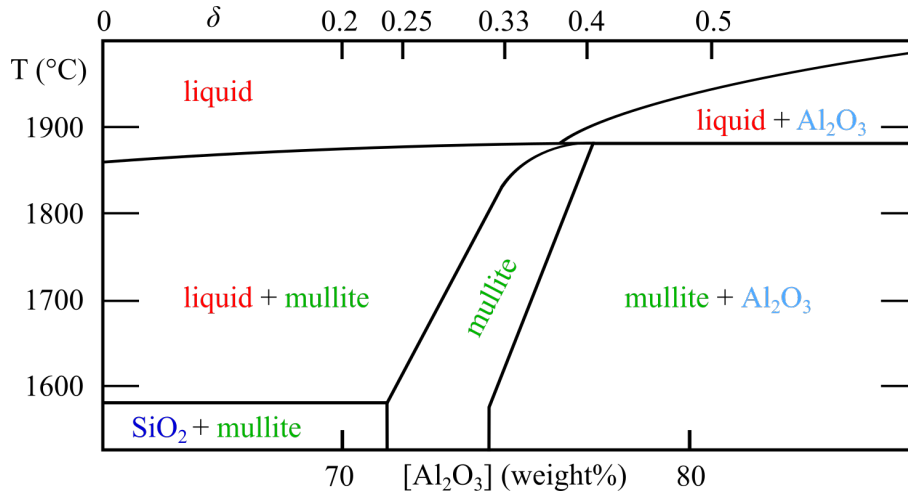
Figure 1.3: Part of SiO_2–Al_2O_3 phase diagram in the range $0 < \delta < 0.65$ adapted from [46]. The metastable range indicated by [16] is not included.

mullite [47]. Highly crystalline and inclusion-free single crystals of mullite can be grown with the Czochralski method despite the incongruent melting behaviaour [48].

1.1.8 Characteristic features in reciprocal space

> "Prolonged exposures, together with shorter ranges of rotation of the crystal, result in the appearance of a few extremely faint spots lying on the layer lines [...] corresponding to an index $\ell = 1$ or 3 referred to a unit cell the same size as sillimanite. There appears to be no doubt about the reality of these faint reflections [...]. The weakness of the spots makes it difficult to measure their positions exactly, but it does not seem to be possible to assign to them indices based on the unit cell of the same size as sillimanite."
>
> William H. Taylor (1928)

Despite the structural similarities between sillimanite and mullite, their diffraction patterns show profound differences. Reciprocal space sections of sillimanite show regularly spaced diffraction spots, the so-called 'main reflections'. Between the main reflections reciprocal space is empty. Taylor (1928) identified "extremely faint spots" in mullite known as 'satellite reflections' which, as he presumed correctly, cannot be indexed in a straight forward manner taking a simple multiple or fraction of the unit cell of sillimanite [30]. Agrell & Smith (1960) investigated a broad range of samples and confirmed the existence of sharp satellite reflections in some samples, for which the term 'S-mullite' was suggested. Other samples only showed diffuse satellite reflections as maxima of a diffuse scattering. These samples were labelled 'D-mullite' [39]. Examples of the different features in reciprocal space are shown in Figure 1.4 with different saturation settings to emphasise that main reflections are significantly stronger than satellite reflections and that the diffuse
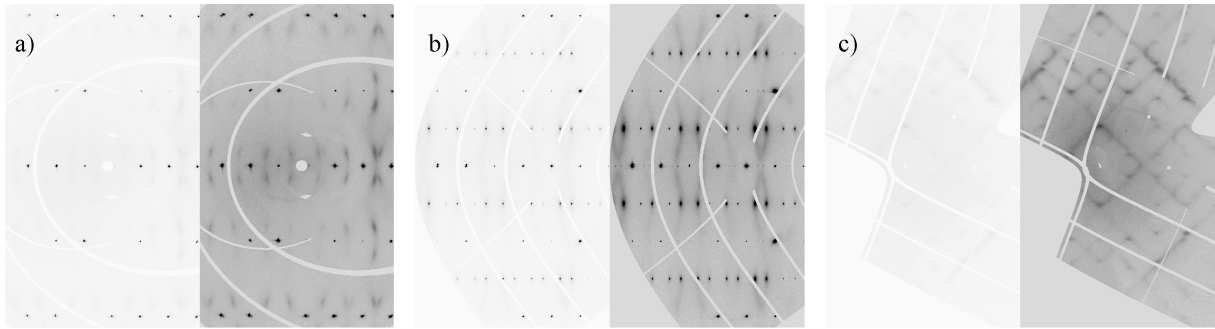
Figure 1.4: Details of different reciprocal space sections of mullite based on X-ray diffraction measurements (ESRF ID28, sample SA1, § 3.3.2) . Each section is shown with two different greyscale settings to distinguish between weak and strong features. a) $2kl$ section with main reflections and diffuse scattering. b) $h3l$ section with main reflections, sharp satellite reflections and diffuse scattering. c) $hk\frac{1}{5}$ with diffuse scattering only.
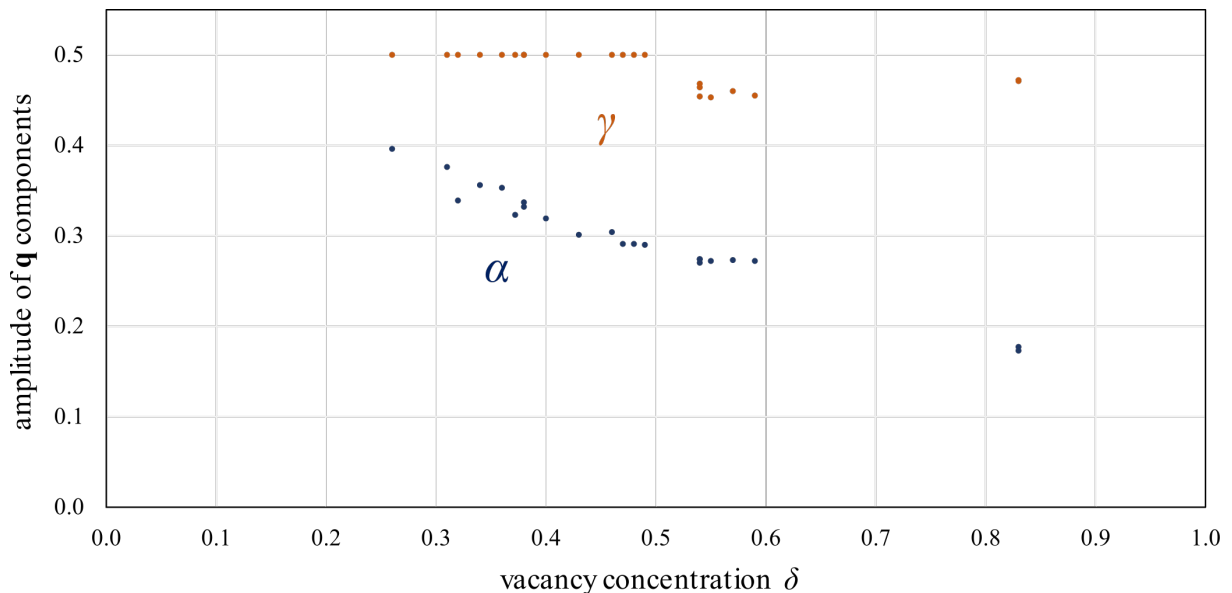
Figure 1.5: Dependence of α and γ on chemical composition expressed as vacancy concentration δ. Data based on Table A.1 described in the appendix.

scattering is relatively weak. Average crystal structure models were developed based on the main reflections (§ 1.3.2) and also the diffuse scattering was investigated in detail [3, 4].

Several electron diffraction studies revealed that the nature of the satellite reflections is very complex: The sharpness, highest observed order, position and symmetry of satellite reflections depends strongly on the synthesis conditions of the sample. The position of satellite reflections is characterised by the distance vector $\mathbf{q} = (\alpha\,\beta\,\gamma)$ between main and satellite reflections. The dependence of $\mathbf{q}$ on the chemical composition was first indicated by Smith and McConnell (1966) and systematically studied by Cameron (1977) [49, 2]. A comprehensive literature survey (details given in the appendix in § A.1) analysed 18 published diffraction patterns to analyse how α and γ change with the composition.

11

According to Figure 1.5 α decreases with increasing vacancy concentration with a short plateau $\delta > 0.5$. γ is constantly $\frac{1}{2}$ for $\delta < 0.5$ indicating orthorhombic symmetry. For higher vacancy concentrations $\delta > 0.5$, though the exact turnover composition is not known, the symmetry is lowered to monoclinic as $\gamma \approx 0.46$. The monoclinic symmetry is clearly visible in the diffraction patterns of [50, 36, 51]. Furthermore, some samples exhibit high order satellite reflections whereas other samples show only first order satellite reflections. These features in reciprocal space sections of mullite lack an explanation, which initiated this thesis.

Ion	CN	Mullite sites	Ion radius	r_c/r_a
Al^{3+}	4	Al2, Al3	0.39	0.29
Al^{3+}	6	Al1	0.535	0.39
Si^{4+}	4	Si2	0.26	0.19
Si^{4+}	6	–	0.40	0.29
O^{2-}	2	O3	1.35	–
O^{2-}	3	O1, O2, O4	1.36	–
O^{2-}	4	–	1.38	–

Table 1.4: Radii of relevant ions in mullite. For the calculation of the ratio of cation radius r_c/r_a the value of three-fold coordinated O^{2-} is used. Radii are taken from [52]

1.2 Crystal chemical foreword: Pauling's heritage

Linus Pauling defined a set of empirical rules which are useful to estimate the stability of a certain configuration of atoms [8]. These rules are applied here to the average structure of mullite to derive restrictions on the possible vacancy and Al/Si ordering. The anion radius r_a of O^{2-} increases slightly with the coordination number (CN), but the dependence is very weak in contrast to the dependence of the cation radii r_c of Al^{3+} and Si^{4+} on the CN (Tab. 1.4). The ideal $r_c : r_a$ ratio is $\sqrt{\frac{3}{2}} - 1 \approx 0.225$ for tetrahedral coordination and $\sqrt{2} - 1 \approx 0.414$ for octahedral coordination. These numbers suggest that in oxides Si^{4+} favours a tetrahedral coordination and Al^{3+} an octahedral coordination. It can be expected that SiO_4 and AlO_6 units are rather rigid because the coordinating oxygen atoms are in close contact to each other. Al^{3+} is rather large for tetrahedral coordination allowing a more flexible tetrahedra shape as the coordinating oxygen atoms are not in close contact. These trends indicate that the octahedral site in mullite is only occupied by Al and the distorted larger tetrahedra of the T^* site is avoided by Si. All average structure refinements of this thesis and of cited work apply this scheme, which is also in agreement with a neutron diffraction study on sillimanite [54].

In section 1.1.3 it was explained that the most likely structural adjustment of a sillimanite model structure to the presence of a vacancy is the introduction of two triclusters next to the vacancy. If triclusters were located anywhere but next to the void of the vacancy, then the T^* tetrahedron must share a face with a T tetrahedron. This must be avoided according to Pauling's rule on 'Sharing Edges and Faces'. The requirement for this tricluster environment introduces constraints on the vacancy distribution to avoid the overlap of triclusters with vacancies or with other triclusters. This constraint does not affect vacancies in different layers and also the joined stacking of vacancies and triclusters along **c** is not forbidden. Pauling's 'Rule of Parsimony' states that a structure tends to minimise the number of different constituents and to keep, if possible, each atom in one environment

Site label	Coordinating cations	ζ	Hypothetical concentration		
			$0 \leq \delta \leq \frac{1}{2}$	$\frac{1}{2} < \delta \leq \frac{2}{3}$	$\frac{2}{3} < \delta \leq 1$
O1	Al^{VI}, Al^{VI}, Al^{IV}	1.75	$2 + 2\delta$	$2 + 2\delta$	$2 + 2\delta$
O1	Al^{VI}, Al^{VI}, Si^{IV}	2.00	$2 - 2\delta$	$2 - 2\delta$	$2 - 2\delta$
O2	Al^{VI}, Al^{IV}, Al^{IV}	2.00	4δ	4δ	4δ
O2	Al^{VI}, Al^{IV}, Si^{IV}	2.25	$4 - 4\delta$	$4 - 4\delta$	$4 - 4\delta$
O2	Al^{VI}, Si^{IV}, Si^{IV}	2.50	0	0	0
O3	Al^{IV}, Al^{IV}	1.50	0	0	0
O3	Al^{IV}, Si^{IV}	1.75	$2 - 4\delta$	0	0
O3	Si^{IV}, Si^{IV}	2.00	δ	$2 - 3\delta$	0
O4	Al^{IV}, Al^{IV}, Al^{IV}	2.25	2δ	$2 - 2\delta$	$2 - 2\delta$
O4	Al^{IV}, Si^{IV}, Al^{IV}	2.50	0	$4\delta - 2$	$2 - 2\delta$
O4	Si^{IV}, Si^{IV}, Al^{IV}	2.75	0	0	0
O4*	Al^{IV}, Al^{IV}, Al^{IV}, Al^{IV}	3.00	0	0	$3\delta - 2$

Table 1.5: Electrostatic bond strength ζ of oxygen atoms in mullite. Roman numbers indicate the number of coordinating oxygen atoms. The hypothetical concentration of atoms with the described environment was determined in a such way to minimize the concentration of oxygen atoms with $|\zeta - 2| \geq 0.5$. This table is partly based on work of [53]. For $\delta > \frac{2}{3}$ tetraclusters with $\zeta = 3$ cannot be avoided.

corresponding to the most stable one. This rule suggests that the stacking of vacancies and triclusters is either preferred or avoided, but it is unlikely that stacked vacancies are present alongside single vacancies. The void structure of andalusite may be taken as indication that stacking of vacancies is not preferred. There are numerous ordered and disordered ways to implement this set of rules in the description of a mullite structure and thus Pauling's rules are not sufficient to derive a general vacancy ordering pattern. There are two exceptions: For the special case of 4/1-mullite ($\delta = \frac{2}{3}$) the vacancy distribution is strongly constrained because each layer is saturated with vacancies and triclusters. The description of the structure is thus simplified to the description of a stacking pattern. A similar description holds for the hypothetical structure of ι-Al_2O_3 ($\delta = 1$, [2]) but with layers saturated with vacancies and tetraclusters instead of triclusters.

Concerning the distribution of Si atoms, Pauling's rule on the 'Nature of Contiguous Polyhedra' states that Si^{4+} cations try to maximise the distance to other cations and therefore SiO_4 tetrahedra never share faces or edges. If two SiO_4 tetrahedra share one corner, this specific corner is not shared with a third polyhedra. The 'Electrostatic Valence Principle' postulates that if an anion is bonded to i cations, then the sum over the strength of the electrostatic valence bond $\zeta = \sum \frac{Z_i}{v_i}$ tends to compensate the electric charge of the anion, with Z_i being the cation charge and v_i the coordination number of the ith cation.

Table 1.5 lists the resulting values of ζ for all possible environments of O1, O2, O3 and O4 of mullite without Si occupying the T^* site. The table also includes the concentration of each oxygen with the given environment as a function of the vacancy concentration δ. Three different ranges must be distinguished because for $\delta > 0.5$ Si atoms must be present in triclusters [36] and for $\delta > \frac{2}{3}$ tetraclusters must be present [53]. O1 prefers to be bonded to a Si tetrahedron over an Al tetrahedron but this does not impose any constraints on the Al/Si ordering. O1 favours a stacking of AlO_4 tetrahedra whereas O3 favours Si-Si dicluster units (Si_2O_7) and strongly avoids Al-Al dicluster units (Al_2O_7). The best possible environment of O4 is made of three Al cations. From this analysis an ideal Al/Si ordering cannot be derived because the optimal environments exclude each other. An interesting observation is that the concentration of oxygen atoms in the ideal environment ($\zeta = 2$) increases in the range $0 \leq \delta \leq 0.5$ from 2 to 3.5 oxygen atoms per unit cell. This trend indicates that the distribution of Si favours higher vacancy concentrations up to $\delta = 0.5$.

In conclusion, the application of Pauling's rules allows to evaluate the crystal chemistry of a local arrangement of tetrahedra, but it is impossible to derive meaningful distribution patterns for vacancies and Si. More structural information is required to describe the ordering phenomena in the crystal structure of mullite.

1.3 Antecedent structural models

1.3.1 Nuclear magnetic resonance studies

Magic angle spinning nuclear magnetic resonance spectroscopy (MAS-NMR) studies on sillimanite are straight forward to interpret. A single peak in the NMR signal of $^{29}_{14}$Si indicates that Si occupies a single site and is completely ordered. The NMR signal of $^{27}_{13}$Al shows two peaks, that are attributed to an octahedral and a tetrahedral site. The $^{29}_{14}$Si signal of mullite contains a peak as in sillimanite, but it is broader and shows two additional peaks indicating that there are (at least) two additional chemical environments of Si in mullite. Simulations based on simple dicluster chains of 3/2-mullite with different Si environments agree qualitatively with measurements if a moderate tendency for Si ordering is introduced to the model, i.e. Si atoms rather repel each other and most Si atoms have 0 or 1 Si neighbour [5]. Another MAS-NMR study concluded that in the basically disordered structure less than 5 % of the overall Si is present in tricluster tetrahedra [55, Section 6.3.3].

The $^{27}_{13}$Al signal shows an additional peak, that was attributed to Al on the T^* site. The fraction of Al in the different environments was determined from the NMR signals, but the agreement with the expected values does not allow a reliable interpretation of the data due to the high uncertainties, i.e. a broad range of samples was investigated but especially the concentration of triclusters is not in agreement with the expected tricluster concentration [56]. So far, NMR studies could not establish a clear Al/Si ordering pattern and its relationship with the distribution of vacancies could not be identified.

1.3.2 Average structure of mullite

The average structure of mullite was first solved in 1962 starting with a difference Fourier map based on the known model of sillimanite and the measured structure factor amplitudes from an X-ray diffraction experiment of 2/1-mullite. From the map the split sites T^* and O4 were identified (Fig. 1.6). The occupancies of Al2, Si2, Al3, O3 and O4 were fixed to values corresponding to a vacancy concentration $\delta = 0.4$ and were not refined [57]. The model is in full agreement with the presence of oxygen vacancies at the O3 site and triclusters accompanying the vacancy. A similar study was presented with the refinement of the occupancies, resulting in a vacancy concentration slightly above 0.4 [58, 59]. The refinement of different samples with different compositions resulted in the same structure model with different occupancies for the T, T^*, O3 and O4 sites [60, 61]. These models only take main reflections into account and no information on the distribution of vacancies or Si are included, though usually Si is excluded from the T^* site as indicated by the NMR results.
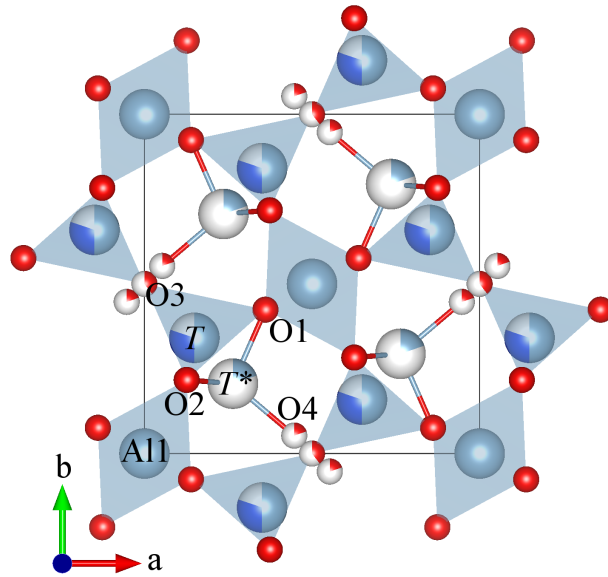
Figure 1.6: Average structure model of mullite with atom site labels. Coordinates and occupancies taken from [57]. An origin shift of $(\frac{1}{2}, \frac{1}{2}, 0)$ was applied.

The average static displacement of O1 and O2 due to Al/Si disorder was investigated based on a high resolution single crystal diffraction experiment (Mo K$_\alpha$, $2\theta < 110°$, $\frac{\sin(\theta_{max})}{\lambda} \approx 1.15$). In the refinement third and fourth order tensors for anisotropic displacement parameters were determined. The interpretation of difference Fourier maps allowed to identify coordinates of O1 and O2, that could be consistently related to expected bond lengths of either Al or Si on the bonded tetrahedral sites. It was concluded, that Al and Si are present on the T site, but Si is probably not present on the T^* site [62]. These results suggest that the anisotropic displacement parameters of the average structure represent a superposition of thermal motion, static displacement due to Al/Si disorder and static displacement due to a displacive modulation.

Single crystal neutron diffraction studies of samples with a vacancy concentration close to 0.4 could not clarify whether Si occupies the T^* site or not. In all cases, the occupancy is 0 within 3σ, and thus the presence of Si was neither confirmed nor excluded [7, 6].

1.3.3 Models with full vacancy ordering

Two models were published that exhibit a fully ordered vacancy distribution, but both models were not refined, and the distribution of Si atoms was not addressed.

1.3.3.1 Superstructure model from difference Patterson functions

Saalfeld (1979) suggested a vacancy distribution for 2/1-mullite from a Patterson synthesis including main and satellite reflections. The model consists of alternating units of sillimanite-like blocks and tricluster blocks. These blocks extend along **b** and **c**, and
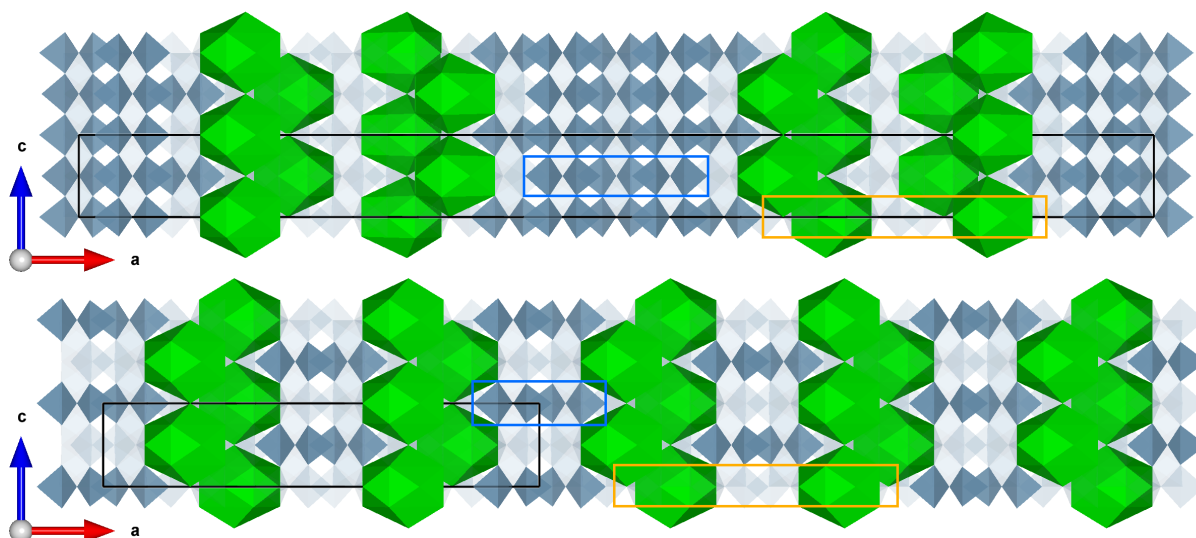
Figure 1.7: Models with full vacancy ordering. Voids are represented by greed polyhedra. Octahedra and tricluster tetrahedra are shown as faint blue tetrahedra. Dicluster tetrahedra are shown in grey blue. Black lines define the borders of the unit cell. Top: Vacancy distribution ($\delta = 0.4$) suggested by Saalfeld (1979). Bottom: Model ($\delta = 0.5$) suggested by Ylä-Jääski & Nissen (1983). Similar units (orange and blue frames) can be identified in both models, but the stacking pattern is different.

alternate periodically along **a**. In the same study it was mentioned that "satellite reflections of higher orders should appear, but they never were observed" [60]. It is worth mentioning that this model was the first model with a defined pattern for the vacancy distribution. The space group of the superstructure (Fig. 1.7) was not determined in the paper, but an inspection of preserved and broken symmetry elements points to the space group $B11\frac{2}{m}$.

1.3.3.2 Superstructure model from transmission electron microscopy

Superstructure models were developed from high-resolution transmission electron microscopy (HRTEM) images of samples ($\delta \approx 0.48$) with a diffraction pattern showing at least fifth order satellite reflections by Ylä-Jääski & Nissen (1983). The model ($\delta = 0.5$) is fully ordered (Fig. 1.7) and simulated HRTEM images are in remarkable agreement with the experimental observations [36]. The model was only published as image indicating the vacancy distribution, but a corresponding structural description[3] in space group $Bb2_1m$ was presented in an independent study [63].

---

[3]In the 'Inorganic Crystal Structure Database' the model has the collection code 41146.

1.3.4 Models with partial vacancy ordering

1.3.4.1 Incommensurate structure from difference Patterson functions

According to a theoretical approach derived from Landau theory [64, 65] the modulation in insulators originates from two competing structural components. A group theoretical analysis of the symmetry of mullite identified that the first component is vacancy ordering and the second component is the ordering of Si on the tetrahedral sites. For the determination of the component symmetry the vacancy ordering of the hypothetical ι-Al_2O_3 and the Al/Si ordering of sillimanite were considered [32].

Qualitative atom shifts and changes in the occupancies for the components were determined from difference Patterson functions based on X-ray and neutron diffraction experiments [66, 7]. However, structural parameters were not refined. The model is discussed and compared with the results of this thesis applying group theory in § 5.1.2. In modern crystallography modulated structures are not investigated by means of component structures because the superspace approach proved to be more powerful and more convenient to describe and characterise structural modulations.

1.3.4.2 Models of disorder from diffuse scattering analysis

The short-range ordering of vacancy was investigated from the diffuse scattering [3, 4]. The studies confirm the tricluster environment and that tetraclusters are avoided [67]. Models based on a large set of parameters describing the probability that a certain vector links two vacancies agree well with the experimentally observed streak pattern. The diffuse scattering of 3/2 and 2/1-mullite was revisited in detail in [18]. However, the models do not account for sharp satellite reflections and a relationship with a superspace description was not established.

1.3.4.3 Superspace model

The superspace approach (cf. § 2.4) allows to describe and investigate structures with satellite reflections and was developed in the 1970s and 1980s. The first crystal structure model based on this approach was published recently in 2015. Birkenstock *et alii* conducted single crystal X-ray diffraction experiments with a Czochralski-grown single crystal [6]. The refinement was carried out in the superspace group $Pbam(\alpha 0\frac{1}{2})0ss$ and describes a mainly disordered structure ($\delta = 0.41$) with little tendency to order vacancies. Al/Si ordering is not addressed and a relationship with the observations in reciprocal space described in § 1.1.8 was not established. The model will be discussed in detail in § 5.1.5 pointing out similarities and differences to the results of this thesis.

1.4 Thesis overview

1.4.1 Objectives

The introduction has shown that mullite was investigated by many different approaches within the last decades. Furthermore, there were five dedicated conferences and workshops about all aspects of mullite and related structures[4]. Despite this large record of investigations and the enormous interest by the ceramics industry, our understanding of the crystal structure of mullite is by no means complete and there are still many questions that are not answered at all or at least not satisfactorily.

1. What is the underlying vacancy distribution pattern in mullite?

2. To what degree does Al/Si ordering take place? Does Si occupy the T^* site in triclusters?

3. What is the fundamental explanation for the dependence of the modulation on the vacancy concentration?

4. Can structural models explain the borders of the solid-solution range?

The main objective of this thesis was to develop a modulated crystal structure model of mullite which explains the dependence of the modulation wave vector on the composition. Some results of the antecedent investigations appear somewhat contradicting, for example highly ordered and highly disordered vacancy distributions were suggested [60, 36, 6]. It is also the aim of this thesis to compare different results reported in the literature and to identify a unifying model that accounts for the broad range of observations. 90 years after the first observation of satellite reflections as "extremely faint spots on the layer-lines" [30] it is time to fundamentally explain the aperiodic nature of mullite.

1.4.2 Content scheme

In Chapter 2 relevant foundations of crystallography, diffraction, higher-dimensional superspace and computational methods are introduced. The samples, diffraction experiments and calculation parameters are described in Chapter 3. The results of Chapter 4 focus on the new findings on several aspects of the crystal structure of mullite. At first, the symmetry and its implications are analysed. A disordered and an ordered model of the crystal structure of mullite are developed for a specific chemical composition. These

---

[4]"First International Workshop on Mullite", Tokyo, Japan (1987); "Mullite Processing, Structure, and Properties", American Ceramic Society Pacific Coast Regional Meeting, Seattle, Washington, USA (1990); "Mullite '94, International Workshop", Irsee, Germany (1994); "Mullite 2000, Conference", Oban, Scotland (2000); "Mullite 2006, International Workshop", Vienna, Austria (2011); "Mullite 2011, Conference", Áviles, Spain (2011)

models are then extended to a broader composition range based on electron diffraction measurements, symmetry considerations and computational methods. In Chapter 5 many different aspects of the work are discussed and compared to round up the understanding of ordering phenomena in mullite. Chapter 6 summarises the thesis work and gives an outlook.

Chapter 2

Theoretical background:
Tools to solve a crystallographic problem

Due to the nature of atoms and visible light, it is impossible to optically 'see' single atoms with the naked eye or visible-light microscopes. The determination of the arrangement of the atoms in mullite crystals therefore must be determined with other methods. X-ray diffraction techniques allow to reconstruct the electron density and thus the crystal structure. This requires understanding the principles of diffraction and how diffraction patterns are related to the diffracting object. Computational methods provide a completely different approach to determine atomic arrangements by simulations based on the fundamental knowledge on atoms and their interactions. Mullite represents a special case of crystal structures due to the presence of the structural modulation. Its characterisation requires to embed the crystal structure of mullite in a higher-dimensional space called 'superspace'.

This chapter introduces parts of the fundamental concepts of crystallography, superspace crystallography and computational methods with a focus on relevant topics for the thesis. For detailed introductions the reader is referred to modern textbooks [34, 68, 69, 70, 71].

2.1 Lattices and coordinates

The concepts of the direct lattice and the reciprocal lattice are fundamentally important for crystallography as they represent the essential symmetry of crystals. A lattice $\Lambda(\mathbf{r})$ in $\mathbb{R}^3$ is spanned by three basis vectors $\mathbf{a}$, $\mathbf{b}$ and $\mathbf{c}$. The lattice exhibits translational symmetry and a translation by $\mathbf{L} = u\mathbf{a} + v\mathbf{b} + w\mathbf{c}$ leaves the lattice invariant ($u, v, w \in \mathbb{Z}$). A position vector $\mathbf{r}$ is defined by three coordinates x, y, and z according to the definition $\mathbf{r} = x\mathbf{a} + y\mathbf{b} + z\mathbf{c}$.

$$\Lambda(\mathbf{r}) = \sum_{u,v,w=-\infty}^{\infty} \delta(\mathbf{r} - \mathbf{L})$$

For each lattice in $\mathbb{R}^3$ there is a corresponding reciprocal lattice in $\mathbb{R}^3$ spanned by three basis vectors $\mathbf{a}^* = \frac{\mathbf{b} \times \mathbf{c}}{V}$, $\mathbf{b}^* = \frac{\mathbf{c} \times \mathbf{a}}{V}$ and $\mathbf{c}^* = \frac{\mathbf{a} \times \mathbf{b}}{V}$. $V = \mathbf{a} \cdot (\mathbf{b} \times \mathbf{c})$ is the volume of the unit cell. A position vector $\mathbf{H}$ is defined by three coordinates h, k and ℓ in reciprocal space [72]. Relevant vectors in higher-dimensional superspace are defined later.

2.2 Scattering and diffraction

Louis de Broglie (1924) discovered the particle-wave duality, stating that particles can be described as waves and vice versa [73, 74]. The description of a particle as wave has a corresponding wavelength $\lambda = \frac{h}{mv}$. The wavelength is the quotient of Planck's constant h and the momentum $p = mv$ of the particle with mass m and velocity v. This relationship is not observable in macroscopic cases, because λ for heavy objects is negligible small in comparison to the size of the object[1]. In the case of particles like neutrons, protons, electrons and even atoms or small molecules, the description as a wave is applicable. *Vice versa*, electromagnetic waves can be described as particles called 'photons'. According to the special theory of relativity, the mass of a particle depends on its velocity [75]. This can be neglected for 'non-relativistic' velocities of about less than 10% of the speed of light.

The principles of scattering are the same for all waves that are scattered by an object. In crystallography, the scattering of photons, electrons and neutrons is the basis for the diffraction by crystals. In this section the basics of X-ray diffraction are described and extended for the case of electron diffraction.

---

[1]For example, the de Broglie wavelength of the author of this thesis, running at a speed of 5 m/s, is about $2 \cdot 10^{-34}$ m.

2.2.1 Elastic scattering of X-rays by charged particles: Thomson scattering

X-ray diffraction is based on the scattering of electromagnetic waves by electrons. To my knowledge, there is no unique and sharp definition of the wavelength range of X-rays, but in crystallography the typical wavelength λ is between 0.4 Å and 2.5 Å [34]. Let us consider a plane monochromatic X-ray wave $\mathbf{E}_{\text{in}}$ traveling along the x axis of an orthogonal coordinate system. The magnetic field component $\mathbf{B}_0$ is parallel to the y axis and the electric field component $\mathbf{E}_0$ is parallel to the z axis. The amplitude of both fields oscillates in space and in time, i.e. they depend on the position x and the time t.

$$\mathbf{E}_{\text{in}} = \mathbf{E}_0 e^{2\pi i \frac{c}{\lambda}(t-x/c)}$$

c is the speed of light. At the origin of the coordinate system we place a charged particle with charge q and mass m. The electric field accelerates this particle with $\mathbf{a} = \frac{q\mathbf{E}_0}{m}$ leading to an oscillating movement of the particle. An accelerated charge is the source of electromagnetic radiation and hence the oscillation causes the emission of secondary radiation [76, 77]. This scattering process is called 'Thomson scattering'. The amplitude of $\mathbf{E}_s$ of the scattered wave observed at position $\mathbf{r}$ is $\mathbf{E}_s = \mathbf{E}_0 e^{2\pi i \frac{c}{\lambda}(t-r/c)-i\xi} \frac{q^2}{mc^2} \frac{1}{r} \sin(\phi)$ and depends on the distance $r = |\mathbf{r}|$ from the scatterer and on the angle ϕ between $\mathbf{E}_0$ and $\mathbf{r}$. For positions $\mathbf{r}$ on the z axis $|\mathbf{E}_s|$ is 0. The phase shift between the incident radiation and the scattered radiation ξ is π for electrons, i.e. the scattering is coherent [34]. The detection of X-rays is possible by measuring the effect of the absorption of X-rays by a detector material. The dominating absorption mechanism is the photoelectric effect which emits a photo electron with a kinetic energy that depends on the energy of the incoming photon [78]. The energy density and intensity of electromagnetic radiation is proportional[2] to the squared amplitude of the electric field component $|\mathbf{E}_s|^2$. For experiments it is therefore important to know the intensity of the radiation scattered by one electron. In general it can be written as

$$I_{\text{Thomson}} = I_0 \frac{q^4}{m^2 r^2 c^4} [K_y + K_z \sin^2(\phi)]$$

where K_y and K_z are the fraction of incoming radiation with $\mathbf{E}_0$ parallel to the y axis and z axis, respectively. If $K_y = K_z = \frac{1}{2}$ then the incoming wave is not polarised and $\mathbf{E}_{\text{in}}$ points uniformly into all directions perpendicular to the x axis. The factor $[K_y + K_z \sin^2(\phi)]$ is

---

[2]The energy density of an electromagnetic wave η in units of J/m^3 depends on the amplitudes of the electric field component and magnetic field component. $\eta = \frac{1}{2}\epsilon_0|\mathbf{E}|^2 + \frac{1}{2\mu_0}|\mathbf{B}|^2$, which can be simplified to $\eta = \epsilon_0|\mathbf{E}|^2$ using the relations $|\mathbf{B}| = \frac{|\mathbf{E}|}{c}$ and $c^2 = \frac{1}{\epsilon_0 \mu_0}$. The intensity I in units of W/m^2 is $I = \langle \eta \rangle c = \frac{1}{2}\epsilon_0 c|\mathbf{E}|^2$. The constants ϵ_0, μ_0, c are the vacuum permittivity, vacuum permeability and the speed of light, respectively.

also called 'polarisation factor'.

Protons and electrons have the same modulus of the charge, but protons are much heavier than electrons by a factor of about 1836 [79]. As $I_{\text{Thomson}} \propto \frac{1}{m^2}$ the Thomson scattering from protons can be neglected. Magnetic X-ray scattering due to magnetic interactions takes place, but again the contribution is weaker by several orders of magnitude so that the contribution to the scattered intensity can be neglected [80, 81].

2.2.2 Interference and the importance of the Fourier transform

Let us consider that there is a second charged particle at position $\mathbf{r}$ in addition to the charged particle at the origin. The direction and wavelength of the incoming X-ray beam is described by the wave vector $\mathbf{s}_0$ with $|\mathbf{s}_0| = \frac{1}{\lambda}$. The waves scattered by the two particles into the same direction have the same wave vector $\mathbf{s}$, but they exhibit a phase shift $2\pi\mathbf{r}^* \cdot \mathbf{r}$ with $\mathbf{r}^* = \mathbf{s} - \mathbf{s}_0$. A very small phase shift means that the scattered waves are mostly in phase and there is little deconstructive interference. In an extreme case if λ is much larger than the distance between the scattering particles the interference becomes negligible, which explains why the diffraction of visible light by crystals does not show noticeable interference effects.

The scattering power $F(\mathbf{r}^*)$ of an object made of N point scatterers is calculated by summing over the scattering factors f_j and a phase shift term. If f_j is defined in such a way that it expresses the number of electrons, the expression for $F(\mathbf{r}^*)$ can be generalised to account for any object described by an electron density $\rho_o(\mathbf{r})$ by integrating over the volume V of the object.

$$F(\mathbf{r}^*) = \sum_{j=1}^{N} f_j e^{2\pi i \mathbf{r}^* \cdot \mathbf{r}_j}$$

$$F(\mathbf{r}^*) = \int_V \rho_o(\mathbf{r}) e^{2\pi i \mathbf{r}^* \cdot \mathbf{r}} d\mathbf{r}$$

The latter formula indicates that $F(\mathbf{r}^*)$ is the Fourier transform of $\rho_o(\mathbf{r})$ [82]. The Fourier transform operator $\mathcal{F}$ acting on a function ('Fourier analysis') decomposes a periodic function into a sum of simple harmonic functions, each defined by a frequency, an amplitude and a phase. The inverse Fourier transform operation $\mathcal{F}^{-1}$ ('Fourier synthesis') constructs a periodic function by summing over these simple harmonic functions with the respective amplitude and phase. Hence, the mathematical relationship between the spaces of $\mathbf{r}$ and $\mathbf{r}^*$ can be defined with $\mathcal{F}[\rho_o(\mathbf{r})] = F(\mathbf{r}^*)$ and $\mathcal{F}^{-1}[F(\mathbf{r}^*)] = \rho_o(\mathbf{r})$ which was first pointed out by Ewald (1921) [83]. In crystallography $\mathbf{r}$ is a vector in direct space, the space in which the positions of atoms are described, and $\mathbf{r}^*$ is a vector in reciprocal space, in which diffraction patterns are described. The scattering angle θ is defined by $|\mathbf{r}^*| = 2\frac{\sin(\theta)}{\lambda}$.

2.2.3 Scattering of X-rays by a single atom

In a simplified picture an atom consists of protons and neutrons in the nucleus, and electrons in a cloud around it. If an incoming X-ray beam is scattered by an atom, the main contribution to the scattered beam originates from the interaction between the electric field of the incoming beam and the charge of the electrons. Thus, the scattering of X-rays by atoms can be approximated by Thomson scattering from the electron density of the atom.

A major result of quantum mechanics is that the state of an atomic electron can be described by a wave function $\psi(\mathbf{r})$ [84] from which the distribution of the probability that an electron is located at a certain position in space can be calculated as $\rho_e(\mathbf{r}) = |\psi(\mathbf{r})|^2$ [85]. The electron density $\rho_a(\mathbf{r})$ of an atom is then described as the superposition of the electron densities of all electrons of the atom. The scattering power of a single atom f, the so-called 'atomic form factor' or simply 'form factor', can be calculated as $f(\mathbf{r}^*) = \mathcal{F}[\rho_a(\mathbf{r})] = \int_V \rho_a(\mathbf{r})e^{2\pi i \mathbf{r}^* \cdot \mathbf{r}} d\mathbf{r}$. By convention, the phase shift is expressed relative to an electron at the nucleus of the atom [72].

For the description of crystal structures with the main objective to describe the position of atoms it is convenient to model the electron density of a crystal using spherical, independent atoms. Then, the electron density of an atom $\rho_a(r)$ only depends on the distance r from the nucleus and is independent of the chemical environment. The corresponding atomic form factor $f_a(\theta, \lambda)$ depends on the scattering angle 2θ and the wavelength λ. Values of f_a for different $\frac{\sin(\theta)}{\lambda}$ are tabulated for all atoms [72]. The advantage is that this reduces significantly the number of parameters that are needed to describe the electron density of a crystal because it allows to use pre-defined atoms as the main scattering objects instead of individual electrons. This 'independent atom model' is used throughout this thesis.

2.2.4 Diffraction of X-rays by crystals

Each electron within an arrangement of atoms scatters electromagnetic radiation into all directions and the constructive and destructive interference of scattered waves causes a variation in the scattered intensity. The coherent elastic scattering of in general a large number of scatterers is called 'diffraction'. The observed pattern of varying intensities caused by diffraction is called a 'diffraction pattern' and is observed at a distance *far* from the diffracting object, i.e. the wave front originating from the object is approximately a plane. We assume that a diffracted wave is not diffracted again as if it was a primary beam of its own (no multiple scattering) and the intensity of the primary beam is constant, which is known as the 'kinematic approximation'.

Crystals are a very special case of solid structures due to their periodic arrangement of

atoms. A perfect defect-free crystal structure is described by an infinite lattice $L(\mathbf{r})$ with lattice vectors $\{\mathbf{a}, \mathbf{b}, \mathbf{c}\}$ and a motif of atoms $\rho_\mathrm{M}(\mathbf{r})$ located on each lattice node (u, v, w). The basic repeating unit with volume $V = \mathbf{a} \cdot (\mathbf{b} \times \mathbf{c})$ is called 'unit cell'. The calculation of the scattering power $F_\mathrm{X}(\mathbf{r}^*)$ of the entire crystal is possible with the formulas of § 2.2.2. However, there are several billions of atoms in a small crystal and the consideration of each single atom is computationally time-consuming. The convolution theorem allows to decompose $F_\mathrm{X}(\mathbf{r}^*)$ into the product of a motif-dependent factor and a lattice-dependent factor.

$$F_\mathrm{X}(\mathbf{r}^*) = \mathcal{F}[\rho_\mathrm{M}(\mathbf{r})] \cdot \mathcal{F}[\Lambda(\mathbf{r})] = \frac{1}{V} F_\mathrm{M}(\mathbf{r}^*) \sum_{h,k,l=-\infty}^{\infty} \delta(\mathbf{r}^* - (h\mathbf{a}^* + k\mathbf{b}^* + \ell\mathbf{c}^*))$$

The δ function is 1 and thus the diffracted intensity not 0 only if the 'Laue conditions' are fulfilled, which is the case if h, k and ℓ are integer [86]:

$$\mathbf{a} \cdot \mathbf{r}^* = h$$
$$\mathbf{b} \cdot \mathbf{r}^* = k$$
$$\mathbf{c} \cdot \mathbf{r}^* = \ell$$

As a consequence, the diffraction pattern of perfect crystals is made of diffraction points as constructive interference only takes place if $\mathbf{r}^* = \mathbf{s} - \mathbf{s}_0$ is a reciprocal lattice vector $\mathbf{H} = h\mathbf{a}^* + k\mathbf{b}^* + \ell\mathbf{c}^*$ $(h, k, l \in \mathbb{Z})$. The scattering power of one unit cell $F_\mathrm{M}(\mathbf{H}) = \mathcal{F}[\rho_\mathrm{M}(\mathbf{r})] = \int_V \rho(\mathbf{r})\mathrm{e}^{-2\pi\mathrm{i}\mathbf{H}\cdot\mathbf{r}}\mathrm{d}\mathbf{r}$ depends on the electron density ρ_M, i.e. the atomic structure in the unit cell. Therefore, $F_\mathrm{M}(\mathbf{H})$ is called 'structure factor'. Crystal structure models are commonly not described by a continuous electron density, but by a set of atoms with discrete positions $\mathbf{x}_j = x_j\mathbf{a} + y_j\mathbf{b} + z_j\mathbf{c}$ with fractional coordinates x_j, y_j and z_j within the unit cell. The structure factor can then be calculated by a sum of all form factors with the respective phase shift of the atom. A broadly used shorthand notation of $F_M(\mathbf{H})$ is $F_{hk\ell}$.

$$F_{hkl} = \sum_{j=1}^{N} f_j(\theta, \lambda)\mathrm{e}^{2\pi\mathrm{i}(hx_j+ky_j+\ell z_j)}$$

The structure factor $F_{hk\ell} = |F_{hk\ell}|\mathrm{e}^{\mathrm{i}\phi_{hk\ell}}$ is a complex number with amplitude $|F_{hk\ell}|$ and phase $\phi_{hk\ell}$. The calculation of the electron density at a point (x, y, z) requires summing over the infinite number of structure factors.

$$\rho(x, y, z) = \frac{1}{V} \sum_{h,k,l=-\infty}^{\infty} F_{hkl}\mathrm{e}^{-2\pi\mathrm{i}(hx+ky+\ell z)} \tag{2.1}$$

A diffraction spot with indices h, k and ℓ of a measured diffraction pattern is called 'reflection' $hk\ell$ originating from the geometric interpretation of the Laue conditions known as 'Bragg's law' [87].

2.2.5 Real crystals

Many assumptions of the last sections are very useful for the description and theoretical explanation of X-ray diffraction, but their validity is limited. First of all, real crystals have a limited volume and a specific shape. Therefore, the diffraction pattern does not consist of points but of spots with a certain volume. Defects in crystals like point defects, line defects and volume defects (cf. § 1.1.5) break the translational symmetry of the crystal. As a consequence, the discreteness of the diffraction pattern is violated. Few, randomly distributed defects contribute to a diffuse background which is extremely weak and can be neglected in diffraction experiments. Correlated disorder causes a non-isotropic diffuse scattering of significant intensity, often with the shape of (partly) continuous streaks or planes [88].

Compton scattering, which is inelastic and incoherent, also contributes to a smooth background of diffraction patterns [89]. The Compton effect becomes more significant if there are very few scatterers, which is not the case in common X-ray experiments. For example, a very small sillimanite crystal with a volume of 1 µm³ $= 10^{12}$ Å^3 contains about 100 billion atoms. Typical crystals for X-ray crystallography are significantly larger than in this example and thus the Compton effect can be ignored [34].

Atoms are displaced from their equilibrium position due to their kinetic energy of the atoms, but also because disorder may be present. This displacement decreases the constructive interference of electrons of the same atom due to an increased phase shift, i.e. the form factor decreases with the scattering angle. The mean square displacement can be described mathematically with a 'displacement factor' $U = \langle \Delta r^2 \rangle$ in units of Å^2. If the displacement is isotropic the factor for the form factor is $e^{-8\pi^2 U (\frac{\sin\theta}{\lambda})^2}$ [90, 91]. Anisotropic displacement[3] is described by six direction-dependent and symmetry-dependent displacement factors U_{ij}. This displacement also causes diffuse scattering which is mostly centred around the diffraction spots.

2.2.6 Electron diffraction

The description of electron diffraction is similar to X-ray diffraction, but the interaction is different. The incoming wave hitting the crystal consists of electrons, which interact with the electrostatic potential field $\varphi_X(\mathbf{r})$ of the crystal. This potential can be approximated by a sum of the electrostatic potential fields φ_a of independent, spherical atoms from which atomic scattering factors f_{ae} can be calculated as

$$f_{ae}(\theta, \lambda) = 4\pi \frac{\sigma}{\lambda} \int_0^\infty r^2 \varphi_a(r) \frac{\sin(sr)}{sr} \mathrm{d}r$$

---

[3]The factor for the form factor is $e^{-2\pi^2 [U_{11}(ha^*)^2 + U_{22}(kb^*)^2 + U_{33}(\ell c^*)^2 + U_{12}hka^*b^* + U_{23}k\ell b^*c^* + U_{13}h\ell a^*c^*]}$.

where $s = 4\pi\frac{\sin(\theta)}{\lambda}$. Respective form factors f_{ae} are tabulated for different $\frac{\sin(\theta)}{\lambda}$ for all atoms [72]. The concepts of scattering as described in § 2.2.2 and subsequent sections also hold for electron diffraction by replacing f_a by f_{ae}. The interaction between electrons and matter is much stronger than the interaction between X-rays and matter which leads to significant multiple scattering described by dynamical diffraction theory [92]. On the other hand, the strong interaction allows to obtain diffraction patterns from crystals with very small volumes [93].

Due to dynamical diffraction the relationship $I_{hk\ell} \propto |F_{hk\ell}|^2$ is strongly violated. The calculation of structure factors based on dynamical diffraction theory is computationally very challenging from a practical point of view, which makes it desirable to decrease the dynamical affects and work with the kinematical approximation. The application of precessing electron diffraction is a quite successful approach to decrease multiple scattering and obtain quasi-kinematical intensities [94]. The electron beam is tilted relative to the microscope column axis by typically 1° and then rotated so that the beam describes a precession movement while the centre of the beam stays at the same sample position. Recording a series of diffraction patterns in analogy to common single crystal X-ray diffraction experiments has become a standard method to investigate crystal structures, known as automated diffraction tomography or precession electron diffraction tomography (PEDT) [95, 96, 97]. Low energy electrons with a typical wavelength $\lambda \approx 1\,\text{Å}$ have a penetration depth of a few Å. Electron diffraction studies therefore use high energy electrons with a corresponding $\lambda \approx 0.05\,\text{Å}$. If large single crystals are available, single crystal X-ray diffraction is usually the method of choice. Electron diffraction has the unique advantage, that in a transmission electron microscope (TEM) single nanocrystals can be used for diffraction experiments. Different diffraction methods can be combined to investigate complicated crystal structures [98].

2.3 Structure solution and refinement of crystal structure models

2.3.1 From experiment to data reduction

The main application of X-ray diffraction experiments for this thesis is to obtain a model that represents the crystal structure of the diffracting crystal. A full description of the atomic distribution in real crystals with this technique is impossible because this requires for example to include every single defect which only causes a negligibly weak signal in diffraction patterns. The concept of the unit cell can still be used, but instead of representing a strictly repeating unit it is an average unit cell. On this basis the so-called 'average structure' can be described and structural details on correlated disorder

and defects are not included in the model, though the disorder and correlations can be characterised and analysed quantitatively based on the diffuse scattering [99, 100].

A basic experimental setup for single crystal X-ray diffraction consists of an X-ray source, a goniometer that controls the position of a single crystal and a detector that records a diffraction pattern. The primary beam of an X-ray source has a certain size, shape, divergence and is not strictly monochromatic, which results in a broadening of the diffraction spots of the diffraction pattern. Only a fraction of reciprocal space can be measured which is limited by a maximum $\frac{\sin(\theta_{\max})}{\lambda}$. This limit determines the so-called 'resolution' of the measurement. For example, a Fourier synthesis truncated a low $\frac{\sin(\theta_{\max})}{\lambda} \approx 0.5\,\text{Å}^{-1}$ gives an electron density in which at most the average coordinates of atoms can be resolved, whereas the identification of fine details like chemical bonds requires a minimum resolution of about $\frac{\sin(\theta_{\max})}{\lambda} = 1.0\,\text{Å}^{-1}$. Another effect of using a truncated list of $F_{hk\ell}$ for the Fourier synthesis is the presence of a wavy background in the resulting electron density maps[4].

With X-ray detectors the reciprocal space can be measured by assigning an intensity amplitude to reciprocal space coordinates. The orientation and metrics of the reciprocal lattice are determined from reflection positions, from which the orientation matrix of the unit cell in direct space is derived. If the detectors were able to measure all structure factors $F_{hk\ell}$ within a certain resolution, the electron density of the unit cell content could be directly determined, but the measurements only contain intensities $I_{hk\ell}$ which are related to the structure factor amplitudes $|F_{hk\ell}|$. The phases $\phi_{hk\ell}$ must be determined by other means. To obtain reliable amplitudes $|F_{hk\ell}|$ the experimental conditions and correction factors must be considered because the reconstructed reciprocal space from the measurement is mathematically not identical to the Fourier transform of the electron density of the crystal. Reflections have a certain size determined by the mosaicity, the size and the shape of the diffracting crystal and the characteristics of the primary beam. The intensity $I_{hk\ell}$ is therefore obtained by integrating over a certain volume around the reflection. Some experimental characteristics like the intensity of the primary beam, the exposure time for a diffraction pattern or the overall volume of the crystal affect the intensities of all reflections in approximately the same way. Absorption and extinction depend on the shape and size of the crystal. The Lorentz correction, which considers that different reflections fulfil the Laue conditions for different periods of time, and Polarisation correction depend on the scattering angle θ. If all these factors and corrections are applied correctly the resulting intensities are proportional to the squared structure factor amplitudes $|F_{hk\ell}|^2$. The processing of diffraction patterns to obtain a list of structure factor amplitudes $|F_{hk\ell}|^2$ and an estimate of the respective uncertainties $\sigma_{hk\ell}$ is called 'data reduction'. The listed values of $|F_{hk\ell}|^2$ contain a common scale factor k_{s} which is not known *a priori* and is determined during the structure solution or refinement.

---

[4]The wavy background is also known as Fourier nipples.

2.3.2 The phase problem and methods to solve it

As pointed out in § 2.2.4 the reconstruction of the exact electron density requires to know the amplitudes $|F_{hk\ell}|$ and the phases $\phi_{hk\ell}$ of an infinite number of structure factors $F_{hk\ell}$, but X-ray diffraction experiments only give the $|F_{hk\ell}|$ for a limited number of reflections $hk\ell$. In crystallography this challenge is known as the 'phase problem'. Fortunately, the electron density of any crystal structure exhibits some very basic properties that allow to estimate the phase: 1) $\rho(\mathbf{r})$ is positive for any $\mathbf{r}$. 2) $\rho(\mathbf{r})$ consists mainly of discrete peaks at the position of the atoms. As crystal chemical constraints exclude a lot of unrealistic atom distributions, simple structures with known chemical composition and few atoms in the unit cell can thus be solved with an educated guess. The careful analysis of a few reflections can then be used to validate, correct or exclude a certain model. However, these methods quickly become impractical with increasing number of atoms in the unit cell. Over the decades several approaches were developed to estimate initial phases and solve the crystal structure, like the 'Patterson method' [101] or 'direct methods' [102, 103, 104]. The latter calculates estimated phases $\phi_{hk\ell}$ based on a statistical analysis of a set of strong and weak amplitudes $|F_{hk\ell}|$.

Here, the basics of the 'charge flipping' method to solve crystal structures are introduced [105, 106] because the algorithm also works in higher dimensional superspace and thus can solve modulated structures in $\mathbb{R}^{3+n}$ [107]. This algorithm developed much later than the other methods because charge flipping without the use of computers, e.g. with pen and paper, is very time consuming and impractical. The algorithm starts with a random electron density $\rho_0(\mathbf{r})$ in the unit cell with which phases $\phi_{hk\ell}$ are calculated for an input set of $|F_{hk\ell}|$. With $\mathcal{F}[\rho_0(\mathbf{r})]$ values for $|F_{0,hk\ell}|$ and $\phi_{0,hk\ell}$ are obtained. For the subsequent Fourier synthesis the phases $\phi_{0,hk\ell}$ are combined with $|F_{hk\ell}|$ to calculate a new electron density $\rho_1(\mathbf{r})$. The key of charge flipping is to modify $\rho_1(\mathbf{r})$ according to certain criteria, usually to change the sign of a point $\mathbf{r}$ if $\rho_1(\mathbf{r}) < D$. The threshold $D > 0$ must be determined empirically for each structure solution, but it is always positive so that negative charge density becomes positive and weak charge density becomes negative. The modified $\rho_1(\mathbf{r})$ is then the new starting model, like $\rho_0(\mathbf{r})$, and the algorithm repeats until convergence is observed.

An input files with quasi-kinematic structure factor amplitudes $|F_{hk\ell}|^2$ based on electron diffraction experiments often allows to solve the crystal structure even though the amplitudes are a very rough representation of the kinematic $|F_{hk\ell}|$ [93].

2.3.3 Refinement of crystal structure models

All structure solution methods provide estimated phases $\phi_{hk\ell}$ with which an electron density $\rho(\mathbf{r})$ of the unit cell is obtained. The interpretation of the electron density in

terms of atoms and molecules is often not trivial. The modelling of disordered sites, weak scatters and the correct atom assignment if two present atom types have a comparable form factor is part of the structure model refinement during which the initial structure model is completed (and, if necessary, corrected).

Refinement algorithms are based on the analysis of so-called 'difference Fourier maps' and the implementation of the method of least squares to maximise the agreement between calculated $|F_{hk\ell}^{\text{calc}}|$ from the model and measured $|F_{hk\ell}^{\text{exp}}|$ from the experiment. The main refinement parameters are the scale factor k_{s}, the coordinates of the atoms and anisotropic displacement parameters (ADP). In the case of modulated structures there are additional refinement parameters for the modulation functions of the atoms. If an atom site is not occupied in all unit cells, then the corresponding site of the average structure has an occupancy $s < 1$. A wrong identification of atoms in most cases has a visible effect on the displacement parameters, but the list of pit falls and possible mistakes during structure solution and refinement is much longer. The agreement between a measurement and a refined model is assessed by so-called 'R factors'. A low R factor indicates that the calculated structure factor amplitudes from the model agree well with the experimentally determined structure factor amplitudes. Weighting factors w may be implemented, or a subset of reflections may be chosen to account for the uncertainties $\sigma_{hk\ell}$. In this thesis R_{obs} is based on a subset of 'observed reflections' and wR takes all unique reflections into account. Reflections with $I_{hk\ell} > 3\sigma_{hk\ell}$ are considered observed.

$$R_{\text{obs}}(F) = \frac{\sum\limits_{hk\ell} |F_{hk\ell}^{\text{exp}}| - |F_{hk\ell}^{\text{calc}}|}{\sum\limits_{hk\ell} |F_{hk\ell}^{\text{exp}}|}$$

$$wR(F^2) = \frac{\sum w_{hk\ell}|F_{hk\ell}^{\text{exp}}|^2 - |F_{hk\ell}^{\text{calc}}|^2}{\sum w_{hk\ell}|F_{hk\ell}^{\text{exp}}|^2}$$

R factors may also be calculated for differently defined subsets, e.g. $R_{\text{obs}}(F, m = 0)$ is the R factor of all observed main reflections and $wR(F, m > 0)$ is the weighted R factor of all unique satellite reflections. Individual R factors may also be calculated for the observed reflections of a chosen part of a diffraction pattern. If the R factor of single frame of a single crystal diffraction experiment is noticeably high this might indicate problems with the experimental conditions in the instance when the frame was recorded. A low R factor does not necessarily indicate a correct model. The final model must always be checked carefully if it is physically and chemically meaningful and consistent with experimental observations obtained e.g. from spectroscopy studies [108].

2.4 Superspace crystallography of modulated structures

> "A crystal is an anisotropic, homogeneous body consisting of a
> three-dimensional periodic ordering of atoms, ions or molecules."
>
> Walter Borchardt-Ott [109]

This definition is found in the third edition of the text book 'Crystallography: An Introduction' (2011) and is in perfect agreement with the three-dimensional lattice description of § 2.1. However, this definition has a critical flaw because it excludes quasicrystals, incommensurately modulated structures and incommensurate composite structures. These structure classes are anisotropic, homogeneous and consist of a $(3+n)$-dimensional periodic arrangement of atomic surfaces, but their three-dimensional structure is aperiodic and lacks lattice periodicity. Their diffraction patterns consist of essentially sharp reflections, but the indexation with integer indices $hk\ell$ fails indicating that three lattice vectors are not enough. Shortly after the discovery of quasicrystals [110] a review titled 'Aperiodic crystals: A contradictio in terminis?' was published [111], but the fact that the stricter traditional definition cited above is still printed in recent text books already indicates that not everybody of the scientific community immediately accepted the existence of aperiodic materials. One of the most famous opponents was Linus Pauling:

> "Danny Shechtman is talking nonsense.
> There is no such thing as quasicrystals, only quasi-scientists."
>
> Linus Pauling
> quoted by Dan Shechtman [112]

The last sections have shown that the periodicity of crystals is very advantageous for the description of crystal structures in real and reciprocal space (e.g. Eqn. 2.1), but a three-dimensional unit cell cannot be defined for aperiodic crystals and thus this advantage is lost in $\mathbb{R}^3$. Fortunately, the concept of periodicity can be extended to higher-dimensional superspace in $\mathbb{R}^{3+n}$. The relevant aspects for the description, analysis and understanding of modulated structures in $(3+n)$d superspace are introduced in the next sections. Quasicrystals and incommensurate composite structures are outside the scope of this introduction as they are not relevant for the thesis. Although an alternative formalism was suggested to describe modulated structures [65], the superspace formalism has become the *de facto* standard for the description of aperiodic structures. The alternative formalism was applied to mullite [32, 7], which will be discussed in § 5.1.2.

x_1	0.0	0.5	1.0	1.5	2.0	2.5	3.0	3.5	4.0	4.5	5.0	5.5	6.0	6.5
$s^{\text{white}}(x_1)$	1	-	1	-	1	-	1	-	1	-	1	-	1	-
$s^{\text{black}}(x_1)$	-	1	-	0	-	1	-	1	-	1	-	0	-	1

Table 2.1: Description of the one-dimensional unit cell of a piano with black and white keys defined by a discrete occupancy functions of the position x_1.
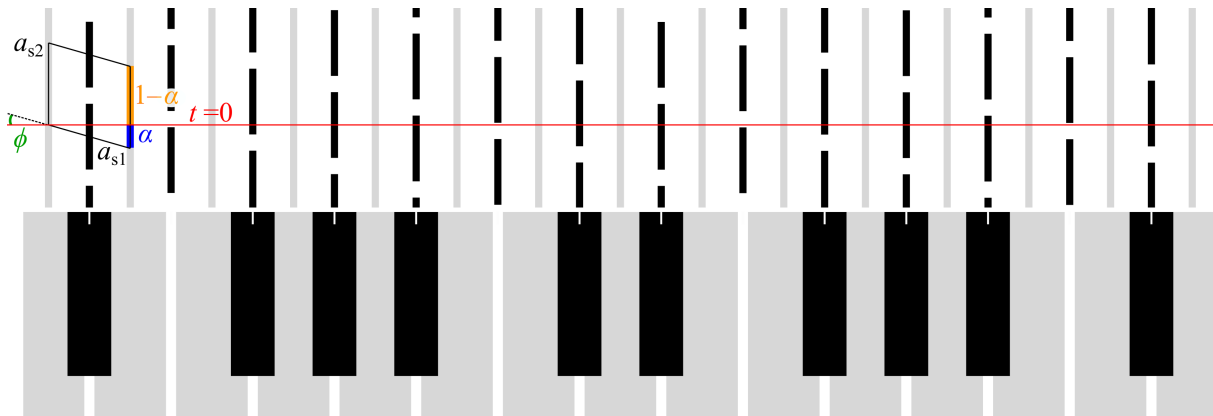
Figure 2.1: Top: Two-dimensional superspace description of the one-dimensional pattern of black and white keys of a piano. Relevant parameters describing the unit cell (black parallelogram) of the superspace model, like α (blue), are illustrated. Bottom: Piano model representing a one-dimensional subspace of the superspace model indicated by the red horizontal line. The one-dimensional pattern is not represented in one dimension to make it optically look like a piano. 'White' is represented by 'grey' for better visibility. More detailed description in the text.

2.4.1 The superspace piano

The first contact with superspace is often rather abstract, especially if the mind gets twisted by the additional dimensions. All superspace dimensions are spatial dimensions and independent of time[5]. To avoid the challenge of imagining four spatial dimensions here an example is presented how a one-dimensional structure, namely the description of black and white keys of a piano, can be described in two-dimensional superspace.

Ignoring the beautiful power of each key to play a different tone, a piano is an instrument that visually consists of evenly spaced white keys and black keys in between. There are less black keys than white keys, i.e. some interstitial sites between two white keys are vacant and not occupied by a black key. For a simplified description we assume that all white keys are equal ignoring the fact that the shape of white keys of a real piano depends on the local environment. The repeating pattern including the coordinate and occupancy of black and white keys can be described by a unit cell with lattice parameter $a_1 = 7$ (Tab. 2.1). We here define the distance between two white keys to be 1 (arbitrary units). White keys with coordinates $x_1^{\text{white}} = N$ ($N \in \mathbb{Z}$) are always occupied. Black keys with coordinates

---

[5]During several poster sessions I often had to clarify that the variable t, which will be introduced later, is *not* the time.
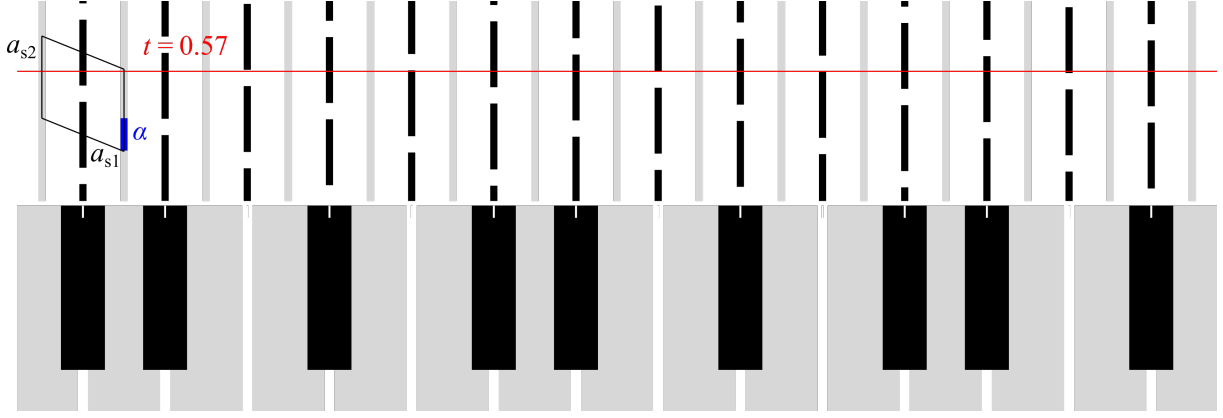
Figure 2.2: Superspace piano with $\alpha = 0.404$ corresponding to an incommensurate modulation. As $0.404 \approx \frac{2}{5}$ the repeating pattern of black and white keys is approximately 5, but the periodicity will be broken at some point. The Figure is too small to show the broken translational symmetry and thus it represents a commensurate approximation.

$x_1^{\text{black}} = N + 0.5$ are occupied except if $x_1^{\text{black}} = 1.5 + 7N$ or $x_1^{\text{black}} = 5.5 + 7N$. These rules describe two different periodicities along the a_1 direction as the pattern of white and black keys exhibit periodicities of 1 and 7, respectively. The two periodicities can be described in a two-dimensional space. In Figure 2.1 the top model is a two-dimensional superspace model and the bottom represents a one-dimensional cut (red line) through superspace, which results in an equivalent description of the piano pattern. The vertical white domains represent the occupancy of white keys, which is always 1 if $x_{\text{s}1}^{\text{white}} = N$. The black domains at $x_{\text{s}1}^{\text{black}} = N + 0.5$ have a vertical length of $\frac{5}{7}$ corresponding to the average occupancy of the black keys. If the horizontal section cuts through a black domain where the occupancy is defined to be 1, the corresponding black key is occupied in the one-dimensional subspace. The vectors $\mathbf{a}_{\text{s}1}$ and $\mathbf{a}_{\text{s}2}$ describe a repeating unit cell as the two-dimensional space exhibits translational symmetry. $\mathbf{a}_{\text{s}1}$ is chosen in such a way that $|7\mathbf{a}_{\text{s}1} + 2\mathbf{a}_{\text{s}2}| = a_1$. For arbitrary angles ϕ between $\mathbf{a}_{\text{s}1}$ and the horizontal section perpendicular to $\mathbf{a}_{\text{s}2}$ with $0° < \phi < 90°$ there are two possible cases. If there is a superspace lattice vector that is perpendicular to $\mathbf{a}_{\text{s}2}$, then the one-dimensional subspace is periodic, and the pattern of black and white keys can be equivalently described as a one-dimensional superstructure. These cases are denominated 'commensurately modulated structures'. If there is no lattice vector perpendicular to $\mathbf{a}_{\text{s}2}$ then a one-dimensional description will be strictly aperiodic and a periodic description in one-dimensional space is impossible. These cases are denominated 'incommensurately modulated'. The length of $\mathbf{a}_{\text{s}2}$ can be chosen arbitrarily without physical meaning and therefore the angle ϕ is not suitable to define a unit cell in superspace. Here the lattice parameters are defined by $\mathbf{a}_{\text{s}1} = (a_1, -\alpha)$ and $\mathbf{a}_{\text{s}2} = (0, 1)$. The parameter $\alpha = -\mathbf{a}_{\text{s}1} \cdot \mathbf{a}_{\text{s}2}$ defines the periodicity of the space perpendicular to $\mathbf{a}_{\text{s}2}$. If $\alpha \in \mathbb{Q}$ then the structure is commensurate, and incommensurate if $\alpha \notin \mathbb{Q}$. In Figure 2.1 $\alpha = \frac{2}{7}$ and thus is a commensurate case.
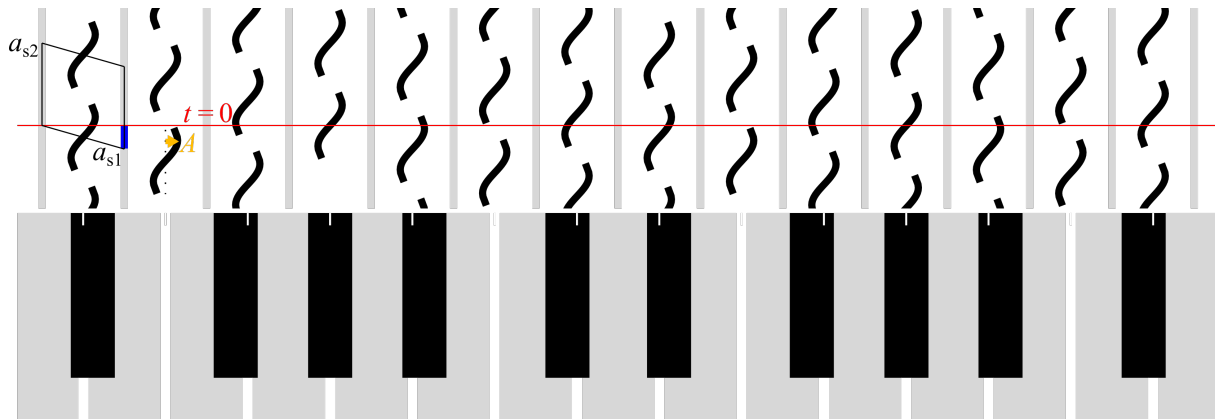
Figure 2.3: Superspace piano with additional, displacive modulation. The coordinates of the black keys are modulated by a sine function with amplitude $A = 0.15$.

If we change α to $0.404 = \frac{101}{250}$ then the model can be equivalently described in a 250-fold cell. A commensurate approximation with $\alpha = 0.4$ is helpful for visualisation purposes (Figure 2.2), but the description in two dimensions is more accurate and more elegant than a description of a very large supercell. The experimental determination of the modulation wave vector $\mathbf{q}$ is always subject to uncertainties and thus commensurate and incommensurate cases cannot be distinguished. Structural details are lost if truly incommensurate cases with e.g. $\alpha = \sqrt{\frac{1}{6}} \approx 0.408$ are described as commensurate approximation because a precise one-dimensional description would require an infinite number of parameters.

If there was some kind of interaction between the black keys, then their coordinates would be displaced depending on the interaction and on the local environment of each key. This displacement can be introduced in the two-dimensional description by changing the shape of the black and white domains. In this example a sine function is used for the domain defining the black keys (Fig. 2.3). In the one-dimensional representation the displacive modulation increases the spacing between black keys as if there was a repelling interaction. Any one-dimensional section or subspace perpendicular to $\mathbf{a}_{s2}$ describes an alternating pattern of black and white keys and each section corresponds to a different piano. For incommensurate cases different one-dimensional sections are related to each other by an origin shift, but different t-sections of commensurate cases are in general not equivalent.

The examples of the superspace piano describing a one-dimensional pattern in two-dimensional space show that periodic patterns can be described with modulation functions implemented in a higher-dimensional space. This principle can be applied to three-dimensional crystal structures with $n = 1$, 2 or 3 modulation waves which are then described in $(3+n)$d superspace.

2.4.2 Lattice vectors in superspace

The history of superspace began with the discovery that satellite reflections in the diffraction patterns of the room temperature structure of Na_2CO_3 could be indexed using four integer indices $hk\ell m$ and a fourth lattice vector $\mathbf{q}$ [113]. Subsequent studies and a generalisation of the concept of additional dimensions established the superspace formalism for the description of modulated structures [114, 115, 116, 117, 118, 119]. A reflection $\mathbf{H}$ of a modulated structure in reciprocal space can be indexed with $3 + n$ integers based on n modulation wave vectors $\mathbf{q}_i$ $(i = 1, ..., n)$ with irrational components $(\alpha_i, \beta_i, \gamma_i \in \mathbb{R})$.

$$\mathbf{H} = h\mathbf{a}^* + k\mathbf{b}^* + l\mathbf{c}^* + m_1\mathbf{q}_1 + ... + m_n\mathbf{q}_n$$

$$\mathbf{q}_i = \alpha_i\mathbf{a}^* + \beta_i\mathbf{b}^* + \gamma_i\mathbf{c}^*$$

In the following we focus on the case $n = 1$, which is most relevant for this thesis. Direct (3+1)d superspace is spanned by four basis vectors $\mathbf{a}_{si}$ $(i = 1, 2, 3, 4)$ in $\mathbb{R}^4$ [72].

$$\mathbf{a}_{s1} = (\mathbf{a}, -\alpha)$$

$$\mathbf{a}_{s2} = (\mathbf{b}, -\beta)$$

$$\mathbf{a}_{s3} = (\mathbf{c}, -\gamma)$$

$$\mathbf{a}_{s4} = (\mathbf{0}, 1)$$

$\mathbf{0}$ is the null vector. Coordinates in (3+1)d superspace are defined by a vector $\mathbf{x}_s$ with coordinates x_{s1}, x_{s2}, x_{s3} and x_{s4} with respect to the lattice vectors $\mathbf{a}_{si}$ $(i = 1, 2, 3, 4)$.

$$\mathbf{x}_s = x_{s1}\mathbf{a}_{s1} + x_{s2}\mathbf{a}_{s2} + x_{s3}\mathbf{a}_{s3} + x_{s4}\mathbf{a}_{s4}$$

Note that $\mathbf{H}$ is a vector in $\mathbb{R}^3$. Reciprocal superspace in $\mathbb{R}^{3+n}$ can be constructed from the condition $\mathbf{a}_{si}^* \cdot \mathbf{a}_{sj} = \delta_{ij}$ with $\delta_{ij} = 1$ if $i = j$ and $\delta_{ij} = 0$ if $i \neq j$. A reciprocal lattice vector $\mathbf{H}_s$ in $\mathbb{R}^{3+n}$ can be projected into reciprocal space in $\mathbb{R}^3$ leading to the above definition of $\mathbf{H}$.

2.4.3 Description of crystal structures in (3+1)d superspace

Crystals are three-dimensional objects consisting of atoms at coordinates $\mathbf{x}$ with respect to a basis $\{\mathbf{a}, \mathbf{b}, \mathbf{c}\}$. For incommensurate structures these vectors do not describe a periodic lattice because of the modulation. The atoms of a modulated structure are embedded in (3+1)d superspace by assigning superspace coordinates x_{si} $(i = 1, 2, 3, 4)$ with respect to lattice vectors $\mathbf{a}_{si}$ $(i = 1, 2, 3, 4)$. For $i = 1, 2, 3$ this is trivial, i.e. $x_{s1} = x$, $x_{s2} = y$, $x_{s3} = z$. The fourth coordinate depends on the first three coodinates and the modulation wave vector $\mathbf{q}$.

$$x_{\text{s}4} = \mathbf{q} \cdot \mathbf{x}$$

With this definition the crystal structure is represented within a three-dimensional section through the origin, the physical space section, of (3+1)d superspace and superspace itself is empty apart from this single section. The application of superspace translational symmetry fills the space and the superspace unit cell then comprises all structural information. In the unit cell the atoms of site μ are represented as 'atomic domains' that run about parallel to $\mathbf{a}_{\text{s}4}$ and are defined by three coordinates $\bar{x}^{\mu}_{\text{s}1}$, $\bar{x}^{\mu}_{\text{s}2}$, $\bar{x}^{\mu}_{\text{s}3}$ and a set of modulation functions $g^{\mu}_p(\bar{x}_{\text{s}4})$. These functions of structural parameter p must be periodic and satisfy the condition $g^{\mu}_p(\bar{x}_{\text{s}4}) = g^{\mu}_p(\bar{x}_{\text{s}4} + N)$ with $N \in \mathbb{Z}$. $\bar{x}_{\text{s}4} = \mathbf{q} \cdot \bar{\mathbf{x}} + t$ is the argument of the modulation functions. $\bar{\mathbf{x}}$ describes the average coordinates of an atom site in an average description of a modulated structure and t describes the initial phase of the modulation function. t can also be described as the distance from the initial physical space section going through the origin. As each value represents one crystal structure, t is often referred to as the physical space section. The most frequent type of modulation is displacive modulation described by functions $g^{\mu}_{x_1}(\bar{x}_{\text{s}4})$, $g^{\mu}_{x_2}(\bar{x}_{\text{s}4})$ and $g^{\mu}_{x_3}(\bar{x}_{\text{s}4})$. The atomic domains are then described by $x^{\mu}_{\text{s}i} = \bar{x}^{\mu}_{\text{s}i} + g^{\mu}_{x_i}(\bar{x}_{\text{s}4})$ ($i = 1$, 2, 3). The modulation functions are conveniently expressed as a finite set of harmonic functions.

$$g^{\mu}_p(\bar{x}_{\text{s}4}) = \sum_{n=1}^{n_{\max}} A^{\mu}_{p,n} \sin(2\pi n \bar{x}_{\text{s}4}) + B^{\mu}_{p,n} \cos(2\pi n \bar{x}_{\text{s}4}) \tag{2.2}$$

$A^{\mu}_{p,n}$ and $B^{\mu}_{p,n}$ are the amplitudes of the sine and cosine component of the harmonic of order n. In general, $n_{\max}$ is chosen to be equal to the highest observed order of satellite reflections $m_{\max}$. For example, in Figure 2.3 the displacive modulation function for the black key is described by $n_{\max} = 1$, $A^{\text{black}}_{x,1} = 0.15$ and $B^{\text{black}}_{x,1} = 0$. Apart from a displacive modulation the description of domains may require to include an occupational modulation function $g^{\mu}_s(\bar{x}_{\text{s}4})$ if the occupancy is modulated or functions $g^{\mu}_{U_{ij}}(\bar{x}_{\text{s}4})$ if the anisotropic displacement parameters U_{ij} (i, $j = 1$, 2, 3) are modulated.

There are cases where the approximation of the modulation function with a few harmonic functions is inconvenient, especially if the function is not continuous. For example, the occupancy of the black key is either 0 or 1. This is accurately modelled by a block wave function[6] (Eqn. 2.3) described by a coordinate x^{μ}_{BW}, which marks the centre of the block wave function, and the block length Δ^{μ}_{BW} [14]. $x^{\text{black}}_{\text{BW}} = 0$ and $\Delta^{\text{black}}_{\text{BW}} = \frac{5}{7}$ in the example

---

[6]An alternative term for block wave function is 'crenel function'.

of the superspace piano.

$$s^\mu(\bar{x}_{s4}) = \begin{cases} 1 \text{ if } & |\bar{x}_{s4} - x^\mu_{\text{BW}}| < \frac{\Delta^\mu_{\text{BW}}}{2} \\ 0 & \text{elsewhere} \end{cases} \tag{2.3}$$

2.4.4 t-plots

The physical space section t is constant for a structure model in physical space and represents one subspace of the superspace model. The analysis of crystal chemical aspects of the model requires to consider all different environments of a selected site, which is an infinite amount in the case of incommensurate structures. Instead of analysing the crystal chemistry of all sites in one crystal, the crystal chemistry of that site in different subspaces, i.e. different values of t, gives the same overview. Similar values of t usually describe a similar environment, but in physical space they describe two sites that are not close to each other. Therefore, t-plots give an overview of all possible crystal chemical environments, but for the analysis of a specific situation like the distance between two atoms it is necessary to compare the coordinates of two atoms at the same value of t and not at the same value of x_{s4}.

2.4.5   Superspace symmetry

In analogy to space groups that describe the symmetry of three-dimensional crystal structures there are superspace groups that describe the symmetry of modulated structures in superspace. Superspace group operators R_s in $(3+1)$d superspace are 4×4 matrices with three sub-components. R is the rotational part in full analogy to space group operators. $\epsilon = -1$ if R turns $\mathbf{q}$ into $-\mathbf{q}$ and is $\epsilon = 1$ otherwise. It can be determined by applying $R : \mathbf{q} \to \mathbf{n}^* + \epsilon \mathbf{q}$. The term $\mathbf{n}^*$ depends on the choice of $\mathbf{q}$ and the unit cell [120].

$$R_s = \begin{pmatrix} R_{11} & R_{12} & R_{13} & 0 \\ R_{21} & R_{22} & R_{23} & 0 \\ R_{31} & R_{32} & R_{33} & 0 \\ n^*_1 & n^*_2 & n^*_3 & \epsilon \end{pmatrix}$$

$$\mathbf{n}^* = (n^*_1 n^*_2 n^*_3) = \sigma R - \epsilon \sigma$$

$\sigma = (\alpha\,\beta\,\gamma)$ a 1×3 matrix containing the components of $\mathbf{q}$. R_s is the rotational part of a symmetry element $\{R_s | \mathbf{v}_s\}$ with translational components $\mathbf{v}_s = (v_{s1}\,v_{s2}\,v_{s3}\,v_{s4})$. The values v_{s1}, v_{s2} and v_{s3} are identical to the corresponding space group symmetry element. v_{s4} is the phase shift between modulation functions of atomic domains that are related

by the respective symmetry element. The values of v_{s4} are determined from reflection conditions for reflections with $|m| > 0$.

2.5 Computational methods

If there was an algorithm that predicted accurately the crystal structure, metastable transition states, optical or electrical properties and so forth for any composition of atoms, then a lot of (expensive and time-consuming) work in the laboratory could be replaced by a computer that would systematically search for better and novel materials. A wonderful discovery would be, for example, a superconductor with a resistivity of 0 Ωm at room temperature consisting of environmentally hazard-free and easily available elements. This ideal algorithm does not exist. However, several methods are available to simulate crystal structures, to calculate their physical properties and evaluate the stability based on the forces acting between the atoms. However, these methods strongly depend on the starting point and the prediction of a structure and its properties only as a function of the chemical composition is still extremely challenging. For all calculations of this thesis an initial structure model was provided that was developed with other methods. These models were then optimised, completed and tested with computational methods.

In this section the basics of force field methods[7] and density functional theory are introduced. With both approaches an initial three-dimensional crystal structure model can be geometrically optimised, i.e. the unit cell size and the atom coordinates are relaxed according to the calculated forces acting between the atoms leading to a structure model that corresponds to the minimal energy. Special aspects like relativistic effects or the presence of external perturbations like pressure, a magnetic field or an electric field are not covered in this brief introduction.

2.5.1 Hamiltonian mechanics

Isaac Newton developed the laws of motion, which are still broadly applied today for simple systems in classical mechanics [121]. For more complex systems of a larger number N of particles, each described by a time-dependent position $\mathbf{r}_i(t)$ and a velocity $\mathbf{v}_i(t)$, the well-known formula $\mathbf{F}_i = m_i \mathbf{a}_i = m_i \frac{\mathrm{d}\mathbf{r}_i^2}{\mathrm{d}^2 t}$ is still valid but is rather painful to solve. William Rowan Hamilton used the fact, that the force is a function of the energy of the system to derive a set of equations, which are easier to solve for many-body systems [122].

$$H(\mathbf{p}, \mathbf{r}) = T(\mathbf{p}) + V(\mathbf{r}) = \sum_{i=1}^{N} \frac{\mathbf{p}_i^2}{2m_i} + V(\mathbf{r}_1, ..., \mathbf{r}_N)$$

H, T, V are the Hamiltonian, the kinetic energy and the potential energy, respectively. $\mathbf{r}_i$ and $\mathbf{p}_i = m_i \mathbf{v}_i$ are the vectors describing the position and the momentum, respectively. The forces acting on each particle are calculated with $\mathbf{F}_i = -\frac{\partial U}{\partial \mathbf{r}_i}$. If the system is allowed to develop with time, the equations of motion of the system can be calculated with the

---

[7]Force field methods are also often denominated 'molecular mechanics'.

following derivates [123]:

$$\frac{\mathrm{d}\mathbf{r}_i}{\mathrm{d}t} = \frac{\partial H}{\partial \mathbf{p}_i} = \frac{\mathbf{p}_i}{m_i}$$

$$\frac{\mathrm{d}\mathbf{p}_i}{\mathrm{d}t} = -\frac{\partial H}{\partial \mathbf{r}_i} = -\frac{\partial V}{\partial \mathbf{r}_i} = \mathbf{F}_i(\mathbf{r}_1, ..., \mathbf{r}_N)$$

With Hamiltonian mechanics a crystal structure can be simulated as a system of electrons and nuclei or as a system of atoms. In any case, the interactions between the particles must be described, which is the basis to calculate the forces between them.

2.5.2 Force field methods

Crystal structures can be simulated by representing atoms by interatomic potentials of the Buckingham type [124]. The parameters of the force fields (FF) are either based on empirical observations or on different kinds of quantum mechanical calculations. The quality of the force field model is the key for a representative simulation of the crystal structure [70], but the accuracy is difficult to evaluate *a priori*. The total energy of a structure obtained with FF calculations should not be considered as a quantity with a corresponding physical observable that can be experimentally measured. The total energy becomes meaningful on a scale relative to a chosen reference structure with the same chemical composition. The great advantage of FF calculations is that the computational cost is extremely low in comparison to quantum mechanical calculations. With modern desktop computers the static relaxation of a structure with hundreds of atoms lasts a few seconds. This allows to geometrically optimise thousands of candidate structure models and compare their relative stability. The term 'simulations' usually refers to Monte Carlo simulations or to molecular dynamics. These methods were not applied in this thesis and all calculations refer to a static arrangement of atoms.

2.5.3 Quantum mechanics

In quantum mechanics the time-independent state of a stationary system with one or more particles is described by a wave function $\Psi(\mathbf{r})$ which is not known *a priori*. Its determination is one of the main challenges of quantum mechanical calculations. It can be determined with the time-independent Schrödinger equation (Eqn. 2.4), which poses an eigenvalue problem. Its solutions give the wave function $\Psi(\mathbf{r})$ as an eigenfunction of the Hamiltonian $\widehat{H}$ and the energy E as eigenvalue [84].

$$\widehat{H}\Psi = \widehat{T}\Psi + \widehat{V}\Psi = E\Psi \tag{2.4}$$

Analytical exact solutions are only possible for very simple systems like the Hydrogen atom. Wave function-based calculations of more complex systems like atoms with more than one electron, arrangements of several atoms and crystal structures must solve a many-body problem to determine numerically the wave function. The interacting particles are electrons (subscript e) and nuclei (subscript n) with the following contributions to the Hamiltonian.

$$\widehat{T} = \widehat{T}_\text{e} + \widehat{T}_\text{n} = -\sum_{i=1}^{N_\text{e}} \frac{\hbar^2}{2m_\text{e}} \widehat{\nabla}_i^2 - \sum_{k=1}^{N_\text{n}} \frac{h^2}{2m_k} \widehat{\nabla}_k^2$$

$$\widehat{V} = \sum_{k=1}^{N_\text{n}} \sum_{l<k}^{N_\text{n}} \widehat{V}_{kl}^\text{nn} + \sum_{i=1}^{N_\text{e}} \sum_{k=1}^{N_\text{n}} \widehat{V}_{ik}^\text{en} + \sum_{i=1}^{N_\text{e}} \sum_{j<i}^{N_\text{e}} \widehat{V}_{ij}^\text{ee}$$

The kinetic energy T of the system is thus the sum of the kinetic energies of N_e electrons and N_n nuclei. The potential energy V of the system depends on the electron-electron Coulomb interaction V^ee, the nucleus-nucleus Coulomb interaction V^nn and the electron-nucleus Coulomb interaction V^en. The electron mass is $m_\text{e} \approx 9.11 \cdot 10^{-31}$ kg and the mass of the nuclei m_k depends on the isotope. Over the decades, different methods developed and different approximations were implemented to make the numerical calculation of more complex systems possible. With the 'Born-Oppenheimer approximation' the coordinates of the nuclei are fixed. Then, $T_\text{n} = 0$ and the distances between nuclei are constant, which makes the sum of all V^nn a constant term. This simplifies the Schrödinger equation a lot because only the electronic wave function ψ_e must be solved for electrons in a static potential described by the fixed nuclei [125].

$$\left[-\sum_{i=1}^{N_\text{e}} \frac{\hbar^2}{2m_e} \widehat{\nabla}_i^2 + \sum_{i=1}^{N_\text{e}} \widehat{V}_i^\text{en} + \sum_{i=1}^{N_\text{e}} \sum_{j<i}^{N_\text{e}} \widehat{V}_{ij}^\text{ee} \right] \psi_\text{e} = E_\text{e} \psi_\text{e}$$

$\psi_\text{e} = \psi_\text{e}(\mathbf{r}_1, \mathbf{r}_2, ..., \mathbf{r}_N)$ is a function with $3N_\text{e}$ dimensions, which still makes the calculation computationally very challenging for larger systems. With the 'mean field approximation' the electronic wave function ψ_e can be approximated as a so-called 'Hartree-product' of non-interacting single particle wave functions $\chi_i(\mathbf{r})$ [126].

$$\psi_\text{e} = \prod_{i=1}^{N_\text{e}} \chi_i(\mathbf{r})$$

This approximation neglects that electrons are Fermions which requires that the wave function must fulfil the antisymmetry principle. It states that the sign of ψ_e must change by exchanging two electrons. This is accurately described by expressing ψ_e in the form of a Slater determinant which is part of the 'Hartree-Fock' method [127, 128, 71].

2.5.4 Density functional theory

The Born interpretation of the wave function is related to the probability to find a particle at a certain coordinate. In the present case with electronic wave functions it describes the electron density $\rho(\mathbf{r}) = \psi^*(\mathbf{r})\psi(\mathbf{r}) = |\psi(\mathbf{r})|^2$ [85]. The origin of density functional theory (DFT) is the Hohenberg-Kohn theorem: There is a functional $E[\rho(\mathbf{r})]$ with which the true ground state energy can be determined using the variational principle [129]. In subsequent work it was shown that the corresponding electron density $\rho(\mathbf{r})$ can be found by solving a set of so-called 'Kohn-Sham equations' [130].

$$\left[-\frac{h^2}{2m_e}\widehat{\nabla}^2 + \widehat{V}^{en}(\mathbf{r}) + \widehat{V}_H(\mathbf{r}) + \widehat{V}_{XC}(\mathbf{r})\right]\psi_i(\mathbf{r}) = \varepsilon_i\psi_i(\mathbf{r}) \tag{2.5}$$

Equation 2.5 is similar to the Schrödinger equation (Eqn. 2.4), but the solutions of the Kohn-Sham equation are three-dimensional single electron wave functions ψ_i. The index i indicates that for each of the N_e electrons the equation must be solved. The energy eigenvalues ε_i are not of importance here. The terms on the left side are the kinetic energy of the single electron, the Coulomb interaction $\widehat{V}^{en}(\mathbf{r})$ between that electron and the nuclei, the Hartree potential $\widehat{V}_H(\mathbf{r}) = e^2 \int \frac{\rho(\mathbf{r}')}{|\mathbf{r}-\mathbf{r}'|}d\mathbf{r}'$ and the exchange-correlation potential $\widehat{V}_{XC}(\mathbf{r}) = \frac{\delta E_{XC}(\mathbf{r})}{\delta\rho(\mathbf{r})}$. The Hartree potential accounts for the Coulomb repulsion of the single electron by the overall electron density based on the mean field approximation. The crucial aspects of DFT deal with the unknown exchange-correlation potential $V_{XC}(\mathbf{r})$, which is not straight forward to determine. Different functionals use different degrees of simplifications, which affects the accuracy of the calculations. The introduced error is difficult to quantify *a priori*, and therefore the use of a certain approximation is often justified by its agreement with experimental observations [71]. The simplest model for which $\widehat{V}_{XC}(\mathbf{r})$ can be determined exactly is the uniform electron gas, which is a rather rough approximation. A better approximation is to express $\widehat{V}_{XC}(\mathbf{r})$ based on the local electron density, which is called the 'local density approximation' (LDA). Another approach is to include the electron density gradient within the so called 'generalised gradient approximation' (GGA). Many different algorithms have developed, and it is therefore essential to describe how $\widehat{V}_{XC}(\mathbf{r})$ was calculated by the used DFT method. In any case, the Kohn-Sham equations for all electrons in the system must be solved iteratively as many terms depend on each other. For example, the calculation of $\rho(\mathbf{r})$ depends on ψ_i and on $V_{XC}(\mathbf{r})$, which in turn depends on $\rho(\mathbf{r})$. The iteration steps are approximately as follows:

1. Define an initial $\rho(\mathbf{r})$, e.g. a refined structure model from X-ray diffraction

2. Calculate ψ_i of all electrons by solving the Kohn-Sham equation (Eqn. 2.5)

3. Calculate $\rho_{new}(\mathbf{r})$ from all occupied Kohn-Sham orbitals ψ_i

4. Compare $\rho_{\text{new}}(\mathbf{r})$ with $\rho(\mathbf{r})$. If they are the same, the solution has converged to the ground-state. Otherwise $\rho(\mathbf{r})$ must be adapted with information gained from $\rho_{\text{new}}(\mathbf{r})$. The adapted electron density is the new input for step 2.

It is important to point out that the Kohn-Sham system describes a system of non-interacting electrons, but the converged density is the same as that of the real system with interacting electrons. Due to the Born-Oppenheimer approximation, the iterations converge to the ground state electron density for the fixed distribution of nuclei. The stability of this distribution can be evaluated from the converged calculations. The forces $\mathbf{F}_k$ acting on a nucleus at position $\mathbf{r}_k$ are determined using the 'Hellmann-Feynman Theorem' [131, 132]:

$$\mathbf{F}_k = - \int \rho(\mathbf{r}) \frac{\partial V^{\text{en}}}{\partial \mathbf{r}_k} \mathrm{d}\mathbf{r} - \frac{\partial V^{\text{nn}}}{\partial \mathbf{r}_k}$$

This allows to determine new coordinates for the nuclei (ionic relaxation), for which again the corresponding ground state $\rho(\mathbf{r})$ must be determined following the iteration steps described above. The geometric optimisation with DFT thus consists of several ionic relaxation steps and each ionic relaxation step consists of several electronic relaxation steps. Convergence is achieved once the forces on each atom are below a certain threshold value. It is not straight forward to estimate standard uncertainties for the parameters of geometrically optimised structures from the calculation alone [133, 134]. It is common practice to present results from computational methods without uncertainties and evaluate the accuracy of selected parameters based on the literature and experience.

2.5.5 Plane wave basis sets and pseudopotentials

Wave functions $\psi(\mathbf{r})$ are complex functions in $\mathbb{C}^3$, which can be represented in many ways. The Bloch theorem states that the wave function of an electron in the periodic potential of a crystal must have the same periodicity like the potential itself [135]. Hence, the wave function must fulfil the equation $\psi(\mathbf{r}) = \psi(\mathbf{r} + \mathbf{L})$, where $\mathbf{L}$ is a lattice vector (cf. $\Lambda(\mathbf{r})$ as described in § 2.1). For DFT calculations it is convenient to express $\psi(\mathbf{r})$ based on plane waves in reciprocal space (k space) [10].

$$\psi_i^{\mathbf{k}}(\mathbf{r}) = \sum_{\mathbf{G}} a_{i,\mathbf{k}+\mathbf{G}} \mathrm{e}^{\mathrm{i}(\mathbf{k}+\mathbf{G})\cdot\mathbf{r}}$$

$\mathbf{G}$ is a reciprocal lattice vector and $\mathbf{k}$ is a vector in reciprocal space within the first Brillouin zone. The task to determine the wave functions thus becomes the task to determine the coefficients $a_{i,\mathbf{k}+\mathbf{G}}$. An exact description requires to include an infinite number of vectors $\mathbf{k}$ and $\mathbf{G}$. Due to the limited life time of DFT users and for other practical reasons a set of discrete points in k space must be chosen. $\mathbf{G}$ can be interpreted in terms of resolution. Large values of $|\mathbf{G}|$ correspond to short-wavelength oscillations of

the wave function. Hence, the description of the fine details of ψ_i require a high resolution, but the details become negligible above a certain cut-off radius G_{max}. This allows to limit the summation to reciprocal lattice vectors with $|\mathbf{G}| \leq G_{max}$. The wave function of less localised valence electrons can be accurately described with a relatively small G_{max}, but the strongly localised core electrons require a large G_{max}. As the chemical environment has almost no influence on the core electrons, they can be represented by 'pseudopotentials' in analogy to the potential of the fixed nuclei. With this simplification the calculation times are significantly reduced by excluding core electrons from the Kohn-Sham equations and by allowing a lower G_{max} [11]. The cut-off radius G_{max} can be interpreted in terms of a cut-off kinetic energy $E_{cut} = \frac{\hbar^2}{2m_e}G_{max}^2$. Then, E_{cut} describes the electron state with the highest kinetic energy that is considered for the Kohn-Sham calculations.

An infinite number of $\mathbf{k}$ vectors must not be considered based on the observation that two discrete points in the Brillouin zone, that are close to each other, contribute in almost the same way to the wave function. This allows to define a grid of k points and assign each k point a weight. In practice several test calculations with increasing number of k points are carried out until convergence is observed and a higher k point density does not further improve the results [70].

2.5.6   Dispersion correction

Nonpolar molecules may form liquids and solids due to the 'Van der Waals' attraction that can be described by London dispersion forces [136]. Spontaneous polarisation of one molecule may induce the polarisation of a neighbouring molecule resulting in an attractive interaction. This interaction is *a priori* not included in the above described DFT method. Empirical potentials can be applied to each atom type to correct for this shortcoming [137]. Several studies have shown that dispersion correction improves the accuracy of the lattice parameters and the total energy resulting from DFT calculations [138, 139, 140].

Chapter 3

Experiments and calculations:
Probing the real and reciprocal space

Label	δ	R_{AS}	EDX	pXRD	BM01	ID28	PEDT
SA	0.25	3:2	×	×			×
SA1	0.25	3:2	×		×	×	
SA2	0.25	3:2			×		
SA3	0.25	3:2			×		
VSG.40	0.40	2:1		×			
VSG.50	0.50	5:2		×			×
VSG.57	0.57	3:1	×	×			×
VSG.62	0.62	6.9:2	×	×			
VSG.64	0.64	7.3:2		×			×
Qa.09	0.09	2.3:2					×
Qa.50	0.50	5:2		×			×
Qg.50	0.50	5:2		×			×
Qg1	0.50	5:2			×		
QSA	0.25	3:2					×

Table 3.1: List of samples and experiments. δ refers to the nominal vacancy concentration of mullite expected from synthesis or as stated by the supplier.
EDX = energy-dispersive X-ray emission spectroscopy, pXRD = powder X-ray diffraction, BM01/ID28 = Synchrotron single crystal X-ray diffraction, PEDT = precession electron diffraction tomography

3.1   Samples and synthesis

Contact metamorphism of clay minerals at low pressures may lead to the formation of mullite. Therefore, mullite occurs rarely as mineral in nature [16]. The first synthetic crystals of mullite were unknowingly produced in China as component of porcelain around 620 BC [18]. In Europe the first 'synthesis' of mullite took place in the region of Hesse, Germany, in the middle ages [141].

The first single phase synthesis of mullite was reported in 1924 from quenching experiments [24]. A broad range of synthesis methods developed since then, including flame fusion synthesis [142], Czochralski method [48], sol-gel methods [143, 144, 145, 146] and chemical vapour deposition [147, 51]. The formation of mullite from kaolinite decomposition was investigated in detail motivated by its relevance for the ceramics industry and manufacturing of porcelain [148, 149, 150].

For this thesis commercial, quenched and sol-gel samples were used. From the samples SA and Qg.50 single crystals appropriate for single crystal X-ray diffraction could be obtained. These specific crystals are labelled SA1, SA2, SA3 and Qg1. All other labels refer to a polycrystalline samples. Table 3.1 gives an overview on all samples and the conducted experiments.

3.1.1   Sample SA: Commercial mullite

Commercial aluminium silicate samples labelled 'Aluminum silicate - powder' with composition $Al_6O_{13}Si_2$ (3/2-mullite) were obtained from Sigma-Aldrich. No details are given on the synthesis as they are considered confidential by the producer. From the analysis in § 3.2 and § 3.3.1 it can be suspected that the sample was probably synthesised in an electric arc furnace at temperatures of 2000 °C or higher. Electro melting is a standard method for the industrial production of mullite which commonly contains α-Al_2O_3 and trace amounts of Fe_2O_3 and Na_2O as impurity phases together with an amorphous phase [18, Sect. 4.1.2.2]. Although the sample is declared as 'powder', single crystalline grains with diameters up to approximately 50 µm are easily identified under a light microscope.

3.1.2   Sample VSG: Sol-gel

Synthesised sol-gel samples of different compositions were provided by Dr. Javier Alarcón (Department of Inorganic Chemistry, University of Valencia, Spain). The precursors for the synthesis were tetraethyl orthosilicate $Si(OC_2H_5)_4$ mixed with water and aluminium ethoxide $Al(OC_2H_5)_3$ dissolved in ethanol. For more aluminous samples tri-sec-butylate $C_{12}H_{27}AlO_3$ instead of aluminium ethoxide was used. The recipe contains several drying and annealing steps at different temperatures, which are described in a series of papers published by the group of Dr. Alarcón [145, 146].

3.1.3   Samples Qa and Qg: Quenching

Another set of samples was obtained by quenching experiments carried out by Dr. Noelia de la Pinta and Prof. Tomasz Breczewski (Department of Condensed Matter Physics and Department of Applied Physics II, University of the Basque Country UPV/EHU). Pressed ceramic bars of cylindrical shape with a length of 50 mm and a diameter of 4 mm were prepared with different concentrations of α-Al_2O_3 and α-SiO_2 by 'Nanoker Research' in Oviedo, Spain. Samples based on these ceramic bars are labelled Qa. Similar precursors were prepared by pressing γ-Al_2O_3 (Alfa Aesar) and amorphous SiO_2 (Alfa) into a pellet (Samples Qg). Another sample was prepared by pressing the commercial powder into a pellet (QSA). The precursors were kept in a flame of about 2000 °C for a couple of minutes until melting was visually observed and then quenched in air to room temperature.

3.2 Scanning electron microscopy and X-ray emission spectroscopy

The experiments of this section were performed together with Prof. Gabriel Lopez (Department of Applied Physics II, University of the Basque Country UPV/EHU) on a 'JEOL JSM6400' scanning electron microscope (SEM). The electron source is a tungsten filament operated at an accelerating voltage of 20 kV and a beam current of 1 nA. Samples SA, VSG.57 and VSG.62 were finely dispersed on a graphite holder using double-sided carbon tape. In addition, the sample holder with the single crystal SA1 was fixed on the graphite holder. A graphite film of about 15 nm was deposited on the samples to make them conductive.

The electron beam hitting the sample interacts with the atoms and induces the emission of several signals that allow to characterise the sample. The intensity of secondary electrons, which is sensitive to the sample topography, was used to construct images of the samples (Fig. 3.1). The chemical composition of the samples was determined by analysing the intensity and energy of characteristic X-rays. The energy dispersive X-ray (EDX) emission spectra were recorded with with an 'Oxford PentaFETx3' detector while the beam was not in scanning mode and only a selected spot on the sample was illuminated by the electron beam. The measurement time was 60 s for each EDX spectrum. The number of recorded spectra N_{m} is given in Table 3.2. The chemical composition of sample SA was determined by measuring 22 EDX spectra from 17 different crystallites. Of most crystallites only one spectrum was obtained, but the single crystal SA1 was studied separately with five spectra. For a random crystallite, here labelled SAr, two spectra were obtained to estimate the homogeneity of individual crystallites. The relative concentration of cations was determined with an automated quantitative analysis of the spectra and the oxygen content was derived by stoichiometry.

The average vacancy concentration $\langle \delta \rangle$ is calculated from R_{AS} (§ 1.1.6) assuming that the mullite sample does not contain significant amounts of crystalline or amorphous impurity phases and that impurity elements do not affect the vacancy concentration (Tab. 3.2). However, this method does not distinguish between different crystalline and amorphous phases and therefore the $\langle \delta \rangle$ must not necessarily be representative for the mullite crystals in the sample. Minor impurities, mainly Na_2O and P_2O_5, amount to less than 1 mol%. In a few crystallites of SA trace amounts of K_2O and Fe_2O_3 were detected, but not included in Table 3.2.
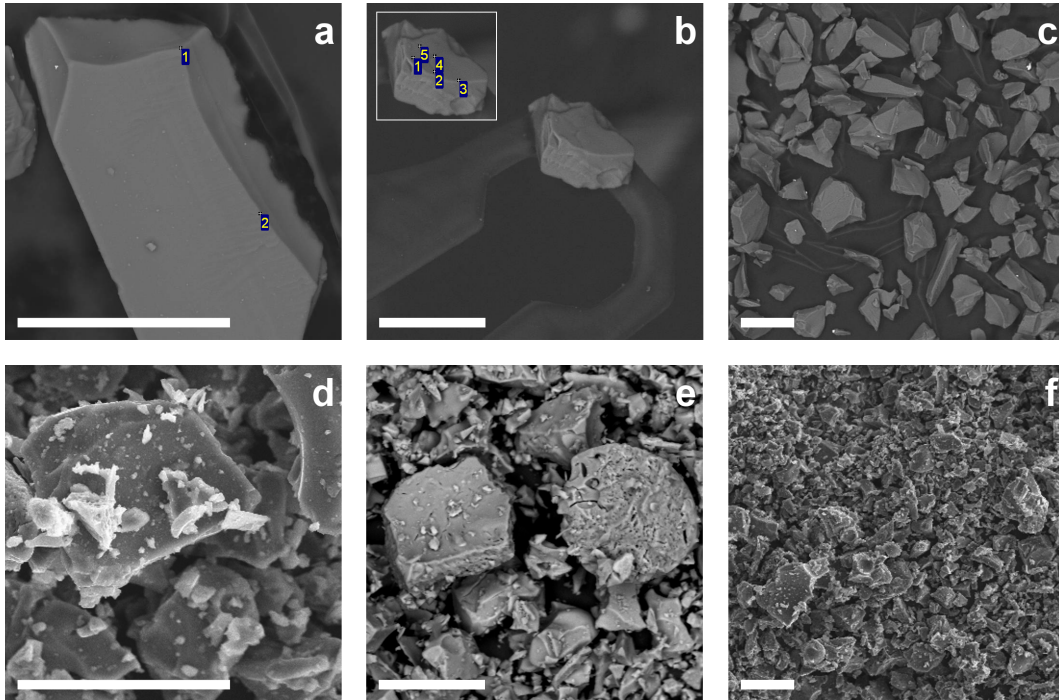
Figure 3.1: SEM micrographs. The white bar has a length of 50 µm in all cases. a) SAr, a random crystallite of the SA sample. Measurement spots for elemental analysis are marked. b) SA1 with single crystal sample holder loop. Measurement spots are marked in the inset. c) Different crystallites of SA sample. Different grains appear mostly single crystalline under a light microscope. d) VSG.57 grains. e) VSG.62. Larger grains are not single crystalline, which was checked with light microscopy. f) VSG.62.

Sample	$\langle\delta\rangle$	N_m	$[Al_2O_3]$	$[SiO_2]$	$[Na_2O]$	$[P_2O_5]$
SAr	0.299 (4)	2	61.93 ± 0.09	37.75 ± 0.06	0.32 ± 0.15	0.0
SA1	0.323 (13)	5	62.8 ± 0.5	36.6 ± 0.6	0.38 ± 0.10	0.21 ± 0.00
SA	0.33 (5)	17	63.2 ± 5.3	36.4 ± 5.1	0.2 ± 0.2	0.09 ± 0.11
VSG.57	0.56 (3)	10	74.7 ± 1.4	25.3 ± 1.4	0.0	0.0
VSG.62	0.60 (3)	17	76.6 ± 1.7	23.4 ± 1.7	0.0	0.0

Table 3.2: Elemental analysis of commercial and sol-gel samples. Oxide concentrations given in mol%. N_m refers to the number of different measurement spots. The measurements of crystallites SA1 and SAr were each included as one averaged measurement for the statistics of sample SA.

3.3 X-ray diffraction

3.3.1 Powder diffraction measurements

The introductory sections on diffraction (§ 2.2) are based on a monochromatic beam and a fixed orientation of one crystal lattice. In powder diffraction experiments a polycrystalline sample is analysed, and each crystallite diffracts if the Laue conditions for a reflection are fulfilled. The superposition of the diffraction patterns of a lot of crystallites results in a powder diffraction pattern made of rings instead of spots. Assuming a statistical distribution of the crystallite orientations it is sufficient to measure the diffracted intensity as a function of the diffraction angle 2θ.

Sample VSG25 was measured by Dr. Inmal Peral at the 'Materials Science and Powder Diffraction Beamline' BL04 at the synchrotron ALBA[1] located in Cerdanyola del Vallès close to Barcelona, Spain. The other samples were measured with a 'STOE STADI-P' powder diffractometer. An X-ray tube with a Cu anode generates a polychromatic X-ray beam with intensity maxima at the characteristic wavelengths. A Ge single crystal is used as a monochromator by orienting it in such a way so that the Laue conditions of the 111 reflection are only fulfilled for X-rays with $\lambda = 1.54059\,\text{Å}$ corresponding to the $K_{\alpha1}$ line of Cu. This monochromatic primary beam points to a sample holder stage located in the centre of a circle on which an X-ray detector can be moved at a constant distance to the sample. The detector is made of a conducting wire in an ionisation chamber filled with gas, which allows to measure the intensity of the incoming ionising radiation as a function of the diffraction angle 2θ with a resolution of about 0.02°. Samples were ground with a mortar before they were filled into a thin glass capillary and fixed in the sample stage of the diffractometer. During the measurement the capillary is spinning along the axis around which the detector is moving. Diffraction intensities were recorded in a range between $10° < 2\theta < 90°$.

For single crystal measurements data reduction and modelling are separate steps whereas the parameters describing the powder diffraction pattern like the lattice parameters or the shape of reflections are refined together with the structure model parameters. A refinement of this type is called 'Rietveld refinement' [151]. Refinements were carried out using the software 'Jana2006' [13]. The strategy was to initially find approximate parameters for the reflection profile shape and the lattice parameters before structural phases were identified from the presence of reflections that cannot be explained with the lattice parameters of mullite. In SA, Qa.50 and Qg.50 about 1.1 (2), 9.5 (2) and 9.47 (15) vol% α-Al_2O_3 are present. In all VSG samples except VSG.40 very broad additional reflections corresponding to highly disordered γ-Al_2O_3 are present. A refinement including γ-Al_2O_3 as second phase was not successful and therefore selected sections of the diffractograms

---

[1] ALBA translates to 'dawn' or 'sunrise' in the Catalan and Spanish language. It is not an acronym.

Site label	$\bar{s}^{\mu}(\bar{s}^{\mathrm{Al3}})$	$\bar{s}^{\mu}(\bar{s}^{\mathrm{O3}})$
Al2	$\frac{1}{2}$	$\frac{1}{2}$
Si2	$\frac{1}{2} - \bar{s}^{\mathrm{Al3}}$	$\frac{1}{6}(1 + 2\bar{s}^{\mathrm{O3}})$
Al3	refinement parameter	$\frac{1}{3}(1 - \bar{s}^{\mathrm{O3}})$
Si3	0	0
O3	$1 - 3\bar{s}^{\mathrm{Al3}}$	refinement parameter
O4	$\bar{s}^{\mathrm{Al3}}$	$\frac{1}{3}(1 - \bar{s}^{\mathrm{O3}})$

Table 3.3: Occupancy constraints by stoichiometry

were ignored and not fitted. Hence, the amount of γ-Al_2O_3 was not determined, but qualitatively it is increasing with the alumina content used in the synthesis. In the diffractogram of Qa.50 an additional impurity of 2.48 (13) vol% α-SiO_2 is present. Satellite reflections could not be identified in any of the powder diffraction patterns and therefore only average structure models were refined. Measured and calculated diffractograms of SA and VSG.50 are shown in Figures 3.2 and 3.3.

The refinement of the occupancy parameters was constrained to guarantee a stoichiometric composition. In Table 3.3 two constraint schemes are presented. For average structure refinements based on powder diffraction measurements the parameter $\bar{s}^{\mathrm{Al3}}$ was chosen as refinement parameter. The refinement of anisotropic displacement parameters (ADPs) failed in most cases except for Al1 in the case of SA. Selected results that are relevant to evaluate the refinements are presented in Table 3.4. The refined compositions deviate significantly from the EDX analyses (Tab. 3.2). The refinement of the diffractogram of the SA sample indicates a lower concentration of SiO_2 relative to the EDX results. The presence of an amorphous silica-rich phase is very common for the synthesis of mullite (e.g. [47], Fig. 16 in [16], Sect. 4.1.1 in [18]) and thus may explain the discrepancy. In the case of the VSG samples EDX indicates a higher concentration of Al_2O_3, which is explained by the presence of γ-Al_2O_3. In VSG.40 the diffraction pattern does not indicate the presence of γ-Al_2O_3 and the nominal composition agrees well with the refined composition within 2σ. This is taken as indication that structural models derived from X-ray diffraction experiments provide a reliable composition, which is important for the later investigation of the dependence of the modulation wave vector $\mathbf{q}$ on the vacancy concentration δ.

3.3.2 Single crystal diffraction measurements at synchrotron facilities

Appropriate samples for single crystal diffraction were selected with the aid of light microscopy. Crystals that appear inclusion-free and show uniform extinction with crossed polarisers were mounted on a 'MiTeGen' polymer loop with a drop of oil to fix the crys-

Sample	δ	$wR(F^2)$	wR_p	$a\,(\text{Å})$	$b\,(\text{Å})$	$c\,(\text{Å})$
SA	0.427 (4)	0.045	0.100	7.58442 (17)	7.68360 (17)	2.88727 (6)
Qa.50	0.470 (4)	0.035	0.089	7.6227 (2)	7.6762 (2)	2.89509 (7)
Qg.50	0.407 (3)	0.035	0.112	7.5753 (2)	7.6806 (2)	2.8858 (4)
VSG.40	0.412 (7)	0.029	0.107	7.5977 (2)	7.6984 (2)	2.89033 (6)
VSG.50	0.460 (3)	0.056	0.053	7.60314 (11)	7.67743 (11)	2.89039 (4)
VSG.57	0.526 (6)	0.039	0.145	7.6374 (4)	7.6738 (3)	2.89846 (10)
VSG.62	0.532 (6)	0.036	0.108	7.6601 (5)	7.6654 (5)	2.90322 (11)
VSG.64	0.494 (13)	0.033	0.073	7.6591 (6)	7.6402 (6)	2.89894 (17)

Table 3.4: Rietveld refinement and investigation of the average composition. wR_p is the agreement factor between the measured and the calculated diffraction pattern.
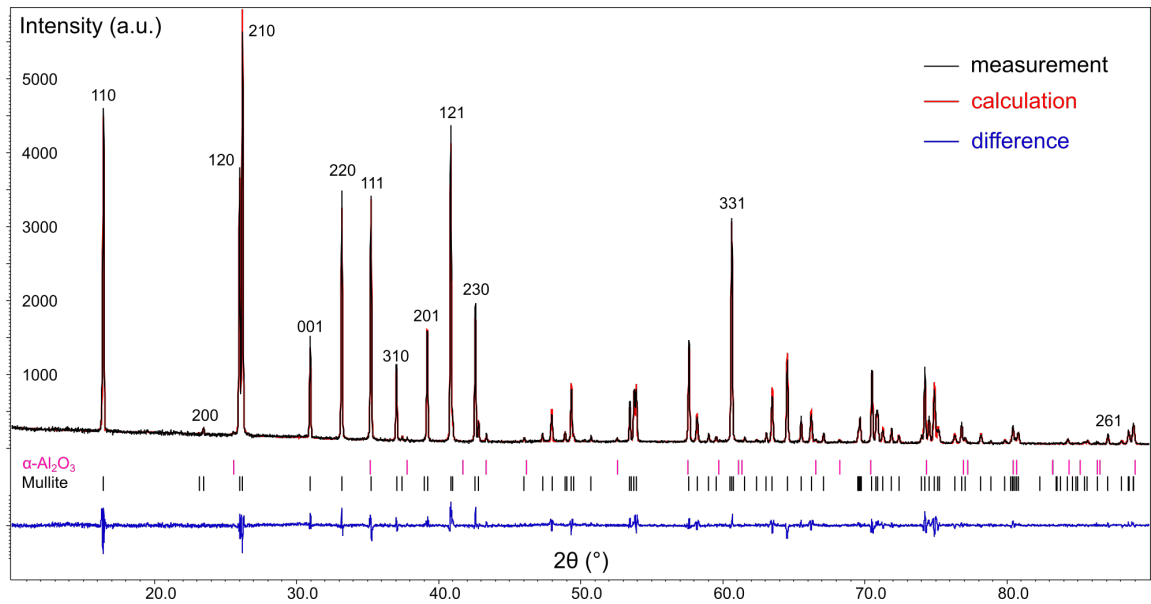

Figure 3.2: Powder diffraction pattern of sample SA. Difference curve between measured and calculated line shown at the bottom in blue. The position of the expected reflection positions of α-Al_2O_3 and mullite are indicated by vertical bars in pink and black, respectively.

56
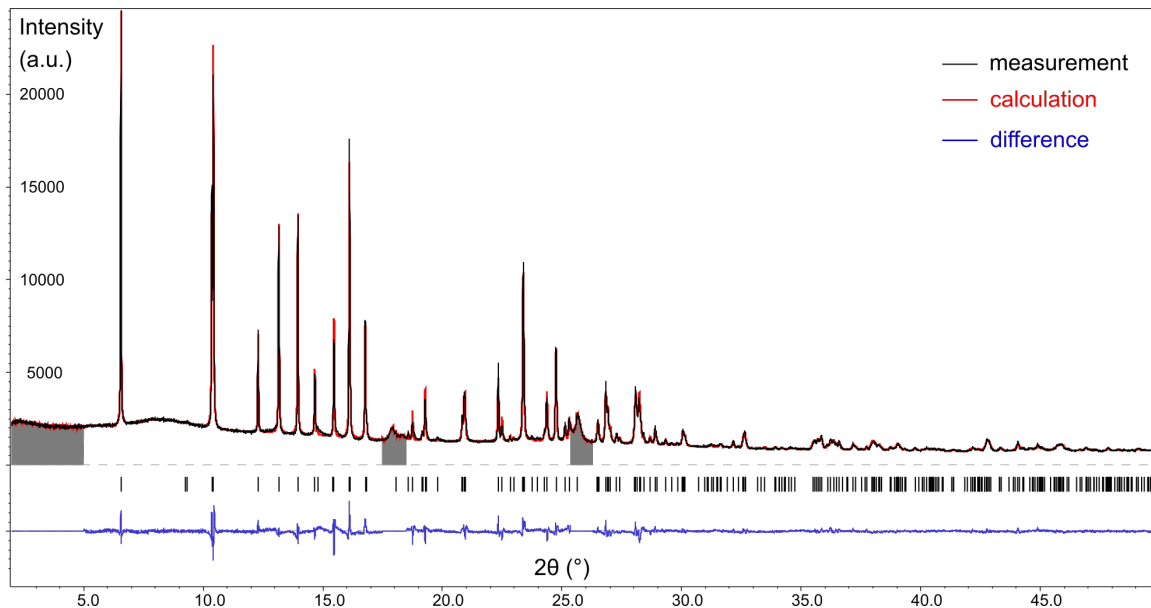
Figure 3.3: Diffraction patterns of sample VSG.50 recorded with synchrotron radiation ($\lambda = 0.61988\,\text{Å}$). The 2θ ranges marked by dark grey blocks where broad reflections from γ-Al_2O_3 are observed were excluded from the refinement.

tal. The loop is attached to the head of a needle pin which is fixed on a magnetic mount optimised for modern goniometers. Measurements were carried out at the 'European Synchrotron Radiation Facility' (ESRF) in Grenoble, France. The synchrotron has a diameter of 300 m with a circumference of 844 m. Electrons are accelerated to velocities close to the speed of light with a final energy of 6 GeV. A dipole bending magnet deflects the path of the electrons, which emit electromagnetic radiation depending on their speed and acceleration due to the curvature of their path. The optical hutch of the 'Swiss-Norwegian beamline' BM01 has the purpose to manipulate the incoming polychromatic radiation so that the outgoing beam is optimised for single crystal X-ray diffraction measurements. A Rh coated X-ray mirror with reflection angle $3\,\text{mrad} \approx 0.17°$ vertically collimates the beam. The (111) lattice planes of a pair of two parallel Si single crystals result in a highly monochromatic beam. One of the monochromators is bent to focus the beam on another X-ray mirror which further focuses the beam on the single crystal. The monochromators are oriented so that the outgoing X-rays have a wavelength $\lambda = 0.7231\,\text{Å}$. The beam size at the sample during the measurements was about $150 \times 150\,\mu\text{m}^2$. Samples SA1, SA2, SA3 and Qg1 were measured with a simple φ-scan during which the crystal is rotated about the vertical axis by 360°. A 'Dectris Pilatus 6M' detector is programmed to record frames during the rotation with a step size of usually $\leq 1°$. The experiment is controlled with an in-house software package called 'Pylatus' and the frames of the measurement were processed with the SNBL-toolbox [152].

Sample SA1 was also measured at beamline ID28 of the ESRF. In comparison to BM01, X-rays of ID28 originate from an undulator. On the path through the undulator the electrons

are oscillating in a plane due to a precisely chosen arrangement of several magnets leading to the interference of the synchrotron radiation of each oscillation. The intensity of the beam is very high for wavelengths at which the waves interfere constructively. The X-ray optics of ID28 with several monochromators and X-ray mirrors of different types result in a highly brilliant X-ray beam with a spot size of 20×40 µm² and a wavelength $\lambda = 0.6968$ Å. During the measurement the sample was rotated about one axis (φ-scan) by 360° and frames were recorded with a 'Dectris Pilatus 1M detector' in steps of 0.1°.

The software package 'CrysAlisPro' was used for the data reduction of the measurements [153]. An empirical absorption correction based on spherical harmonics was performed using the 'SCALE3 ABSPACK' scaling algorithm as implemented in CrysAlisPro. Undistorted reciprocal space sections were reconstructed with the unpublished program 'rec2D3D' written by the ID28 beam line scientist Dr. Alexei Bossak. The experimental conditions, parameters of the data reduction and details on the crystal structure model refinement are given in Table 4.6 (§ 4.2.1)

3.4   Precession electron diffraction tomography

The experimental setup of electron diffraction experiments is very different from X-ray diffraction setups. Up to now there is no dedicated 'electron diffractometer' and electron diffraction experiments are carried in transmission electron microscopes (TEM). The main components of a TEM are an electron gun, a sequence of electron lenses above and below a sample stage and an electron detector. These parts a placed in a vertical column structure in which an ultra-high vacuum is maintained. Samples must be very thin in the range of several nanometres to be electron-transparent.

3.4.1   Sample preparation

The VSG samples are fine powders with crystallites of appropriate size, i.e. they are electron transparent. Nevertheless, the samples were briefly ground with a mortar and then dispersed in ethanol. A single drop of the dispersion was then trickled on a Cu grid covered with a holey carbon film ('SPI supplies'). Each square of the grid has a width of 58 µm and is separated from neighbouring squares by Cu bars with a width of 25 µm. The bar thickness is about 20 µm. The ethanol quickly evaporates while the crystallites remain on the carbon film.

The preparation of Qa and Qg samples was more challenging as the quenched samples were in direct contact with the precursor. Special care was taken to separate the molten part of the sample from the part which did not melt during the synthesis in order to avoid the presence of any precursor components in the further sample preparation. After this step the sample was ground for several minutes, dispersed in ethanol and trickled on a Cu grid.

3.4.2   Electron diffraction experiments

Each Cu grid was fixed on a specimen holder and slowly introduced into the sample stage of a 'Philips CM120' transmission electron microscope (TEM). A mechanical vacuum pump establishes pre-vacuum conditions in the TEM column. An oil diffusion pump is located close to the sample stage to reduce the amount of contaminating gas originating from the sample. Ultra-high vacuum conditions ($< 10^{-7}$ Pa) are achieved and maintained with an ion-getter pump. The microscope is equipped with an LaB_6 thermionic cathode operated at an acceleration voltage of 120 kV. The accelerated electrons travel at relativistic velocities of around 176×10^6 m/s. The corresponding wavelength λ is 0.0335 Å [154]. The path of the electrons through the column is controlled by an overall of eight magnetic lenses, three stigmators, different scan coils and piezo-mechanical alignment controls for e.g. the gun tilt. The stigmators are used to correct the elliptical shape of the beam and

maintain a symmetric, circular beam on the sample. The condenser lens system focuses the beam on the sample. The objective lens magnifies the image formed by the transmitted electrons. In imaging mode, the lenses below the objective lens magnify the image plane of the objective lens. In diffraction mode, the back focal plane is magnified and the diffraction pattern of the sample is projected onto the screen or onto the camera.

A key part of this TEM is the 'NanoMegas SpinningStar' precession device, which controls shift-tilt coils within the illumination system to generate a precessing electron beam on the sample. Descan coils in the imaging system of the microscope are controlled in a synchronized way so that the projected image is not moving or rotating. The precession frequency is set to 100 Hz so that the detector shows a static image representing the superposition of all diffraction patterns of the different beam orientations on the sample.

All components for standard operation, including the precession device, are controlled electronically via computers. The TEM operator controls the position of the sample stage and the current through the lenses to manipulate the magnification and focus or to switch between imaging and diffraction mode. The projected image is either shown on a fluorescent screen at the bottom of the microscope column or it is recorded with an 'Olympus SIS Veleta' Camera with a charge-coupled device (CCD) chip. At the beginning of each session the microscope was aligned, including the electron gun tilt, condenser system, imaging system and the precession device. The alignment was checked before every diffraction experiment.

For each measurement a crystallite on the grid was chosen according to the single crystalline appearance in imaging mode and an initial check of the diffraction pattern. The sample stage can be rotated about one axis perpendicular to the primary beam from approximately $-60°$ to $+60°$. Thus, the experimental setup is comparable to X-ray diffraction experiments that perform a φ-scan by 360°, but here the angular range is limited. The experimental conditions often further limited the range to less than 120° due to overlapping contributions of surrounding crystallites or the blocking of the beam by the Cu grid. A software was used to control the CCD camera and the microscope to automatically tilt the sample by 1° (or less) and then record a diffraction pattern with typical exposure times between 2 and 4 seconds per frame. Data reduction was carried out with the software PETS [155, 97]. The main steps include the identification of reflections positions in reciprocal space, the determination of the orientation matrix, determination of the modulation wave vector $\mathbf{q}$ and extraction of integrated intensities. For kinematical refinement one integrated intensity is determined per reflection $hk\ell$ combining the intensity of a reflection with the same index on subsequent frames and finally the merging of symmetrically equivalent reflections. For dynamical refinement the integrated intensities are determined without merging because dynamical diffraction intensities depend on the frame orientation. A broad range of different samples was measured to investigate the reciprocal space and refine structural models. Details on the measurements and the average

structure refinements are given in Tables 4.13 and 4.14 in § 4.4.3.

3.4.3 Refinements based on electron diffraction data

The input files generated with PETS were used to refine the average structure of mullite using 'Jana2006' [13]. The parameters for dynamical refinement were set as recommended by the authors of PETS [97]. The calculation of the dynamical diffraction intensities depends on the crystal structure, the crystallite thickness, the orientation of the sample, a scale factor and the experimental geometry like the precession angle. There are many parameters that could be refined independently for each frame, which would drastically increase the number of refinement parameters. The recommended approach is to refine one common sample thickness parameter for all frames, fix the orientation of each frame and refine one scale factor for each frame. With this approach there is only one additional refinement parameter per frame. If the ratio between the number of observed unique reflections and the number of refinement parameters was less than 10, the parameter $R_{S_g}^{\max}$ was increased until the ratio was close to 10 or larger. $R_{S_g}^{\max}$ is the ratio between the excitation error and the maximum amplitude of the precession motion and thus defines which reflections on a frame are considered to be fully covered by the precessing Ewald sphere and which reflections should be neglected. If this increase was not enough to achieve the desired reflections to parameter ratio, frames with the smallest number of observed reflections were removed from the refinement. Once convergence was achieved, the orientation of each frame was optimised, i.e. for one refinement cycle only the frame orientations are refined. The orientation is defined by the experimental setup and a deviation from the expected orientation described by an inclination Θ towards a direction Φ. Frames with refined Θ larger than half the tilt step between two subsequent frames were removed as the orientation clearly deviates from the expected orientation. The most frequent reason to remove a frame was to increase the reflections to parameters ratio. In very few cases frames were also removed if the R factor for all reflections on a frame was significantly higher relative to all other frames indicating problems with the experimental conditions.

For the refinement of the average structure the occupancy of Al3 was chosen as refinement parameter and the occupancies of Si2, O3 and O4 were constrained to meet the requirements of stoichiometry (Tab. 3.3 in § 3.3.1). The refinement of anisotropic displacement parameters in most cases resulted in non-positive definite tensors and sometimes even the refinement of isotropic displacement parameters resulted in negative values of U_{iso}. This mostly concerned Al3 and O4. If necessary the refinement was constrained so that Al3, Al2 and Si2 are refined with a common U_{iso} and likewise O4 and O3 have the same U_{iso}. After convergence of the refinement the orientation of the frames was optimised before the final refinement cycles.

HRTEM studies showed that mullites with $\delta > \frac{1}{2}$ and monoclinic modulation wave vector $\mathbf{q} = (\alpha\, 0\, \gamma)$ with $\gamma < \frac{1}{2}$ are twinned [50, 36]. Single twin domains thus exhibit monoclinic symmetry with the space group $P1\frac{2_1}{a}1$ or possibly even lower symmetry. However, in several studies on Al-rich mullite a deviation of the angles between unit cell vectors from 90° was not observed as no splitting of reflections, typical for unit cell angles close to 90°, could be detected [53, 2, 51]. Here, it is assumed that PEDT experiments of samples with $\gamma < \frac{1}{2}$ are twinned as suggested in the literature. The symmetry of reciprocal space reconstructions from the measured diffraction patterns exhibits in all cases point symmetry $\frac{2}{m}\frac{2}{m}\frac{2}{m}$. Therefore, all average structure model refinements were carried out in space group *Pbam*. The results are presented in Tables 4.13 and 4.14 in § 4.4.3.

Structure	GULP				X-ray diffraction [160]		
	a (Å)	b (Å)	c (Å)	E (eV)	a (Å)	b (Å)	c (Å)
Sillimanite	7.5193	7.5358	5.7695	−323.77	7.4883 (7)	7.6808 (7)	5.7774 (5)
Andalusite	7.7802	7.9892	5.4773	−321.54	7.7980 (7)	7.9031 (10)	5.5566 (5)
Kyanite	7.1374	7.8006	5.4964	−324.23	7.1262 (12)	7.8520 (10)	5.5724 (10)

Table 3.5: Test of force field model with Al_2SiO_5 polymorphs. Angles of the lattice parameters of the triclinic kyanite structure are not compared.

3.5   Calculations with empirical force fields

The initial models used as input structures were developed during the thesis and are presented in Chapter 4. Therefore, in this and the following section the general approach and the used programs are described. The 'General Utility Lattice Program' GULP version 4.3.5 [9] was used to statically relax different models of the mullite crystal structure and the Al_2SiO_5 polymorphs. The Buckingham-type potentials describing the interactions between Al, Si and O were taken from a molecular dynamics study by Matsui (1996), in which a broad range of silicates including sillimanite, andalusite and kyanite could be successfully simulated with acceptable accuracy [156]. All previous computational studies on mullite applying force field methods used the potentials from the cited study [157, 158, 159]. An example GULP input file including the parameters describing the Buckingham potentials is included in the appendix (§ A.2).

Structures of the Al_2SiO_5 polymorphs sillimanite, andalusite and kyanite were geometrically optimised for test purposes (Tab. 3.5). Some lattice parameters differ by more than 0.1 Å from the corresponding value determined by X-ray diffraction. The overall performance of the force field model gives acceptable results and the geometry of the relaxed structures looks reasonable, but the accuracy for the study of structural details and their influence on the overall stability is rather considered as a rough indicator.

Crystal structures of mullite with different Si distributions were statically relaxed with GULP to estimate the relative stability. 46814 structures were geometrically optimised in total. The generation of input files and the analysis of output files was automated. Different algorithms implemented in the GULP code were tested to determine the relaxed atom distribution. The default convergence criteria were not always achieved. However, in test cases the energetic difference between the converged ground state and a local minimum was negligible so that the application of the default relaxation algorithm is considered to give representative results. Details on the generation of input structures and their analysis are described in § 4.3 and § 4.4.

3.6 Calculations applying density functional theory

Density functional theory (DFT) calculations were carried out using the commercial 'Vienna Ab initio Simulation Package' program VASP version 5.4.4 [10, 11] running on a Linux-based cluster with 96 cores ('Intel Xeon CPU E7-8890') and 1 TB of memory. Exchange and correlation effects were treated within the generalized gradient approximation (GGA) as suggested in [161] and [162]. The respective functionals are labelled PBE and PBEsol, respectively. If dispersion correction was included the suffix 'D' is added to the label (PBE-D, PBEsol-D) [138]. Wave functions were represented in a plane-wave basis truncated at 520 eV. The same set of ultrasoft pseudopotentials provided by the VASP program was used. The k grid was chosen as recommended in [163] except for calculations with hexagonal lattices (α-SiO$_2$ and α-Al$_2$O$_3$) for which a Γ centred grid was chosen. The spacing between k points was less than 0.02 Å^{-1} in all cases. The electronic relaxation was considered as converged if the total free energy and the eigenvalues ε_i of the Kohn-Sham equations (Eqn. 2.5) changed by less than 10^{-4} eV in two consecutive cycles. If the forces acting on the atoms based on an electronically relaxed model were less than 0.02 eV/Å the ionic relaxation was stopped, and the result accepted as the geometrically optimised structure. Apart from the forces on the atoms also the stress tensor was calculated to relax the lattice parameters. No kinetic energy or external forces were added to the system and so the temperature[2] and pressure in the calculations are 0 K and 0 bar, respectively. All the described parameters were controlled with three input files (INCAR, KPOINTS, POTCAR) and the initial structures were provided as VASP-specific structure format file (POSCAR). Relevant lines of the INCAR file for calculations based on PBEsol-D are given in the appendix (§ A.2).

For benchmark tests of different functionals the structures of the Al$_2$SiO$_5$ polymorphs sillimanite, andalusite and kyanite were geometrically optimised and compared with values from the literature (Tab. A.2, A.3, A.4 in § A.3 of the appendix). The structures of α-SiO$_2$ [164] and α-Al$_2$O$_3$ [165] were studied with DFT to evaluate the stability of mullite with respect to a system with the same composition but made of quartz and corundum. The results of these calculations are listed together with published values from the literature in Tables 3.6 and 3.7. It was reported that DFT calculations on the SiO$_2$ polymorphs without dispersion correction indicated that cristobalite was more stable than quartz in contrast to experimental observations, and that the implementation of dispersion correction results in the expected relative stabilities [140]. Demichelis et al. (2010) reported that the relative stability of the Al$_2$SiO$_5$ polymorphs is correctly calculated with the PBEsol functional but not in the case using PBE [166]. The benchmark tests confirm the latter results and the best agreement with experiments is achieved with PBEsol-D. For this thesis

---

[2]In fact the atoms do not move at all which should not be the case due to the zero-point energy at $T = 0$ K. Therefore, one may argue that the model does not qualify to correspond to an absolute temperature.

the PBE functional was applied to evaluate a large set of mullite superstructures with different Al/Si ordering and more accurate calculations using the PBEsol-D functional were carried out for final structure optimisations for comparisons with experimentally determined results.

Functional	a (Å)	c (Å)	V (Å^3)	$d(\text{Si}^{\text{IV}}\text{–O})$	E (eV)
PBE	5.0203	5.5084	120.23	1.6274	-71.14
PBE-D	4.9509	5.4581	115.86	1.6264	-71.99
PBEsol	4.9489	5.4441	115.47	1.6229	-74.01
PBEsol-D	4.8956	5.4027	112.14	1.6222	-74.69
Experimental powder XRD references:					
NIST 1878b[167]	4.91378 (30)	5.40536 (30)	113.03		
[168]	4.9070 (6)	5.3997 (4)	112.60	1.5999	
Antecedent calculations:					
PBE [140]	5.031	5.514	120.84	1.616	
TS [140]	4.928	5.428	114.15	1.616	

Table 3.6: Comparison of calculated and reported structure parameters of α-SiO$_2$. Distances are given in units of Å.

Functional	a (Å)	c (Å)	V (Å^3)	$d(\text{Al}^{\text{VI}}\text{–O})$	E (eV)
PBE	4.8100	13.1231	262.94	1.9330	-224.45
PBE-D	4.7874	13.0612	259.25	1.9240	-229.09
PBEsol	4.7757	13.0158	257.09	1.9182	-236.00
PBEsol-D	4.7600	12.9656	254.41	1.9116	-239.74
Experimental powder XRD references:					
NIST 676a [169]	4.759355 (80)	12.99231 (15)	254.87		
[168]	4.7585 (6)	12.9824 (6)	254.58	1.9133	
Antecedent calculation:					
PBE [170]	4.807	13.115	262.45		

Table 3.7: Comparison of calculated and reported structure parameters of α-Al$_2$O$_3$. Distances are given in units of Å.

Chapter 4

Results:
The crystal structure of mullite

The crystal structure of mullite was characterised in detail based on diffraction experiments and computational methods. First, the synchrotron measurements are analysed to explore the symmetry of mullite and to build constraints on the vacancy distribution considering the superspace symmetry. In the subsequent parts structure models for $\delta \approx 0.4$ are developed for different degrees of order. The models are subsequently extended to a unified superspace model in the range $0 \leq \delta \leq 0.5$ based on electron diffraction measurements, force field calculations and DFT calculations.

Reflection group	Reflection condition	Symmetry element
$00\ell 0$	$-$	$\{\, 2_z,\ -1 \mid -\ \ -\ \ 0\ \ - \,\}$
$0k00$	$k = 2n$	$\{\, 2_y,\ -1 \mid -\ \ \tfrac{1}{2}\ \ -\ \ - \,\}$
$h000$	$h = 2n$	$\{\, 2_x,\ 1 \mid \tfrac{1}{2}\ \ -\ \ -\ \ - \,\}$
$hk00$	$-$	$\{m_z,\ 1 \mid 0\ \ 0\ \ -\ \ - \,\}$
$h0\ell m_1$	$h + m_1 = 2n$	$\{m_y,\ 1 \mid \tfrac{1}{2}\ \ -\ \ 0\ \ \tfrac{1}{2} \,\}$
$0k\ell 0$	$k = 2n$	$\{m_x,\ -1 \mid -\ \ \tfrac{1}{2}\ \ 0\ \ - \,\}$

Table 4.1: Reflection conditions and derived symmetry elements. Note that the reflection conditions of $h000$ and $0k00$ are not sufficient to identify 2_1 screw axes parallel to **a** and **b**, respectively, because the presence of the glide planes already includes the reflection conditions for the screw axes.

Seitz symbol	Symmetry operation			
$\{\, E,\ \ 1 \mid 0\ \ 0\ \ 0\ \ 0 \,\}$	$(\quad x_{s1}$	x_{s2}	x_{s3}	$x_{s4}\quad)$
$\{\, 2_z,\ -1 \mid 0\ \ 0\ \ 0\ \ \tfrac{1}{2}+x_3 \,\}$	$(\ -x_{s1}$	$-x_{s2}$	x_{s3}	$-x_{s4}+\tfrac{1}{2}+x_{s3}\ )$
$\{\, 2_y,\ -1 \mid \tfrac{1}{2}\ \ \tfrac{1}{2}\ \ 0\ \ \tfrac{1}{2} \,\}$	$(\ -x_{s1}+\tfrac{1}{2}$	$x_{s2}+\tfrac{1}{2}$	$-x_{s3}$	$-x_{s4}+\tfrac{1}{2}\ )$
$\{\, 2_x,\ \ 1 \mid \tfrac{1}{2}\ \ \tfrac{1}{2}\ \ 0\ \ -x_3 \,\}$	$(\quad x_{s1}+\tfrac{1}{2}$	$-x_{s2}+\tfrac{1}{2}$	$-x_{s3}$	$x_{s4}-x_{s3}\ )$
$\{\ \ i,\ -1 \mid 0\ \ 0\ \ 0\ \ 0 \,\}$	$(\ -x_{s1}$	$-x_{s2}$	$-x_{s3}$	$-x_{s4}\ )$
$\{m_z,\ \ 1 \mid 0\ \ 0\ \ 0\ \ \tfrac{1}{2}-x_3 \,\}$	$(\quad x_{s1}$	x_{s2}	$-x_{s3}$	$x_{s4}+\tfrac{1}{2}-x_{s3}\ )$
$\{m_y,\ \ 1 \mid \tfrac{1}{2}\ \ \tfrac{1}{2}\ \ 0\ \ \tfrac{1}{2} \,\}$	$(\quad x_{s1}+\tfrac{1}{2}$	$-x_{s2}+\tfrac{1}{2}$	x_{s3}	$x_{s4}+\tfrac{1}{2}\ )$
$\{m_x,\ -1 \mid \tfrac{1}{2}\ \ \tfrac{1}{2}\ \ 0\ \ x_3 \,\}$	$(\ -x_{s1}+\tfrac{1}{2}$	$x_{s2}+\tfrac{1}{2}$	x_{s3}	$-x_{s4}+x_{s3}\ )$

Table 4.2: Symmetry elements and superspace group operators of $Pbam(\alpha 0\tfrac{1}{2})0ss$

4.1 Symmetry of mullite

The features in reciprocal space can be divided into three categories: main reflections, satellite reflections and diffuse scattering. In the literature the orthorhombic space group $Pbam$ and the superspace group $Pbam(\alpha 0\tfrac{1}{2})0ss$ were applied [57, 6]. In this section the symmetry of reciprocal space is reinvestigated with a focus on the superspace symmetry to derive constraints on the vacancy distribution. The determination of symmetry elements from electron diffraction measurements is not straight forward because reflections that are forbidden by symmetry are often present due to dynamical diffraction effects. The measurement that provided the greatest level of detail and contrast is the measurement of sample SA1 on beamline ID28 at the ESRF, which is therefore used for the subsequent symmetry analysis.
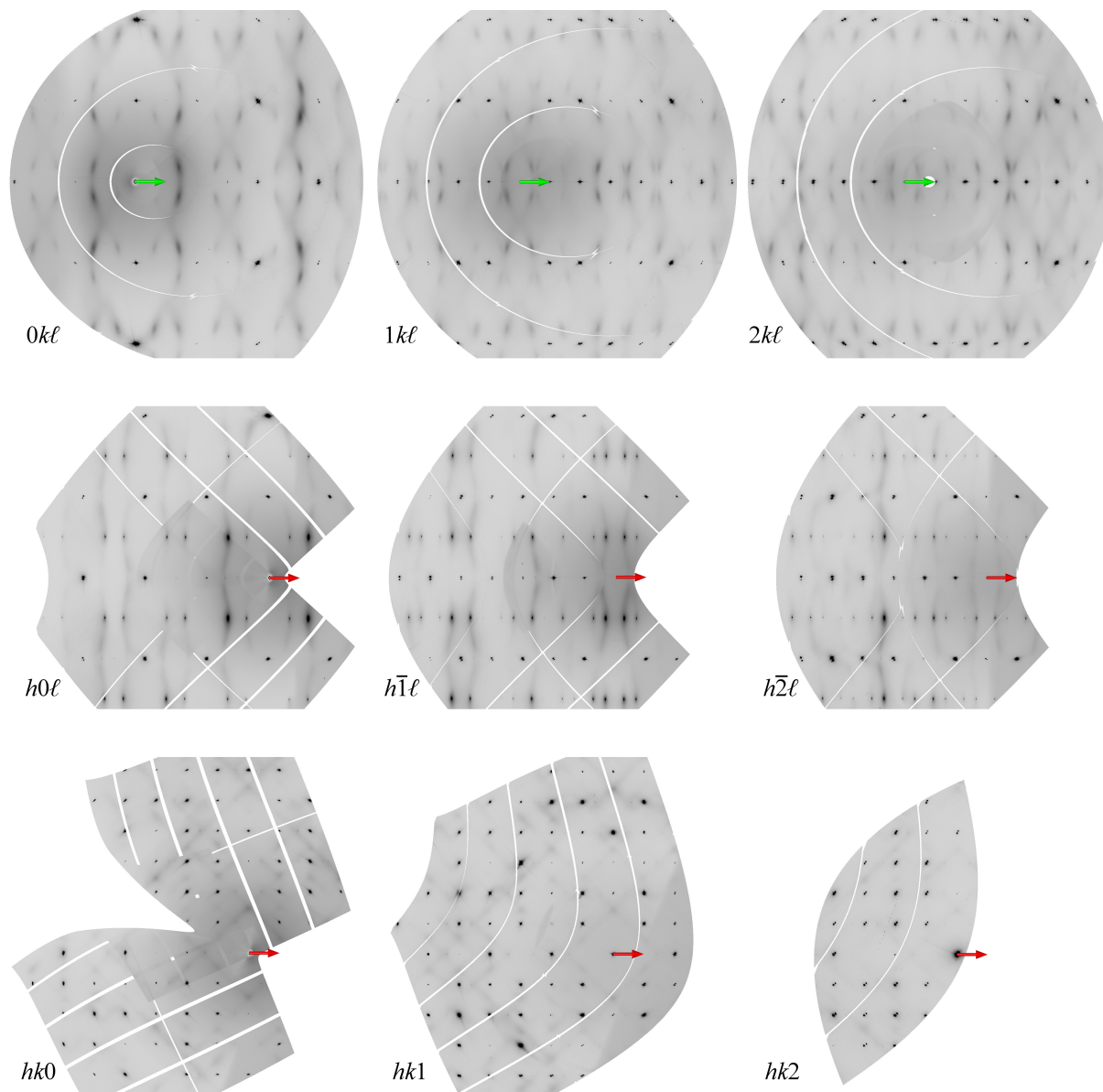
Figure 4.1: Reciprocal space sections reconstructed from the measurement of SA1 on ID28 (ESRF). Green and red arrows indicate the direction and length of $\mathbf{b}^*$ and $\mathbf{a}^*$, respectively. In the $h0\ell$ section systematic absences of satellite reflections are observed: For the reflection group $h0\ell m_1$ the reflection condition is $h + m_1 = 2n$. Pixel saturation limit represented by black pixels is 64000 counts.
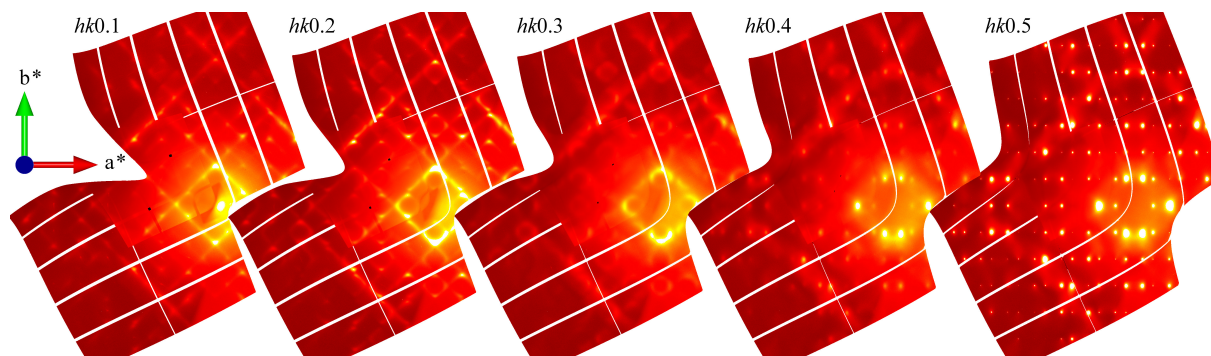
Figure 4.2: Reciprocal space sections perpendicular to $\mathbf{c}^*$. Pixel saturation limit represented by white pixels is 16000 counts. Th extinction conditions for $h0\ell m_1$ also hold for the diffuse discs visible in $hk0.4$ and $hk0.5$.

Figure 4.3: Reciprocal space sections perpendicular to $\mathbf{a}^*$. Pixel saturation limit represented by white pixels is 16000 counts.

4.1.1 Reciprocal space analysis and reflection conditions

Figure 4.1 shows reciprocal space sections from which the reflection conditions for main and satellite reflections were determined. Figures 4.2 and 4.3 show details of the diffuse scattering and the relationship with satellite reflect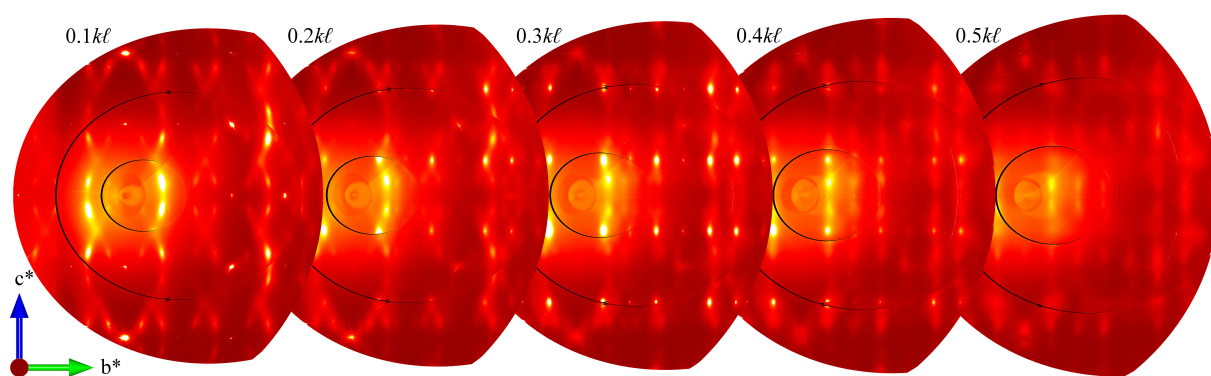ions. The overall point symmetry of reciprocal space is described by the point group $\frac{2}{m}\frac{2}{m}\frac{2}{m}$. Tetragonal symmetry, which once was suggested for certain compositions [2], is incompatible with the satellite reflections and the diffuse features (see appendix § A.4).

In sections perpendicular to $\mathbf{c}^*$ a diffuse streak pattern forming a diamond grid is visible. The streaks appear as continuous and well-defined lines in sections where ℓ is close to integer values $N \in \mathbb{Z}$. For an increasing fractional part of the reciprocal space coordinate ℓ the streak pattern dissociates into separate and more localised features. In sections with $\ell = N + \frac{1}{2}$ sharp first order satellite reflections defined by a modulation wave vector $\mathbf{q}_1 = [0.2978\,(8)\ 0.0000\,(11)\ 0.5000\,(5)]$ are present. Diffuse discs are located around these satellite reflections with an intensity that is approximately proportional to the intensity of the corresponding satellite reflection. These diffuse discs are the strongest diffuse features in the entire reciprocal space. The presence of a b glide plane perpendicular to $\mathbf{a}$ and an a glide plane perpendicular to $\mathbf{b}$ was derived from extinction conditions in the $0k\ell$ and $h0\ell$ plane, respectively. A few main reflections violating the extinction conditions are present, but this can be explained with dynamical diffraction effects due to the extraordinary brilliance of the primary beam. The extinction conditions are perfectly fulfilled in the measurement of the same sample on BM01. With increasing diffraction angle a splitting of main reflections is observed, indicating that the sample SA1 is not strictly single crystalline but contains at least two grains with almost the same orientation. However, no splitting of first and second order satellite reflections is observed.

In the $h0\ell$, $h1\ell$ and $h2\ell$ sections first and second order satellite reflections of $\mathbf{q}_1$ are present, but the first order satellites are much more intense by about two orders of magnitude. Diffuse discs are located around the strongest first order satellites and are slightly elongated along $\mathbf{c}^*$. The reflection condition for reflections $h0\ell m_1$ is $h + m_1 = 2n\ (n \in \mathbb{Z})$. Diffuse streaks are observed that run approximately parallel to $\mathbf{q}_1$ or $m_x{:}\mathbf{q}_1$ from intense first order to second order satellites, but the intensity approaches 0 towards integer values of ℓ.

Similar streaks are observed in the sections $0k\ell$, $1k\ell$ and $2k\ell$, but here the streaks interpenetrate so that they resemble the shape of a cross[1]. The height of the cross is approximately $0.8\mathbf{c}^*$. The termini of the streaks forming the cross are significantly more intense then the crossing region. These more intense spots can be treated as satellite reflections corresponding to a second and third modulation wave vector, although satellite reflections of $\mathbf{q}_2$

---

[1]Interestingly, this X-shape or saltire is also part of many flags of the region around the Isle of Mull after which mullite is named, e.g. the flag of Scotland.

and $\mathbf{q}_3$ are clearly diffuse whereas the satellite reflections of $\mathbf{q}_1$ are sharp. The respective modulation wave vectors were determined to be $\mathbf{q}_2 = [0.000\,(3)\ 0.397\,(4)\ 0.1834\,(19)]$ and $\mathbf{q}_3 = [0.000\,(3)\ 0.403\,(5)\ -0.181\,(2)]$. A comparison of $\mathbf{q}_2$ and $\mathbf{q}_3$ indicates that they are related by symmetry due to the similarity of the component amplitudes, which was also pointed out by [6] and is further analysed in § 5.1.5. In the $0k\ell$ section systematic extinctions of the cross-shapes with the corresponding satellites are observed. Reflections $0k\ell m_2$ and $0k\ell m_3$ are present if $k + m_2 = 2n$ and $k + m_3 = 2n$, respectively. Similar reflection conditions can be defined for the presence of the cross-shapes themselves, which are absent in the $0k\ell$ plane if the respective satellites are absent. Some of the cross-shapes are relatively weak and mainly the satellites are visible whereas the trace of the cross is only faintly visible.

The combination of the cross-shapes in the $0k\ell$ plane, the streaks in the $h0\ell$ plane and the diffuse features in Figures 4.2 and 4.3 resembles approximately the three-dimensional shape of a sand clock. The streaks in $0k\ell$ and $h0\ell$ define the edges of the bulbs, the middle of the crosses define the necks of each sand clock viewing along $\mathbf{a}^*$ and two sharp satellites of $\mathbf{q}_1$ define an extended neck viewing along $\mathbf{b}^*$. The cross section of the sand glasses are of circular shape close to the necks and become rather square-shaped with increasing distance from the satellite reflections defining the neck (Fig. 4.2). The contact plane of two stacked sand clocks are the sections perpendicular to $\mathbf{c}^*$ with integer ℓ, i.e. the planes showing a weak trace of the diffuse diamond streaks. The diffuse scattering seems to originate from the $\mathbf{q}_1$ satellite reflections, which form the strongest signal in reciprocal space after the main reflections. None of the diffuse features passes through main reflections.

The reflection conditions for main reflections and satellite reflections of $\mathbf{q}_1$ are summarised in Table 4.1. The centrosymmetric space group $Pbam$ (full symbol: $P\frac{2_1}{b}\frac{2_1}{a}\frac{2}{m}$) or the polar space group $Pba2$ can be derived from the extinction conditions of the main reflections. Mark & Rosbaud (1926) determined that the space group is $Pbam$, although no reason was given why $Pba2$ was not considered [15]. In both space groups the coordinates x and y of all oxygen sites are not constrained by symmetry elements with respect to the average structure of mullite. The presence of a mirror plane perpendicular to $\mathbf{c}$ requires that all atoms lie on a mirror plane forcing tetrahedra and octahedra to be more symmetric. It is very likely that the mirror plane is present because it relates atoms that in the average structure are in exactly the same environment and no reason for a distortion of the polyhedra can be identified. All structural studies since then assumed that the space group is $Pbam$.

A crystal structure with three modulation wave vectors may be described in (3+3)d superspace. However, the intensities of $\mathbf{q}_1$ satellite reflections are significantly stronger than the diffuse satellites of $\mathbf{q}_2$ and $\mathbf{q}_3$. Furthermore, it cannot be excluded that mullite is twinned as it is also observed for $\mathbf{q}_1$ satellites of mullites with $\delta > 0.5$ [50, 36] with

a mirror plane m_z being the twin law. If there are domains in mullite in which either $\mathbf{q}_2$ or $\mathbf{q}_3$ are present, then the structure of each domain could be described in (3+2)d superspace considering $\mathbf{q}_1$ and one of the other modulation wave vectors. Nevertheless, in all cases a (3+1)d superspace group can be defined for a structural description that neglects the other two modulations. In the case of $\mathbf{q}_2$ and $\mathbf{q}_3$ the superspace group is $P\frac{2_1}{b}(0\beta\gamma)ss$. In the case of $\mathbf{q}_1$ the superspace group could either be $Pbam(\alpha0\frac{1}{2})0s0$ or $Pbam(\alpha0\frac{1}{2})0ss$. The description of mullite in its standard setting with Al1 at the origin does not allow first order harmonic terms in the modulation functions of Al2, Si2, Al3, O3 and O4. In the superspace group $Pbam(\alpha0\frac{1}{2})0ss$ this restriction holds for Al1 and O2, which are not expected to show an occupational modulation. Hence, $Pbam(\alpha0\frac{1}{2})0ss$ seems more appropriate. All superspace models of this thesis are described and refined in this superspace group. The symmetry operators are listed in Table 4.2. The superspace groups that allow an equivalent description in a different setting are listed in the appendix in § A.5.

4.1.2 Superspace symmetry restrictions on the distribution of vacancies

Based on the assumption that vacancies are fully ordered and each vacancy is accompanied by the specific tricluster environment, a basic vacancy distribution scheme can be derived from the superspace symmetry. Let us consider a vacancy with label Q centred at coordinates $(0, \frac{1}{2}, \frac{1}{2})$. The Wyckoff position of that site in the space group $Pbam$ is 2d with a symmetrically equivalent site with coordinates $(\frac{1}{2}, 0, \frac{1}{2})$. The average vacancy concentration on both sites is $\bar{s}^{\mathrm{Q}} = \frac{\delta}{2}$. In superspace the distribution of vacancies can be represented by an occupational modulation function like a block wave function (Eqn. 2.3) in analogy to the description of the black keys of the superspace piano in § 2.4.1. Let us call the respective atomic domain the 'vacancy domain'. An ordered vacancy distribution can be described by defining $\Delta_{\mathrm{BW}}^{\mathrm{Q}}$ and $x_{\mathrm{BW}}^{\mathrm{Q}}$. Constraints on $x_{\mathrm{BW}}^{\mathrm{Q}}$ can be derived considering the symmetry elements of $Pbam(\alpha0\frac{1}{2})0ss$. Only cases with $0 \leq x_{\mathrm{BW}}^{\mathrm{Q}} \leq 0.25$ must be considered because all other cases are symmetrically related. The two-fold rotation axis 2_z acting on a point $(0, \frac{1}{2}, \frac{1}{2}, x_{\mathrm{s}4})$ gives a point $(0, -\frac{1}{2}, \frac{1}{2}, -x_{\mathrm{s}4})$. If $x_{\mathrm{BW}}^{\mathrm{Q}} = 0$ or $x_{\mathrm{BW}}^{\mathrm{Q}} = \frac{1}{2}$ then $\Delta_{\mathrm{BW}}^{\mathrm{Q}} = \bar{s}^{\mathrm{Q}} = \frac{\delta}{2}$ because the vacancy domain is on a special position as the two-fold rotation axis maps the domain on itself. In the case $x_{\mathrm{BW}}^{\mathrm{Q}} > 0$ and $\Delta_{\mathrm{BW}}^{\mathrm{Q}} = \frac{\bar{s}^{\mathrm{Q}}}{2} = \frac{\delta}{4}$ an overlap of the domain with itself must be avoided by fulfilling the condition $x_{\mathrm{BW}}^{\mathrm{Q}} > \frac{1}{2}\Delta_{\mathrm{BW}}^{\mathrm{Q}}$. The a glide plane of the superspace group $Pbam(\alpha0\frac{1}{2})0ss$ defines that if there is a vacancy at $(0, \frac{1}{2}, \frac{1}{2}, x_{\mathrm{s}4})$ then there is also a vacancy at $(\frac{1}{2}, 0, \frac{1}{2}, x_{\mathrm{s}4} + \frac{1}{2})$. In the same t-section these two positions may not be simultaneously occupied by vacancies because each vacancy requires its own tricluster environment. Likewise, a vacancy at $(0, \frac{1}{2}, \frac{1}{2}, x_{\mathrm{s}4})$ excludes a vacancy at $(1, \frac{1}{2}, \frac{1}{2}, x_{\mathrm{s}4} + \alpha)$ because otherwise their triclusters overlap corres-

Requirement	Conditions for $x^{\mathrm{Q}}_{\mathrm{BW}} \in [0, 0.25]$
no tetraclusters	$x^{\mathrm{Q}}_{\mathrm{BW}} < \frac{\alpha - \Delta^{\mathrm{Q}}_{\mathrm{BW}}}{2}$ or $x^{\mathrm{Q}}_{\mathrm{BW}} > \frac{\alpha + \Delta^{\mathrm{Q}}_{\mathrm{BW}}}{2}$
no superposition of triclusters and vacancies	$x^{\mathrm{Q}}_{\mathrm{BW}} < \frac{1}{4}(1 - \alpha - 2\Delta^{\mathrm{Q}}_{\mathrm{BW}})$ or $x^{\mathrm{Q}}_{\mathrm{BW}} > \frac{1}{4}(1 - \alpha + 2\Delta^{\mathrm{Q}}_{\mathrm{BW}})$
no stacking of vacancies along **c**	$x^{\mathrm{Q}}_{\mathrm{BW}} < \frac{1}{4}(1 - 2\Delta^{\mathrm{Q}}_{\mathrm{BW}})$

Table 4.3: Constraints on $x^{\mathrm{Q}}_{\mathrm{BW}}$ to avoid the specified crystal chemical environments. If $0 < x^{\mathrm{Q}}_{\mathrm{BW}} \leq 0.25$ then $x^{\mathrm{Q}}_{\mathrm{BW}} > \frac{1}{2}\Delta^{\mathrm{Q}}_{\mathrm{BW}}$ must be fulfilled to avoid a partial overlap of symmetrically related domains.

ponding to the presence of a tetracluster. The modulation functions of Q at $(0, \frac{1}{2}, \frac{1}{2}, x_{\mathrm{s}4})$ and $m_z : \mathrm{Q}$ at $(0, \frac{1}{2}, -\frac{1}{2}, x_{\mathrm{s}4})$ exhibit a phase shift of $\frac{1}{2}$ in t-space because $\gamma = \frac{1}{2}$. If the vacancy domain is occupied at $(0, \frac{1}{2}, \frac{1}{2}, x_{\mathrm{s}4})$ and at $(0, \frac{1}{2}, \frac{1}{2}, x_{\mathrm{s}4} + \frac{1}{2})$, then two vacancies are stacked along **c**. Although this is crystal chemically not forbidden it can be assumed that it is avoided as indicated by investigations of the diffuse scattering [3, 4]. A summary of the conditions is given in Table 4.3.

In Figure 4.4 superspace models with $x^{\mathrm{Q}}_{\mathrm{BW}} = 0$, 0.07, 0.15 and 0.25 are shown for 2/1-mullite with $\delta = 0.4$ and $\alpha = 0.3$. This set of simplified parameters was also used in other structural studies [60, 7]. The model with $x^{\mathrm{Q}}_{\mathrm{BW}} = 0.25$ can be excluded due to the presence of vacancy channels. The model with $x^{\mathrm{Q}}_{\mathrm{BW}} = 0.15$ can also be excluded due to the presence of tetraclusters and vacancies that are too close to each other so that there is no space for triclusters (blue model in Fig. 4.4). The model with $x^{\mathrm{Q}}_{\mathrm{BW}} = 0.07$ fulfils all the conditions of Table 4.3 and thus describes a plausible mullite structure. In fact, this vacancy distribution is identical to the distribution derived by Saalfeld (1979) from difference Patterson maps (cf. Fig. 1.7). The model with Q at a special position, i.e. $x^{\mathrm{Q}}_{\mathrm{BW}} = 0$, also fulfils the established requirements and results in blocks that have a length of four vacancies (bottom model in Fig. 4.4). Saalfeld's model as well as the model with $x^{\mathrm{Q}}_{\mathrm{BW}} = 0$ are promising candidates, but the symmetry of the physical space sections is different. Saalfeld's model is described in the monoclinic space group $B11\frac{2}{m}$, whereas the vacancy distribution of a mullite model with $x^{\mathrm{Q}}_{\mathrm{BW}} = 0$ allows a description in the orthorhombic space group $Bb2_1m$. Pauling's Rule of Parsimony is an additional argument that favours the model with $x^{\mathrm{Q}}_{\mathrm{BW}} = 0$ because it contains less different environments. Therefore, all superspace models of the subsequent sections are based on mullite in which vacancies occupy a special position. Different models with $x^{\mathrm{Q}}_{\mathrm{BW}} = 0$ and $x^{\mathrm{Q}}_{\mathrm{BW}} = 0.07$, respectively, will be further compared and discussed in § 5.1.3.
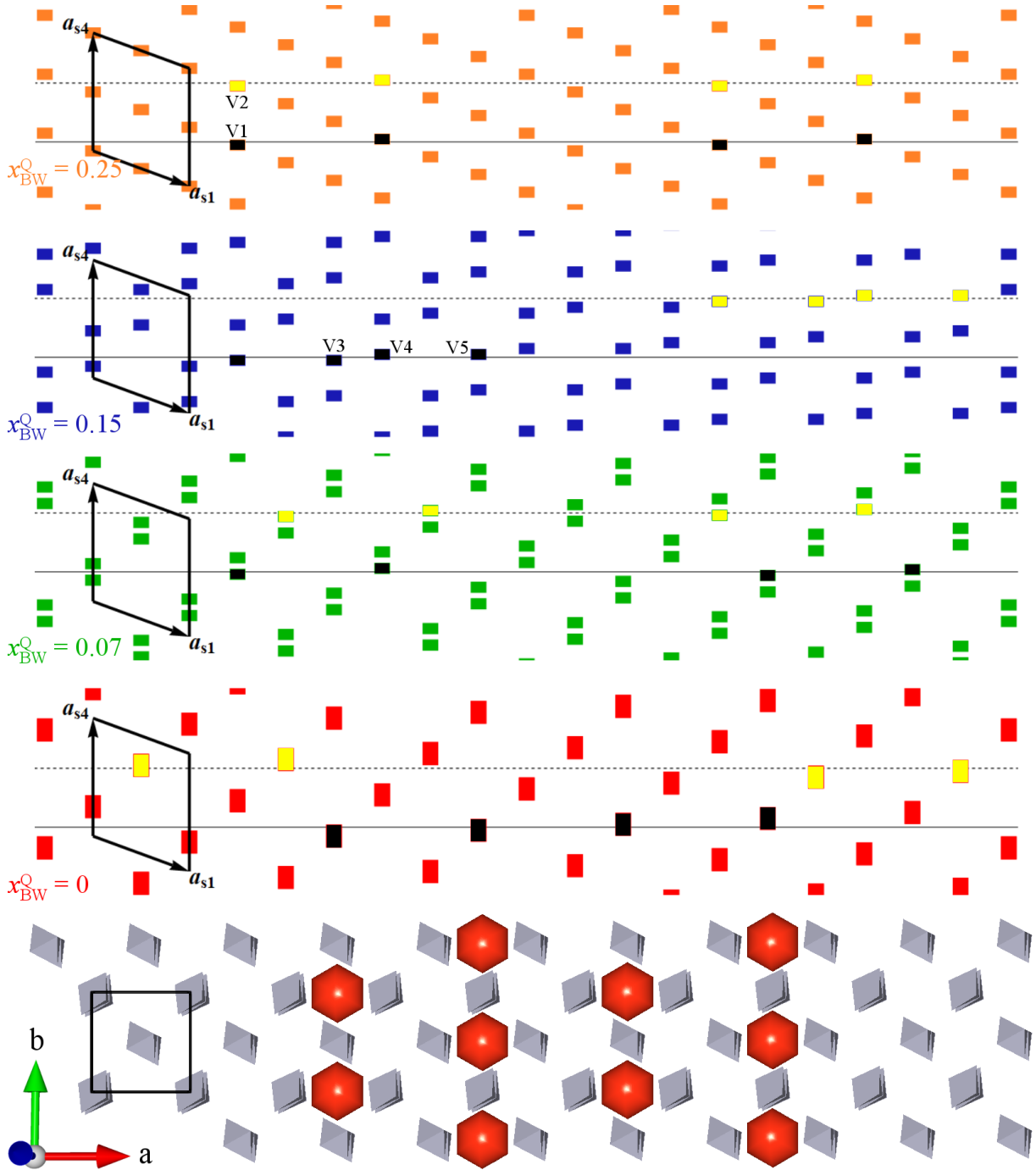
Figure 4.4: Hypothetical superspace models with different $x_{\mathrm{BW}}^{\mathrm{Q}}$ in the superspace group $Pbam(\alpha 0\frac{1}{2})0ss$ from which different vacancy distributions of 2/1-mullite ($\alpha = 0.3$, $\delta = 0.4$) can be derived. The physical space sections of an arbitrary t are indicated by a solid horizontal line. Vacancy domains with $z = \frac{1}{2}$ that are 'occupied' are marked in black. As the vacancy domains of vacancies at $z = \frac{3}{2}$ are related to those at $z = \frac{1}{2}$ by an origin shift of $\Delta t = 0.5$, the dashed horizontal lines indicate where vacancies with $z = \frac{3}{2}$ are present (marked in yellow). A physical space model of the bottom model ($x_{\mathrm{BW}}^{\mathrm{Q}} = 0$) is shown below. Vacancies with $z = \frac{1}{2}$ are represented by red hexagons and octahedra are shown for better orientation (not included in the superspace models). The vacancies V1 and V2 in the upper model ($x_{\mathrm{BW}}^{\mathrm{Q}} = 0.25$) indicate that vacancies are stacked along **c**. Vacancies V3, V4 and V5 ($x_{\mathrm{BW}}^{\mathrm{Q}} = 0.15$) are too close to each other so that there is no space for all the required triclusters. V4 occupies the space required for a tricluster of V3 and between V4 and V5 there is only space for a tricluster of V4 or V5 but not for both.

4.1.3 Constraints for block wave occupational modulation functions

The last section has shown that meaningful vacancy distributions can be derived from the superspace group $Pbam(\alpha 0\frac{1}{2})0ss$. As each vacancy is accompanied by two triclusters and the octahedra chains are interlinked by either triclusters or diclusters the distribution of octahedra and tetrahedra is fully determined by the vacancy distribution. In this section the symmetrical relationships between different atomic domains are used to define the corresponding constraint scheme for the respective occupational modulation functions $g_s^\mu(\bar{x}_{s4}^\mu)$ for the atom sites Al2, Si2, Al3, O3 and O4 based on the closeness condition [171]. To clearly identify an atom site μ the superscripts $\mathcal{R}$, $\mathcal{B}$, $\mathcal{A}$ and $\mathcal{M}$ are used to reference a site that is related to the respective site of the asymmetric unit ($0 \le \bar{x}_{si} < 0.5$, $i = 1, 2$) by the following symmetry operators:

$$
\begin{aligned}
\mathcal{R} &= \{\, 2_z, -1 \mid \quad 0 \quad 1 \quad 0 \quad \tfrac{1}{2} + \bar{x}_{s3} \,\} \\
\mathcal{B} &= \{\, m_x, -1 \mid \quad \tfrac{1}{2} \quad \tfrac{1}{2} \quad 0 \quad \bar{x}_{s3} \,\} \\
\mathcal{A} &= \{\, m_y, 1 \mid \quad -\tfrac{1}{2} \quad \tfrac{1}{2} \quad 0 \quad \tfrac{1}{2} \,\} \\
\mathcal{M} &= \{\, m_z, 1 \mid \quad 0 \quad 0 \quad 0 \quad \tfrac{1}{2} - \bar{x}_{s3} \,\}
\end{aligned}
$$

Note that additional translational parts were included in $\mathcal{R}$ and $\mathcal{A}$ with respect to Table 4.2. The starting point is a vacancy domain Q defined by a block wave function with parameters $\Delta_{BW}^Q = \frac{\delta}{2}$ and $x_{BW}^Q = 0$, as derived in the last section. At this stage Al/Si is not considered and it is assumed that Si is randomly distributed on the T site but not present on the T^*site. The presence of a vacancy requires that the sites T, $T^\mathcal{R}$, Al3$^\mathcal{A}$, Al3$^\mathcal{B}$, O4$^\mathcal{A}$, O4$^\mathcal{B}$ and O3 are not occupied (Fig. 4.5). Al3, O4, Al3$^\mathcal{R}$ and O4$^\mathcal{R}$ must be occupied to form the tricluster environment. The T site is occupied if there is no vacancy. Consequently, the block wave functions of T and Q are shifted in phase by $\frac{1}{2}$ and $\Delta_{BW}^Q = \Delta_{BW}^{O4} = \Delta_{BW}^{Al3} = 1 - \Delta_{BW}^T$. Thus, the definition of the block waves of T, Al3 and O4 can be directly derived from the parameters of Q. O3 is present if the T site is occupied but the triclusters with O4$^\mathcal{A}$ and O4$^\mathcal{B}$ are not present. This is expressed as $g_s^{O3}(t) = g_s^{Al2}(t) - g_s^{O4^\mathcal{A}}(t) - g_s^{O4^\mathcal{B}}(t)$. It turns out that the atomic domain of O3 is split into three parts described by the block wave functions of O3a, O3b and O3b$^\mathcal{R}$. The position of O3a is a special site with $x_{BW}^{O3a} = 0.5$. As an origin shift by $(0, 0, 0, \frac{1}{2})$ leaves the structure invariant, a setting with $x_{BW}^{O3a} = 0$ is preferred (Fig. 4.5).

An important symmetry consideration to derive constraints on x_{BW}^μ is the site symmetry $\frac{2}{m}$ of the vacancy site and hence also of the O3 site. If the T site is occupied in a certain t–section, then $T^\mathcal{R}$ must be occupied as well. As a consequence, $g_s^T(t)$ must be identical to $g_s^{T^\mathcal{R}}(t)$.
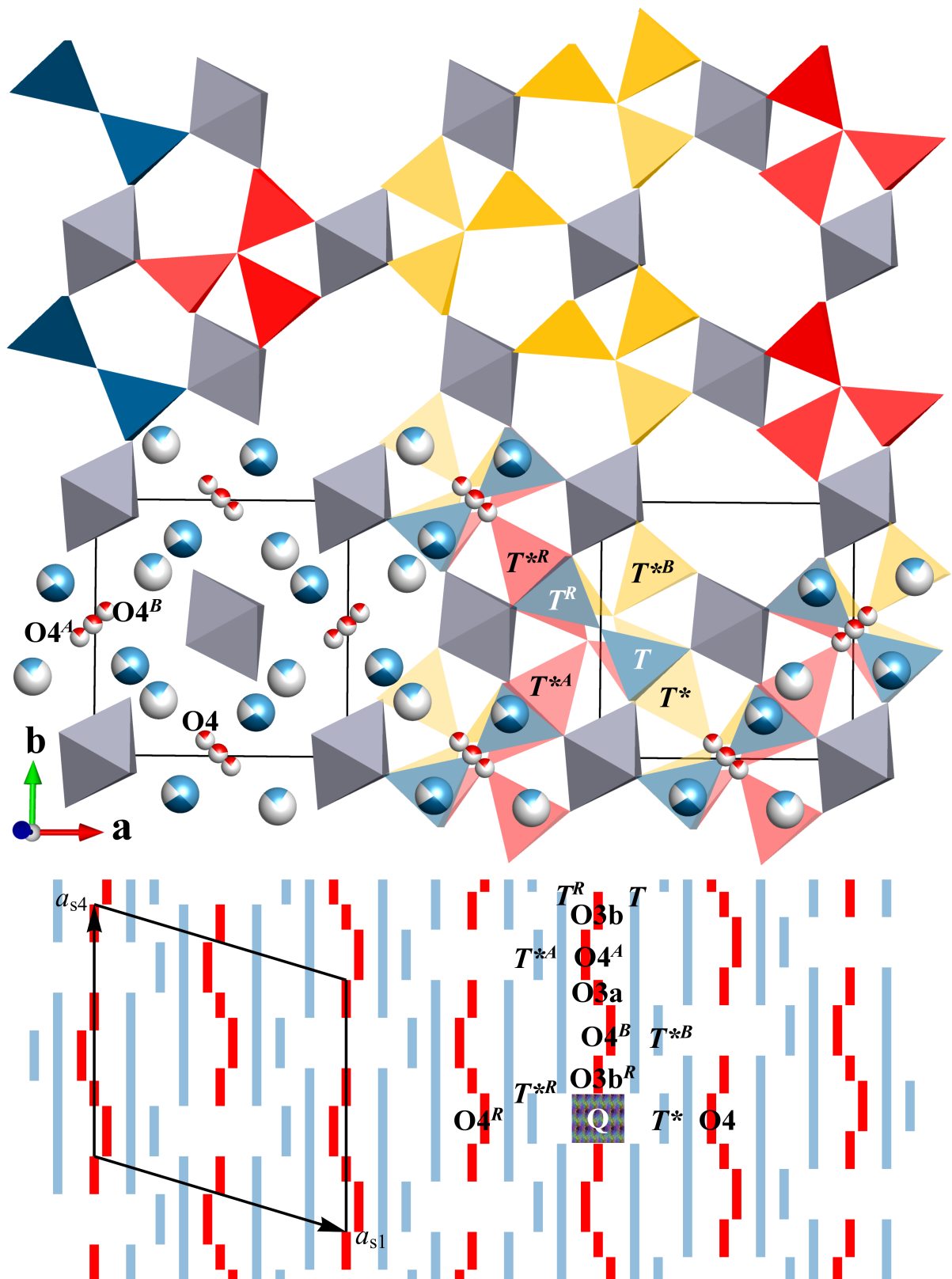
Figure 4.5: Top: Average structure model of mullite with split sites and its decomposition into diclusters and triclusters. Unit-cell borders are marked by black lines. Atoms forming octahedra are not shown. Relevant sites are labelled. The coloured polyhedra indicate how the split sites represent the superposition of diclusters, triclusters and vacancies. Bottom: Superspace model for tetrahedral sites and O3 and O4 derived from a vacancy domain Q (only one is shown) from which the block wave parameters of O4, $T*$ and T are trivial to deduce.

μ	Δ_{BW}^{μ}	x_{BW}^{μ}	s^{μ}
Al2	$1 - \frac{\delta}{2}$	$\alpha \bar{x}_{\text{s1}}^{\text{Al2}}$	$\frac{1}{2-\delta}$
Si2	$1 - \frac{\delta}{2}$	$\alpha \bar{x}_{\text{s1}}^{\text{Si2}}$	$\frac{1-\delta}{2-\delta}$
Al3	$\frac{\delta}{2}$	$\frac{1}{2} + \alpha \bar{x}_{\text{s1}}^{\text{Al3}}$	1
O3a	$\alpha - \frac{\delta}{2}$	0	1
O3b	$\frac{1}{2}(1 - \alpha - \delta)$	$\frac{1}{4}(1 + \alpha)$	1
O4	$\frac{\delta}{2}$	$\frac{1}{2} + \alpha \bar{x}_{\text{s1}}^{\text{O4}}$	1

Table 4.4: Constraints on the block wave modulation functions expressed as functions of the α component of $\mathbf{q}$, the vacancy concentration δ and coordinates $\bar{x}_{\text{s1}}^{\mu}$.

$$
\begin{aligned}
g_s^T(t) &= g_s^{T^{\mathcal{R}}}(t) \\
x_{\text{BW}}^T - \mathbf{q} \cdot \bar{\mathbf{x}}^T &= (-x_{\text{BW}}^T - \tfrac{1}{2} + \bar{x}_{\text{s3}}) - \mathbf{q} \cdot \bar{\mathbf{x}}^{T^{\mathcal{R}}} \\
x_{\text{BW}}^T &= \alpha \bar{x}_{\text{s1}}^T
\end{aligned}
$$

In analogy, the presence of a tricluster with Al3 and O4 requires the presence of a tricluster with Al3$^{\mathcal{R}}$ and O4$^{\mathcal{R}}$ in the same t-section. The block wave length $\Delta_{\text{BW}}^{\text{O3a}}$ is defined by the symmetry relationships between O4 and $\{\, 2_z, -1 \,|\, 1,\, 0,\, 0,\, \frac{1}{2} + \overline{x}_{\text{s3}} \,\} : \text{O4} \rightarrow \text{O4}'$.

$$
\begin{aligned}
x_{\text{BW}}^{\text{O4}} &= \alpha \bar{x}_{\text{s1}}^{\text{O4}} + \frac{1}{2} \\
x_{\text{BW}}^{\text{O4'}} &= \frac{1}{2} - \alpha(1 - \bar{x}_{\text{s1}}^{\text{O4}}) \\
x_{\text{BW}}^{\text{O4}} - x_{\text{BW}}^{\text{O4'}} &= \Delta_{\text{BW}}^{\text{O3a}} + \Delta_{\text{BW}}^{\text{O4}} \\
\Delta_{\text{BW}}^{\text{O3a}} &= \alpha - \Delta_{\text{BW}}^{\text{O4}} = \alpha - \frac{\delta}{2} \\
\Delta_{\text{BW}}^{\text{O3b}} &= \frac{1}{2}(\Delta_{\text{BW}}^T - 2\Delta_{\text{BW}}^{\text{O4}} - \Delta_{\text{BW}}^{\text{O3a}})
\end{aligned}
$$

The full list of constraints is given in Table 4.4.

4.1.4 Constraints for harmonic occupational modulation functions

If the probability to encounter a vacancy is not just 0 or 1 but is described by a harmonic function $s^{\text{Q}}(t) = \frac{\delta}{2} + g_s^{\text{Q}}(t)$ then a similar constraint scheme for the occupational modulation functions of T, Al3, O3 and O4 can be derived. Again, we start with an atomic domain Q representing the probability to find a vacancy at coordinates $(0, \frac{1}{2}, \frac{1}{2}, x_{\text{s4}})$.

Results

Symmetry restrictions require that the occupational modulation function $g_s^Q(t)$ consists of cosine terms only as sine terms are forbidden.

$$g_s^\mu(t) = \sum_n A_{s,n}^\mu \sin[2\pi n(\alpha\bar{x}_{s1}^\mu + \gamma\bar{x}_{s3}^\mu + t)] + B_{s,n}^\mu \cos[2\pi n(\alpha\bar{x}_1^\mu + \gamma\bar{x}_{s3}^\mu + t)]$$

$$g_s^Q(t) = \sum_n B_{s,n}^Q \cos[2\pi n(\alpha\bar{x}_{s1}^Q + \gamma\bar{x}_{s3}^Q + t)] = \sum_n B_{s,n}^Q \cos\left[2\pi n\left(\frac{1}{4} + t\right)\right]$$

The presence of a vacancy requires the well-defined tricluster environment and therefore the occupancy of Al3 and O4 must be modulated like Q.

$$s^Q(t) = s^{O4}(t) = s^{Al3}(t)$$

The terms $A_{s,n}^\mu$ of Al3 and O4 are calculated from the phase shift between the modulation functions in t-space originating from the different coordinates.

$$A_{s,n}^\mu = B_{s,n}^Q \sin(2\pi n\alpha\bar{x}_1^\mu)$$
$$B_{s,n}^\mu = B_{s,n}^Q \cos(2\pi n\alpha\bar{x}_1^\mu)$$

If there is no vacancy the T and $T^\mathcal{R}$ site are always occupied together, either forming a dicluster or as part of a tricluster. The occupational modulation of T is therefore in anti-phase relationship to the modulation of Q.

$$A_{s,n}^T = - B_{s,n}^Q \sin(2\pi n\alpha\bar{x}_1^T)$$
$$B_{s,n}^T = - B_{s,n}^Q \cos(2\pi n\alpha\bar{x}_1^T)$$

The O3 site is occupied if T and $T^\mathcal{R}$ form a dicluster, but not if the split sites $O4^\mathcal{A}$ and $O4^\mathcal{B}$ with the respective triclusters are occupied.

$$s^{O3}(t) = s^T(t) - s^{O4^\mathcal{A}}(t) - s^{O4^\mathcal{B}}(t) = \sum_n B_{s,n}^{O3} \cos\left[2\pi n\left(\frac{1}{4} + t\right)\right]$$

$s^{O4}(t)$ and $s^T(t)$ are already known. As the O3 site also exhibits site symmetry $\frac{2}{m}$, sine terms are forbidden ($A_{s,n}^{O3} = 0$) and only cosine terms must be considered. The calculation of $B_{s,n}^{O3}$ must consider the amplitudes of $g_s^{O4^\mathcal{A}}(t = \frac{3}{4})$ and $g_s^{O4^\mathcal{B}}(t = \frac{3}{4})$ because at $t = \frac{3}{4}$ the amplitude of $g_s^T(t)$ is at its maximum. At this t-section the phase shift between g_s^{O4} and $g_s^{O4^\mathcal{A}}$ is identical to the phase shift between $g_s^{O4^\mathcal{B}}$ and g_s^{O4}.

$$\bar{x}_{s4}^{O4} - \bar{x}_{s4}^{O4^\mathcal{A}} = \frac{1+\alpha}{2}$$
$$g_s^{O4^\mathcal{A}}(t = \frac{3}{4}, n = 1) = g_s^{O4}(t = \frac{3}{4}, n = 1) \cos\left(2\pi\frac{1+\alpha}{2}\right)$$

Site	$\zeta_n^\mu = \sqrt{(A_{s,n}^\mu)^2 + (B_{s,n}^\mu)^2}$	$A_{s,n}^\mu/\zeta_n^\mu$	$B_{s,n}^\mu/\zeta_n^\mu$
O3	$\zeta_n^{O3} = B_{s,n}^{O3}$	$\sin(2\pi n\alpha\bar{x}_{s1}^{O3}) = 0$	$\cos(2\pi n\alpha\bar{x}_{s1}^{O3}) = 1$
O4	$-\zeta_n^{O3}/\{1 + 2\cos[\pi n(1+\alpha)]\}$	$\sin(2\pi n\alpha\bar{x}_{s1}^{O4})$	$\cos(2\pi n\alpha\bar{x}_{s1}^{O4})$
T	$\zeta_n^{O3}/\{1 + 2\cos[\pi n(1+\alpha)]\}$	$\sin(2\pi n\alpha\bar{x}_{s1}^{T})$	$\cos(2\pi n\alpha\bar{x}_{s1}^{T})$
Al3	$-\zeta_n^{O3}/\{1 + 2\cos[\pi n(1+\alpha)]\}$	$\sin(2\pi n\alpha\bar{x}_{s1}^{Al3})$	$\cos(2\pi n\alpha\bar{x}_{s1}^{Al3})$

Table 4.5: Constraints on occupational modulation functions. ζ_n^μ expresses the amplitude of the nth harmonic term of the occupational modulation function.

In the general case the amplitude of $g_s^{O4^{\mathcal{A}}}$ and $g_s^{O4^{\mathcal{B}}}$ at $t = \frac{3}{4}$ is $B_{s,n}^Q \cos[\pi n(1+\alpha)]$. The anti-phase relationship between g_s^{O4} and g_s^T leads to

$$B_{s,n}^{O3} = B_{s,n}^Q\{1 + 2\cos[\pi n(1+\alpha)]\} \quad .$$

In Table 4.5 the constraint scheme is summarised. Note that in all refinements $B_{s,1}^{O3} < 0$ to make sure that all models can be compared without the necessity of additional origin shifts. A simple way to implement occupational modulation functions of Al2 and Si2 assumes that Al2 and Si2 are modulated identically and in phase with T, which corresponds to $A_{s,n}^{Al2} = A_{s,n}^{Si2} = \frac{1}{2}A_{s,n}^T$ and $B_{s,n}^{Al2} = B_{s,n}^{Si2} = \frac{1}{2}B_{s,n}^T$. These modulation functions are based on pure simplicity and it is very unlikely that in mullite Al and Si behave identically due to their different cation radius and different oxidation state.
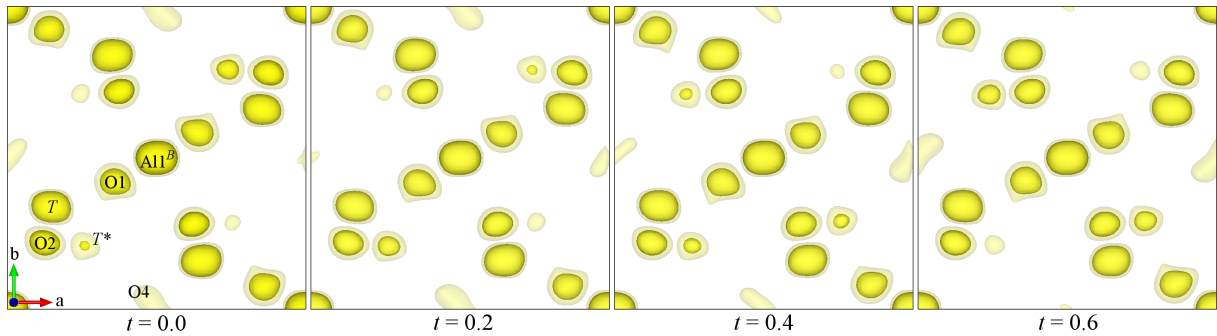
Figure 4.6: Electron density of the structure solution for different t-sections within one unit cell. Solid yellow surfaces correspond to electron density level of about 7 electrons/Å^3 and the semi-transparent yellow surfaces correspond to about 2 electrons/Å^3.

4.2 Disordered SSM: Superspace model with partial vacancy ordering

The models and constraints of the last sections were mainly based on the analysis of the superspace symmetry. In the following sections these predictions are experimentally tested. The reciprocal space of a mullite crystal structure with a fully ordered vacancy distribution exhibits high order satellite reflections, independent of Al/Si ordering. The diffraction patterns obtained by single crystal X-ray diffraction experiments mainly showed first order satellite reflections alongside diffuse scattering. From this observation it can be expected that the mullite samples are not fully ordered. The 'disordered superspace model' (disordered SSM) uses harmonic functions for the description of the occupational modulation. 'Disordered' here means that the Si and vacancy distribution is described by short-range and long-range order which gives rise to diffuse scattering and satellite reflections. In the disordered SSM only the long-range ordered component is implemented, and the short-range ordered component requires a separate analysis of the diffuse scattering. The structure solution and initial refinement is based on the sample SA1 measured on BM01 at the ESRF.

4.2.1 Structure solution and refinement

The program 'Superflip' [107] based on the charge flipping method (§ 2.3.2) was used to obtain an initial structure solution based on main reflections and first order satellite reflections. Superflip confirms the superspace group $Pbam(\alpha 0\frac{1}{2})0ss$. The resulting electron density directly reveals the sites of the octahedron and the T site. The electron density of the T^* site is significantly weaker than that around the T site, which is not surprising because the expected ratio of $\bar{s}^T$ to $\bar{s}^{T^*}$ is about 0.8 to 0.2. The electron density around the O3 and O4 split site does not allow to resolve the atom sites from the initial solution as the electron density forms an elongated bulge. The comparison of the electron density

Label	SA1	SA2	SA3	Qg1
Experimental				
Radiation type	X-ray, $\lambda = 0.7231\,\text{Å}$			
Crystal size (µm)	$60 \times 50 \times 30$	$70 \times 50 \times 30$	$50 \times 50 \times 20$	diameter < 80
Diffractometer	Four-circle diffractometer, ESRF beamline BM01, $T = 273\,\text{K}$			
$\frac{\sin(\theta_{\max})}{\lambda}$	0.733	0.730	0.724	0.731
Data reduction				
a (Å)	7.5787 (7)	7.577 (2)	7.5768 (13)	7.577 (2)
b (Å)	7.6707 (4)	7.6727 (18)	7.6760 (16)	7.6738 (19)
c (Å)	2.88360 (10)	2.8804 (10)	2.8833 (12)	2.8823 (10)
V (Å^3)	167.64 (2)	167.46 (8)	167.67 (8)	167.59 (8)
Superspace group	$Pbam(\alpha 0\frac{1}{2})0ss$			
α	0.2988 (9)	0.301 (2)	0.3068 (19)	0.2948 (19)
Absorption correction	Empirical with SCALE3 ABSPACK (CrysAlisPro)			
Reflection statistics				
Measured	3363	3079	3299	3567
Independent	678	768	667	797
$I_{hkl} > 3\sigma_{hkl}$	555	544	382	454
$h_{\max}, k_{\max}, l_{\max}, m_{\max}$	8, 11, 4, 1	10, 10, 4, 1	11, 10, 3, 1	11, 10, 4, 1
R_{int}	0.014	0.020	0.030	0.014
Refinement				
$R(I_{hkl} > 3\sigma_{hkl})$	0.037	0.031	0.037	0.025
$wR(F^2)$	0.104	0.089	0.111	0.097
No. of reflections	678	768	667	797
No. or parameters	101	101	101	101
No. of constraints	33	33	33	33
$\Delta\rho_{\max}, \Delta\rho_{\min}$ (e Å^{-3})	0.37, -0.33	0.35, -0.39	0.43, -0.46	0.28, -0.30
Chemical composition	Al$_{4.856}$Si$_{1.144}$O$_{9.572}$	Al$_{4.832}$Si$_{1.168}$O$_{9.584}$	Al$_{4.868}$Si$_{1.132}$O$_{9.566}$	Al$_{4.852}$Si$_{1.148}$O$_{9.574}$
Vacancy concentration	0.428 (4)	0.416 (4)	0.434 (6)	0.426 (3)

Table 4.6: Relevant parameters of the diffraction experiments on BM01, data reduction and refinement. R_{int} is a residual factor of the averaged intensities of symmetry-equivalent reflections. $\Delta\rho_{\max}$ and $\Delta\rho_{\min}$ are the global maximum and minimum electron density, respectively, in the difference Fourier map.

Sample	p SA1	p SA2	p SA3	p Qg1	$A^\mu_{p,1}$ SA1	$A^\mu_{p,1}$ SA2	$A^\mu_{p,1}$ SA3	$A^\mu_{p,1}$ Qg1	$B^\mu_{p,1}$ SA1	$B^\mu_{p,1}$ SA2	$B^\mu_{p,1}$ SA3	$B^\mu_{p,1}$ Qg1
Al1												
$\bar{x}^{Al1}$	0	0	0	0	0	0	0	0	0	0	0	0
$\bar{y}^{Al1}$	0	0	0	0	0	0	0	0	0	0	0	0
$\bar{z}^{Al1}$	0	0	0	0	−0.00471 (7)	−0.00305 (6)	−0.00138 (8)	−0.00201 (9)	0	0	0	0
$\bar{s}^{Al1}$	1	1	1	1	0	0	0	0	0	0	0	0
$\bar{U}^{Al1}_{eq}$	0.0109 (3)	0.00863 (17)	0.0089 (3)	0.01054 (17)	0	0	0	0	0	0	0	0
T												
$\bar{x}^{T}$	0.14896 (9)	0.14885 (5)	0.14905 (5)	0.14908 (4)	−0.00131 (3)	−0.00084 (2)	−0.00047 (4)	−0.00054 (3)	0.00050 (3)	0.00037 (2)	0.00016 (4)	0.00021 (3)
$\bar{y}^{T}$	0.33959 (6)	0.33985 (4)	0.34005 (5)	0.33987 (4)	−0.00152 (3)	−0.00096 (2)	−0.00047 (2)	−0.00065 (3)	−0.00010 (3)	−0.00012 (2)	−0.00008 (2)	−0.00012 (3)
$\bar{z}^{T}$	0.5	0.5	0.5	0.5	0	0	0	0	0	0	0	0
s^{T}	0.786 (2)	0.7920 (19)	0.783 (3)	0.7868 (17)	0.02792 (28)	0.01974 (16)	0.00764 (14)	0.01116 (14)	0.0972 (10)	0.0682 (6)	0.0258 (4)	0.0394 (4)
$\bar{s}^{Al2}$	0.5	0.5	0.5	0.5	0.01396 (14)	0.00987 (8)	0.00382 (7)	0.00558 (7)	0.0486 (5)	0.0341 (3)	0.0129 (2)	0.0197 (2)
s^{Si2}	0.286 (2)	0.2920 (19)	0.283 (3)	0.2868 (17)	0.01396 (14)	0.00987 (8)	0.00382 (7)	0.00558 (7)	0.0486 (5)	0.0341 (3)	0.0129 (2)	0.0197 (2)
$\bar{U}^{T}_{eq}$	0.0121 (3)	0.00933 (17)	0.0096 (3)	0.01046 (17)	0.00072 (6)	0.00058 (4)	0.00017 (8)	0.00030 (7)	−0.00041 (7)	0.00016 (5)	−0.00039 (7)	−0.00031 (7)
Al3												
$\bar{x}^{Al3}$	0.2630 (4)	0.2626 (2)	0.2624 (2)	0.26226 (19)	−0.00078 (15)	−0.00064 (9)	0.00004 (15)	−0.00035 (13)	0.0009 (2)	0.00063 (11)	0.00049 (17)	0.00049 (14)
$\bar{y}^{Al3}$	0.2056 (3)	0.2043 (2)	0.2058 (2)	0.2054 (2)	−0.00089 (13)	−0.00081 (9)	−0.00026 (9)	−0.00060 (12)	0.00052 (18)	−0.00008 (10)	0.00029 (8)	0.00016 (13)
$\bar{z}^{Al3}$	0.5	0.5	0.5	0.5	0	0	0	0	0	0	0	0
s^{Al3}	0.214 (2)	0.2080 (19)	0.217 (3)	0.2132 (17)	−0.0479 (5)	−0.0339 (3)	−0.0131 (2)	−0.0191 (2)	−0.0891 (9)	−0.0625 (5)	−0.0236 (4)	−0.0362 (5)
$\bar{U}^{Al3}_{eq}$	0.0112 (7)	0.0086 (4)	0.0105 (6)	0.0121 (4)	0.0012 (3)	0.00003 (19)	0.0016 (3)	0.0013 (3)	0.0023 (4)	0.0001 (2)	0.0019 (3)	0.0018 (3)
O1												
$\bar{x}^{O1}$	0.35894 (15)	0.35912 (10)	0.35841 (11)	0.35879 (9)	−0.00230 (5)	−0.00157 (4)	−0.00072 (8)	−0.00104 (7)	−0.00180 (6)	−0.00121 (4)	−0.00058 (8)	−0.00079 (6)
$\bar{y}^{O1}$	0.42166 (14)	0.42179 (11)	0.42165 (16)	0.42178 (11)	0.00234 (5)	0.00164 (4)	0.00073 (4)	0.00088 (6)	0.00428 (6)	0.00276 (4)	0.00129 (4)	0.00171 (6)
$\bar{z}^{O1}$	0.5	0.5	0.5	0.5	0	0	0	0	0	0	0	0
s^{O1}	1	1	1	1	0	0	0	0	0	0	0	0
$\bar{U}^{O1}_{eq}$	0.0168 (4)	0.0151 (2)	0.0166 (4)	0.0165 (3)	−0.00026 (9)	−0.00010 (9)	0.00002 (15)	0.00003 (16)	−0.00006 (10)	−0.00006 (9)	−0.00012 (16)	−0.00020 (16)
O2												
$\bar{x}^{O2}$	0.12752 (15)	0.12766 (11)	0.12754 (11)	0.12793 (9)	−0.00285 (11)	−0.00194 (10)	−0.00109 (14)	−0.00114 (14)	−0.00653 (12)	−0.00431 (11)	−0.00207 (15)	−0.00271 (14)
$\bar{y}^{O2}$	0.21786 (19)	0.21705 (13)	0.21837 (15)	0.21778 (13)								
$\bar{z}^{O2}$	0	0	0	0	0	0	0	0	0	0	0	0
s^{O2}	1	1	1	1	0	0	0	0	0	0	0	0
$\bar{U}^{O2}_{eq}$	0.0175 (4)	0.0161 (2)	0.0173 (4)	0.0173 (2)								
O3												
$\bar{x}^{O3}$	0	0	0	0	−0.0029 (5)	−0.0017 (3)	−0.0016 (5)	−0.0007 (5)	0	0	0	0
$\bar{y}^{O3}$	0.5	0.5	0.5	0.5	0.0034 (4)	0.0018 (3)	0.0013 (3)	0.0008 (5)	0	0	0	0
$\bar{z}^{O3}$	0.5	0.5	0.5	0.5	0	0	0	0	0	0	0	0
$\bar{s}^{O3}$	0.357 (7)	0.376 (6)	0.349 (8)	0.360 (5)	0	0	0	0	−0.01838 (19)	−0.01212 (10)	−0.00379 (7)	−0.00826 (10)
$\bar{U}^{O3}_{eq}$	0.020 (3)	0.0196 (19)	0.017 (3)	0.021 (2)	0	0	0	0	0.0017 (14)	0.0011 (13)	−0.0001 (13)	0.0002 (18)
O4												
$\bar{x}^{O4}$	0.449 (2)	0.4483 (9)	0.4534 (10)	0.4543 (9)	0.0004 (10)	0.0004 (4)	0.0003 (5)	0.0012 (5)	−0.0015 (10)	−0.0014 (6)	−0.0008 (7)	0.0007 (8)
$\bar{y}^{O4}$	0.0509 (12)	0.0466 (9)	0.0482 (9)	0.0499 (8)	0.0000 (6)	−0.0013 (4)	−0.0004 (3)	0.0002 (4)	0.0006 (8)	−0.0008 (6)	−0.0007 (5)	0.0004 (8)
$\bar{z}^{O4}$	0.5	0.5	0.5	0.5	0	0	0	0	0	0	0	0
s^{O4}	0.214 (2)	0.2080 (19)	0.217 (3)	0.2132 (17)	−0.0755 (8)	−0.0533 (5)	−0.0207 (4)	−0.0305 (4)	−0.0674 (7)	−0.0470 (4)	−0.0173 (3)	−0.0273 (3)
$\bar{U}^{O4}_{eq}$	0.017 (3)	0.0114 (17)	0.0120 (19)	0.0124 (16)	0.0013 (15)	−0.0015 (7)	0.0000 (8)	0.0003 (9)	0.0010 (17)	−0.0007 (10)	0.0022 (11)	0.0013 (15)

Table 4.7: Modulated structure model parameters from the refinement of the disordered SSM based on the measurements of samples SA1, SA2, SA3 and Qg1 on BM01 (ESRF).
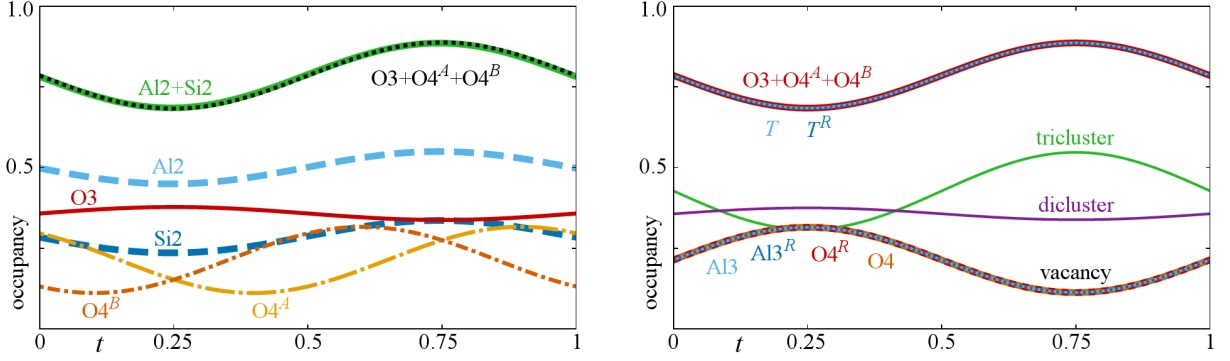
Figure 4.7: Occupational modulation functions and its interpretation in terms of the presence of diclusters, triclusters and vacancies occupying the volume around $(0 \frac{1}{2} \frac{1}{2})$. Functions shown on the left were not constrained. The graph on the right represents the final model with constraints. The probability for the presence of a tricluster is represented by the function $s^{O4^{\mathcal{A}}}(t) + s^{O4^{\mathcal{B}}}(t)$, that of a dicluster by $s^{O3}(t)$.

of different t-sections provides a first idea of the modulated structure of mullite (Fig. 4.6). The T^* site clearly indicates an occupational modulation that seems to be coupled with an occupational modulation of the O4 site. A strong displacive modulation is not observed, but it seems that O1 moves slightly as a function of t.

The implemented algorithm that interprets the structure solution in terms of atomic domains and modulation functions does not determine partial occupancies, occupational modulation functions, ADPs or ADP modulation functions and the structural model resulting from the solution gives a very high $R_{\text{obs}}(F) = 0.30$ after refining the suggested parameters. The completion of the average structure with partial occupancies of Al2, Si2, Al3, O3 and O4 with the respective constraints by stoichiometry improves the R factor for main reflections a lot, but without including occupational modulation functions the overall R factor still is very high. A free refinement of the occupancies $\bar{s}^{\mu}$ is unstable and results in high standard uncertainties. Only the refinement of the occupancy of Al3 is stable independent from the other atoms. A refinement of $\bar{s}^{\text{Si2}}$, $\bar{s}^{\text{Al3}}$, $\bar{s}^{\text{O3}}$ and $\bar{s}^{\text{O4}}$ is possible by fixing $\bar{s}^{\text{Al2}} = 0.5$ and leads to an acceptable composition close to a stoichiometric composition, but again with large uncertainties. Therefore, only $\bar{s}^{\text{O3}}$ was refined and the other occupancies $\bar{s}^{\mu}$ were constrained using the scheme of Table 3.3. A free refinement of the occupancies and occupational modulation parameters of Al2 and Si2 failed which is explained by the similar form factors of Al^{3+} and Si^{4+}. Different models, many of them physically meaningless, hardly affect the R factors. Therefore, the refinement parameters of Al2 and Si2 were constrained to be equal except for the average occupancies $\bar{s}^{\text{Al2}}$ and $\bar{s}^{\text{Si2}}$. The refinement of this model without further constraints on the occupational modulation function parameters converges to a physically meaningful model with acceptable R factors for main and satellite reflections. However, within one standard uncertainty the requirements established by the constraint scheme in § 4.1.4 are

fulfilled. This confirms the derived constraint scheme and the tricluster environment for vacancies (Fig. 4.7). The standard uncertainties improve significantly by implementing the constraint scheme, which was therefore used in all subsequent refinements of the disordered SSM. Displacive modulation parameters, anisotropic displacement parameters (ADP), and ADP modulation parameters of all atoms were refined. Strong correlations between refinement parameters of O3 and O4 were observed. Apparently, the resolution of the measurement was not sufficient to resolve the details of the electron density of O3 and O4 due to the very short distance of less than 0.6 Å between both sites. Disabling the modulation of U_{12} strongly decreased the correlations and resulted in realistic ADPs of O3 and O4 after the final refinement cycles with $wR(F^2) = 0.104$. Details on the experimental conditions, data reduction and refinement are given in Table 4.6. Refined parameters of the structural model are given in Table 4.7. In the tables also the measurements and results of samples SA2, SA3 and Qg1 are included, which are described and compared in § 4.2.5. Digital CIF files are available (§ A.9).

4.2.2 Vacancy distribution

The probability to find a vacancy at $(0\,\frac{1}{2}\,\frac{1}{2})$ is described by $s^Q(t)$, which is equal to $s^{\mathrm{Al3}}(t)$. Likewise, $s^{Q^{\mathcal{B}}}(t)$ is the probability to find a vacancy at $(\frac{1}{2}, 1, \frac{1}{2})$ and $(\frac{1}{2}, 0, \frac{1}{2})$. This probability ranges between 11.3 % and 31.5 % and thus vacancies can be present at all sites with a certain probability. The probability functions $s^Q(t)$ and $s^{Q^{\mathcal{B}}}(t)$ are shifted in phase by $\frac{1-\alpha}{2}$ according to superspace symmetry. As $s^Q(t)$ is described by first order harmonics relatively small values of α correspond approximately to an anti-phase relationship and large values to an in-phase relationship. Here, $\alpha \approx 0.3$ and thus a maximum of $s^Q(t)$ corresponds to a small value of $s^{Q^g}(t)$ and vice versa. The modulation functions of two vacancies upon each other, e.g. at $(0, \frac{1}{2}, \frac{1}{2})$ and $(0, \frac{1}{2}, \frac{3}{2})$, are shifted in phase by exactly $\frac{1}{2}$. Hence, a probability maximum of $s^Q(t)$ means that the probability to find a vacancy stacked below or above it is rather small. The vacancy distribution in physical space sections of the disordered SSM is depicted in Figure 4.8. The refined superspace model describes a probability distribution of vacancies with a small tendency to long-range vacancy ordering. The driving force for ordering seems to be the avoidance of close contacts of vacancies themselves and the avoidance of an overlap of the tricluster environments of the vacancies.

4.2.3 Displacive modulation and bond lengths

The displacive modulation of most atomic domains is not strong resulting in an absolute displacement from the average position by less than 0.02 Å (Fig. 4.9). The largest displacement occurs for O1 within the *ab*-plane by about 0.04 Å. In the case of Al1 and
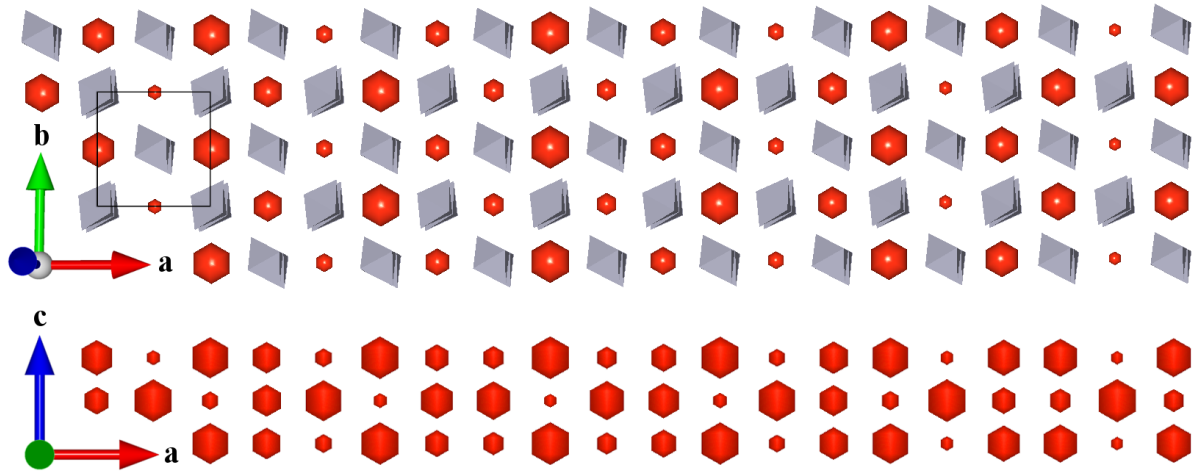
Figure 4.8: *ab* section (top) and *ac* section (bottom) through the disordered SSM showing the distribution of vacancies. The probability for the presence of a vacancy is represented by the size of red hexagons. Large and small hexagons correspond to 31.5% and 11.3%, respectively. Note that at each site only one of two vacancy orientations is possible. The distribution of triclusters and diclusters is thus fully defined by the distribution of vacancies and tetrahedra are omitted for clarity. In the bottom view also octahedra are not shown.

O2 the displacement within the *ab*-plane is forbidden by symmetry as only first order harmonics were used. Correlations are clearly visible as O1 and Al1 exhibit the strongest displacement for $t \approx \frac{1}{4}$ and $t \approx \frac{3}{4}$, though in the case of Al1 it is a consequence of symmetry constraints. All the other atoms exhibit the displacement maximum at $t \approx 0$ and $t \approx \frac{1}{2}$. The displacive modulation of O4 exhibits the displacement minimum at $t \approx \frac{1}{3}$, i.e. it is most off-phase relative to the other atoms. However, uncertainty in the refined displacive modulation parameters of O4 are noticeably large. The details of the displacive modulation should thus be analysed with care.

Despite the displacive modulation of Al1, O1 and O2, the bond lengths within the octahedra are almost constant for any value of t (Fig. 4.10). The modulations of the bond lengths of the tetrahedral cations are more pronounced. The distance Al3–O1 is correlated with the occupancy of Al3, i.e. O1 is closest to Al3 for t $\approx$ ¼, when $s^{Al3}(t)$ is at its maximum. The amplitude of the bond length modulation of T–O3 is larger than that of T–O1 or T–O2. It is most likely that the bond length modulation of T–O3 mainly originates from Al/Si ordering on the T site, whereas that of T–O1 and T–O2 is a superposition of the contributions of Al/Si ordering and the overall tetrahedra distribution. The average bond lengths of Al3 are significantly larger than that of the T site supporting the assumption that Si is exclusively, or at least predominantly, present on T sites. In the next section the displacive modulation functions are used to derive an Al/Si ordering pattern based on the observed modulation of the volume of the T site tetrahedron.
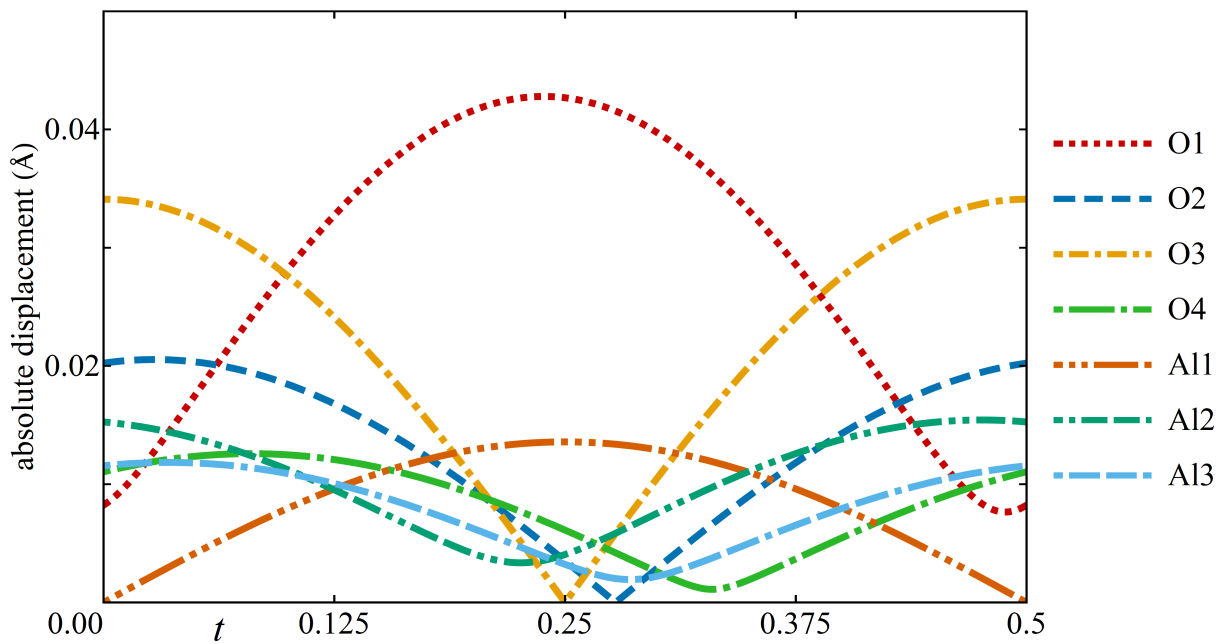
Figure 4.9: Absolute displacement from average position due to the displacive modulation functions. The phases of the displacive modulation functions of Al1 and O3 are fixed due to their site symmetry $\frac{2}{m}$. Note that the horizontal axis goes from $0 \leq t \leq 0.5$.
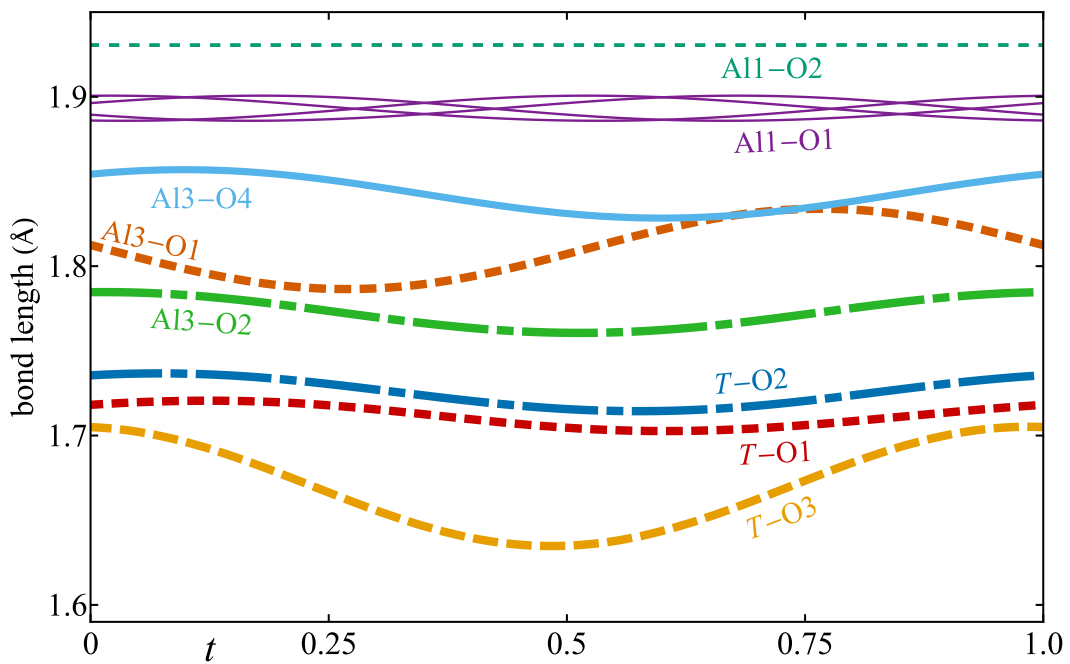

Figure 4.10: Cation-oxygen bond lengths.

Reference	Structure	Method	$V_{\mathrm{Ref}}^{\mathrm{Al}}$	$V_{\mathrm{Ref}}^{\mathrm{Si}}$	$\bar{s}_V^{\mathrm{Al2}}$
Tab. 1.4 [52]	many	geometry	2.75	2.18	0.51
[173]	Sillimanite	sXRD	2.782 (3)	2.192 (3)	0.477 (4)
[54]	Sillimanite	sND	2.7677 (18)	2.1890 (15)	0.491 (3)
§ 4.3.3 (FFID 3)	2/1-mullite	FF	2.62 (6)	2.23 (5)	0.65 (10)
§ 4.3.3 (#1)	2/1-mullite	PBE	2.70 (4)	2.26 (4)	0.51 (7)
§ 4.4.6 (M40 AS1)	2/1-mullite	PBEsol-D	2.69 (5)	2.26 (4)	0.53 (7)

Table 4.8: Candidates for $V_{\mathrm{Ref}}^{\mathrm{Al}}$ and $V_{\mathrm{Ref}}^{\mathrm{Si}}$ from different sources. The reference volumes calculated geometrically assume that the tetrahedron is a regular tetrahedron. Reference volumes from geometrically optimised structures (FF, PBE, PBEsol-D) are calculated as average of ten independent Al2 tetrahedra and six independent Si2 tetrahedra, respectively. In the ideal case $\bar{s}_V^{\mathrm{Al2}}$ gives 0.5 assuming that the T^* site is only occupied by Al. sXRD = single crystal X-ray diffraction, sND = single crystal neutron diffraction, FF = force field calculations

4.2.4   Al/Si ordering

The occupational modulation functions of Al2 and Si2 could not be determined in the refinement. A relationship can be established between the volume of the T site tetrahedron $\overline{V}_r^T$, that can be directly calculated from the refined average coordinates of the atoms, and the occupancies $\bar{s}^{\mathrm{Al2}}$ and $\bar{s}^{\mathrm{Si2}}$. At first the approach is checked with the average structure.

$$\overline{V}_r^T = \frac{1}{6} \sum_\mu \frac{\bar{s}^\mu}{\bar{s}^T} |(\overline{\mathbf{x}}^{\mathrm{O1}} - \overline{\mathbf{x}}^\mu) \cdot ((\overline{\mathbf{x}}^{\mathrm{O1}} - \overline{\mathbf{x}}^{\mathrm{O2}}) \times (\overline{\mathbf{x}}^{\mathrm{O1}} - \overline{\mathbf{x}}^{\mathrm{O2}^{\mathcal{M}}}))|$$

The sum goes over O3, O4$^{\mathcal{A}}$ or O4$^{\mathcal{B}}$ because the observed volume is the superposition of three tetrahedra (cf. Fig. 4.5). The occupancy $\bar{s}^T$ is related to the other occupancies as $\bar{s}^T = \bar{s}^{\mathrm{O3}} + \bar{s}^{\mathrm{O4}^{\mathcal{A}}} + \bar{s}^{\mathrm{O4}^{\mathcal{B}}} = \bar{s}^{\mathrm{Al2}} + \bar{s}^{\mathrm{Si2}} = 1 - \frac{\delta}{2}$. The radius of the Al^{3+} cation is about 50% larger than the Si^{4+} cation in tetrahedral coordination (Tab. 1.4) and thus the volume of the T site tetrahedron can be calculated from the Al/Si ratio on the T site in analogy to Vegard's law [172] if the volumes of pure SiO$_4$ and AlO$_4$ tetrahedra $V_{\mathrm{Ref}}^{\mathrm{Al}}$ and $V_{\mathrm{Ref}}^{\mathrm{Si}}$ are known.

$$\overline{V}_s^T = \frac{\bar{s}^{\mathrm{Al2}}}{\bar{s}^T} V_{\mathrm{Ref}}^{\mathrm{Al}} + \frac{\bar{s}^{\mathrm{Si2}}}{\bar{s}^T} V_{\mathrm{Ref}}^{\mathrm{Si}}$$

In a consistent model $\overline{V}_s^T$ must be equal to $\overline{V}_r^T$ and thus the occupancies $\bar{s}_V^{\mathrm{Al2}}$ and $\bar{s}_V^{\mathrm{Si2}}$ can be calculated from $\overline{V}_r^T$ which directly results from the refinement.

$$
\begin{aligned}
\bar{s}_V^{\mathrm{Al2}} &= \frac{|V_{\mathrm{Ref}}^{\mathrm{Si}} - \overline{V}_r^T|}{V_{\mathrm{Ref}}^{\mathrm{Al}} - V_{\mathrm{Ref}}^{\mathrm{Si}}} \bar{s}^T \\
\bar{s}_V^{\mathrm{Si2}} &= \frac{V_{\mathrm{Ref}}^{\mathrm{Al}} - \overline{V}_r^T}{V_{\mathrm{Ref}}^{\mathrm{Al}} - V_{\mathrm{Ref}}^{\mathrm{Si}}} \bar{s}^T = \bar{s}^T - \bar{s}_V^{\mathrm{Al2}}
\end{aligned}
\tag{4.1}
$$

One problem is that the reference volumes $V_{\mathrm{Ref}}^{\mathrm{Al}}$ and $V_{\mathrm{Ref}}^{\mathrm{Si}}$ are not known as they cannot

be derived from the refinement itself and hence must be determined by other means. In a first approximation they can be calculated by constructing a regular tetrahedron based on empirical ionic radii or from refined models of sillimanite. Another possibility is to analyse geometrically optimised models of mullite based on computational methods. As the expected occupancy of Al2 is $\bar{s}_V^{\text{Al2}} = 0.5$ based on the assumption that Si does not occupy the T^* site, the eligibility of of a source of $V_{\text{Ref}}^{\text{Al}}$ and $V_{\text{Ref}}^{\text{Si}}$ can be evaluated (Tab. 4.8). The force field calculations are neither accurate nor precise enough to determine representative structural details of the structural geometry like the volumes of polyhedra. $V_{\text{Ref}}^{\text{Al}}$ and $V_{\text{Ref}}^{\text{Si}}$ of the DFT calculations are both suitable as $\bar{s}_V^{\text{Al2}}$ is close to 0.5 within less than $\frac{1}{2}\sigma$, but the standard uncertainty is rather high with a relative uncertainty of about 14 %. On the other hand, the calculations may be an indication that some Si atoms occupy the T^* site. The refined structural model of sillimanite based on single crystal X-ray diffraction [173] provides precise volumes with a low standard uncertainty, but the resulting $\bar{s}_V^{\text{Al2}}$ deviates from 0.5 by more than 3σ. The neutron diffraction study [54] performs very good as the standard uncertainties for $V_{\text{Ref}}^{\text{Al}}$, $V_{\text{Ref}}^{\text{Si}}$ and $\bar{s}_V^{\text{Al2}}$ are small and with $\bar{s}_V^{\text{Al2}} = 0.491\,(3)$ the result is within 3σ from the expected value. For the determination of corrected occupational modulation functions the subsequent steps used either reference volumes of sillimanite (sND, [54]) or of a DFT calculation (M40 AS1, PBEsol-D, § 4.4.6). According to Table 4.8 the DFT calculations using the PBE functional provides better reference volumes than dispersion corrected calculations using on the PBEsol functional, but § 3.6, § 4.4.6 and § A.3 indicate that calculations using PBEsol-D are in better agreement with experimental observations especially concerning the lattice parameters. Therefore, PBEsol-D calculations were chosen for this section.

The test of the reference volumes with the average structure confirms that with this method the occupancy of Al2 and Si2 can be determined from the coordinates of the coordinating oxygen atoms. The method presented in this section also can be applied to the modulated structure of mullite by implementing the respective modulation functions so that $V_r^T(t)$ is calculated from $\mathbf{x}^\mu(t)$. The occupational modulation functions $s_V^{\text{Al2}}(t)$ and $s_V^{\text{Si2}}(t)$ are the determined with Equation 4.1. The steps are visualised in Figure 4.11. The trivial modulation functions used in the refinement are clearly not consistent with $V_r^T(t)$. With the new determined $s_V^{\text{Al2}}(t)$ and $s_V^{\text{Si2}}(t)$ the functions $V_r^T(t)$ and $V_s^T(t)$ perfectly overlap, but $\bar{s}_V^{\text{Al2}}$ and $\bar{s}_V^{\text{Si2}}$ slightly deviate from the occupancies of the refinement (Tab. 4.9). For the plot of $V_s^T(t)$ in Figure 4.11 $\bar{s}_V^{\text{Al2}}$ and $\bar{s}_V^{\text{Si2}}$ were replaced by the occupancies of the refinement and only the new values of $A_{s,1}^\mu$ and $B_{s,1}^\mu$ (μ = Al2, Si2) were taken (Tab. 4.9) leading to an offset between $V_s^T(t)$ and $V_r^T(t)$. The deviation is within the uncertainty. Implementing the corrected modulation function amplitudes for Al2 and Si2 based either on the sillimanite reference volumes or the DFT reference volumes in the refinement of SA1 improves in both cases the overall $wR(F^2)$ from 0.104 to 0.103 and the $wR(F^2, m = 1)$ of first order satellite reflections from 0.083 to 0.080. This little

source for $V_{\text{Ref}}^{\text{Al}}, V_{\text{Ref}}^{\text{Si}}$	$\bar{s}_V^{\text{Al2}}$	$A_{s,1}^{\text{Al2}}$	$B_{s,1}^{\text{Al2}}$	$\bar{s}_V^{\text{Si2}}$	$A_{s,1}^{\text{Si2}}$	$B_{s,1}^{\text{Si2}}$
Peterson & McMullan (1986) [54]	0.490	0.063	0.031	0.296	−0.035	0.066
DFT (PBEsol-D)	0.530	0.079	0.027	0.256	−0.051	0.070

Table 4.9: Modulation function parameters of Al2 and Si2 derived from the displacive modulation of SA1. Note that $s_V^{\text{Al2}}(t)$ and $s_V^{\text{Si2}}(t)$ are functions of coordinates, reference volumes and occupational modulation functions and not simple harmonic functions like Equation 2.2. The parameters listed in this table were determined with a numerical fitting procedure.
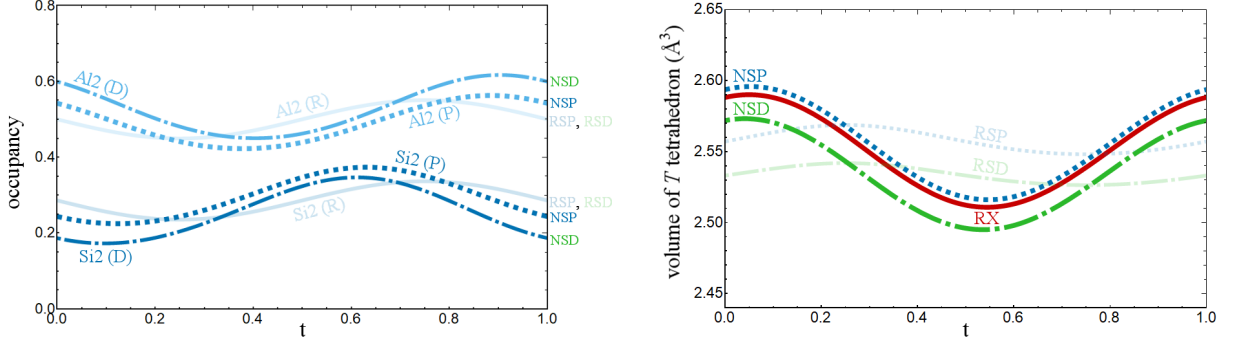
Figure 4.11: Occupational modulation functions of Al2 and Si2 (left) and volume of the tetrahedral T site (right). A 'P' in the labels means that the reference volumes $V_{\text{Ref}}^{\text{Al}}$ and $V_{\text{Ref}}^{\text{Si}}$ were taken from the study by Peterson & McMullan (1986) [54]. A 'D' in the label indicates that they were taken from the DFT calculation (PBEsol-D). Modulation functions (faint solid lines, label R) correspond to the initial refinement of § 4.2.1 and the expected volume modulation shown on the right (faint blue dotted line for label RSP, faint greed dot-dashed line for label RSD) clearly deviates from the observed volume modulation calculated from the refined displacive modulation parameters (red solid line, label RX). From the curve RX corrected modulation functions were calculated which lead to a consistent description of the displacive and the occupational modulation.

improvement is rather negligible because the consistency of the overall model is more relevant. With the corrected occupational modulation functions the disordered SSM is complete in the sense that the occupational modulation functions describe vacancy and Al/Si ordering.

4.2.5 Modulation amplitudes

The refinement as described above for the sample SA1 was also carried out for the samples SA2, SA3 and Qg1. The same constraint schemes were applied. The final $wR(F^2)$ are 0.089, 0.111 and 0.097 for SA2, SA3 and Qg1, respectively. Details on the experimental conditions, data reduction and refinement are given in Table 4.6. The average structures are basically the same with refined compositions corresponding to vacancy concentrations of 0.416 (4), 0.434 (6) and 0.426 (3), respectively. The composition determined with the Rietveld refinement based on the SA sample resulted in a vacancy concentration
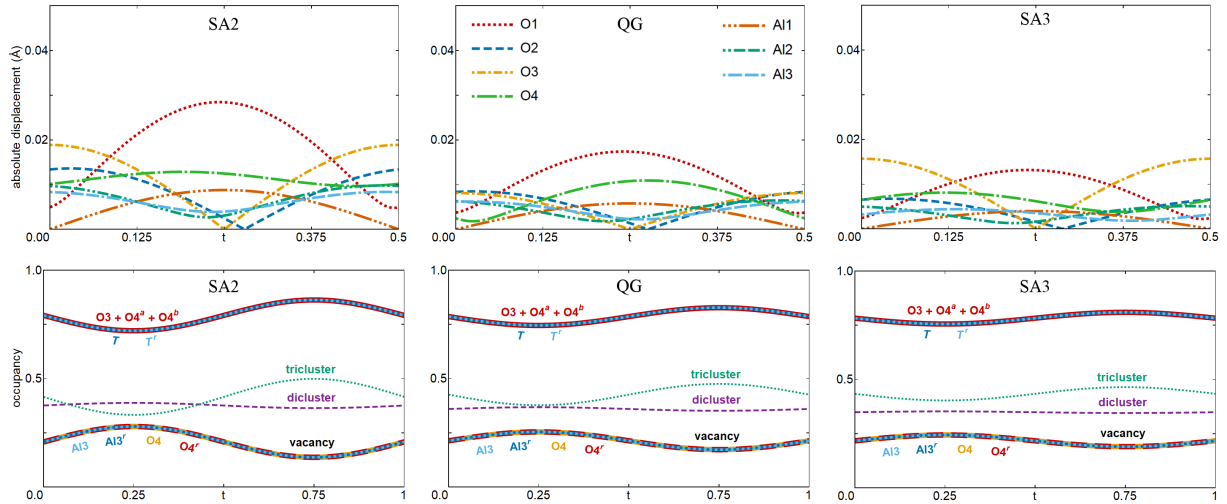
Figure 4.12: Comparison of modulation functions of SA2, Qg1 and SA3.

$\delta = 0.429\,(5)$ in good agreement with the refinements based on SA1, SA2 and SA3. The average coordinates are identical within the limits of the standard uncertainty indicating a consistent refinement for all of mullite samples with a comparable composition. The largest uncertainty concerns the coordinates of O4, probably due to the lack of sufficient resolution as already mentioned in § 4.2.1. The refinement of the modulation functions yields qualitatively the same model. Again, some uncertainty concerns the displacive modulations of O3 and O4. There is, however, a remarkable difference between the refinements concerning the amplitudes of the modulation functions. A comparison of $s^{\mathrm{Al3}}(t)$ of different measurements shows that the relative occupational modulation amplitude ratio is about 3.7:2.6:1.5:1 for the refinements of SA1:SA2:Qg1:SA3. The same trend is observed for displacive modulation functions (Fig. 4.12). In different samples the modulation is qualitatively the same indicating that there is an underlying long-range ordering pattern, but it is only partially maintained in the different structures. In samples with larger modulation amplitudes the ordering probably adheres more to the underlying ordering pattern, and in samples with lower modulation amplitudes the range within which the ordering pattern is maintained is rather limited. Thus, the modulation amplitudes can be interpreted as an indicator for the degree of order. This raises the question how a model representing the highest degree of order looks like, which is addressed in the next sections.

4.3 Ordered SSM: Superspace model with full vacancy and Al/Si ordering

The refinement based on harmonic occupational modulation functions revealed that the tendency to long-range vacancy and Al/Si ordering is not very strong and thus the disordered SSM describes at which coordinates in superspace it is more likely or less likely to encounter a vacancy or a specific dicluster type like Si-Si diclusters. It is, however, not straight forward to define a precise ordering pattern from it. In the next sections an 'ordered superspace model' (ordered SSM) of 2/1-mullite ($\delta = 0.4$) is presented based on the constraints of § 4.1.3. The distribution of Si on the tetrahedral sites is not implemented in this constraint scheme. Therefore, the Al/Si ordering was investigated with computational methods.

4.3.1 Refinement with different scale factors

Block wave functions can be approximated with a large set of harmonic functions. The refinement of superspace models with block wave functions are usually based on crystals that show high order satellite reflections on the diffraction patterns [174, 175]. In most measurements of this thesis only first order satellite reflections were observed indicating that the occupational modulation functions are adequately described by the disordered SSM. On the other hand, the simultaneous presence of sharp satellite reflections and diffuse scattering in combination with the observation of different degrees of order in different samples suggest that two polymorphs may exist and are simultaneously present. An ordered polymorph then accounts for sharp satellite reflections and a disordered polymorph for the diffuse scattering. The dominance of one polymorph or the other then mimics different degrees of order. Based on this assumption a refinement with two phases can bet set up. The first phase is an average structure model representing the disordered polymorph. The second phase is an ordered (3+1)d superspace model which requires to refine the phase fraction ν_{ordered}. Assuming that for both fractions the average position and ADPs of the atoms are identical, the first phase can be eliminated from the refinement by using independent scale factors S_{main} and S_{sat} for main and satellite reflections, respectively, based on the relationship $\nu_{\text{ordered}} = (S_{\text{sat}}/S_{\text{main}})^2$.

The latter approach was used for the refinement of the ordered SSM based on the measurements of SA1, SA2, SA3 and Qg1 on BM01 at the ESRF. The disordered SSM without occupational modulation functions served as a starting model. As expected, difference Fourier maps show clear maxima along the atomic domains of T, T^*, O3 and O4 which at first glance is in agreement with the constraint scheme of § 4.1.3. A free refinement of the parameters of displacive modulation, ADPs and ADP modulation was partly unstable and results in unrealistic ADPs. This affects mainly the atomic domains with short Δ_{BW}^{μ},
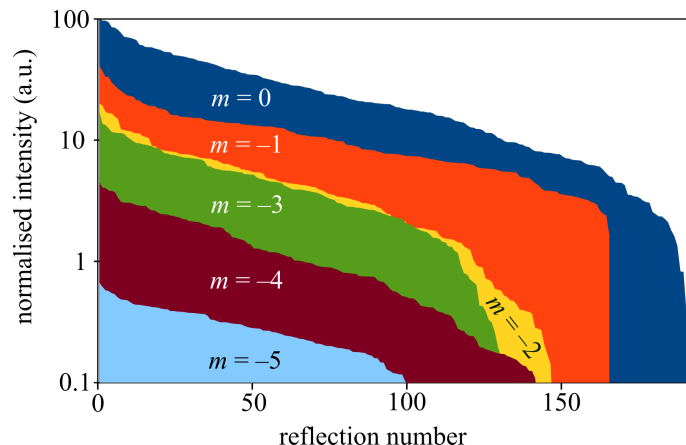
Figure 4.13: Expected intensity distribution of main and satellite reflections (unique scale) based on the refined model (different scale factors). Thus, only the occupational modulation contributes to higher order satellite reflections because only first order harmonics were used for the displacive modulation.

i.e. Al3, O3a, O3b and O4. The refinement converges smoothly if the respective ADP modulation parameters are set to 0, the displacive modulation of Al3 and O4 is deactivated and the displacive modulation of O3a and O3b is constrained to be equal. The data sets of SA1, SA2, SA3 and Qg1 give acceptable values for $wR(F^2)$ of 0.138, 0.124, 0.149 and 0.113, respectively

A refinement including second order satellite reflections of the measurement of SA1 was not successful. Structure factor calculations indicate that increasing the satellite reflection order m by two approximately decreases the intensity by one order of magnitude. The ratio of the mean intensity of first and second order satellite reflections in the measurement of SA1 on ID28 is about 100:1. Hence, the ordered SSM cannot explain the presence of weak second order satellite reflections. The initial assumption that disordered mullite consists of an ordered polymorph within a disordered polymorph is not supported. If there are ordered domains, they must be very small as suggested in [63].

4.3.2 Vacancy distribution

Although the refinement indicates that the ordered SSM does not represent the samples or ordered domains of the samples, the model is very valuable for the understanding of the crystal structure and ordering phenomena in mullite. Physical space sections of a commensurate approximation with $\delta = 0.4$ and $\mathbf{q} = (\frac{3}{10}\,0\,\frac{1}{2})$ are suitable to analyse the structural units and building blocks. The backbone of the $10 \times 1 \times 2$ superstructure are the octahedra chains in which tetrahedral dicluster units and triclusters around vacancies are embedded. As $\gamma = \frac{1}{2}$ the repeating distance along the c direction is $2\mathbf{c}$ and hence an alternating pattern of triclusters, diclusters and vacancies emerge. Two identical units never stack upon each other, i.e. vacancy channels, dicluster chains and tricluster chains
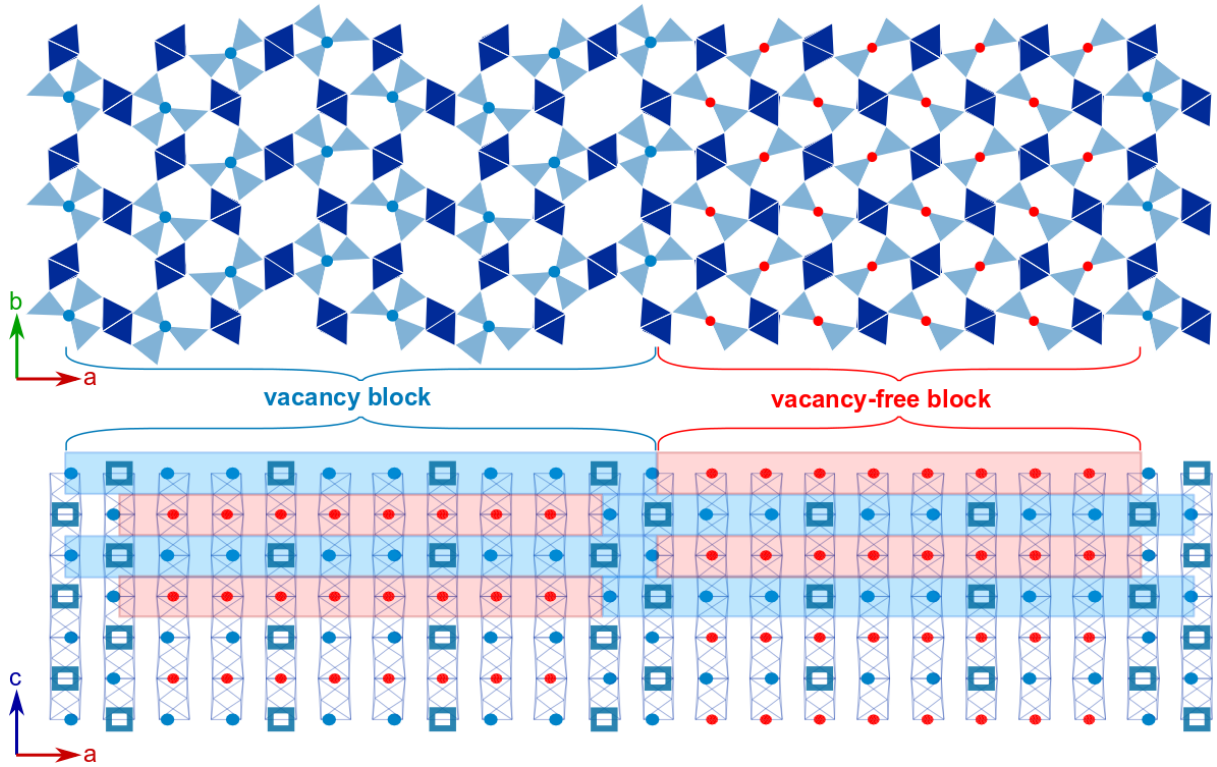
Figure 4.14: Physical space section of the ordered superspace model with $\mathbf{q} = \left(\frac{3}{10}\, 0\, \frac{1}{2}\right)$ and $\delta = 0.4$. O4 atoms are represented by blue and O3 atoms by red spheres so that diclusters and tricluster can be easily distinguished by the colour code. Other atoms are omitted. In the top view octahedra are shown in dark blue and tetrahedra in grey blue. In the bottom view the tetrahedra network is omitted and the octahedra backbone is shown as skeleton. Vacancies are represented by thick blue squares.

are not present. Both vacancies and diclusters group together into block-like units (Fig. 4.14), which are here called 'vacancy blocks' (VBs) and 'vacancy-free blocks' (VFBs). VFBs consist of diclusters only, and VBs consist of a dense packing of triclusters with the corresponding vacancies. The blocks alternate along $\mathbf{a}$ and $\mathbf{c}$ resulting in a brick pattern. The block size in both cases is $5\mathbf{a} \times 1\mathbf{b} \times 1\mathbf{c}$, though the extension along the a direction depends on the definition whether or not the outermost T site tetrahedra of triclusters belong to the VBs or VFBs. If they are considered as part of the VBs then the VBs are longer as the VFBs and overlap as shown in Figure 4.14.

In physical space sections of the refined ordered SSM of SA1 ($\alpha = 0.2988$, $\delta \approx 0.41$) the brick pattern of VBs and VFBs is maintained, but the block lengths change. VBs consists of either four or five vacancies. VFBs consist of either five or eight diclusters. On average, VBs are extended and VFBs are shortened resulting in an increased vacancy concentration which corresponds to the refined composition. As a consequence, tricluster-tricluster chains are present. In the latter case the two triclusters are not of the same orientation, i.e. if in one tricluster Al3$^{\mathcal{A}}$ and O4$^{\mathcal{A}}$ are occupied then the subsequent tricluster contains Al3$^{\mathcal{B}}$ and O4$^{\mathcal{B}}$.

94

4.3.3 Determination of ideal Al/Si ordering pattern of 2/1-mullite

In the last section it was shown that the vacancy concentration and the modulation wave vector are sufficient to define an ordered vacancy distribution for mullite, from which the polyhedra structure can be fully derived. However, it is not known how Al and Si atoms are distributed over the T sites. Furthermore, the assumption that Si does not occupy the T^* site must not necessarily be true. Al/Si ordering can be implemented in the ordered superspace model by replacing the atomic domains of the T and T^* site by a set of block wave functions that define that either Al or Si occupies a certain place in super space. As there is no restriction on the number of domains and the respective length the investigation of Al/Si ordering in superspace of incommensurate mullite was not tried. Instead, the Al/Si ordering was investigated with computational methods applied to a superstructure based on physical space sections of the ordered SSM with $\delta = 0.4$ and $\mathbf{q} = (\frac{3}{10}\, 0\, \frac{1}{2})$. The space group symmetry of the commensurate structure of 2/1-mullite depends on the physical space section t because an arbitrary t will brake all symmetry elements except for m_z leading to the space group $B11m$. If $t = \frac{3}{40} + \frac{n}{10}$ $(n \in \mathbb{Z})$ the displacive modulation preserves the symmetry of the b glide plane perpendicular to $\mathbf{a}$ and the 2_1 screw axis parallel to $\mathbf{b}$. However, due to the occupational modulation only physical space sections with $t = \frac{3}{40} + \frac{2}{10}$ or $t = \frac{3}{40} + \frac{7}{10}$ comply with the space group $Bb2_1m$. Throughout this thesis commensurate superstructures of 2/1-mullite are represented with $t = 0.275$. The chemical formula with $Z = 4$ is $Al_{10}(Al_{14}Si_6)O_{48}$. In the asymmetric unit there are 20 tetrahedral sites for 14 Al and 6 Si atoms. The number of Al/Si permutations on all tetrahedral sites, including T^* sites, is $\binom{20}{6} = 38760$ and each represents a different Al/Si ordering pattern in physical space as well as in superspace. In order to systematically evaluate which Al/Si ordering is energetically favourable corresponding $10\times1\times2$ supercells with 312 atoms were generated. With the available computer power it is not possible to perform accurate DFT calculations with all of the generated structures[2]. The chosen strategy was to run force field (FF) calculations with all 38760 structures and then perform DFT calculations with the most promising candidates.

The force field calculations were carried out using the GULP code [9]. The default convergence criteria were fully achieved for 18394 structures and partly for 20159 structures. The structural relaxation failed for 207 structures. Nevertheless, the energy of the last optimisation cycle in all cases yields an energy value that is sufficiently accurate for the present purpose. The energy of the most and least stable structures are -2996.60 eV (FFID 1) and -2943.12 eV (FFID 38760), respectively (Fig. 4.15). For a better comparison each permutation is assigned a number (FFID) which indicates the relative stability. The superstructure with FFID 1 corresponds to the lowest energy and represents the

---

[2]DFT calculations of all 38760 superstructures take more than 200 years with 48 cores of the available computer facilities. The 38760 relaxations with force field calculations require less than 24 hours.
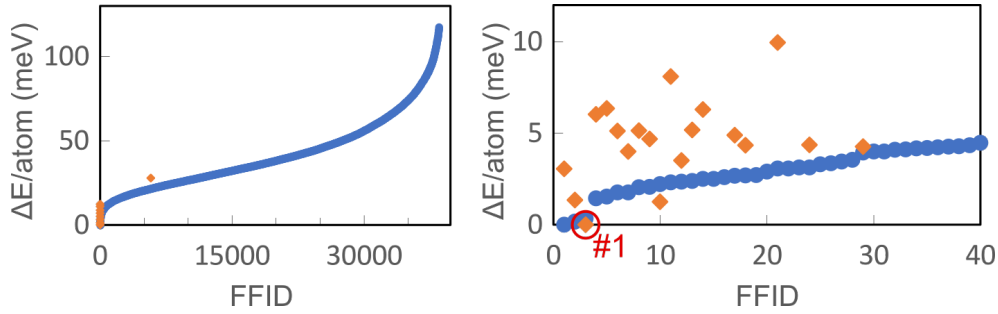
Figure 4.15: Relative energy/atom of the statically relaxed supercells of 2/1-mullite with different Si distributions sorted by FFID. Blue circles correspond to FF calculations, orange diamonds to DFT calculations. The left plot gives the complete overview on the energy range, the right plot only shows the details of the most promising structures for which DFT calculations were performed. The most stable Al/Si ordering pattern according to DFT calculations (#1, FFID 3) is marked with a red circle.

most stable Al/Si ordering according the force field calculations. FFID 10, 20, 50 and 100 have relative energy differences with respect to FFID 1 of 2.22, 2.89, 4.84 and 6.06 meV/atom. If we assume that the accuracy of the total energy calculations is approximately 2 meV/atom then it is sufficient to perform more accurate calculations on the best 10 to 20 candidates.

DFT calculations were carried out with the structures of FFIDs 1 to 14, 17, 18, 21, 24, 29, 86 and 4022 using the PBE functional, standard accuracy and a k point grid with $1 \times 10 \times 13$ points. Each optimised superstructure was assigned a rank indicated by the hashtag symbol in analogy to the FFID. The total energy[3] of the most stable structure (rank #1) is -2363.83 eV. The comparison of FF energies versus DFT energies suggests that the FF ranking is a good estimate and therefore it can be expected that the ideal Al/Si ordering is one of the candidates that was investigated with DFT (Fig. 4.15). Selected results of the calculations are given in Table 4.10. In Figure 4.16 the Al/Si ordering patterns of the five most stable superstructures are represented. The four most stable Al/Si ordering patterns only differ in the position of one Si atom, that is either in a tricluster or in a dicluster. Consequently, five of six Si positions are determined with high certainty and some doubt remains concerning the position of the sixth Si. Furthermore, from the Al/Si ordering a few simple ordering patterns can be derived, which are analysed in more detail in § 4.4 considering different compositions. It turns out that a full parametrisation of the Al/Si ordering of a certain supercell is rather cumbersome to set up, to analyse and to describe. This becomes even more complicated if different compositions with different cell sizes are compared. Hence, the used approach to identify the ideal Al/Si ordering in physical space with computational methods is effective, but the characterisation of the Al/Si ordering is more efficient and elegant in (3+1)d superspace based on modulation

---

[3]In § 2.5.2 it was mentioned that only relative energies are significant. Total energies are provided so that the interested reader may reproduce the results.

| DFT | E/atom | | | | FF | E/atom |
Rank	(meV)	a (Å)	b (Å)	c (Å)	FFID	(meV)
#1	−7576.39	7.6513	7.7134	2.9270	3	-9604.49
#2	1.24	7.6782	7.7232	2.9228	10	1.88
#3	1.34	7.6822	7.7011	2.9268	2	-0.17
#4	3.05	7.6760	7.7160	2.9241	1	-0.33
#5	3.50	7.6924	7.6957	2.9234	12	2.00
#6	3.99	7.6712	7.7293	2.9217	7	1.42
#7	4.26	7.6428	7.7206	2.9250	29	3.59
#8	4.33	7.6641	7.7207	2.9251	18	2.36
#9	4.35	7.6502	7.7342	2.9265	24	2.79
#10	4.67	7.6807	7.7207	2.9268	9	1.73
#11	4.89	7.6797	7.7209	2.9269	17	2.33
#12	5.11	7.6893	7.7216	2.9261	6	1.42
#13	5.13	7.6734	7.7366	2.9239	8	1.71
#14	5.17	7.6740	7.7375	2.9237	13	2.06
	11.52	7.6796	7.7038	2.9225	86	5.38
	25.32	7.6673	7.7220	2.9229	4022	18.90

Table 4.10: Rank refers to the relative stability of the supercell according to DFT calculations. The FFID is an analogue ranking according to the FF calculations. E/atom is the absolute value for #1 (FFID 3) and in all other cases the relative energy per atom with respect to #1.

functions. In the next section the geometrically optimised superstructures are used to establish superspace models by embedding the atoms in a (3+1)d unit cell.

4.3.4 Ideal superspace model of 2/1-mullite

As explained in § 2.4.3 a superstructure model can be embedded in (3+1)d superspace based on an average structure model and a modulation wave vector $\mathbf{q}$. To determine the modulation functions of the different sites, for example the occupational modulation functions of Al2 and Si2, it is convenient to represent the atoms that belong to the same atomic domain in a t-plot. In order to relate the setting of the $10 \times 1 \times 2$ superstructure described in the space group $Bb2_1m$ to a superspace description in $Pbam(\alpha 0 \frac{1}{2})0ss$ with Al1 at the origin it is necessary to consider the physical space section $t_0 = 0.275$ and an
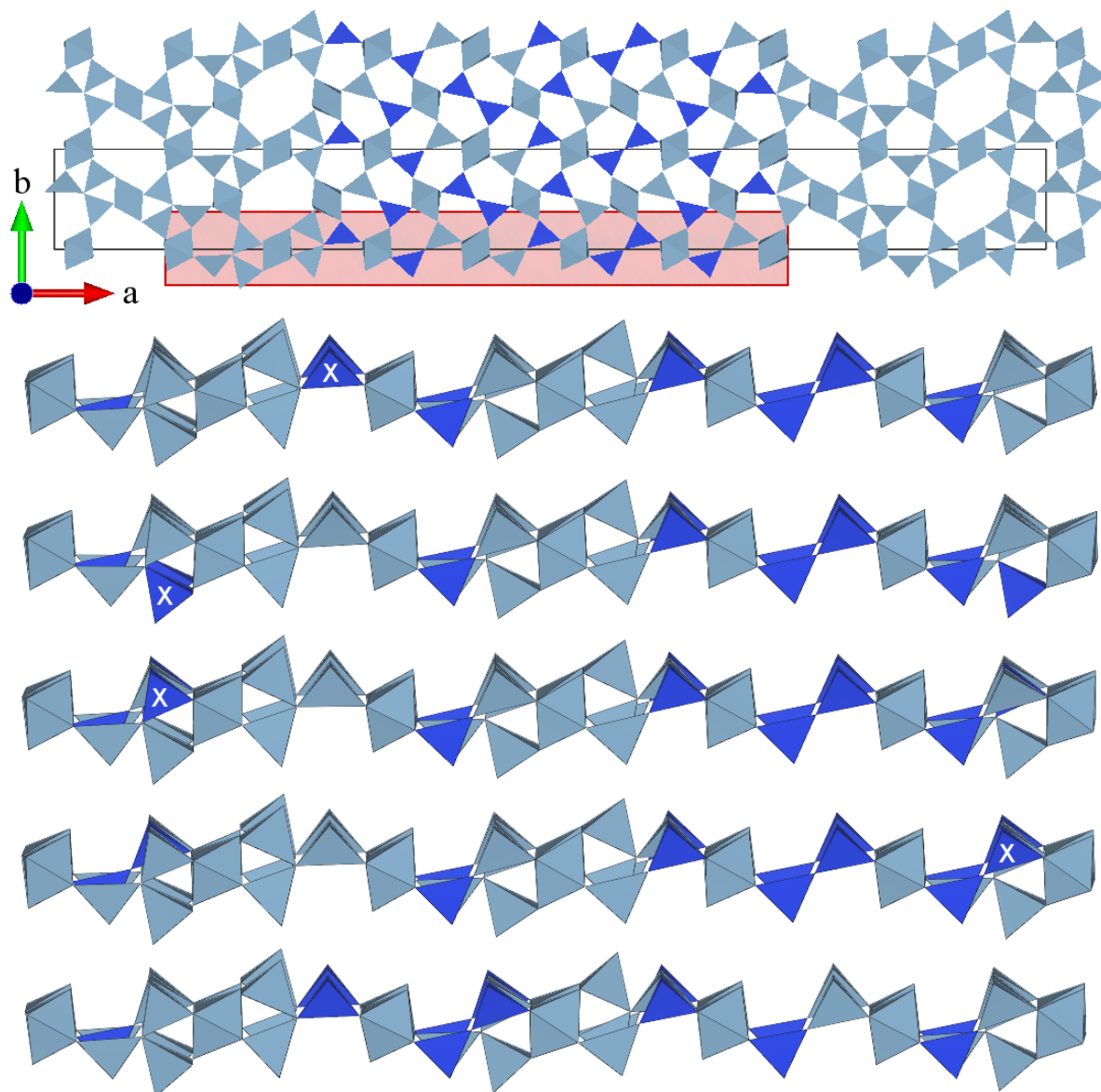
Figure 4.16: Al/Si ordering patterns of ranks #1 to #5. The top view shows a model of #1 perpendicular to **c**. The red frame marks the section that is shown for #1 to #5 with subsequent layers. The distribution of most Si atoms in structures #1 to #4 is identical and only the Si atom marked with a white 'X' changes position with an Al site.

origin shift $\mathbf{p}$.

$$\mathbf{x}' = \begin{pmatrix} 10 & 0 & 0 \\ 0 & 1 & 0 \\ 0 & 0 & 2 \end{pmatrix} \mathbf{x} + \mathbf{p}$$

$$x_{\mathrm{s4}} = \mathbf{q} \cdot \mathbf{x}' + t_0$$

Here, $p_1 = \frac{3}{4}$ and $p_3 = \frac{1}{4}$. During the geometric optimisation the atoms may shift along the b direction because the structure is described in the polar space group $Bb2_1m$. Therefore, p_2 was determined by averaging over a set of atoms with the expectation value 0.5 and the difference from this value was used as p_2. Translational symmetry and the application of the symmetry operators of $Pbam(\alpha 0\frac{1}{2})0ss$ finish the embedding of the superstructure in superspace. At this stage, atomic domains are represented by up to 20 points, depending on the average occupancy of the respective site.

To determine the occupational modulation functions that define the Al/Si ordering in mullite the geometrically optimised superstructure with the lowest energy (DFT rank #1) was embedded in superspace (Fig. 4.17). The inspection of the atomic domain of the T site shows that four block wave functions, here labelled Al21, Al22, Si21 and Si22, are required to describe the occupational modulation of Al2 and Si2. Without external constraints, the precision for the determination of $\Delta^{\mu}_{\mathrm{BW}}$ and x^{μ}_{BW} is limited because the atomic domains are not continuous. In the case of mullite the block wave parameters of O3a, O3b and O4 are already known from the constraint scheme of Table 4.4 and the borders of these known block wave functions can be used to fix reference points for the definition of the unknown occupational modulation functions. The parameters of Si22 and Al22 are straight forward to determine because Si22 is always bonded to O3b and Al22 only occurs in triclusters together with Al3. The other parameters can be derived by simple arithmetic operations because $\Delta^{\mathrm{Al21}}_{\mathrm{BW}} = 2\Delta^{\mathrm{O3b}}_{\mathrm{BW}}$ and $\Delta^{\mathrm{Si21}}_{\mathrm{BW}} = \Delta^{\mathrm{Si22}}_{\mathrm{BW}}$. A scheme of the determined superspace model is shown in Figure 4.18.

The displacive modulation functions of the refinement of § 4.3.1 based on first order harmonics do not adequately describe the atomic positions in the ordered SSM as Figure 4.17 clearly indicates that higher order harmonics play an important role for the description of the displacive modulation. From the t-plots the parameters $A^{\mu}_{x_i,n}$ and $B^{\mu}_{x_i,n}$ of displacive modulation functions as defined by Equation 2.2 can be determined with the method of least-squares. The maximum order of harmonics n to be used for the fit depends on the parameters to observables ratio. Symmetry restrictions decrease the number of parameters for atoms occupying special positions. For example, a modulation of x_{s3} is forbidden for all atomic domains except Al1 and O2. The atomic domains of Al1, O1 and O2 are represented by 20 coordinate points in t-space and thus fifth order or higher harmonics
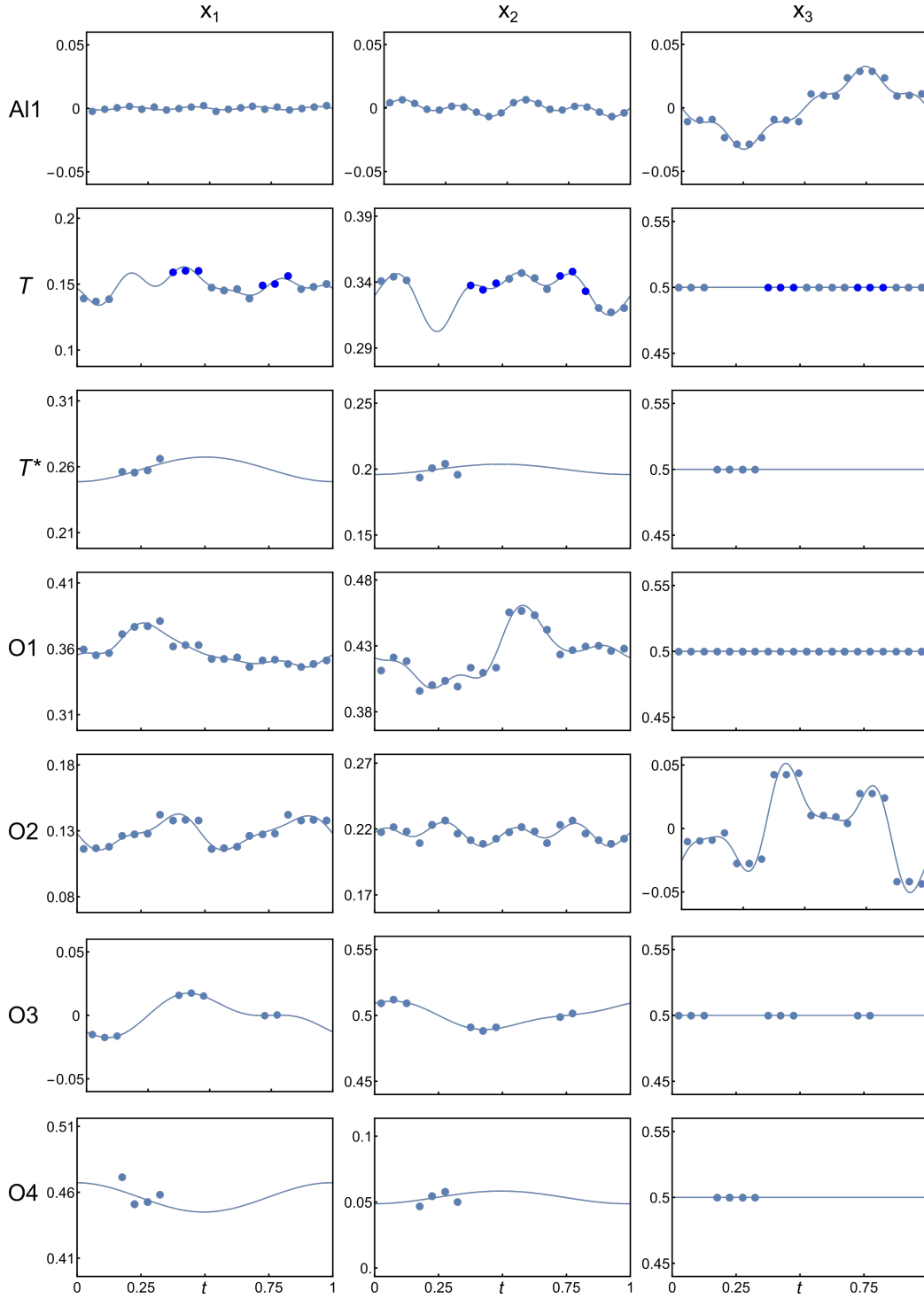
Figure 4.17: Superspace model obtained by embedding the geometrically optimised superstructure. The left, middle and right column plot the x_{s1}, x_{s2} and x_{s3} coordinate, respectively. The horizontal axis is the physical space section t. Points are coordinates of the supercell description embedded in superspace. Solid lines represent displacive modulation functions with up to fifth order harmonic terms determined by the fit procedure described in the text. For O3 first and second harmonics were used. For Al3 and O4 only first order harmonics were used. Dark blue points in the atomic domains of T (second row) indicate t sections for which Si occupies the T site. The T^* site is only occupied by Al3.

can be determined. The atomic domains of Al3 and O4, in contrast, only consist of four points in a limited range in *t*-space. Therefore, only first order harmonics can be determined. In Figure 4.17 modulation functions including up to fifth order harmonics are shown.

With the presented approach superspace models can be established from geometrically optimised superstructures of commensurate cases. ADPs are not included here, but a method was presented to use phonon calculations to estimate the displacement parameters that can be expected from the thermal motion of the atoms [176].
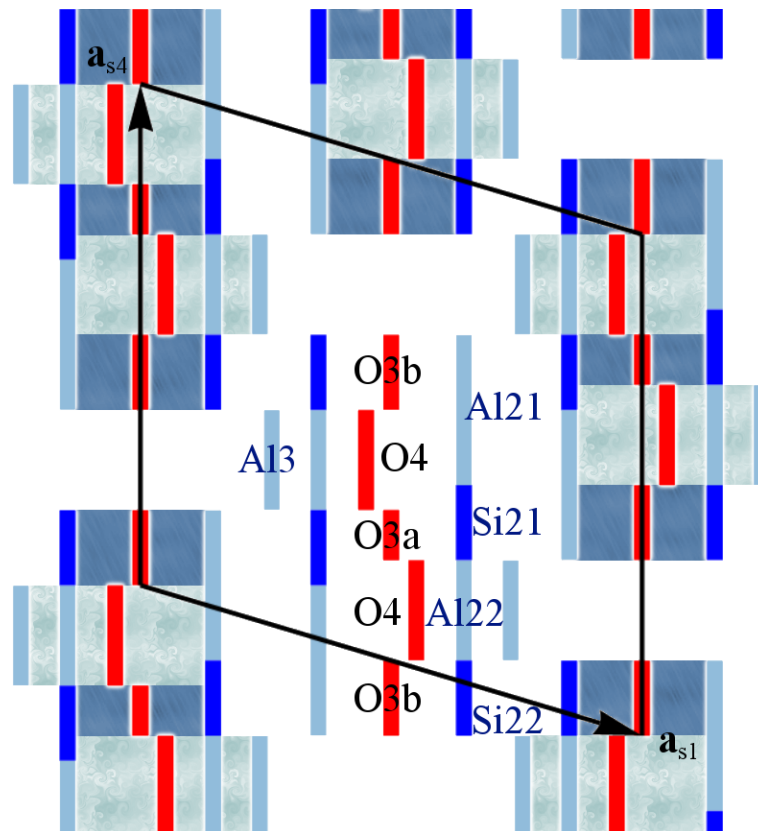
Figure 4.18: Section of superspace model showing atomic domains relevant for Al/Si ordering. Displacive modulations are not included. Al1, O1 and O2 and not shown as these atomic domains are not relevant to describe the vacancy and Al/Si ordering. Atomic domains belonging to the same dicluster or tricluster are linked by the same background colour.

Parameter	Examples				$0 \le \delta \le \frac{1}{3}$		$\frac{1}{3} \le \delta \le \frac{1}{2}$	Examples			
δ	0	$\frac{1}{7}$	0.2	0.25	$\frac{n_V}{3n_V+2}$	$\frac{1}{3}$	$\frac{n_V}{3n_V-2}$	0.4	$\frac{3}{7}$	$\frac{5}{11}$	0.5
α	0.5	$\frac{3}{7}$	0.4	0.375	$\frac{1-\delta}{2}$	$\frac{1}{3}$	$\frac{1-\delta}{2}$	0.3	$\frac{2}{7}$	$\frac{3}{11}$	0.25
n_V	0	0.5	1	2	$\frac{2\delta}{1-3\delta}$	∞	$\frac{2\delta}{3\delta-1}$	4	3	2.5	2
L_a^{VB}	0	0.75	0.5	2	$\frac{3}{2}n_V$	∞	$\frac{3}{2}n_V$	6	4.5	3.75	3
n_D	4	5.5	7	10	$3n_V+4$	∞	$3n_V-4$	8	5	3.5	2
L_a^{VFB}	2	2.75	4.5	6	$\frac{3}{2}n_V+2$	∞	$\frac{3}{2}n_V-2$	4	2.5	1.75	1
$L_a^{VB}+L_a^{VFB}$	2	3.5	5	8	$3n_V+2$	∞	$3n_V-2$	10	7	5.5	4

Table 4.11: Characteristics of example cases and the general block model of mullite. Formulas are valid for $n_V \in \mathbb{R}$. L_a^{VB} and L_a^{VFB} are the lengths of vacancy blocks and vacancy-free blocks, respectively. If $(L_a^{VB} + L_a^{VFB}) \in \mathbb{N}$ then this number expresses the length of the periodic superstructure in units of $\mathbf{a}$.

4.4 Unified SSM: Ordering mechanisms in ordered mullite

4.4.1 Block model in the range $0 < \delta \le 0.5$

From Figure 1.5 in § 1.1.8 it is clear that the modulation wave vector $\mathbf{q}$ depends on the composition. In this section it is analysed how the block pattern describing the ordered SSM can be maintained for different vacancy concentrations. In § 4.3.2 it was already indicated that the lengths of vacancy blocks (VB) and vacancy-free blocks (VFB) depends on $\mathbf{q}$ and the vacancy concentration δ. In the commensurate case of 2/1-mullite ($\delta = 0.4$) each vacancy block contains four vacancies. However, alternative block models can be easily developed. For example, in a $20 \times 1 \times 2$ supercell with 16 vacancies in total ($\delta = 0.4$) the VBs contain eight vacancies and VFBs contain 16 diclusters. In the latter example VBs overlap and tricluster chains cannot be avoided. In the ordered SSM as described in § 4.3.2 VBs and VFBs have approximately the same length minimising the overlap of VBs and avoiding the formation of tricluster chains. Based on the empirical rule that tricluster chains must be avoided a set of mullite structures with different compositions can be constructed. A shortening of the blocks increases the vacancy concentration and a lengthening decreases the vacancy concentration. For example, a $7 \times 1 \times 2$ supercell with three vacancies in the VBs has a vacancy concentration $\delta = \frac{3}{7} \approx 0.429$. A $13 \times 1 \times 2$ supercell with five vacancies in the VBs has a vacancy concentration $\delta = \frac{5}{13} \approx 0.385$.

This procedure can be generalised so that a mullite structure of any vacancy concentration in the range $\frac{1}{3} \le \delta \le 0.5$ can be described by the stacking of VBs and VFBs defined by n_V, the number of vacancies per VB. From this number several characteristics of the block model can be derived like n_D, the number of diclusters per VFB, and the block lengths L_a^{VFB} and L_a^{FB} along the a direction. If $n_V \to \infty$ the block model consists of infinite layers

of VBs and VFBs stacked along the c direction resulting in a vacancy concentration of $\frac{1}{3}$. A description of block structures with $\delta < \frac{1}{3}$ is possible by increasing the length of the VFBs relative to the VBs so that stacked VFBs overlap. This effectively introduces a 'sillimanite-like block' as in the overlapping regions two dicluster chains emerge. Tricluster chains are still avoided in the overall structure. Several examples and general formulas to describe characteristics of the block models are given in Table 4.11.

With the limitation $n_V \in \mathbb{N}$ the model cannot describe an arbitrary vacancy concentration. If that was the case, then there would be only 13 allowed compositions for mullite in the range $0.35 \leq \delta \leq 0.5$. However, block models can be constructed in which VBs with two different lengths are present and then n_V expresses the average number of vacancies per VB. A comprehensive example is mullite with $n_V = 2.5$, which can be described as mullite with half of the VBs containing two vacancies and the other half containing three vacancies. The overall vacancy concentration is $\delta = \frac{5}{11} \approx 0.455$. In this example $L_a^{VB} + L_a^{VFB} = 5.5$. In the same way the parameters n_D, L_a^{VB} and L_a^{VFB} are not limited to integer values (Tab. 4.11).

Apart from $\delta = \frac{1}{3}$ two special cases must be considered. If $\delta < 0.2$ and $n_V < 1$ then the block structure contains VFBs with $n_D = 4$ and $n_D = 7$, and VBs with $n_V = 0$ and $n_V = 1$. The presence of VBs with $n_V = 0$ means that neighbouring VFBs merge together so that the effective length of VFBs is different from the calculated length in Table 4.11. As $\delta \to 0$ the length of the overlapping region of VFBs approaches ∞, i.e. the fraction of the model that consists of dicluster chains like in sillimanite also approaches ∞. If $\delta > 0.5$ and $n_V < 2$ then the block structure contains VFBs with $n_D = -1$ and $n_D = 2$, and VBs with $n_V = 1$ and $n_V = 2$. The presence of VFBs with $n_D = -1$ is physically not possible and means that the triclusters of neighbouring VBs overlap. Therefore, the described block model is limited to the range $0 \leq \delta \leq 0.5$ and higher vacancy concentrations cannot be described by the described orthorhombic stacking of VBs and VFBs.

4.4.2 q–δ relationship derived from the block model

The constraint scheme of Table 4.4 used for the description of the occupational modulation of T, Al3, O3a, O3b and O4 does not exclude the presence of tricluster chains. It was also not considered in § 4.1.2. The implementation of a respective constraint on x_{BW}^{O4} can be implemented so that tricluster chains are strictly avoided. The atomic domains of O4$^{\mathcal{A}}$ and O4$^{\mathcal{B}}$ with $\bar{x}_{s3} = \frac{1}{2}$ are occupied if $|\frac{3}{4} - \frac{\alpha}{2} - t| < \frac{\delta}{2}$ and $|\frac{1}{4} - \frac{\alpha}{2} + t| < \frac{\delta}{2}$, respectively. The respective domains with $\bar{x}_{s3} = -\frac{1}{2}$, symmetrically related by the mirror plane $\{m_z - 1 \,|\, 0, 0, 0, \frac{1}{2}\,\}$, are occupied if $|\frac{1}{4} - \frac{\alpha}{2} - t| < \frac{\delta}{2}$ and $|\frac{3}{4} - \frac{\alpha}{2} + t| < \frac{\delta}{2}$, respectively. The condition that none of the four symmetrically related atomic domains of O4 maybe

simultaneously occupied in any physical space section t is fulfilled if

$$\Delta_{BW}^{O3b} + \Delta_{BW}^{Q} + \Delta_{BW}^{O3b} \geq \frac{1}{2}$$

$$\Delta_{BW}^{O4} + \Delta_{BW}^{O3a} + \Delta_{BW}^{O4} \leq \frac{1}{2}$$

This establishes a relationship between the modulation wave vector component α and the vacancy concentration δ.

$$2\alpha + \delta = 1 \tag{4.2}$$

If the block pattern of § 4.4.1 describes the underlying vacancy ordering mechanism for orthorhombic mullite, including not fully ordered mullite structures, then the expected modulation wave vector component is $\alpha = \frac{1}{2} - \frac{1}{2}\delta$. A fit based on the literature analysis (Fig. 1.5) in the range $0 < \delta < 0.5$ results in the relationship $\alpha = 0.550\,(17) - \delta \cdot 0.57\,(4)$. This is in agreement with Equation 4.2 within 3σ, but the standard uncertainty is relatively high and a systematic offset with respect to $\alpha = \frac{1}{2} - \frac{1}{2}\delta$ cannot be excluded. However, the vacancy concentration of the samples of this dataset was mostly determined with X-ray spectroscopic methods [2, 36, 47]. In § 3.3.1 and in § 4.2.5 it has been shown that the EDX analyses may result in a composition that does not correctly represent the vacancy concentration due to the presence of impurity phases. Structure model refinements provide a more reliable estimate of the vacancy concentration. Therefore, the $\mathbf{q}$–δ relationship was investigated with electron diffraction to assess if the predicted relationship $\alpha = \frac{1}{2} - \frac{1}{2}\delta$ represents the experimental dependence or if there is a systematic deviation which requires a different or an additional explanation.

4.4.3   q–δ relationship derived from experiments

A large set of refinements from single crystal X-ray diffraction (sXRD) experiments and precession electron diffraction tomography (PEDT) measurements was combined to establish an experimental relationship between the modulation wave vector $\mathbf{q}$ and the vacancy concentration δ. In the powder X-ray diffraction (pXRD) patterns, satellite reflections could not be detected. However, the Rietveld refinements are useful to support the electron diffraction measurements as the uncertainty of refinement parameters based on electron diffraction measurements is in general slightly higher in comparison to X-ray diffraction measurements [93]. Furthermore, pXRD provides an average model that represents a large sample volume, whereas the volume that is investigated with PEDT is smaller by many orders of magnitude. Hence, the combination allows to evaluate if the measurement is representative for the overall sample or if it is rather an exception.

Tables 4.13 and 4.14 list details on the PEDT measurements and refinements. In Table 4.12 a concise list is given of the refined vacancy concentrations from different refinements

SA	Qa.09	Qa.50	Qg.50	VSG.50	VSG.57	VSG.64
# 0.429 (5)	◇ 0.331 (7)	# 0.470 (4)	# 0.407 (3)	# 0.460 (3)	# 0.526 (6)	# 0.494 (13)
♮ 0.416 (4)	◇ 0.441 (9)	◇ 0.418 (6)	♮ 0.426 (3)	◇ 0.456 (5)	◇ 0.570 (6)	◇ 0.650 (10)
♮ 0.428 (4)		◇ 0.459 (5)	◇ 0.315 (7)			
♮ 0.434 (6)		◇ 0.490 (9)	◇ 0.403 (5)			
◇ 0.373 (6)		◇ 0.528 (7)				

Table 4.12: Overview of refined vacancy concentrations for different samples from Tables 4.6, 3.4, 4.13 and 4.14. Symbols indicate the type of measurement: # pXRD, ♮ sXRD, ◇ PEDT

Sample type	Commercial			Sol-Gel			Quenched	
Crystallite origin	SA	QSA	VSG.50	VSG.57	VSG.64	Qg.50	Qg.50
a (Å)	7.63 *	7.63 *	7.60	7.64	7.39	7.54	7.55
b (Å)	7.73 *	7.77 *	7.68	7.67	7.63	7.68	7.65
c (Å)	2.90 *	2.90 *	2.89	2.90	2.88	2.87	2.87
V (Å^3)	164.4	184.9	168.8	169.8	162.0	166.3	166.1
α	0.326 (7)	0.289 (2)	0.272 (3)	0.251 (2)	0.2470 (14)	0.345 (3)	0.318 (4)
γ	0.500 (3)	0.4997 (8)	0.4963 (10)	0.456 (3)	0.4606 (4)	0.500 (2)	0.5000 (12)
Precession angle (°)	1.0	1.0	1.0	1.0	1.0	1.0	1.0
Tilt step (°)	0.5	1.0	1.0	1.0	1.0	1.0	1.0
Recorded frames	210	111	106	88	100	93	105
Used frames	159	104	106	85	77	91	102
Measured reflections	8747	5190	5163	4066	3489	3755	3779
Unique reflections (obs.)	1732	1252	1642	1102	1031	1192	1221
Unique reflections (all)	2281	1519	1995	1951	1115	1376	1442
$\sin(\theta_{max})/\lambda\,[\text{Å}^{-1}]$	0.70	0.70	0.71	0.71	0.70	0.70	0.70
Data completeness	0.88	0.93	0.91	0.66	0.77	0.60	0.54
Refinement parameters							
Parameters	177	122	124	103	95	109	120
Constraints	7	7	7	7	7	7	7
$R_{S_g}^{max}$	0.50	0.45	0.55	0.7	0.55	0.55	0.55
$R_{obs}(F)$	0.084	0.072	0.075	0.070	0.088	0.064	0.060
$wR(F)$	0.093	0.081	0.086	0.068	0.115	0.074	0.076
refined thickness (Å)	287 (3)	268 (3)	262 (3)	242 (3)	272 (7)	549 (5)	374 (5)
refined vacancy concentration	0.373 (6)	0.456 (6)	0.456 (5)	0.570 (6)	0.650 (10)	0.315 (7)	0.403 (5)

Table 4.13: Electron diffraction measurements. Used frames refer to the number of frames used in the final refinement of the average structure. Lattice parameters marked with a * were corrected after the measurement due to wrong calibration parameters during the measurement.

Crystallite origin	Qa.09	Qa.09	Qa.50	Qa.50	Qa.50	Qa.50	Qa.57
a (Å)	7.63 *	7.61	7.61	7.63 *	7.60	7.54	7.55
b (Å)	7.78 *	7.80	7.69	7.73 *	7.66	7.57	7.65
c (Å)	2.90 *	2.89	2.89	2.90 *	2.87	2.87	2.87
V (Å^3)	187.2	171.7	169.3	162.6	167.2	163.9	166.1
α	0.2902 (12)	0.341 (5)	0.286 (1)	0.3038 (15)	0.2677 (12)	0.2668 (7)	0.2701 (11)
γ	0.5009 (5)	0.5007 (15)	0.4992 (6)	0.4986 (6)	0.4593 (5)	0.4606 (3)	0.4553 (4)
Precession angle (°)	1.0	1.0	1.0	0.6	1.0	0.6	1.0
Tilt step (°)	1.0	1.0	1.0	1.0	1.0	1.0	1.0
Recorded frames	90	117	94	99	88	107	112
Used frames	80	103	93	99	80	103	111
Measured reflections	4157	5077	4224	4039	4191	4962	4561
Unique reflections (obs.)	1044	1276	1298	1157	951	1223	1343
Unique reflections (all)	1268	1356	1319	1180	1091	1245	2146
$\sin(\theta_{max})/\lambda\,[\text{Å}^{-1}]$	0.70	0.70	0.70	0.70	0.70	0.70	0.70
Data completeness	0.79	0.99	0.79	0.74	0.86	0.91	0.76
Refinement parameters							
Parameters	98	119	111	116	96	121	130
Constraints	7	7	7	7	7	7	6
$R_{S_g}^{max}$	0.50	0.45	0.45	0.70	0.45	0.60	0.70
$R_{obs}(F)$	0.096	0.089	0.089	0.075	0.092	0.089	0.061
$wR(F)$	0.102	0.111	0.113	0.097	0.110	0.113	0.070
refined thickness (Å)	623 (7)	603 (5)	631 (7)	619 (7)	400 (6)	879 (5)	406 (3)
refined vacancy concentration	0.441 (9)	0.331 (7)	0.459 (5)	0.418 (6)	0.528 (7)	0.490 (9)	0.511 (7)

Table 4.14: Electron diffraction measurements of Qa samples. Used frames refer to the number of frames used in the final refinement. Lattice parameters marked with a * were corrected after the measurement due to wrong calibration parameters during the measurement.

sorted by sample and measurement type. In all the listed cases with a nominal composition corresponding to $\delta > 0.4$ the refined vacancy concentration determined with pXRD is lower than expected from the synthesis. In the case of the VSG samples this can be explained with the formation of $\gamma\text{-}Al_2O_3$, but it must also be considered that the presence of $\gamma\text{-}Al_2O_3$ could not be adequately modelled (cf. Fig. 3.3) and thus the refinement might contain systematic errors making the refinement of the composition of the VSG samples less reliable. Apart from that, within the same synthesis batch a broad range of compositions is observed which cannot be explained by the standard uncertainty. With respect to the phase diagram (Fig. 1.1.7) the composition range of the samples must be considered metastable, i.e. during the synthesis different compositions may form and the formation of a homogeneous, single-phase mullite sample is not likely. Fischer *et al.* (1994) reported that in very aluminous mullite samples synthesised with the sol-gel method a broad composition range was observed for different crystallites of the same synthesis batch [53]. Ylä-Jääski & Nissen (1983) also observed the presence of different vacancy concentrations between $\delta \approx 0.48$ and $\delta \approx 0.54$ in the same mullite sample with a nominal composition of $\delta = 0.58$ [36]. All in all the refined vacancy concentrations are considered to be a reliable estimate for the chemical composition of the sample for which the modulation wave vectors **q** were determined (Tab. 4.13 and 4.14), although a higher standard uncertainty could be anticipated.

In Figure 4.19 α and γ are plotted against the vacancy concentration δ. Two composition ranges with different symmetry and different **q**–δ relationship can be clearly identified. The plot suggests that the turnover vacancy concentration is around 0.5. Mullite with $\delta <$ 0.5 ('orthorhombic mullite') has a modulation wave vector $\mathbf{q} = (\alpha\, 0\, \frac{1}{2})$. For higher vacancy concentrations a reduction of the symmetry is observed because γ is approximately 0.46 and seems to be constant independent of the vacancy concentration ('monoclinic mullite'). A linear least squares fit (Fig. 4.19) considering all model refinements of orthorhombic mullite including the results from this section, Table 4.6 and [6] leads to the relationship $\alpha = 0.494\,(16) - \delta \cdot 0.46\,(4)$. This is in good agreement (1σ) with the prediction $\alpha = \frac{1-\delta}{2}$. The experimental **q**–δ relationship also deviates clearly, but within the 3σ limit, from the initial analysis based only on the literature $\alpha = 0.550\,(17) - \delta \cdot 0.57\,(4)$. However, there are two aspects that require a deeper examination: Most PEDT and XRD data points in Figure 4.19 are located slightly above the prediction and thus a systematic offset cannot be excluded. Furthermore, for $\delta < 0.55$ the minimum α is clearly not 0.25 in contrast to the prediction by Equation 4.2. The experimental results thus suggest that the validity of the established relationship only holds up to $\delta \approx 0.45$ and not up to $\delta = 0.5$. On the other hand, the block model predicts that a new ordering pattern is required for $\delta > 0.5$ in perfect agreement with the observation that mullite exhibits a different symmetry for $\delta > 0.5$. Another interesting observation is that Equation 4.2 was derived from the symmetry of a completely ordered model, but the experiments were exclusively based
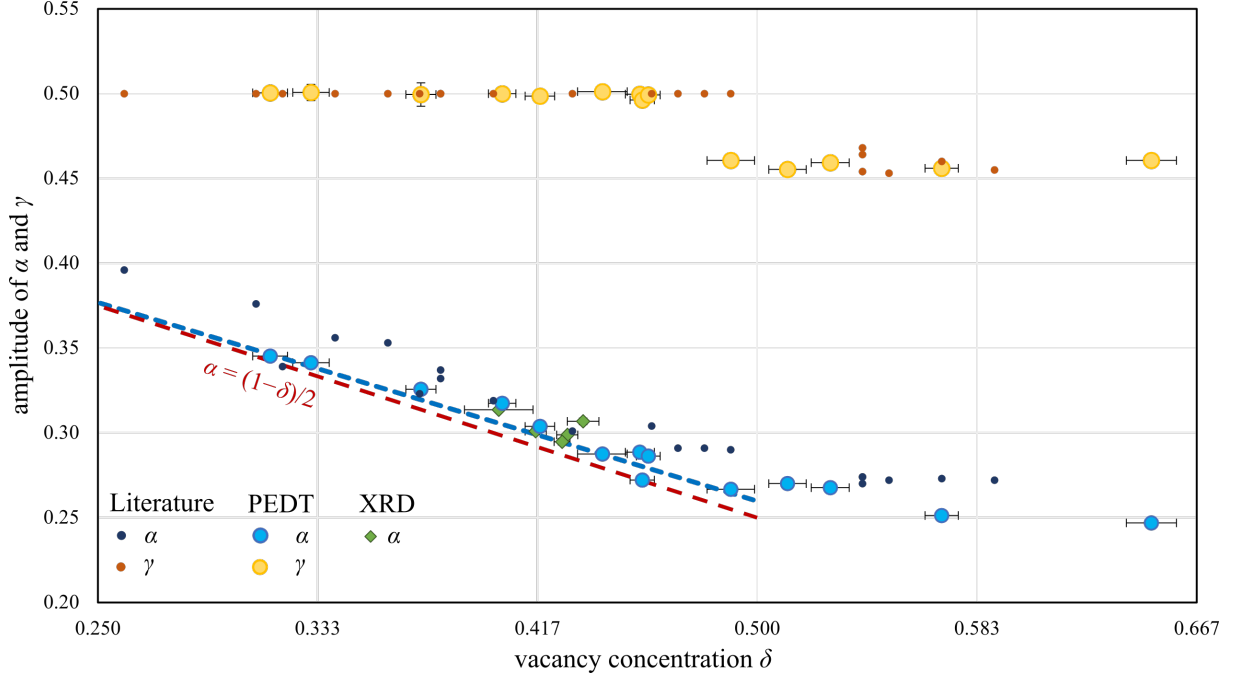
Figure 4.19: Experimental relationship between $\mathbf{q}$ and the vacancy concentration δ (cf. Fig. 4 in [2] and Fig. 9 in [36]). α (cold colours) and γ (warm colours) of the literature (small dots without error bars, § A.1), PEDT measurements (circles with error bars) and sXRD (green diamonds, § 4.2.1, [6]) are shown. The blue dashed line is the interpolated least-squares fit using results of samples with refined compositions and $\mathbf{q} = (\alpha\, 0\, \frac{1}{2})$. The red dashed line represents the relationship $\alpha = \frac{1-\delta}{2}$ derived from the block model.

on disordered samples without high order satellite reflections. The degree of order might influence the $\mathbf{q}$–δ relationship and the range for which Equation 4.2 is valid. Nevertheless, the overall agreement is a strong indicator that the block model describes the fundamental vacancy ordering pattern of orthorhombic mullite. For the upcoming sections, in which fully ordered commensurate cases of the unified SSM are statically relaxed, it will be assumed that Equation 4.2 describes the $\mathbf{q}$–δ relationship in the range $0 \leq \delta \leq 0.5$. A detailed analysis of monoclinic mullite is outside the scope of this chapter, but it will be revisited in § 5.3.2 and § 6.3.3.

4.4.4 Determination of the ideal Al/Si ordering with computational methods

The examples in Table 4.11 can be described as superstructures of mullite corresponding to commensurate cases with $\alpha \in \mathbb{Q}$. In these superstructures the vacancy distribution and thus the distribution of oxygen atoms is exactly defined, but the distribution of Si atoms is not known. In analogy to the computational approach of § 4.3.3 the ideal distributions of Si atoms for different compositions in the range $0 \leq \delta \leq 0.5$ were determined by a combination of FF calculations and DFT calculations. An overview on the input super-

Label	R_{AS}	δ	α	Supercell size	Space group	$\langle n_V \rangle$	N_{atoms}	Al/Si permutations	FF cells	DFT cells
M0	1/1	0	1/2	$2 \times 1 \times 2$	$Bb2_1m$	0	64	3	3	3
M11	19/16	1/9	4/9	$9 \times 1 \times 2$	$Pnnm$	$\frac{1}{3}$	286	43758	0	2
M14	5/4	1/7	3/7	$7 \times 1 \times 2$	$Pbam$	$\frac{1}{2}$	222	3003	0	2
M20	11/8	1/5	2/5	$5 \times 1 \times 2$	$Pnnm$	1	158	210	0	2
M25	3/2	1/4	3/8	$8 \times 1 \times 2$	$Bb2_1m$	2	252	8008	8008	15
M27	25/16	3/11	4/11	$11 \times 1 \times 2$	$Pnnm$	3	346	319770	0	2
M33	7/4	1/3	1/3	$3 \times 1 \times 2$	$Pbam$	∞	94	15	15	15
M37	15/8	7/19	6/19	$19 \times 1 \times 2$	$Pnnm$	7	594	2.7×10^9	0	1
M40	2/1	2/5	3/10	$10 \times 1 \times 2$	$Bb2_1m$	4	312	38760	38760	21
M43	17/8	3/7	2/7	$7 \times 1 \times 2$	$Pnnm$	3	218	1001	0	2
M45	9/4	5/11	3/11	$11 \times 1 \times 2$	$Pbam$	$\frac{5}{2}$	342	74613	0	1
M50	5/2	1/2	1/4	$4 \times 1 \times 2$	$Bb2_1m$	2	124	28	28	28

Table 4.15: Superstructures for computational study on the solid solution range of mullite. N_{atoms} is the total number of atoms in the supercell. The number of Al/Si permutations is calculated considering only space group compliant Al/Si distributions. Si on the *T** site is not forbidden. FF supercells and DFT supercells refer to the number of structures with different Al/Si permutations for which FF and DFT calculations were carried out, respectively.

structures is given in Table 4.15. Each composition is labelled as capital letter M followed by the first two decimal places of the rounded vacancy concentration, e.g. the vacancy distribution of the ordered SSM investigated in § 4.3.3 is M40. Initial structure models were generated based on the coordinates of the ordered SSM (§ 4.3.1) and a systematic adaptation of the Si distribution, which automatically also defines the distribution of Al atoms. It was tested that small variations of the initial coordinates have no influence on the optimised structure and the result is independent of an initial displacive modulation. The total energy of all symmetry compliant Al/Si ordering patterns of M0, M33 and M50 were determined with FF and DFT calculations (PBE). For M25 all Al/Si permutations were investigated with FF calculations and, in analogy to § 4.3.3, the most promising candidates were further investigated with DFT calculations (PBE). Each Al/Si permutation is assigned an FFID corresponding to its stability according to the FF calculations and a rank corresponding to its stability according to the DFT calculations (Fig. 4.20).

The FFID ranking of M33 deviates by about 1 position relative to the DFT ranking. However, the first and last FFID correctly represent the most and least stable supercell, respectively. In the case of M50 the uncertainty of the ranking is about 2 positions and neither the first nor the last rank are correctly identified. The geometric optimisation of the least stable structures with DFT in many cases results in a strong deformation and larger deviation from the bond lengths expected from X-ray diffraction studies. In
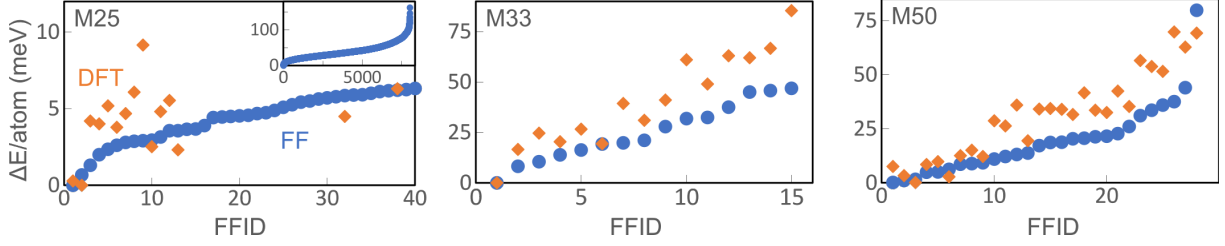
Figure 4.20: Total energies E/atom (meV) of FF calculations (blue circled) and DFT calculations (orange diamonds) relative to the most stable superstructure of M25, M33 and M50.

contrast, the coordinates of the most stable structures are only slightly displaced from the expected coordinates. These results are taken as indication that a qualitative assessment of the relative stability of a certain supercell is possible with the FF calculations, but for the determination of the ideal Al/Si ordering more accurate DFT calculations must be carried out. This also supports the results of § 4.3.3 because it could not be excluded that a more stable Al/Si ordering was 'hidden' behind the lack of accuracy of the FF calculations, but apparently the FF rankings are reliable enough as estimated in § 4.3.3.

The qualitative analysis of the most stable and the least stable Al/Si permutations allows to evaluate the stability of certain structural units. M0 #3, the least stable supercell, contains Al_2O_7 units (O3 bonded to two Al atoms), which is an unstable configuration according to Pauling's bond valence rules (§ 1.2). M0 #2 contains chains of Si-Si diclusters (Si_2O_7) which is avoided according to Pauling's bond valence rules and nature of contiguous polyhedra because O2 atoms are shared by two Si atoms and one Al atom. These bonding situations are also avoided in the other superstructures of all compositions and the structures containing equally overbonded O2 atoms or underbonded O3 atoms are relatively unstable. In M25, M33 and M40 there are dicluster-vacancy columns, which in the most stable structures are consistently of the Si-Si type. M40 #1 and M50 #1 contain Si in the triclusters indicating that Si in triclusters is favoured over Si-Si diclusters in dicluster-tricluster chains (Fig. 4.21). Si occupies the T^* site in the structures of M25 #8 (FFID 32), M33 #3 (FFID 6), M40 #2 (FFID 10, Fig. 4.16) and M50 #2 (FFID 6). Hence, the presence of Si3 atoms is energetically stable and the energetic cost of such a configuration is very low with respect to the most stable configuration. Structural studies should not generally exclude the presence of Si on the T^* site.

4.4.5 Al/Si ordering of unified SSM

A comparison of M0 #1, M25 #2, M33 #1, M40 #1 and M50 #1 indicates that the global Al/Si ordering pattern follows the same rules (Fig. 4.21):

1. Diclusters stacked between vacancies are always of the type Si-Si.

Site label	O3a	O3b	O4	T	T^*	Al21	Al22	Si21	Si22
Δ^μ_{BW}	$\frac{1}{2}-\delta$	$\frac{1}{4}(1-\delta)$	$\frac{\delta}{2}$	$1-\frac{\delta}{2}$	$\frac{\delta}{2}$	$\frac{1}{2}(1-\delta)$	$\frac{\delta}{2}$	$\frac{1}{4}(1-\delta)$	$\frac{1}{4}(1-\delta)$
x^μ_{BW}	0	$\frac{1}{4}(1+\alpha)$	$\frac{1}{2}+\alpha\bar{x}^{O4}_{s1}$	$\alpha\bar{x}^T_{s1}$	$\frac{1}{2}+\alpha\bar{x}^{Al3}_{s1}$	$\frac{1}{4}+\alpha\bar{x}^T_{s1}$	$\alpha(\bar{x}^T_{s1}-\frac{1}{2})$	$\frac{\delta}{4}+\alpha(\bar{x}^T_{s1}-\frac{1}{4})$	$-\frac{1}{4}+\alpha(\bar{x}^T_{s1}-\frac{1}{4})$
t^μ_{BW}	$-\frac{1}{4}$	$\frac{1}{8}(1-\delta)$	$\frac{1}{4}$	$-\frac{1}{4}$	$\frac{1}{4}$	0	$\frac{1}{4}(2-\delta)$	$\frac{3}{8}(\delta-1)$	$\frac{1}{8}(\delta-5)$

Table 4.16: Constraints on block wave functions including Al/Si ordering. t^μ_{BW} is the centre of the block wave function in t space. The relationship $\alpha = \frac{1-\delta}{2}$ is presumed.

2. In dicluster-tricluster chains triclusters contain no Si atoms and diclusters one Si atom. The orientation of the Al-Si diclusters is uniquely defined by the tricluster orientation.

3. If $\delta > \frac{1}{3}$ then triclusters in tricluster-vacancy chains host one Si atom on the T site that forms the border to the neighbouring VFB.

4. If $\delta < \frac{1}{3}$ then dicluster-dicluster chains are made of Al-Si diclusters with alternating orientations so that each Si is linked to three Al tetrahedra and each Al is linked to three Si tetrahedra.

The list of rules to describe the Al/Si ordering could be further expanded, but a full parametrisation is rather inconvenient. Embedding the structures in superspace as described in § 4.3.4 allows an easier comparison by means of the block wave parameters describing the occupational modulation of Al2 and Si2. The analysis of the embedded structures suggests that the displacive modulation and the occupational modulation can be described by one set of composition-dependent modulation functions (Fig. 4.22). Here, the focus is on the occupational modulation, for which the constraints for a unified description are given in Table 4.16. The resulting superspace model is similar to that of M40 #1 depicted in Figure 4.18.

The unification of the Al/Si ordering is possible for $0 \leq \delta \leq 0.5$ assuming that M25 #2 represents the ideal Al/Si ordering and not M25 #1. This is justified by the following observations: (1) The total energy difference between M25 #1 and M25 #2 is 0.085 eV or 0.68 meV/atom. It is difficult to estimate the accuracy of these calculations, but the scale can be appreciated by comparing similar calculations. The total energy difference of (PBE) between sillimanite and andalusite is 7.00 meV/atom, it is 16.54 meV/atom between M33 #1 and M33 #2, 1.24 meV/atom between M40 #1 and M40 #2 and 2.69 meV/atom between M50 #1 and M50 #2. Hence, 0.68 meV/atom is a very small amount of energy which might be in the range of the uncertainty. (2) The essential difference between M25 #1 and M25 #2 is the orientation of Al-Si diclusters in dicluster chains (Fig. 4.21). Hence, both Al/Si ordering patterns are almost the same and the ambiguity only concerns the block borders at which the vacancy-free blocks overlap. (3) The embedding of M25 #1 in superspace reveals a more complex Al/Si ordering scheme as six instead of four block wave functions are needed to describe the occupancy of Al2 and Si2. If
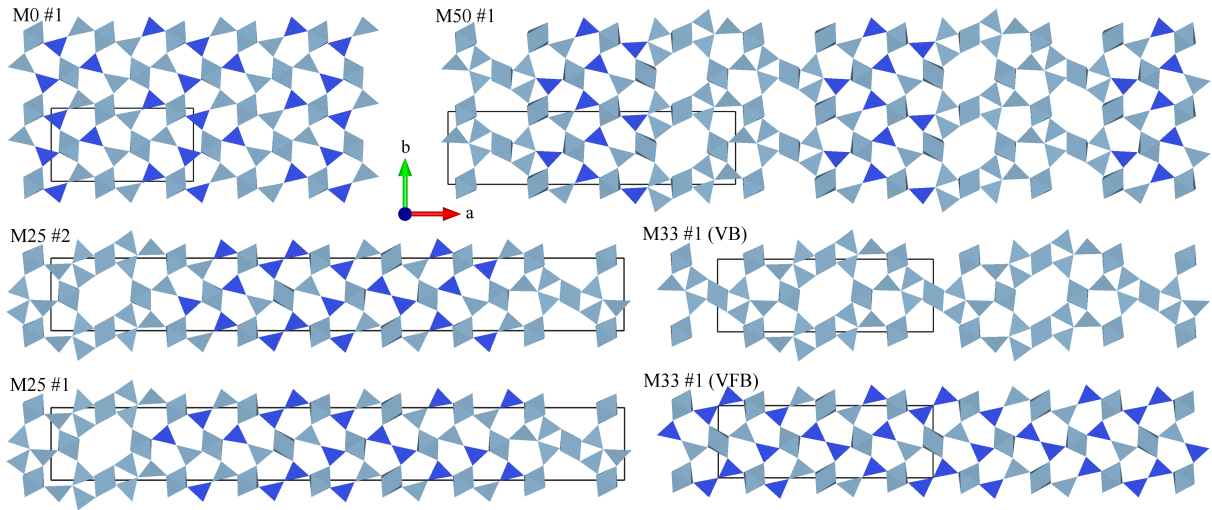
Figure 4.21: Relaxed superstructures (PBE) of M0, M25, M33, and M50. The two most stable Al/Si ordering patterns of M25 are shown, which only differ in the orientation of two Al-Si diclusters at the border of the VFBs. Two subsequent layers of M33 are shown representing the infinitely repeating unit of the VB and VFB, respectively.
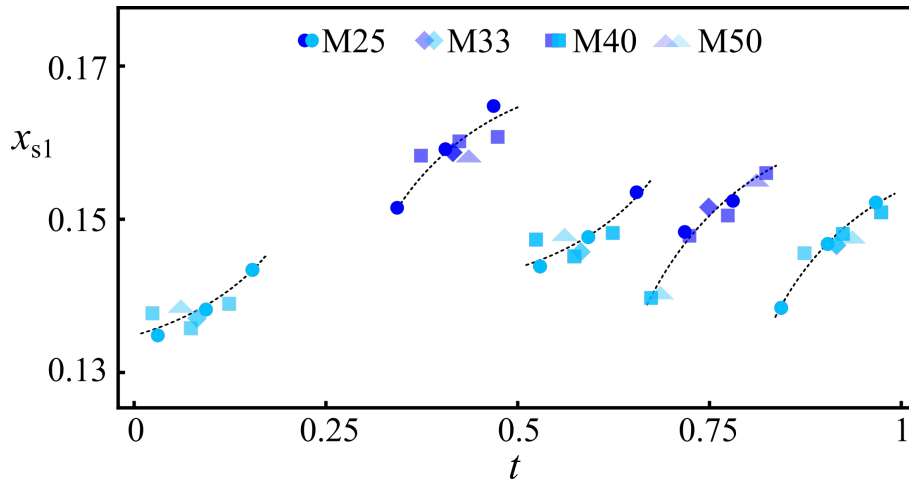

Figure 4.22: Coordinate x_{s1} of tetrahedral Al2 (light blue) and Si2 (dark blue) atoms of M25 #2 (circles), M33 #1 (diamonds), M40 #1 (squares) and M50 #1 (triangles) embedded in superspace. The displacive and occupational modulation functions follow the same trend allowing a description of the solid solution range by a unified superspace model. Dashed lines indicate trend lines fitted by hand.
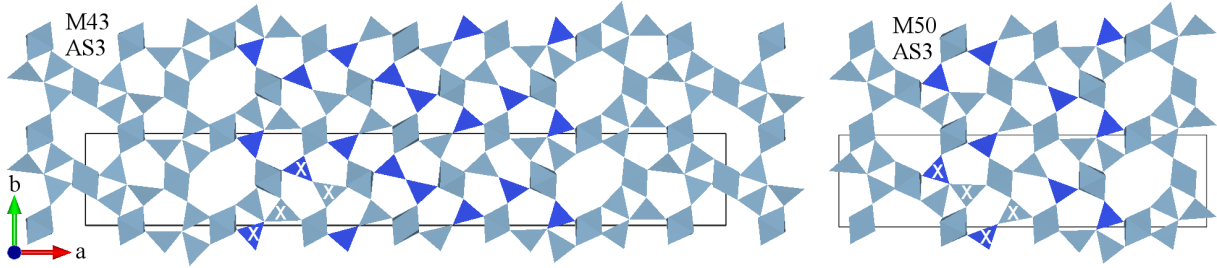
Figure 4.23: Alternative Al/Si ordering patterns of M43 AS3 and M50 AS3. In each model the two Al-Si pairs that are exchanged with respect to AS1 are marked by white crosses. Symmetrically related pairs are not marked. Geometries correspond to the relaxed structures resulting from the DFT calculations (PBEsol-D)

Pauling's rule of parsimony can be applied to superspace, then a description with less parameters would be favoured. (4) Furthermore, the Al/Si ordering scheme can only be extended to the range $0 \leq \delta \leq \frac{1}{3}$ because the two extra domains needed to describe the Al/Si ordering in diclusters disappear if $\frac{1}{3} < \delta$. At $\delta = 0$ and $\delta = \frac{1}{3}$ the ordering schemes derived from M25 #1 and M25 #2 are identical. In the appendix a superspace model of the Al/Si ordering pattern of M25 #1 is shown (§ A.7).

4.4.6 Sophisticated calculations of commensurate cases of the unified SSM

So far, the calculations were based on M0, M25, M33, M40 and M50 using the PBE functional without dispersion correction. The last section presented strong evidence that a unified description of the ordered mullite structure in the composition range $0 \leq \delta \leq 0.5$ is possible in superspace by implementing the constraints of Table 4.16 and Equation 4.2. In § 3.6 it was pointed out that dispersion corrected DFT calculations achieve a better agreement with experimental lattice parameters and bond lengths. Therefore, more accurate dispersion corrected DFT calculations based on the PBEsol functional (PBEsol-D) were performed on eleven superstructures of mullite with the ideal Al/Si ordering pattern derived in the last section (label AS1). For selected superstructures with $0 < \delta < \frac{1}{3}$ also the Al/Si ordering pattern of M25 #1 was investigated (label AS2). For M43 and M50 a second Al/Si ordering scheme was tested (Fig. 4.23). With respect to the force field calculations this scheme corresponds to M40 FFID 86 and M50 FFID 12 (M50 # 11). This Al/Si ordering pattern will be labelled AS3 and is related to M25 #1 because the only difference is that if $\frac{1}{3} < \delta$ the outermost Si atoms, with respect to the middle of the vacancy-free block, occupy tricluster T sites instead of dicluster T sites as in M25 #1. To avoid confusion with the labels of the FF calculations, the labels of other DFT calculations and the different Al/Si ordering patterns, an overview of the labels is given in 4.17 including the total energies of the calculations based on PBEsol-D.

	Ideal Al/Si ordering (§ 4.4.5)				Alternative Al/Si ordering			
	FFID	PBE	PBEsol-D	E/atom (meV)	FFID	PBE	PBEsol-D	ΔE/atom (meV)
M0	1	#1	AS1	-8084.88	–	–	–	–
M11	–	–	AS1	-8066.59	–	–	AS2	0.05
M14	–	–	AS1	-8061.29	–	–	AS2	0.04
M20	–	–	AS1	-8051.74	–	–	AS2	-0.44
M25	1	#2	AS1	-8043.15	2	#1	AS2	-0.09
M33	1	#1	AS1	-8028.80	–	–	–	–
M40	3	#1	AS1	-8015.72	86		–	–
M43	–	–	AS1	-8010.16	–	–	AS3	15.17
M45	–	–	AS1	-8005.17	–	–	–	–
M50	3	#1	AS1	-7996.55	12	#11	AS3	28.73

Table 4.17: List of labels of relevant calculations. E/atom refers to the total energy of AS1 resulting from the calculations with the PBEsol-D functional. ΔE/atom (meV) of the alternative Al/Si ordering (AS2 if $\delta < \frac{1}{3}$, AS3 otherwise) is expressed relative to AS1 of the ideal mullite structure with the same vacancy concentration.

The calculations of M20 and M25 confirm that AS2 is energetically more stable than AS1, but interestingly for M11 and M14 AS1 is more stable than AS2. A property of block models with $\delta < 0.2$ is that $\langle n_{\mathrm{V}} \rangle < 1$ and thus neighbouring VFBs are not separated leading to extended blocks with more than two neighbouring dicluster chains (Tab. 4.11). According to the calculations the unified superspace model as described in the last section (Tab. 4.16) thus is confirmed without ambiguity in the range $0 \leq \delta < 0.2$ and $\frac{1}{3} \leq \delta \leq 0.5$. In the range $0.2 \leq \delta < \frac{1}{3}$ the distribution of most Si atoms is defined with certainty except for the orientation of Al-Si diclusters in dicluster chains.

Lattice parameters of all geometrically optimised supercells are plotted in Figure 4.24 for comparison with lattice parameters determined from X-ray diffraction measurements (see figure caption). Experimental lattice parameters were measured at ambient conditions, whereas the calculations correspond to a temperature of 0 K and a pressure of 0 Pa. No measurements of thermal expansion coefficients or lattice parameters close to these conditions are available, but the extrapolation of measurements at elevated temperatures [177] allows to estimate that a temperature correction would decrease the experimental a and c by less than 0.01 Å and b by less than 0.02 Å. This has no relevant influence on the present analysis. The dependence of the lattice parameters of AS1 on the composition is different for the ranges $\delta < \frac{1}{3}$ and $\frac{1}{3} < \delta$, respectively. For lower vacancy concentrations the parameter a increases linearly with δ resembling experimental observations remarkably well. In the same region b decreases slightly, but neither the slope nor the absolute values agree with experimental observations. In the range $\frac{1}{3} < \delta$ the parameter a slightly decreases and deviates from the experimental observations, for which the linear behaviour is not separated into two regions. b increases but still shows a clear offset from the
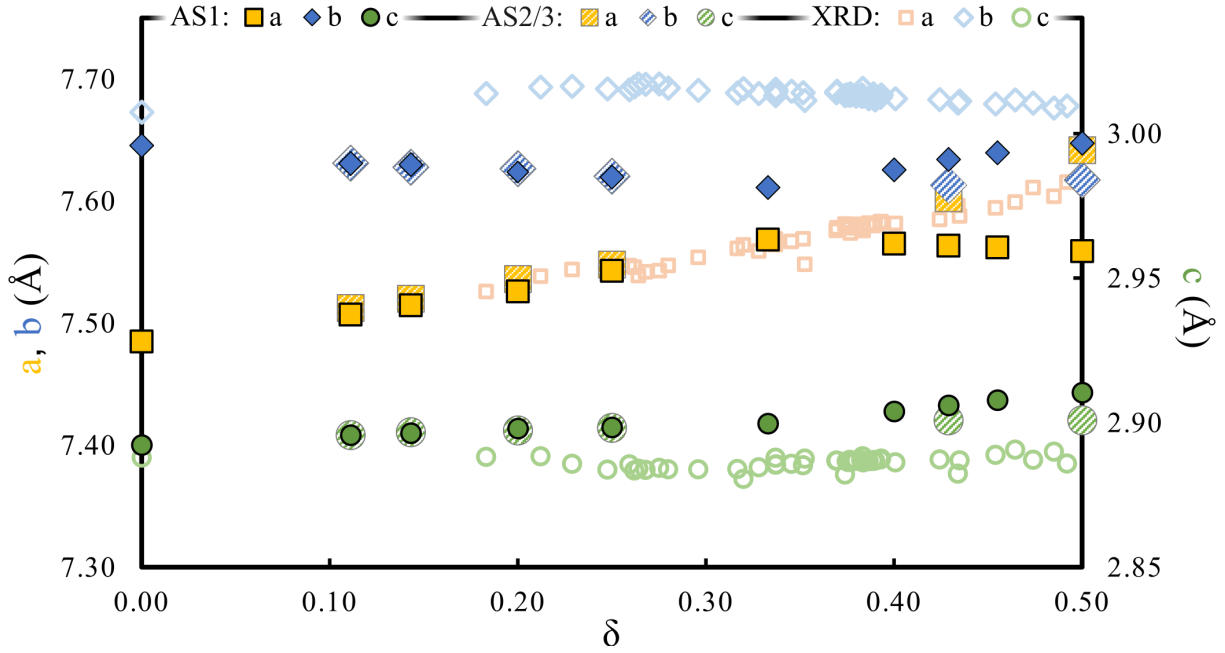
Figure 4.24: Lattice parameters of geometrically optimised supercells for Al/Si ordering patterns AS1, AS2 ($\delta < \frac{1}{3}$) and AS3 ($\frac{1}{3} < \delta$). The parameters a and c were divided by an integer to account for the supercell size. Experimental values of a, b and c of mullite based on X-ray diffraction measurements are taken from [178, 46, 179]. Sillimanite lattice parameters are also included with data from [173] for comparison with lattice parameters of M0. Several experimental values of parameter a are 'hidden' behind the data points of the DFT calculations.

reference values. The lattice parameters of AS1 and AS2 ($\delta < \frac{1}{3}$) are almost identical and seem to be not affected by the different orientations of the Al-Si dicluster chains. The lattice parameter c varies very little over the whole composition range independent of the Al/Si ordering pattern. Despite the good overlap of a for $\delta < \frac{1}{3}$, the overall picture indicates that the model does not account for all relevant structural aspects. This is not surprising because the calculations are based on fully ordered models with strict lattice periodicity along the b direction whereas the real structures are disordered. Investigations of the diffuse scattering revealed that important inter-vacancy vectors are, among others, $[\frac{3}{2}, \frac{1}{2}, 0]$ and $[\frac{1}{2}, \frac{3}{2}, 0]$ [4]. The first also plays a crucial role in all supercells with $n_V > 1$, but $[\frac{1}{2}, \frac{3}{2}, 0]$ breaks the lattice periodicity along b. The lattice parameters of AS3 show that small changes of the Si distribution result in a significant change of the lattice parameters. The discrepancy of the determined values of a and b thus are likely to originate from deviations of the Al/Si ordering pattern implemented in the unified SSM.

The lattice parameters a and c of M0 AS1 are almost identical to a and c of sillimanite, only b deviates a little bit. This is not surprising, because structurally they only differ in the orientation of Al-Si diclusters. Nevertheless, it must be emphasised that M0 AS1 is not sillimanite.

Chapter 5

Discussion

In Chapter 4 different superspace models of mullite in the vacancy concentration range $0 \leq \delta \leq 0.5$ were presented. Based on the symmetry analysis, crystal chemical considerations and experimental observations an ordered unified superspace model was developed. In this chapter the results are put into a broader context considering especially the different degrees of order, antecedent structure models and the experimentally observed phase diagram.
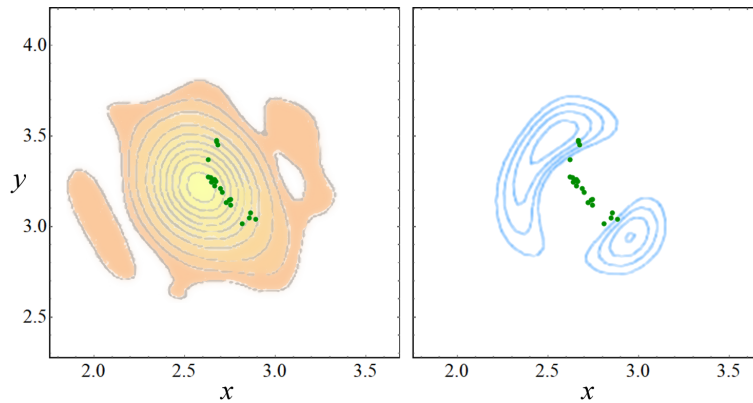
Figure 5.1: Electron density maps around the O1 site adapted from Figure 3 of [62] plotted together with the transformed O1 coordinates from M40 AS1 (green points). Left: Electron density from a refinement using third and fourth order tensors to describe the displacement of O1. Right: Difference density map relative to a refinement based on ADPs. x and y are absolute coordinates in Å as in the published Figure 3.

5.1 Comparison with antecedent models

5.1.1 Displacement parameters of O1 in the average structure

A high resolution single crystal X-ray diffraction study of a disordered 2/1-mullite sample[1] analysed the anharmonic displacement parameters of O1 and O2 determined from an average structure model refinement [62], which was also mentioned in the introduction (§ 1.3.2). In Figure 5.1 high resolution electron density maps are compared with the O1 coordinates of M40 AS1. The displacement distribution can be approximated considering the static displacement of O1 atoms relative to the average coordinates. For O2 atoms a smaller displacement was reported in agreement with the developed superspace models, in which the amplitude of the displacive modulation of O1 is larger than that of O2. This comparison indicates that the displacement of atoms in disordered mullite is related to the displacement of atoms described by the modulation functions of the ordered SSM.

5.1.2 Component structures from group theoretical analysis of $Pbam(\alpha 0\frac{1}{2})0ss$

McConnell & Heine suggested in 1981 an alternative to the superspace approach to explain the origin of modulations and describe modulated structures [65] based on group theory and Landau theory of phase transitions [64]. According to their theory the incommensurate phase can be described by "two independent modulation component structures [...] C1 and C2 oscillating 90° out of phase with one another" and that the symmetry

---

[1]The measured single crystal originates from sample with label '5' in the study by Cameron (1977)[2]. Angel *et al.* used the same sample for their subsequent studies of the modulation (§ 5.1.2) and it was also used by Welberry *et al.* to study the diffuse scattering [67, 180].

R-irep label [181]	BCS	Displacement component	Affected sites	E	2_z	2_y	2_x	i	m_z	m_y	m_x
X_7	Z_2^+	$A_{x,1}^\mu$ $(z=\frac{1}{2})$	T, T^*, O1, O3, O4	1	1	-1	-1	1	1	-1	-1
X_8	Z_4^-	$B_{x,1}^\mu$ $(z=\frac{1}{2})$	T, T^*, O1, O4	1	-1	1	-1	-1	1	-1	1
X_1	Z_1^+	$A_{y,1}^\mu$ $(z=\frac{1}{2})$	T, T^*, O1, O3, O4	1	1	1	1	1	1	1	1
X_2	Z_3^-	$B_{y,1}^\mu$ $(z=\frac{1}{2})$	T, T^*, O1, O4	1	-1	-1	1	-1	1	1	-1
X_7	Z_2^+	$A_{z,1}^\mu$ $(z=0)$	Al1, O2	1	1	-1	-1	1	1	-1	-1
X_8	Z_4^-	$B_{z,1}^\mu$ $(z=0)$	O2	1	-1	1	-1	-1	1	-1	1

Table 5.1: Character table showing how the displacement amplitudes of first order harmonics transform under the operations of the superspace group $Pbam(\alpha 0\frac{1}{2})0ss$. Full symmetry operators are given in Table 4.2. The R-ireps were determined with the tool 'SUBGROUPS' of the Bilbao Crystallographic Server (BCS) [182]. Labels of R-ireps are given as found in the work by McConnell & Heine (1984) [181] and as provided by the BCS.

of C1 and C2 must be subgroups of the space group of the average structure [181]. The application of this approach to the modulated structure of 2/1-mullite assumed that C1 and C2 represent the competing contribution of vacancy ordering on the one hand and Al/Si ordering on the other. C1 was expected to resemble the vacancy distribution of the hypothetical ι-Al_2O_3 structure [183] and C2 the Al/Si ordering of sillimanite. C1 and C2 are $1 \times 1 \times 2$ supercells, that are also called difference structures as they contain the information in which way the respective component differs from an average double cell. A symmetry analysis assigned the space group $Pnnm$ to C1 and $Pbnm$ to C2.

Angel & Prewitt (1987) characterised experimentally the component structures. Difference Patterson maps based on single crystal X-ray diffraction measurements and single crystal neutron diffraction experiments [66, 7] with crystals originating from the same sample batch were analysed to determine the atomic displacement directions of O1 and O2 relative to the average structure in analogy to a displacive modulation. Likewise, a decrease or increase of the occupancies was determined for the different sites in the component structures. However, the amplitudes were not refined, and the structural model was developed based on the assumption that the structure is maximally ordered. The symmetry of the component C2 does not allow vacancy ordering and it was assumed that the vacancies of this component are randomly distributed over the incommensurate structure. In C1 the vacancy concentration varies within the half cells as a sinusoidal function between 0 and 0.8 with a relative phase shift of π between vacancies with $z = 0$ and $z = \frac{1}{2}$. As a consequence, the bottom cell ($z = 0$) has a maximum vacancy concentration if the top cell ($z = \frac{1}{2}$) has a minimum vacancy concentration and *vice versa*. This is essentially in agreement with the picture of stacked vacancy blocks and vacancy-free blocks, but instead with a harmonic modulation of the vacancy concentration like in the disordered SSM. From the analysis of the displacement Angel *et al.* (1991) concluded that

Si does not occupy tricluster sites and that diclusters are either of the $AlSiO_7$ or Si_2O_7 type [7]. Clear ordering patterns were not presented apart from the indicated trends, but they qualitatively agree with the results of this thesis.

Component structures can also be derived from the superspace models. For an easier comparison $1 \times 1 \times 2$ component structures labelled $C1_s$ and $C2_s$ were analysed based on the geometrically optimised superstructure of 2/1-mullite (M40 AS1, § 4.4.6). In a first step the component structures must be identified. This requires to check how the superspace symmetry operators of $Pbam(\alpha 0\frac{1}{2})0ss$ transform the displacement amplitudes of the coordinates of all atoms in the unit cell. A comparison of the resulting character table with the irreducible representations (R-irep) of the space group $Pbam$ allows to determine the symmetry of $C1_s$ and $C2_s$ (Tab. 5.1). The sine and cosine components of the displacive modulation of x and z transform according to the R-ireps $Z_2^+(X_7)$ and $Z_4^-(X_8)$, and of y according to $Z_1^+(X_1)$ and $Z_3^-(X_2)$. McConnell & Heine (1985) rejected the presence of the distortion modes Z_1^+ and Z_3^- based on electrostatic considerations, but the symmetry analysis of superspace symmetry analysis shows that it must be included. Depending on the origin shift and the t-section the component structures exhibit different symmetries. Here, an origin shift of $\frac{1}{4}\mathbf{a} + \frac{1}{2}\mathbf{c}$ was applied[2]. The resulting $C1_s$ (Z_1^+, Z_4^-) and $C2_s$ (Z_2^+, Z_3^-) are described in space groups $Pb2_1m$ and $Pn2_1m$, respectively. In Figure 5.2 the superstructure of M40 AS1 is shown with the position of the component structures. The respective $1 \times 1 \times 2$ subcells of the superstructure are shown with more details in Figure 5.3 together with the original component structures of C1 and C2 for a direct comparison [66].

Now that the component structures are identified, they can be compared with C1 and C2. In the initial symmetry analysis [181] the presence of more than one distortion mode was not considered. Thus, monoclinic or non-centrosymmetric space groups were rejected. The component structures $C1_s$ and $C2_s$ were derived systematically from the superspace group considering the relevant Wyckoff positions. Nevertheless, in C1 and C2 the approximate displacement directions of O1 and O2 atoms agree with those of $C1_s$ and $C2_s$ (Fig. 5.3), although the displacement amplitudes exhibit different symmetry relationships because the distortion modes Z_1^+ and Z_3^- were not included in C1 and C2. Despite this minor difference, it can be concluded that both models describe the same underlying displacement pattern. The indicated trends of the occupancies in C1 and C2 agree well with the absence and presence of diclusters and triclusters in $C1_s$ and $C2_s$, but the description of the latter is more accurate as atoms are either present or absent. An analogue description is not possible under the symmetry constraints of C1 and C2.

---

[2]The origin shift is expressed relative to the average structure. The shift component along $\mathbf{c}$ was included for easier comparison with the setting of C1 and C2 used in the other studies. Also note that McConnell & Heine (1985) assigned the labels C1 (X_8) to the 'sillimanite' component ($Pbnm$) and C2 (X_7) to the 'ι-Al_2O_3' component ($Pnnm$) [32]. Angel & Prewitt (1987) used a reversed enumeration for ρ_1 ('ι-Al_2O_3') and ρ_2 ('sillimanite') [66]. Here, the labels of McConnell & Heine are used.
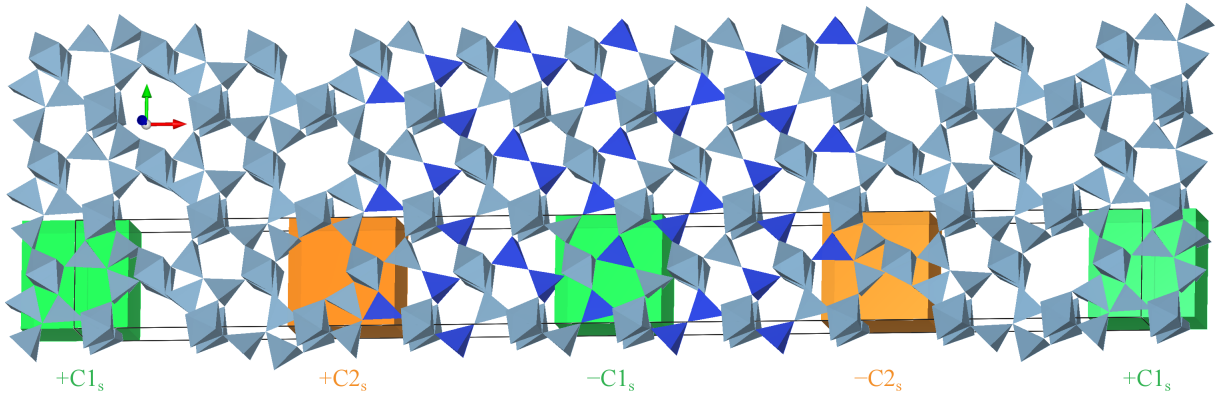
Figure 5.2: Model of ordered 2/1-mullite in space group $Bb2_1m$ with ideal Al/Si ordering (§ 4.3.3) based on the ordered SSM at $t = 0.275$. Only tetrahedra of cations (Al polyhedra in grey blue, Si tetrahedra in dark blue) with $z = 1$ are shown with the interconnecting octahedra. The coloured boxes indicate the positions of the component structures. $C1_s$ and $C2_s$ describe the structural difference with respect to the average structure. Here, the resulting structure is shown and the boxes do not show the component structures. The sign of the label indicates if the respective component structure was added or subtracted from the average structure. In the superspace approach the difference with respect to an average structure is described by modulation functions.
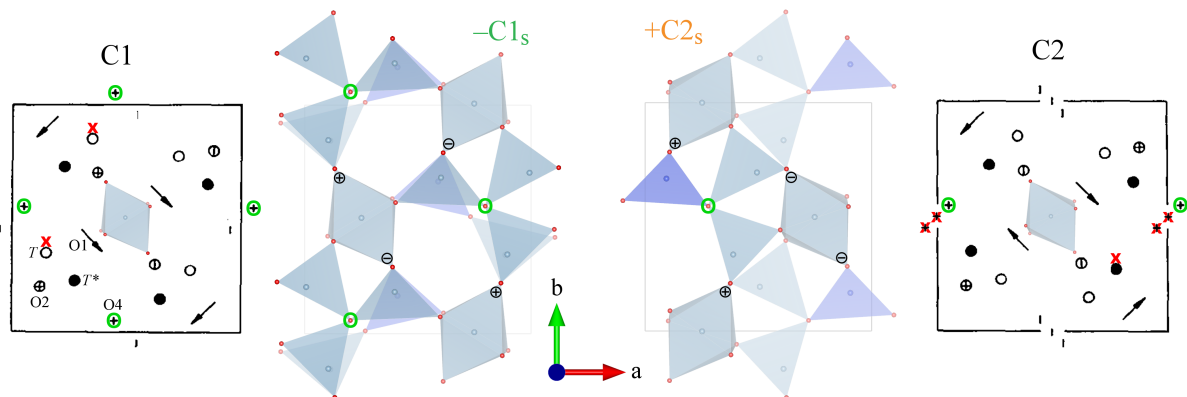
Figure 5.3: Component structures C1 and C2 in comparison to the atomic displacements and occupancies caused by the component structures $C1_s$ and $C2_s$. In C1 and C2 a decreased (open circles or '−') and increased (filled circles or '+') occupancy of the T, T^*, O3 and O4 sites ($z = \frac{1}{2}$) is indicated together with the displacements of O1 ($z = \frac{1}{2}$) and O2 ($z = \frac{1}{4}$). In $C1_s$ and $C2_s$ the atoms occupying the sites described in C1 and C2 are shown ($0.2 < z \leq \frac{1}{2}$) together with the subsequent layer ($-0.3 < z \leq 0$, decreased opacity). In all cases the displacement of O2 along the c direction is indicated by $\ominus$ and $\oplus$. A comparison of C1 with C_{1s} and C2 with C_{2s} reveals that the displacement directions agree qualitatively, but there are differences concerning the occupancies. O4 atoms with an increased occupancy in C1 and C2 that coincide with an occupancy of 1 in $C1_s$ and $C2_s$ are marked with a green circle. Occupancy trends that are not in agreement with $C1_s$ and $C2_s$ are marked with a red cross. Component structures of C1 and C2 are adapted from Figure 9 in [66]. Note that the original figures were rotated and therefore minus signs in C1 and C2 are vertical bars. Also note the origin shift of $\frac{1}{4}\mathbf{a}$.

Initially it was assumed that one component structure defines the vacancy ordering and the other the Al/Si ordering. This picture is not supported by C1$_s$ and C2$_s$. Both components are important for vacancy ordering and Al/Si ordering and a separation of the Si distribution from the vacancy distribution is not possible in terms of $1 \times 1 \times 2$ subcells. C1$_s$ describes the stacking of VBs and VFBs in agreement with C1. The first component is thus responsible for the vacancy ordering within VBs and for the Al/Si ordering within the VFBs. C2$_s$ describes the tetrahedra distribution at the block borders. The component structures derived from the ordered SSM thus emphasises the importance of the block structure and the stacking pattern of the blocks for the description of the underlying ordering mechanisms.

The comparison has shown that the alternative description of modulated structures in terms of component structures can be easily derived from a superspace model. The step into the opposite direction, i.e. the construction of a superspace model, is not straight forward from the component structures. A comparison of the component structures C1 and C2 with C1$_s$ and C2$_s$ contains minor differences concerning the displacement of atoms and significant differences concerning the occupancies of diclusters and triclusters (Fig. 5.3). These disagreements can be attributed to the different space groups and partly to the fact that the parameters of C1 and C2 were not refined. The superspace description thus provides a more complete description of the structure of mullite that takes the full symmetry into account.

5.1.3 Alternative vacancy ordering pattern

Saalfeld (1979) suggested the first model for 2/1-mullite with an ordered vacancy distribution [60]. In § 4.1.2 (Fig. 4.4) it was shown that this vacancy distribution can be derived from the superspace group $Pbam(\alpha0\frac{1}{2})0ss$ if the vacancy domain is not on a special position, but $x^{\mathrm{Q}}_{\mathrm{BW}} = 0.07$. In Saalfeld's model (Fig. 1.7) also vacancy blocks and vacancy-free blocks can be identified. Using the terminology of § 4.4.1 VBs with $n_{\mathrm{V}} = 2$ alternate with VFBs with either $n_{\mathrm{D}} = 3$ and $n_{\mathrm{D}} = 5$ along $\mathbf{a}$, which is clearly a different pattern in comparison to the ordered SSM of 2/1-mullite described in § 4.3. The stacking along $\mathbf{c}$ is also different because in Saalfeld's model VBs are stacked upon VBs and VFBs upon VFBs resulting in the presence of tricluster-tricluster chains and dicluster-dicluster chains. In § 4.4 the absence of tricluster-tricluster chains was identified as unifying mechanism, but this avoidance rule must not necessarily hold for alternative block stacking patterns as in Saalfeld's model. However, there is one major drawback of the alternative vacancy distribution described in the space group $B11\frac{2}{m}$. The 2-fold rotation axis goes through the O3 atoms of dicluster columns and thus excludes Al-Si diclusters in that column because only alternating patterns of Si-Si and Al-Al diclusters may be present. Nevertheless, the limitations on the Si distribution by the symmetry necessarily destabilise the structure

according to the Al/Si ordering trends identified in § 4.4.4 and also according to Pauling's rules.

A few Al/Si ordering patterns were investigated with force field methods by geometrically optimising the trial structures using the GULP code [9]. This quick survey is by far not complete and here the focus lies on two structures which are considered to be representative examples of a stable ('the good') and an unstable ('the bad') structure with Saalfeld's vacancy distribution. The bad structure was constructed by completely avoiding Si in triclusters so that all Si atoms are concentrated in VFBs and Al-Al diclusters are not present (bottom model in Fig. 5.4). A relaxation of the model with GULP leads to strong distortions, e.g. a single Si tetrahedron without the dicluster partner tetrahedron or a three-membered ring instead of a tricluster without a central O4 oxygen emerge during the relaxation. A geometric optimisation with DFT failed as within four relaxation cycles the lattice parameters increased by more than 40% and the structure fully decomposes. Furthermore, phonon calculations with GULP show several physically meaningless phonons indicating that the structure is unstable[3]. The total energy of the distorted relaxed structure is -9537.16 meV/atom, which is 67 meV/atom greater than M40 FFID 3 (Tab. 4.10 in § 4.3.3).

The good structure (top model in Fig. 5.4) was obtained by interchanging Al and Si atoms in a series of relaxation steps until the geometry of the optimised structure did not show any visible distortions with respect to the expected polyhedra geometry. The important stabilising elements relative to the bad structure are the presence of Si in the tricluster chains and Al-Al diclusters alternating with Si-Si diclusters along the 2-fold rotation axis. According to GULP all phonons are stable and the total energy is -9596.43 meV/atom, which is 7.72 meV/atom greater than FFID 3 (Tab. 4.10 in § 4.3.3). Preliminary DFT calculations (PBEsol-D) indicate that the structure is stable with a total energy that is about 13 meV/atom greater than M40 AS1. The normalised lattice parameters a, b and c resulting from geometric optimisation are 7.5711 Å, 7.6332 Å and 2.9082 Å, respectively. These values are slightly above those of M40 AS1. From this it can be deduced that the vacancy distribution has only a minor effect on the lattice parameters and that mainly the Si distribution on the tetrahedral sites determines the geometry of the lattice.

The comparison between the ordered SSM and Saalfeld's model of 2/1-mullite indicates that different vacancy distributions are stable. It also confirms that Al/Si ordering is crucial for the successful simulation of mullite structures. The stacking of VFBs on VFBs and VBs on VBs increases the complexity of the structure in a physical space description and in a superspace description as well. Hence, the models developed in this thesis

---

[3]Phonon calculations of the geometrically optimised 2/1-mullite superstructures were not carried for the determination of the ideal Al/Si ordering in § 4.3.3. For a set of tested structures all phonons were stable, including structures with relatively high energy like FFID 30658 and FFID 32337. Highly unstable structures like FFID 38760 also show unstable phonons according to calculations with GULP.
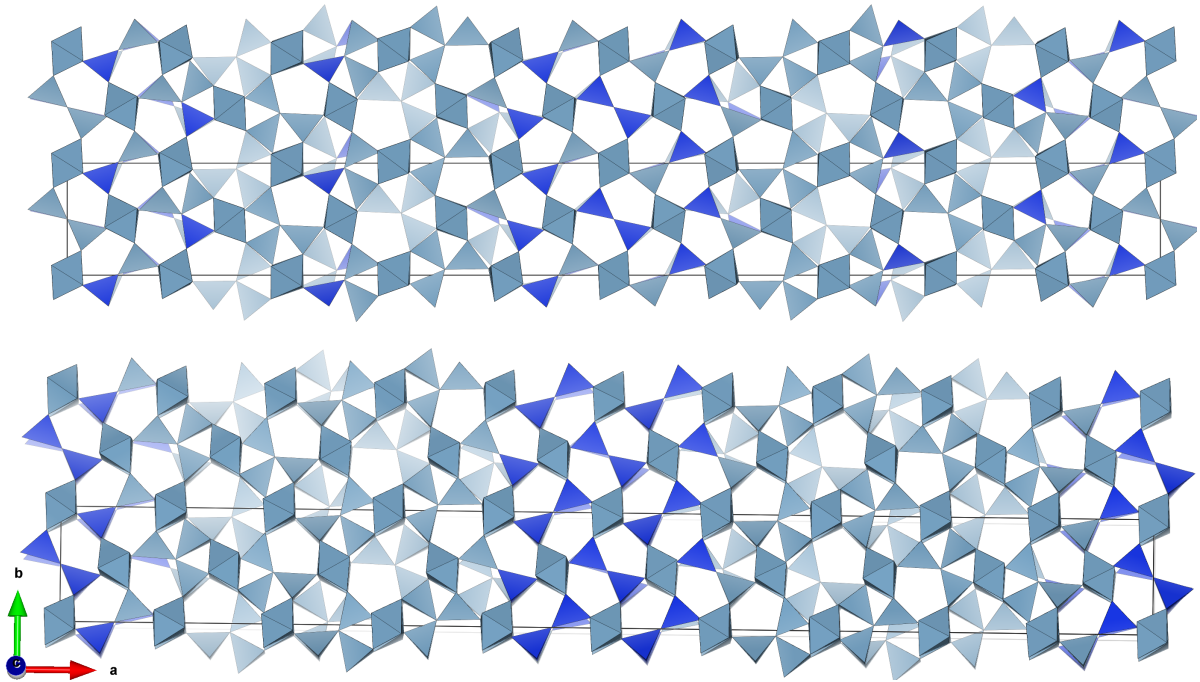
Figure 5.4: Two trial Al/Si ordering patterns based on Saalfeld's vacancy distribution of 2/1-mullite. Two subsequent layers are shown. The upper model shows the 'good' candidate with Si in the tricluster chains and Si-Si diclusters alternating with Al-Al diclusters along the 2-fold rotation axis. The bottom model, which is not stable, has no Si in any tricluster and thus all Si atoms are concentrated in the stacked VFBs. The upper model shows the geometrically optimised structure, whereas the bottom model shows the input structure because the geometric optimisation leads to a strong deformation.

are favoured according to Pauling's rule of parsimony. Although a refinement was not attempted, a comparison of the simulated diffraction patterns (Fig. 5.7) shows significant differences of the diffracted intensities. In conclusion, a relationship between Saalfeld's model and the ordered SSM can be established in physical space using the description of block units and also in superspace using different block wave parameters to describe the vacancy domain. The simulated diffraction patterns, the symmetry analysis with respect to Al/Si ordering and the DFT calculations indicate that the ordered SSM is the appropriate description of the underlying ordering mechanisms in mullite.

5.1.4 Full vacancy ordering in 5/2-mullite

Ylä-Jääski & Nissen (1983) developed an ordered structural model of 5/2-mullite based on high-resolution TEM micrographs of a sample with an approximate vacancy concentration $\delta \approx 0.48$ [36]. The model was described quantitatively as a $4 \times 1 \times 2$ supercell by Kahn-Harari *et al.* in the space group $Bb2_1m$ (Tab. 1 and Fig. 8 in [63]). A refinement was not attempted in the studies. The vacancy distribution of that model is identical to that of physical space sections of the unified SSM with $\delta = 0.5$ and $\alpha = 0.25$ shown as M50 #1 in Figure 4.21 (cf. Fig. 1.7). In the study also selected area electron diffraction
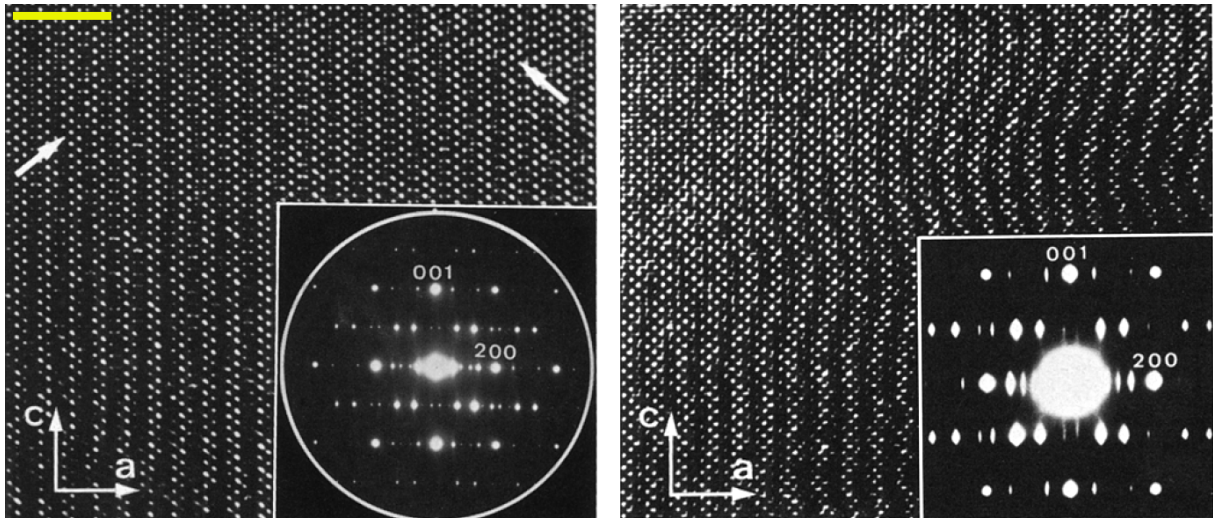
Figure 5.5: High-resolution TEM micrographs with respected diffraction pattern of highly ordered mullite (left) and mullite with disorder setting in (right). Each micrograph has a width of approximately 300 Å corresponding to the size of about 40**a** × 90**c**. The yellow bar represents a scale of 50 Å. The diffraction pattern on the left shows up to fifth order satellite reflections, the one on the right up to the third order. Work based on Figures 3 and 6 of Ylä-Jääski & Nissen (1983) [36]. © 1983 Springer Nature, adapted with permission.

patterns are presented, that show high order satellite reflections (Fig. 5.5). A modulation wave vector $\mathbf{q} = (0.291\,0\,0.5)$ was determined by analysing Figure 3 in [36] (§ A.1). The expected composition for $\alpha = 0.291$ is $\delta = 0.418$, which strongly deviates from the reported composition $\delta = 0.48 \pm 0.03$ based on EDX measurements [36]. However, the nominal composition of the crystal used for the study corresponds to a vacancy concentration of $\delta = 0.58$ and the composition of other crystallites of the same sample showing a monoclinic modulation was determined to be $\delta = 0.54 \pm 0.05$. This indicates that the sample is strongly inhomogeneous which might affect the measured value of δ and of α. Nevertheless, this observation suggests that Equation 4.2 describes the lower limit of the α and mullite with correspondingly increased L_a^{VB} may form. In this case tricluster chains are avoided but not forbidden. An alternative explanation is that there is an additional mechanism that favours a minimum block lengths with $n_{\mathrm{V}} > 2$ and therefore the lower limit of α is higher than 0.25 as indicated in Figure 4.19, but a reliable conclusion requires the structural analysis of a larger set of ordered samples.

In the paper by Ylä-Jääski & Nissen (1983) it is stated that the "idealized commensurate superstructures" do not "persist in larger areas" and in their Figure 6 a high-resolution micrograph shows how the structure becomes wavy and seemingly dissolves into a disordered structure the superstructure can no longer be recognised (Fig. 5.5). The effect on the electron diffraction pattern is that on the one hand higher order satellite reflections disappear as only first, second and third order satellite reflections remain, and on the other hand the satellite reflections are no longer spot-like but become elongated parallel

to $\mathbf{c}^*$ indicating disorder in the *ab* plane. Although the observed modulation wave vector deviates from the prediction, considering the inhomogeneity of the sample and the uncertainty in the composition the high-resolution TEM and electron diffraction study strongly supports the findings of this thesis: 1. Different degrees of order are directly observed in real and reciprocal space. 2. Lower degrees of order do not show high order satellite reflections. 3. Higher degrees of order are described by a structure of vacancy blocks and vacancy-free blocks. These observations are in very good agreement with the results of the ordered and the disordered SSM and their interpretation in terms of different degrees of order. Although in the study it is also mentioned that the characteristic diffuse scattering observed in other studies could not be detected in the samples with high order satellite reflections, a careful analysis of Figure 3 in [36] shows a weak trace of streaks running from first to second order satellite reflections as described in § 4.1.1. This indicates that very high degrees of order, still not perfectly ordered, contain weak diffuse features that are also observed in mainly disordered samples. Kahn-Harari *et al.* (1991) concluded that disordered samples are composed of "ordered zones within a disordered mullite matrix", and that the vacancy distribution in ordered zones corresponds to the model suggested by Ylä-Jääski & Nissen, hence the block models of VBs and VFBs. This again supports the importance of the ordered SSM as a basis for the description and understanding of ordering phenomena in mullite. It is also in agreement with the observation that the main diffuse features seem to originate from the satellite reflections (§ 4.1.1).

5.1.5 Comparison with the work by Birkenstock *et al.* (2015)

In 2015 the first superspace description of mullite was published by Johannes Birkenstock *et al.* [6] based on a X-ray diffraction measurement of a single crystal grown with the Czochralski method. In this section the measurement and refinement are labelled BS. The diffraction patterns showed the characteristic diffuse scattering and rather diffuse first order satellite reflections. No second order satellite reflections were detected. The refinement in the superspace group $Pbam(\alpha 0 \frac{1}{2})0ss$ used harmonic modulation functions to model the displacive, occupational and ADP modulation. The BS constraint scheme forced the occupational modulation functions (cf. Fig. 5 in [6]) to fulfil the relationships $g_s^{\text{Al3}}(t) = g_s^{\text{Si2}}(t + \frac{1}{2}) = g_s^{\text{Al2}}(t + \frac{1}{2}) = g_s^{\text{O3}}(t + \frac{1}{2}) = g_s^{\text{O4}}(t)$. As Al2 and Si2 occupy the same T site, the amplitude of the occupational modulation of the T site is twice as large as that of the T^* site. Furthermore, the relationship between O3 and O4 suggests that the absence of O3 implies the presence of a vacancy. As described in § 1.1.3 and § 1.1.5 this is not true because the absence of O3 only implies that there is no dicluster. As a consequence the equation $g_s^{\text{O3}}(t) + g_s^{\text{O4}^{\mathcal{A}}}(t) + g_s^{\text{O4}^{\mathcal{B}}}(t) = g_s^{T}(t)$ is not fulfilled (cf. § 4.2.1) and the structural model is locally not charge balanced. The constraints scheme leads to some suspicious modulation functions, for example a strong ADP modulation of the atomic

domains of O3 and O4 leads to non-postive definite ADP tensors for some t-sections. The amplitude of the displacive modulation of the O4 atom is significantly stronger than the other displacive modulation functions leading to a strong modulation of the Al3-O4 and T-O4 bond lengths (cf. Fig. 5 in [6]). Neglecting the displacive modulation of O4, the bond length modulations are in good agreement with the refinement of the disordered SSM (cf. Fig. 4.10) and the overall phase relationships between occupational and displacive modulations indicate that the BS model and the disordered SSM are indeed very similar despite the mentioned differences that probably originate from the problems of the constraint scheme. The published dataset [6] was used for a refinement using the constraint scheme of the disordered SSM (§ 4.1.4) and a unit weight of the structure factor amplitudes neglecting σ_{hkl}. Only one constraint on the ADPs was used ($B_{U_{22},1}^{O3} = 0$). The resulting disordered SSM based on the BS dataset is physically meaningful for all t-sections indicated by a consistent shape of the ADPs and similar amplitudes of all displacive modulation functions, including O4. The phase of the displacive modulation of x_{s1}^{O4} of this new refinement agrees well with the disordered SSM (§ 4.1.4), but the phase of the modulation of x_{s2}^{O4} is clearly different. The parameters for $A_{x_i,1}^{O4}$ and $B_{x_i,1}^{O4}$ ($i = 1, 2$) of this new refinement are considered to be more reliable than the parameters determined in § 4.2.1 because the BS measurement has a better resolution with $\frac{\sin(\theta_{\max})}{\lambda} = 0.838$, but the estimated standard uncertainties are in both cases rather large. The $R_{\mathrm{all}}(F, m = 1)$ improves significantly to 0.213 and $wR_{\mathrm{all}}(F)$ improves from 0.059 (BS) to 0.029 (new BS refinement). The occupational modulation amplitude of O4 is 0.0590 (13) which is in between that of SA2 and Qg1.

In the BS data reduction three modulation wave vectors $\mathbf{q}_1$, $\mathbf{q}_2$ and $\mathbf{q}_3$ were determined. It was reported that a refinement with the latter two was not possible due to the weakness and diffuse character of the corresponding satellite reflections which inhibited a successful integration of the reflections, but Birkenstock $et\ al.$ assumed that a refinement of a superspace model including $\mathbf{q}_2$ and/or $\mathbf{q}_3$ would probably result in a similar model characterised by a soft modulation of the occupancies [6]. From the measurement of SA1 on ID28 at the ESRF (§ 4.1.1) $\mathbf{q}_2$ and $\mathbf{q}_3$ were also determined and exhibit essentially the same amplitudes. The different sets of modulation wave vectors are compared in Table 5.2. Considering the uncertainties, it can be concluded that $\mathbf{q}_2$ and $\mathbf{q}_3$ are identical in both measurements (SA1 and BS) and that the respective satellite reflections do not depend on the chemical composition like it is the case for the satellite reflections of $\mathbf{q}_1$.

Birkenstock $et\ al.$ (2015) concluded that "on a larger scale there is a weak long-range order within the overall disorder" and that "the driving force for this weak long-range order is probably the tendency for compositional homogeneity" [6]. This suggests that local variations of the chemical composition are the origin of the disorder in mullite, which is a plausible explanation as several studies indeed reveal that mullite crystals are not homogeneous (§ 4.2.5, § 5.1.4, [53]). With respect to the ordered SSM, the question arises

| Reference | $\mathbf{q}_1 = (\alpha_1\,0\,\frac{1}{2})$ | $\mathbf{q}_2 = (0\,\beta_2\,\gamma_2)$ | | $\mathbf{q}_3 = (0\,\beta_3\,\gamma_3)$ | | $\mathbf{q}_2 - m_z : \mathbf{q}_3$ | |
	α_1	β_2	γ_2	β_3	γ_3	$|\beta_2 - \beta_3|$	$|\gamma_2 + \gamma_3|$
BS	0.3137 (2)	0.4021 (5)	0.1834 (2)	0.4009 (5)	-0.1834 (2)	0.0011 (7)	0.0000 (4)
SA1	0.2978 (8)	0.397 (4)	0.1834 (19)	0.403 (5)	-0.181 (2)	0.006 (11)	0.002 (4)
Difference	0.0159 (10)	0.005 (4)	0.000 (2)	0.002 (6)	0.002 (2)		

Table 5.2: Comparison of modulation wave vectors from BS [6] and the measurement of SA1 (§ 4.1.1).

the other way around: What is the driving force that leads to a disordered vacancy distribution or a certain vacancy concentration? The next section the observation of different degrees of order is discussed together with the most important ordering mechanisms.

5.2 Ordering phenomena in mullite

5.2.1 Comparison of geometrically optimised structures with refined structure models

The occupational modulation of the ordered and the disordered SSM are strongly related. This is not surprising as the respective constraints were derived from the same symmetry considerations (§ 4.1.3). From § 5.1.1 a structural relationship is expected concerning not only the occupational modulation, but also the Al/Si ordering and the displacive modulation. The Al/Si ordering patterns of the disordered SSM and the ordered SSM were derived independently with different methods. A comparison of the different models may be used to evaluate the reliability of the Al/Si ordering and displacive modulation established from DFT calculations and in turn evaluate the consistency of the Al/Si ordering scheme derived from the displacive modulation of the disordered SSM. In the following the refinement of § 4.2.1 (SA1) is compared with M40 AS1 (§ 4.4.6).

In § 4.2.4 occupational modulation functions of Al2 and Si2 were determined from the modulation of the volume of the tetrahedra site. The maxima of $\bar{s}_V^{\mathrm{Al2}}(t)$ and $\bar{s}_V^{\mathrm{Si2}}(t)$, based on the reference volumes derived from [54], are observed at $t = 0.88$ and $t = 0.63$, respectively. In M40 AS1 the centre of the ten points defining the Al2 domain is found at $t = 0.84$ and that of the six points of the Si2 domain at $t = 0.60$. This is in acceptable agreement and thus it is concluded that the Al/Si ordering pattern of M40 AS1 qualitatively describes the underlying Al/Si ordering pattern of the disordered SSM.

The displacive modulation functions of M40 AS1 determined with the method described in § 4.3.4 are significantly stronger than the modulation functions from the refinement, which is expected due to the different degrees of order they represent. First order harmonic terms $A_{x_i,1}^{\mu}$ and $B_{x_i,1}^{\mu}$ and the average coordinate $\bar{x}_{si}^{\mu}$ were determined by a least squares fitting procedure from the embedded coordinates. For Al3 and O4 the fit procedure gives coordinates that strongly deviate from the mean because the four coordinates are concentrated at similar t-sections. Therefore, the coordinates of Al3 and O4 were determined with $\bar{x}_{si}^{\mu} = \langle x_{si}^{\mu} \rangle$. The modulation functions from the refinement were amplified by a scale factor ζ to account for the different degrees of order. ζ was determined by minimising a residual factor

$$R = \sum_{\mu} \frac{|\bar{x}_{si,\mathrm{DFT}}^{\mu} - \bar{x}_{si,\mathrm{XRD}}^{\mu}|}{\bar{x}_{si,\mathrm{XRD}}^{\mu}} + \sum_{\mu} \frac{|A_{x_i,1,\mathrm{DFT}}^{\mu} - \zeta A_{x_i,1,\mathrm{XRD}}^{\mu}|}{\zeta A_{x_i,1,\mathrm{XRD}}^{\mu}} + \sum_{\mu} \frac{|B_{x_i,1,\mathrm{DFT}}^{\mu} - \zeta B_{x_i,1,\mathrm{XRD}}^{\mu}|}{\zeta B_{x_i,1,\mathrm{XRD}}^{\mu}}.$$

The minimum $R = 0.03$ is obtained if $\zeta = 4.0$. In Figure 5.6 the amplified modulation functions are shown together with the embedded coordinates and the calculated modulation functions from the fitting procedure. An excellent agreement is observed for x_{s3}^{Al1},
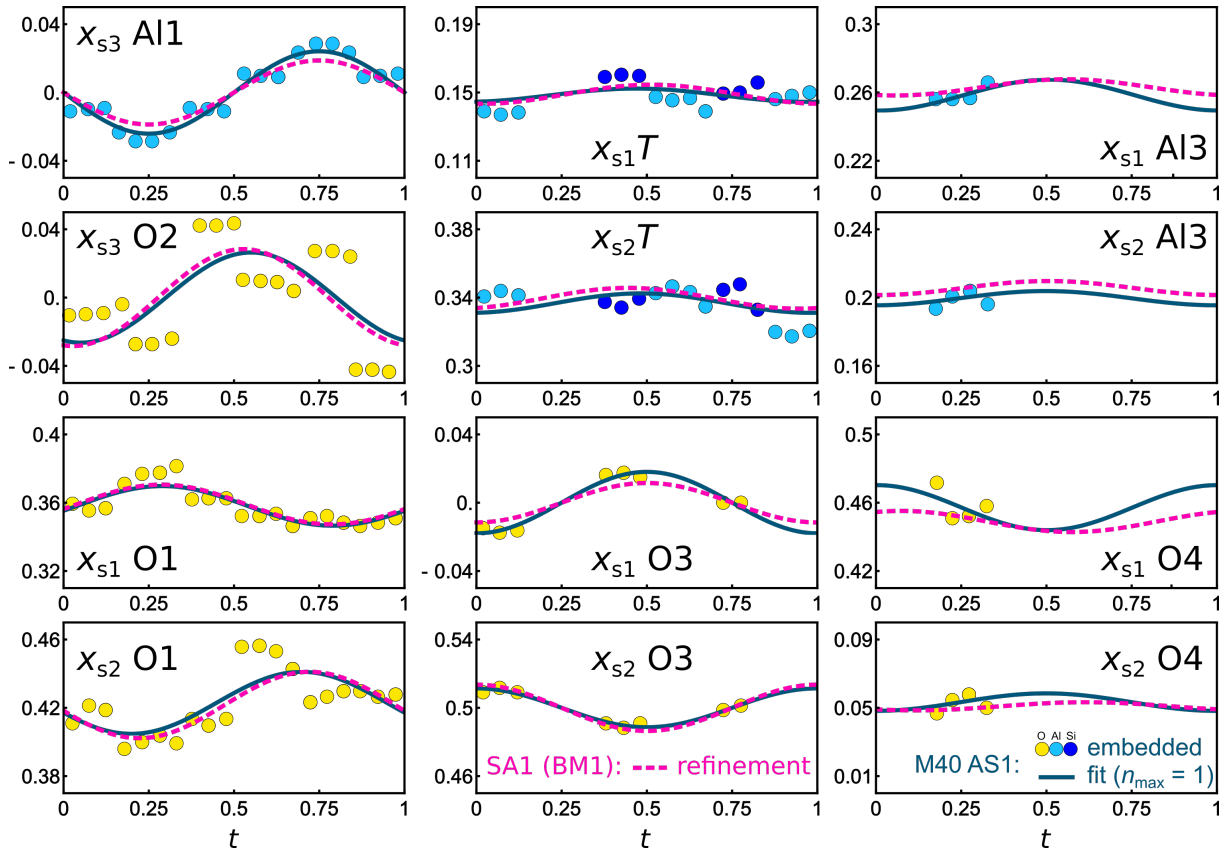
Figure 5.6: Amplified modulation functions from the refined disordered SSM (SA1, dashed lines) are plotted with harmonic fits of first order displacive modulation functions of M40 AS1 (solid lines).

$x_{\mathrm{s}i}^T$, $x_{\mathrm{s}i}^{\mathrm{O1}}$, $x_{\mathrm{s}3}^{\mathrm{O2}}$ and $x_{\mathrm{s}i}^{\mathrm{O3}}$ ($i = 1$, 2), i.e. the modulation functions almost overlap indicating a consistent phase, amplitude and average coordinate. The average coordinates of Al3 and O4 are slightly shifted indicating that averaging a set of coordinates over a limited t-range is not appropriate. The phases of the modulation functions of O4 deviate quite a lot and also the amplitudes are different. Considering that relevant differences are only observed for the atomic domains with short block wave functions that are defined over a small range of t-sections, the comparison as a whole supports both the ordered SSM represented by the geometrically optimised superstructure and the disordered SSM based on diffraction experiments. It also supports the view that the underlying ordering patterns of the displacive modulations, Al/Si ordering and vacancy ordering are correctly described by the ordered SSM.

5.2.2   Different degrees of order

If mullite structures were usually ordered as described by the ordered SSM, then in routine powder diffraction patterns at least the strongest satellite reflections should be visible. In Figure 5.7 several simulated powder diffraction patterns are plotted alongside the measured powder diffraction pattern of sample SA. The comparison shows that the strongest satellite reflections of the disordered SSM are also the strongest satellite reflections of the ordered SSM. Nevertheless, in the measured diffraction pattern satellite reflections are not observed at the expected diffraction angles. The simulated diffraction patterns thus unequivocally indicate that mullite samples are commonly disordered. This conclusion was drawn by many other studies before, e.g. by [63, 3, 4, 6], but only the work by Kahn-Harari *et al.* (1991) defined the most ordered state of a 5/2-mullite model (§ 5.1.4). A unifying picture explaining the ordering phenomena in mullite for different compositions was missing.

The results of this thesis suggest that the characterisation of the crystal structure of mullite samples must not only consider the chemical composition, but also the intrinsic degree of order. The refined model for SA1 exhibits the largest modulation amplitudes indicating a stronger trend to long-range ordering in comparison to the model for SA3 with weaker modulation amplitudes. However, all refinements have in common that the occupancies are modulated within a small amplitude range. A physically meaningful model requires the occupancies to be modulated within a range between 0 and 1, which introduces limitations on the allowed amplitudes depending on the order of harmonics that are used to describe the modulation function. For example, the occupancy of the T site is $1 - \frac{\delta}{2}$ and that of O4 and T^* is $\frac{\delta}{2}$. As a consequence a model limited to first order harmonics is restricted to modulation amplitudes $\leq \frac{\delta}{2}$ and stronger amplitudes require higher order harmonics leading to higher order satellite reflections. There are several electron diffraction studies that provide a good overview on the order of satellite
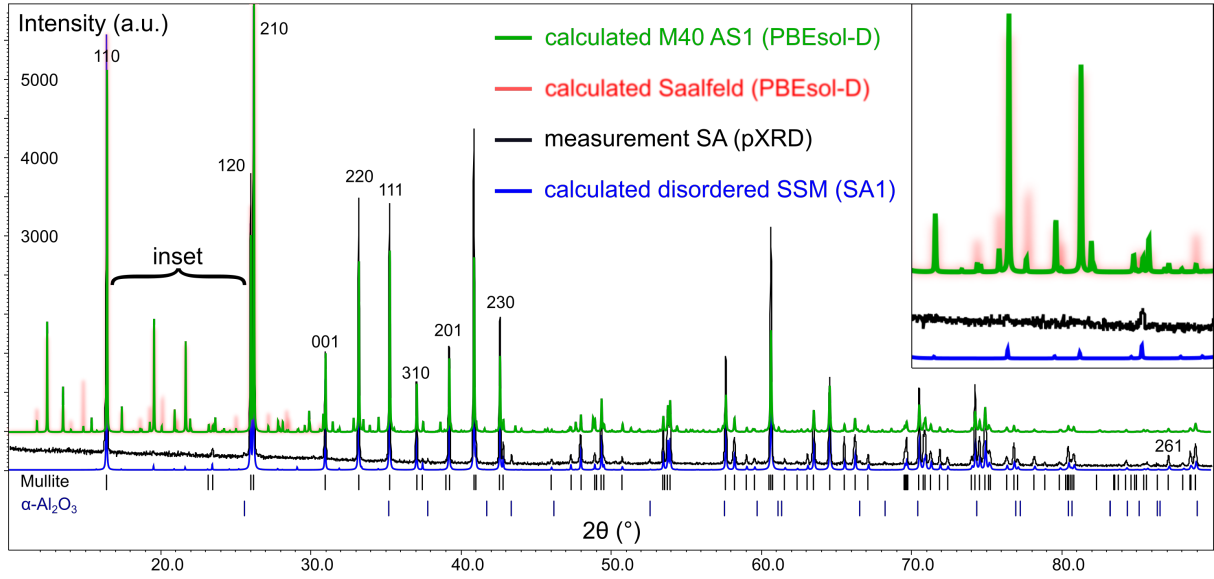
Figure 5.7: Comparison of measured powder diffraction pattern (SA1, cf. Fig. 3.2) with simulated diffraction pattern of the geometrically optimised M40 AS1 superstructure representing the ordered SSM (green solid line). In the range $2\theta < 31°$ a simulated diffraction pattern based on the model suggested by Saalfeld (1979) is included (red blurred line, § 5.1.3). A simulated diffraction pattern based on a ten-fold superstructure generated from the refined disordered SSM is also plotted (§ 4.2.1). Diffraction patterns were calculated with VESTA3 [184] ($\lambda = 1.54059$ Å) using the refined lattice parameters of SA for easier comparison. The inset shows the details of the diffractograms between the main reflections 110 and 120 ($16.7° < 2\theta < 25.5°$). The most pronounced measured reflection in the inset is the 200 reflection and satellite reflections were not detected at the expected diffraction angles. Positions of main reflections of mullite and α-Al$_2$O$_3$ are indicated by vertical bars at the bottom. Some main reflections are indexed with three indices $hk\ell$.
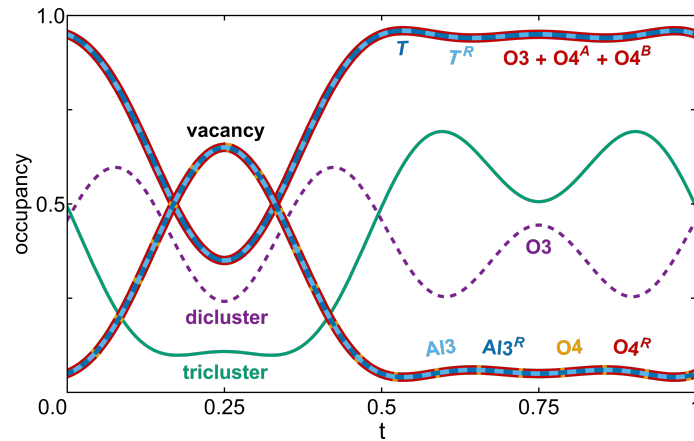
Figure 5.8: Hypothetical occupational modulation functions with first, second and third order harmonics. The used parameters are $\delta = 0.4$, $\alpha = 0.3$, $B_{s,1}^{O3} = -0.044$, $B_{s,2}^{O3} = -0.057$, $B_{s,3}^{O3} = 0.15$ based on the constrain scheme presented in Table 4.5. The resulting occupational modulation function amplitudes of first, second and third harmonic of Al3 and O4 are 0.25, -0.15 and 0.05, respectively. The analogy between the function representing the occupancy of diclusters in this figure and the block wave functions of O3a, O3b and O3b$^{\mathcal{R}}$ can already be grasped.

reflections present in the diffraction patterns of orthorhombic mullite. The diffractograms of Cameron (1977) show first (Fig. 3a-d in [2]), second (Fig. 3e-f) and fourth order satellite reflections (Fig. 3g). Sayir & Farmer (1995) and Nakajima et al. (1975) reported on mullites with third order satellite reflections [185, 186]. Similar patterns but with fifth order satellites were reported in [36]. Concerning monoclinic mullite even higher orders were reported. In [50, 36, 51] at least seventh order satellite reflections were observed, but in this section only orthorhombic mullite structures are discussed. A structural model was not refined in any of the studies and only [36] suggested a model based on HRTEM simulations (§ 5.1.4).

The disordered SSM provides a model that can explain the observed range of satellite reflection orders. The constraint scheme of § 4.1.4 is valid for any order of harmonics and for different vacancy concentrations. The refinements in § 4.2.1 are examples of mainly disordered mullites with first order satellite reflections and only SA1, the sample with the strongest modulation amplitudes, exhibits weak second order satellite reflections. The occupational modulation functions of a hypothetical mullite structure with moderate degree of order is depicted in Figure 5.8. A simulated diffraction pattern based on this model would show first, second and third order satellite reflections. The similarity of the occupational modulation between this example and the ordered SSM can already be identified as three maxima of $s^{O3}(t)$ indicate the t-sections at which the block wave functions of O3a, O3b and O3b$^{\mathcal{R}}$ are defined in the ordered SSM. The degree of order in mullite structures can thus be characterised by the occupational modulation functions and in a first approximation by the highest order of satellite reflections on diffraction patterns. This suggests that with increasing degree of order the disordered SSM develops into the ordered SSM.

5.2.3   Diffuse scattering simulations based on the disordered SSM

A comparison of the equivalent isotropic displacement parameters U_{eq} of mullite-type compounds reveals that the average displacement of atoms in mullite is significantly stronger than in andalusite, sillimanite and sillimullite (Tab. 5.3). The low concentration of vacancies in sillimullite ($\delta = 0.12$) induces some displacements in its local environment leading to a slight increase of the ADPs with respect to sillimanite. In the case of mullite with δ between 0.4 and 0.5 the refined displacement parameters are much larger, although a large range is observed depending on the diffraction method and resolution of the measurement. Independent of the uncertainty, the trend is clear and the increased displacement parameters are only slightly reduced by modelling the displacive modulation. Taking into account that the thermal motion, static displacement due to short-range order and static displacement due to the long-range ordered modulation contribute to the displacement parameters, it can be deduced that the disordered SSM does not give a complete descrip-

Compound	Model	Method	$< U_{\mathrm{eq}} >$ of cations	$< U_{\mathrm{eq}} >$ of anions	Reference
Andalusite	average	sXRD	0.005	0.007	[187]
Sillimanite	average	sXRD	0.005	0.008	[173]
Sillimullite	average	sXRD	0.006*	0.010	[188]
Mullite VSG.50	average	pXRD	0.007	0.012	§ 3.3.1
Mullite SA	average	pXRD	0.016	0.021	§ 3.3.1
Mullite SA1	average	sXRD	0.012	0.019	§ 4.2.1
Mullite SA1	disorderd SSM	sXRD	0.011	0.018	§ 4.2.1
Mullite SA2	disorderd SSM	sXRD	0.009	0.016	§ 4.2.5
Mullite SA3	disorderd SSM	sXRD	0.010	0.016	§ 4.2.5
Mullite Qg1	disorderd SSM	sXRD	0.011	0.017	§ 4.2.5
Mullite BS	disorderd SSM	sXRD	0.008	0.014	§ 5.1.5

Table 5.3: Comparison of average U_{eq} of cations and oxygens. *Fe atoms were not considered in the case of sillimullite.

tion of the real crystal structure of mullite. This also raises a question about the meaning of the ADP modulation implemented in the disordered SSM. Possibly it is related with the likelihood that a certain site is disordered, which is supported by a clear antiphase relationship between the ADP modulation and the occupational modulation (§ A.6). If a site is less occupied for a certain t-section then the ADPs are larger and apparently the site is more disordered. A deeper analysis and discussion are outside the scope of this section.

Crystal structures with partially occupied sites necessarily show diffuse scattering because the periodicity of the average structure is violated. The partial occupancies of Al2, Si2, Al3, O3 and O4 in each unit cell are defined by the disordered SSM, which describes a long-range ordered modulation of the partial occupancies. Nevertheless, in each unit cell vacancies are found with a certain probability and the diffuse scattering in mullite contains information about short-range ordered correlations of atomic displacements and occupancies. In the following the diffuse scattering that is expected from the disordered SSM is investigated. Al/Si ordering and atom displacements, except for isotropic thermal displacements, were not considered and thus the modelled short-range order only considered the occupational modulation function with further constraints on the local vacancy environment.

Vacancies were distributed in a model crystal with the probabilities defined by the disordered SSM (§ 4.2.1). Constraints were applied so that that each vacancy is accompanied by two triclusters, tetraclusters are forbidden and stacking of vacancies is also forbid-
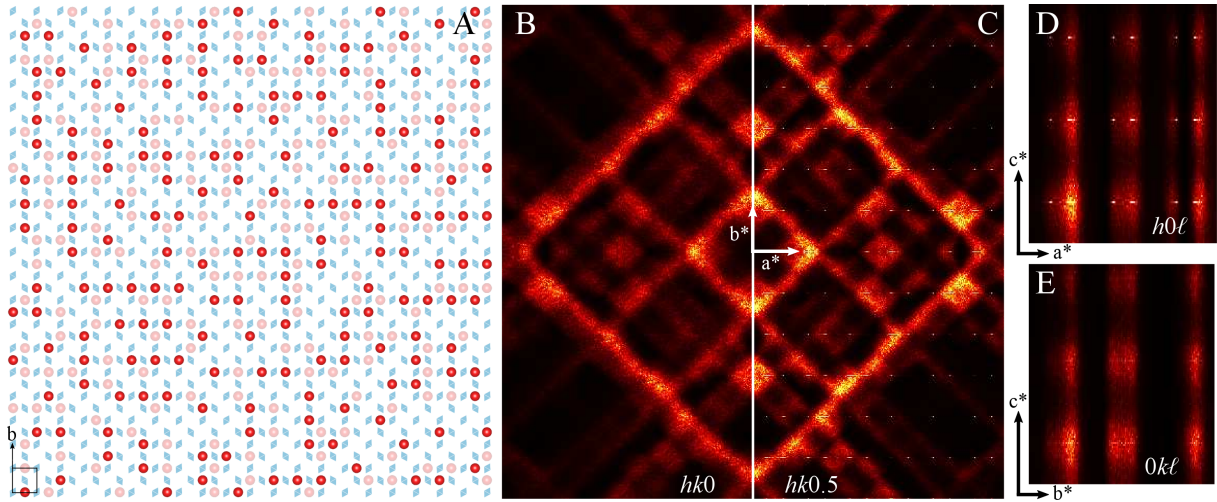
Figure 5.9: Real structure model of 2/1-mullite and calculated reciprocal space section. (A) A $64 \times 64 \times 64$ model crystal was generated, of which a $20 \times 20 \times 2$ section is shown. Vacancies at $z = \frac{1}{2}$ are represented by faint red spheres, at $z = \frac{3}{2}$ as red spheres. Tetrahedra are omitted for clarity. The vacancy distribution complies with the occupational modulation of the disordered SSM of AS1. (B) All sections perpendicular to $\mathbf{c}^*$ show the characteristic diamond grid similar. (C) The $hk0.5$ section shows satellite reflections, which are also visible in the $h0\ell$ section (D). Arrows indicating the origin of the coordinate system have the respective length of the reciprocal lattice vector. For (D) and (E) the origin is at the bottom left corner.

den. For the generation of crystal models and calculation of reciprocal space sections the DISCUS suite was used [99]. Reciprocal space sections show sharp first order satellite reflections at the expected positions and sections perpendicular to $\mathbf{c}^*$ are characterised by streaks resembling a diamond grid. The characteristic streak pattern of crosses in the $0k\ell$ section and the streaks originating from satellite reflections in the $h0\ell$ section is not observed. Consequently, the disordered SSM combined with the basic constraints on the vacancy environment does not result in a crystal structure description that accounts adequately for all observations in reciprocal space (Fig. 5.9).

The relationship between the modulation wave vector $\mathbf{q}$ and the vacancy concentration δ was explained by superspace symmetry with the additional constraint, that tricluster chains are forbidden in the ordered SSM (§ 4.4). Diffuse satellite reflections of disordered mullite crystals also follow the $\mathbf{q}$–δ relationship (§ 4.4.3) indicating that the avoidance of tricluster chains is independent of the degree of order. Another model crystal ($64 \times 64 \times 64$) was generated with the additional constraint that tricluster chains are forbidden. Calculations of reciprocal space sections show profound differences in comparison to Figure 5.9 as the diffuse features in the $h0\ell$ and $0k\ell$ sections form crosses (Fig. 5.10). The corresponding streaks are relatively broad and the intensity distribution differs from experimental observations, for example the intensity maxima described by $\mathbf{q}_2$ and $\mathbf{q}_3$ in § 4.1.1 cannot be identified on the calculated sections. Hence, the short-range order parameters used
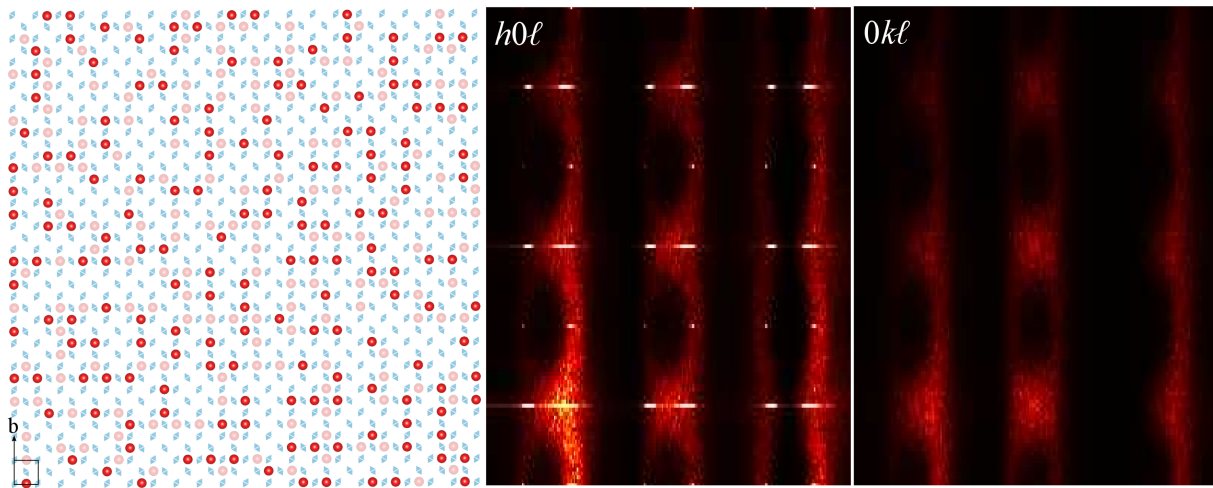
Figure 5.10: Real structure model of 2/1-mullite and calculated reciprocal space section, which show the same region as in Figure 5.9. The only difference between the models is that tricluster chains were forbidden. However, a stacking of two tricluster was allowed.

here still require further improvement for completion. Nevertheless, this model comprises qualitatively the most essential features in reciprocal space indicating that the tricluster-tricluster interactions are crucial for the stability of mullite independent of the degree of order.

5.3 Interpretation of the phase diagram

5.3.1 Turnover compositions of the phase diagram

According to the SiO_2–Al_2O_3 phase diagram presented in the introduction (Fig. 1.3) the width of the solid solution range of stable mullite corresponds to a vacancy concentration difference of about 0.06. The borders of the range shift to higher vacancy concentrations with increasing temperature and close to the melting point the width of the solid solution range becomes very narrow around $\delta \approx 0.4$. The temperature dependence of the phase borders agrees with other studies on mullite formation from mineral decomposition [148, 189, 150, 190] and especially mullite-mullite transformations at higher temperatures [191, 192], although other phase diagrams were suggested with a negligible dependence of the mullite composition on the temperature of formation [45]. Composition analyses of Czochralski-grown mullites suggest that at the melting point the solid solution range is $0.35 < \delta < 0.41$ and the growth of 3/2-mullite with the Czochralski method was not possible [193], which clearly supports the temperature dependence of the solid solution range suggested by Klug *et al.* (1987) [46]. The synthesis of metastable mullite samples with higher vacancy concentrations is possible and strongly depends on the method used. The synthesis from the melt has an upper vacancy concentration limit of $\delta = 0.57$ [47]. The synthesis with the sol-gel method or chemical vapor deposition (CVD) allows to further extend the vacancy concentration to about 0.83 [53, 51]. Here the focus is on stable and metastable mullite without tetraclusters in the range $0 < \delta < \frac{2}{3}$ neglecting sol-gel and CVD samples. Several approximate turnover compositions can be identified:

1. $\delta_{\text{low}} \approx 0.2$ marks the silica-rich border of the solid solution range [1].

2. $\delta_{\text{high}} \approx 0.4$ marks the alumina-rich border of the phase field of mullite at the melting point.

3. $\delta_{\text{mono}} = 0.5$ marks the turnover vacancy concentration between orthorhombic and monoclinic symmetry of the modulation wave vector.

4. $\delta_{\text{meta}} = 0.57$ marks the alumina-rich border of metastable mullite.

Minerals of mullite with intermediate composition between sillimanite and 3/2-mullite were described, but either a significant concentration of Fe and Ti was present in the samples [194, 188] or artificial samples were synthesised at increased pressure [195]. Both cases are thus not part of the discussed phase diagram.

5.3.2 Turnover compositions of the block model

The unified superspace model explains the dependence of the ordering patterns in mullite on the composition. In § 4.4.1 the block model and a few special cases of the range

$0 \leq \delta \leq 0.5$ were analysed. For $\delta < 0.2$ with $n_V < 1$ some vacancy-free blocks merge together so that blocks consisting only of dicluster chains form. As mentioned in the last section, mullite with $\delta < 0.2$ only exists if further stabilisation mechanisms like the presence of impurities are present indicating that larger 'sillimanite-like' zones in the crystal structure are not stable. This is a possible explanation for δ_{low}. A very important composition of the unified SSM is $\delta = \frac{1}{3}$, which describes a layered structure instead of a block structure. Interestingly, this composition is not important at all for the description of the phase diagram and mullite with the corresponding composition (7/4-mullite, 63.6 mol% Al_2O_3) was described in the literature but it is clearly not a special composition with an outstanding stability or instability [196]. The unified superspace model and the orthorhombic stacking of blocks collapses if $\delta > 0.5$ because $\Delta_{\text{BW}}^{\text{O3a}} = \frac{1}{2} - \delta$ becomes negative (Tab. 4.16) corresponding to a negative number of diclusters (§ 4.4.1). Thus, 5/2-mullite ($\delta = 0.5$) is special because it describes the endmember of the block model. However, alternating block patterns can still be constructed. For example, an alternating pattern of VBs with $n_V = 2$ and $n_D = 1$ leads to a mullite with $\delta = \frac{4}{7}$ described in a $7\mathbf{a} \times 1\mathbf{b} \times 1\mathbf{c}$ block, that can be stacked in many different ways. A trivial orthorhombic stacking, however, leads in either case to the formation of tricluster chains, which can be limited to units of two stacked triclusters by choosing an appropriate monoclinic stacking. For $\delta > \frac{4}{7}$ neighbouring VBs merge in analogy to merging VFBs for $\delta < 0.2$. Hence, special cases of the block model coincide with the turnover compositions of δ_{low}, δ_{mono} and δ_{meta}. However, δ_{mono} seems to be not relevant for the phase diagram. Furthermore, the block model of 2/1-mullite does not seem to be an extraordinary member of the solid solution range. Hence, the stability of 2/1-mullite cannot be explained by block model.

5.3.3 Relative stability of ordered mullite

The total energies of the DFT calculations were analysed to investigate the solid solution range of mullite. It is not straight forward to compare the energies of different phases if the chemical composition is not identical. Therefore the total energy of a mullite superstructure was subtracted from a chemically identical system consisting of α-SiO_2 and α-Al_2O_3 (cf. Tables 3.6, 3.7 and 4.17). This approach allows to estimate the driving force to form mullite from α-SiO_2 and α-Al_2O_3. In Figure 5.11 this energy difference is plotted against the vacancy concentration. The main observation is that the stability of mullite decreases with increasing vacancy concentration. The energies of AS1 and AS2 are essentially identical, whereas AS3 is significantly less stable than AS1. However, all mullite superstructures as well as sillimanite and andalusite are energetically less stable than a corresponding mixture of α-SiO_2 and α-Al_2O_3. According to the DFT calculations the only compound that is more stable is kyanite.

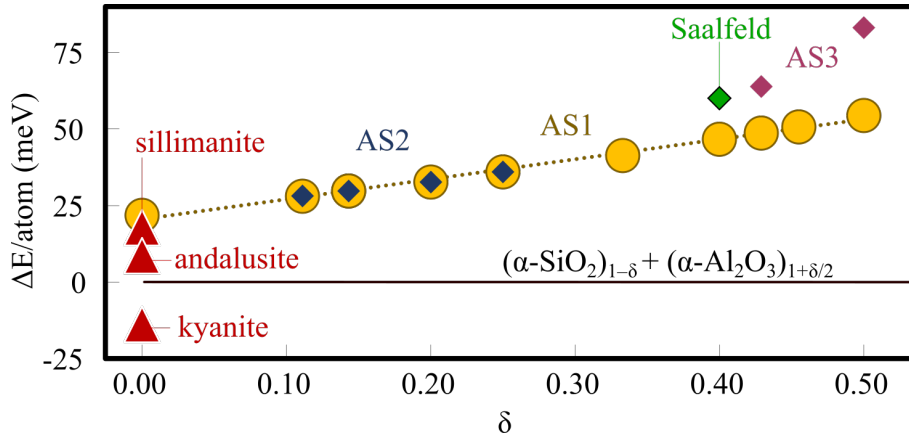The dependence of the relative stability of mullite superstructures with the ideal Si dis-

Figure 5.11: Comparison of total energies (PBEsol-D) of aluminium silicates with total energies of a chemically identical system made of α-SiO$_2$ and α-Al$_2$O$_3$. Energies of different Si distributions (AS1, AS2, AS3) are included. The energy of the good Saalfeld model analysed in § 5.1.3 is also included (green diamond). Energies of the Al$_2$SiO$_5$ polymorphs are given in § A.3.

tribution (AS1) linearly depends on the vacancy concentration and is independent of the block lengths. In fact, it seems that the vacancy distribution itself has a negligible effect on the total energy because M0 without any vacancies and M33 with a unique layer structure follow the same linear dependence as any other vacancy distribution in the analysed range. The decreased stability of Saalfeld's model (§ 5.1.3) relative to M40 AS1 is probably related to the presence of Al-Al diclusters or tricluster chains and less to the vacancy distribution itself. Consequently, the chemical composition and the Si distribution are considered to significatnly influence the stability of mullite.

The fact that at elevated temperatures the formation of mullite from SiO$_2$ and Al$_2$O$_3$ is observed indicates that the structural dynamics at the temperature of formation must play an important role. All simulations of this thesis described a static system, and thus we can only speculate about the structural dynamics that may play an important role. Independent of the temperature, the voids forming around vacancies are an essentially empty volume without an intrinsic equilibrium shape, in contrast to e.g. the AlO$_6$ octahedra. Hence, the presence of vacancies provides structural flexibility because the polyhedra network can relax and change the geometry of the vacancies. An example unit that makes use of this mechanism can be identified from the DFT calculations. The SiO$_4$ tetrahedra are probably the most rigid structural units in mullite (cf. § 1.2), which is supported by the observation that the volume of Si tetrahedra in Si-Si diclusters varies only between $2.296\,\text{Å}^3$ and $2.304\,\text{Å}^3$ in the range between M11 AS1 and M45 AS1. It can then be expected that the most rigid unit, i.e. Si-Si diclusters, are found in the most flexible environment. This is exactly what is observed: In the most stable mullite superstructures Si-Si diclusters are always sandwiched between two vacancies (§ 4.3.3, § 4.4.4).

This mechanism naturally depends on the concentration of vacancies and the temperat-

ure, but less on the distribution of vacancies. Based on the assumption, that for each temperature there is an ideal vacancy concentration that stabilises the mullite structure, the observed borders of the solid solution range may be explained. Mullite with $\delta < \delta_{\text{low}}$ does not form because the ideal vacancy concentrations correspond to a temperature that is lower than about 1000 °C and the kinetics of the atoms hinder the formation of mullite, at least at ambient pressure. With increasing temperature the mechanism stabilises higher vacancy concentrations until the melting point is reached. In this case, the alumina-rich border (δ_{high}) corresponds to the vacancy concentration that stabilises the mullite structure just below the melting point. Pressure decreases the flexibility of the system and counter-balances the identified mechanism leading to lower vacancy concentrations. This is in agreement with the experiments described in [195], in which it is concluded that at elevated pressures the miscibility gap between $0 < \delta < 0.2$ disappears. Although this stabilising mechanism based on the flexible geometry of vacancies may explain the borders of the solid solution range observed in the phase diagram, it should rather be considered as a potential starting point for further studies to better understand the stability and high temperature properties of mullite. Molecular dynamics simulations of disordered mullite structures seem to be a promising approach.

5.3.4   Driving force for order and disorder

Due to its outstanding properties there are numerous investigations of traditional and potential applications of mullite. In many of them a phase analysis is carried out with powder X-ray diffraction (pXRD) to confirm the presence of mullite. Some recent examples can be found in [197, 198, 199, 200]. The vast majority of investigations related to mullite have in common, that only main reflections are considered and in routine phase analysis with pXRD the satellite reflections and diffuse scattering are neither mentioned nor considered. This can be easily explained by the observation, that in pXRD measurements, including those of § 3.3.1, satellite reflections are not observed. Large inclusion-free single crystals grown with the Czochralski method only show first order satellite reflections and diffuse scattering [6]. Natural samples of mullite usually exhibit lower vacancy concentrations around $\delta \approx 0.25$, but so far it was not reported that any mineral sample was ordered [39, 49, 2]. It seems that under equilibrium conditions of formation mullite can be highly crystalline, but with a disordered vacancy and Si distribution. On the other hand, many structural studies reported on ordered mullites with high order satellite reflections (§ 5.2.2). The models developed in this thesis are capable to describe the crystal structure of mullite for different compositions and degrees of order, but they cannot explain why mullite is mostly disordered and what is the underlying driving force. A full investigation of this question is outside the scope of this chapter, but an answer that is at least consistent with the presented results shall be sketched here.

One of the most important findings of the detailed symmetry analysis and the dependence of the modulation on the composition is expressed by Equation 4.2: $\alpha = \frac{1-\delta}{2}$. This relationship emerges from the ordered SSM if tricluster chains are avoided and it agrees very well with experimental observation of the $\mathbf{q}$–δ relationship (§ 4.4.3). However, the vast majority of these samples is only little ordered, but the avoidance of tricluster chains is also crucial for the short-range order in disordered mullite according to preliminary simulations of the diffuse scattering (§ 5.2.3), which explains why the satellite reflections follow Equation 4.2 independent of the degree of ordering. The formation of ordered mullite requires that triclusters concentrate in vacancy blocks with a well-defined length and are not present in vacancy-free blocks. However, the DFT calculations indicate that the energetic difference between different vacancy distributions is probably negligible and that the Si distribution has a stronger influence on the stability (§ 4.3.3, § 5.1.3, § 4.4.6). On the other hand, a disordered distribution of Si on the tetrahedral sites may be stabilised by the structural flexibility of the vacancies, thus leading to a disordered mullite structure. Many possible configurations with similar energies are likely to lead to a disordered structure, especially if the structure crystallises at high temperatures. The comparison of the ordered SSM and the disordered SSM has shown that the tricluster distribution and the Si distribution follow the same ordering mechanisms (§ 5.2.1). From that it can be derived, that the requirements by triclusters and diclusters can be sufficiently fulfilled in a short-range ordered manner, like the avoidance of tricluster chains or Si-Si diclusters in the vicinity of vacancies. Ordered mullite probably only forms on the length scale of a few unit cells or not at all. Thus, the interactions defining the Al/Si ordering in the structure and the tricluster distribution determine the crystal structure of mullite during formation.

Chapter 6

Summary and outlook

6.1 Summary

This thesis was motivated by the observation that the satellite reflections on diffraction patterns of different mullite samples show remarkable differences concerning the respective modulation wave vector, highest observable reflection order and sharpness. These aspects were separately analysed over the last decades, but a model that fundamentally describes a consistent crystal structure was not developed.

For this thesis the symmetry of mullite was analysed in detail using the superspace approach. The combination of crystal chemical constraints on the polyhedra environment of vacancies with the symmetry operators of the superspace group $Pbam(\alpha0\frac{1}{2})0ss$ leads to a small set of possible vacancy distributions for a certain chemical composition and a respective modulation wave vector $\mathbf{q}$. On this basis constraints for the description of the mullite crystal structure in superspace were derived.

Four single crystalline samples were measured with synchrotron radiation. The refinement of superspace models based on harmonic occupational modulation functions confirm the constraint scheme from the symmetry analysis and indicate that the samples are mainly disordered. However, different samples exhibit different modulation amplitudes, which is interpreted in terms of different degrees of order. Although a completely ordered sample was not available, a structural model representing the highest degree of order based on block wave modulation functions to describe the occupancy was developed. Its analysis allowed to define a general vacancy distribution pattern which agrees with the experimentally observed dependence of $\mathbf{q} = (\alpha\,0\,\frac{1}{2})$ on the vacancy concentration δ. This dependence was investigated based on electron diffraction measurements and the refinement of average structure models, which confirmed that the modulation follows the relationship $\alpha = \frac{1-\delta}{2}$. This equation emerges if the stacking of tricluster units is avoided. This unified superspace model describes the ordered vacancy distribution in the composition range $0 \leq \delta \leq 0.5$.

The ordering of Al and Si on the tetrahedral sites could not be determined from the symmetry analysis or the refinements. Nevertheless, harmonic occupational modulation functions describing Al/Si ordering on the T site were derived from the modulated volume of the tetrahedra leading to a consistent structure model. In addition to that, the Si distribution was investigated systematically with force field calculations. For several commensurate cases of the unified superspace model in the range $0 \leq \delta \leq 0.5$, all symmetry compliant Al/Si permutations were investigated with force field calculations. Promising structures were then investigated with DFT calculations. The most stable structure model of each composition was embedded in superspace leading to a unified superspace description that accounts for vacancy ordering and Al/Si ordering as well.

The comparison of different models indicated that the ordering mechanisms accounting for Al/Si ordering, displacive modulations and vacancy ordering are the same independent of the degree of order. The analysis of the diffuse scattering emphasises the importance

of tricluster ordering, which was also identified as the key mechanism to understand and describe the unified superspace model.

6.2   Conclusion

"The starting structure of mullite is obtained from the sillimanite structure by removing randomly chosen O^{2-} ions from Oc crystallographic positions, replacing randomly chosen Si^{4+} with Al^{3+} ions for each O^{2-} ion removed, and randomly distribution the remaining tetrahedrally coordinated cations."
Daniel J. Lacks, Bernd Hildmann & Hartmut Schneider (2005)

"The mullite structure was constructed by randomly removing oxygen vacancies at the Oc sites and randomly replacing Si by Al in the supercell."
Jen-Chang Chen *et alii* (2008)

"O vacancies were created by removing some O atoms that were close together [...]"
Sitaram Aryal, Paul Rulis & Wai-Yim Ching (2012)

"[...] removing random O atoms from the Oc positions and replacing two random Si atoms with two Al [...]"
Esmaeil Adabifiroozjaei *et alii* (2018)

Structural models of the last decades were usually accepted as valid descriptions of the crystal structure, but they were mostly not refined or considered for further analysis. This becomes evident by analysing the literature of computational studies on mullite applying molecular dynamics or DFT. Without exception, model crystals were generated by randomly distributing vacancies [157, 158, 201, 202, 159, 203]. In some cases the presence of Si in triclusters was avoided and constraints originating from the supercell size were considered, but the results of antecedent models like those described and discussed in § 1.3 and § 5.1 or constraints by superspace symmetry were not implemented in the mentioned computational studies. The advantage of the models developed in this thesis is the more accurate representation of the crystal structure and their capability to fundamentally understand and describe different ordering phenomena in mullite accounting for Al/Si ordering and vacancy ordering. The atomic structure of the most ordered state was precisely defined and a small set of local rules describing disordered mullite was established. Thus, the models can be easily applied in further studies on the structure and its properties. The ordering mechanisms were investigated with different approaches leading to a consistent overall picture. The DFT calculations of Chapter 4 demonstrate

the usefulness of computational methods to characterise the structure of mullite in detail. The used approach to develop superspace models from *ab initio* methods is a pioneering method that was never applied before. Its application enables the investigation of structural details of modulated and/or disordered structures that are difficult to access experimentally, for example the Al/Si ordering in minerals or the energetic and structural analysis of transition states.

The search for publications that contain the words 'mullite' and 'vacancy' in the title scores twelve hits. If the keyword 'vacancy' is replaced by 'tricluster' there are no hits in the database of 'Web of Science' (Clarivate Analytics) and one hit with 'Google Scholar' [204]. This suggests that the investigation of the crystal structure of mullite from the beginning on focused on the characterisation of the vacancies[1]. The unified superspace model, the DFT calculations and the analysis of the diffuse scattering jointly emphasise the importance of triclusters. The vacancies are appropriate and useful to describe the polyhedra network in mullite, but the understanding of the aperiodic nature of mullite requires to shift the focus to the triclusters embracing them.

---

[1]Fun fact: Two journal publications and two conference contributions presented by Paul B. Klar *et al.* contain the word 'vacancy'. The word 'tricluster' was not considered in their titles.

6.3   Outlook

6.3.1   Mineral classification and Al/Si order

The mineral classification of silicates is based on the polyhedra network formed by SiO_4 tetrahedra. In the current classification of Nickel–Strunz and Dana, the mineral mullite is classified as a nesosilicate with insular SiO_4 units [205, 206]. Pauling's rules predict that the bridging O3 site prefers Si-Si dicluster (§ 1.2) and it is highly unlikely that Si-Si diclusters are systematically avoided in mullite. The models of this thesis clearly favour the presence of Si-Si diclusters alongside Al-Si diclusters and, to a lesser extent, Al-Al-Si triclusters. From the DFT calculations it was derived that Si-Si diclusters are a main component of mullites with a vacancy concentration $\delta < 0.5$ including the case of 3/2-mullite, which is commonly assumed to represent the mineral composition [24, 1]. If isolated SiO_4 tetrahedra are present alongside Si_2O_7 units, then mullite is a sorosilicate and not a nesosilicate. In this case mullite should be classified in Dana class 58 (instead of 52) and Nickel–Strunz class 09.BF (instead of 09.AF). Furthermore, mullite is in the sillimanite subgroup 52.02.02a in the classification of Dana. Although there is a clear structural relationship with sillimanite, there is a similar relationship with andalusite, which in addition contains voids with a very similar geometry to the vacancy voids in mullite (Fig. 1.2). Therefore, the classification in the sillimanite subgroup has an ambiguous character, which would be corrected by the suggested reclassification. Future work on the Si distribution in andalusite, sillimanite, sillimullite and mullite should be able to classify the nature of Al/Si ordering in these minerals and their relationship.

6.3.2   Details of the crystal structure

The developed models are complete in the sense that they describe the polyhedra distribution and Si distribution for ordered and disordered mullite. Nevertheless, some details are not satisfactorily described. The experimentally observed $\mathbf{q}$–δ relationship agrees with Equation 4.2 within the standard uncertainty. Nevertheless, a systematic offset could not be fully excluded. For example, the short-range order might affect the periodicity of the modulation. Furthermore, the predicted α for 5/2-mullite is 0.25, but the measurements with a composition close to $\delta = 0.5$ indicate that α adopts values around 0.28. High resolution diffraction experiments combined with accurate measurements of the chemical composition with ordered and disordered samples in the range $0.45 < \delta < 0.55$ could clarify the mentioned questions.

The simulations of the diffuse scattering in § 5.2.3 qualitatively show the most essential features observed in measured diffraction patterns, but the intensity distribution is not satisfactory. Especially the diffuse maxima that were described by $\mathbf{q}_2$ and $\mathbf{q}_3$ in § 4.1.1 and

§ 5.1.5 are completely missing in the simulations. Birkenstock *et al.* (2015) assumed that they originate, like $\mathbf{q}_1$, from a soft occupational modulation. The fact that the maxima lie on the diffuse streaks which originate from the interaction between triclusters, suggests that these diffuse maxima might originate from mid-range ordering of triclusters. The DFT calculations revealed that the Si atoms in triclusters are less stable than the Si atoms in the diclusters (Fig. 4.16). This clue might be the starting point for an explanation of $\mathbf{q}_2$ and $\mathbf{q}_3$. If large single crystals of ordered mullite samples could be obtained, then neutron diffraction measurements are a promising technique for an experimental characterisation of the details of the Si distribution. Independent of that, the models of this thesis may serve as a good starting point for spectroscopic studies to verify the suggested models by means of other experimental techniques.

6.3.3 Al-rich mullite in superspace

This thesis focused on the composition range $0 \leq \delta \leq 0.5$. Structural models of monoclinic mullites with $\delta > 0.5$ and $\gamma \neq \frac{1}{2}$ were not presented. In comparison to orthorhombic mullite the modulation wave vector changes slightly the direction, indicating that the underlying superspace model is similar. It can be assumed that the description of the unified superspace model can be extended to vacancy concentrations $0.5 < \delta$ by applying minor changes to the constraint schemes presented in Chapter 4. The most ordered state can then be described by a set of three unified superspace models (Fig. 6.1). The first corresponds to the unified SSM developed in this thesis (Chapter 4). The second, for which α and γ seem to be constant, describes a monoclinic distribution of diclusters and triclusters in the range $0.5 < \delta \leq \frac{2}{3}$ and the third unified superspace model in the range $\frac{2}{3} \leq \delta \leq 1$ describes a monoclinic distribution of triclusters and tetraclusters. If the ordering mechanisms of triclusters in the first unified superspace model are also valid for tetraclusters, then a similar dependence of δ on α can be expected. A shift of Equation 4.2 so that $\alpha = \frac{7}{12} - \frac{\delta}{2}$ nicely agrees with experimental observations [18, 51] as shown in Figure 6.1. Preliminary DFT calculations of mullite structures with $\delta = \frac{2}{3}$ ($3 \times 1 \times 2$, $Pnam$) and $\delta = \frac{5}{6} \approx 0.83$ ($6 \times 1 \times 2$, $B11\frac{2}{m}$) indicate that ordered structure models are stable (Fig. 6.2). The latter model exemplifies a member of the third unified superspace model consisting of 'tricluster blocks' and 'tetracluster blocks'. These predictions require a deeper analysis of the symmetry and more experimental work on the synthesis and structural characterisation. Independent of that, the synthesis parameters that determine the resulting degree of order seem to be not understood at all. This is one major challenge for the experimental investigation of the aperiodic nature of mullite in the future.
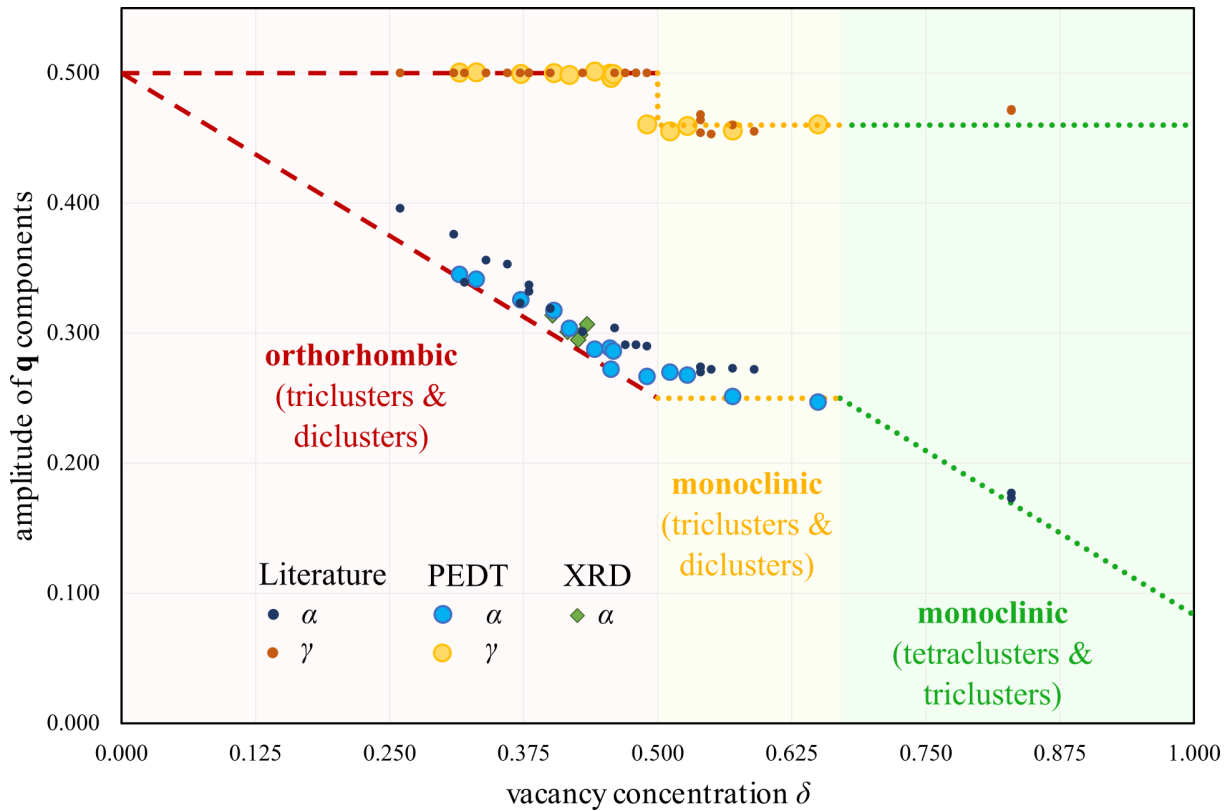
Figure 6.1: Extended $\mathbf{q}$–δ relationship based on experimental observations (cf. Fig. 4.19) and predicted ranges for three unified superspace models to describe the full composition range $0 \leq \delta \leq 1$.
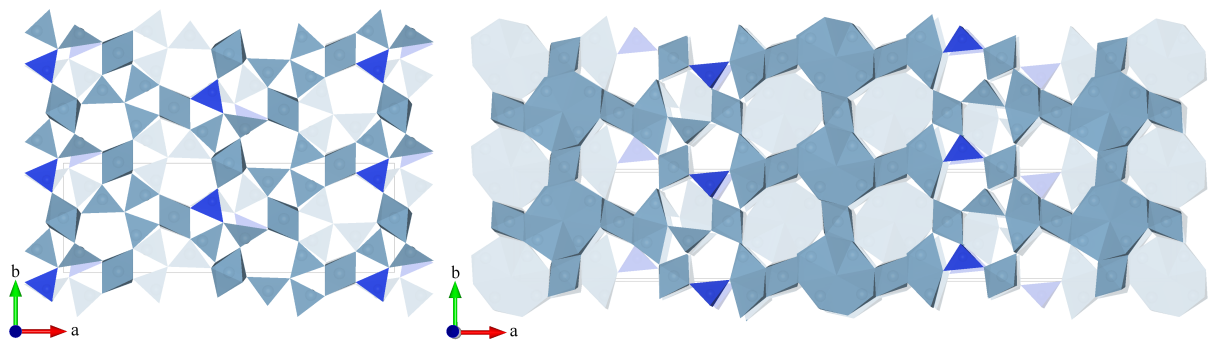

Figure 6.2: Geometrically optimised superstructures of 4/1-mullte (left, $\delta = \frac{2}{3}$) and 17/2-mullite (right, $\delta = \frac{5}{6}$). Note that a similar vacancy distribution for 4/1-mullite was already suggested in [53]. According to the experimentally observed $\mathbf{q}$–δ relationship for $\delta > 0.5$ the value of γ is constant around $0.46 \approx \frac{6}{13}$ suggesting that a 13-fold repeating unit along the c direction is required for more representative simulations.

Appendix A

Supplements

A.1   Literature survey: q–δ relationship

Several studies published diffraction patterns of mullite with visible satellite reflections. In many cases the composition was determined or estimated, but the modulation wave vector **q** was not determined. To make use of this wealth of studies using different samples of different compositions, **q** was determined by putting a grid on published figures and extract relevant coordinates for several data points using the tool 'DataThief III' [209]. This is straight forward in the case of single crystal diffraction patterns: The indexation of a diffraction pattern and the coordinates of the satellite reflections allows to determine the average values of α and γ. This approach was checked based on the samples 'Forster', '1' and '58480' as the respective diffraction patterns were published (Fig. 3 in [2]) alongside a plot of α against the chemical composition (Fig. 4 in [2]), which indicated that from the diffractograms the modulation wave vector **q** can be determined with sufficient accuracy. This approach is also confirmed by the agreement between the determination of the modulation wave vector of sample '5' based on two independent studies [2, 180]. A single crystal X-ray diffraction study of the same sample '5' published the modulation wave vector to be $\mathbf{q} = (0.30\,0\,0.5)$, which is in agreement with the values given in Table A.1 within the standard uncertainty. The results of the overall literature survey are listed chronologically in Table A.1. If the vacancy concentration is marked with a question mark (?) the uncertainty of the provided composition could not be evaluated. Either no information on how the composition was determined could be found or the composition was derived from the mullite label, but for example 2/1-mullite must not necessarily correspond to a vacancy concentration of exactly 0.4 as described in § 1.1.6.

In one case the modulation wave vector **q** could be determined from a powder diffractogram. Kriven & Pask (1983) mentioned extra reflections that could not be indexed with the average unit cell of mullite or any other phase and were expected to be satellite reflections, although the corresponding modulation wave vector was not determined [47].

δ	α	γ	Fitted satellites	Sample	Fig. type	Reference
0.38	0.348 (10)	0.5	4	58480	EDP	Fig. 3c in [2]
0.43	0.299 (10)	0.5	9	Forster	EDP	Fig. 3d in [2]
0.49	0.292 (7)	0.5	11	1	EDP	Fig. 3e in [2]
0.57	0.273 (6)	0.460 (6)	11	Q1	EDP	Fig. 3f in [2]
0.59	0.272 (6)	0.455 (4)	11	Q2	EDP	Fig. 3g in[2]
0.26	0.396	–	–	10	plot	Fig. 4 in [2]
0.31 (?)	0.376	–	–	Rα	plot	Fig. 4 in [2]
0.32	0.339	–	–	9	plot	Fig. 4 in [2]
0.34	0.356	–	–	7	plot	Fig. 4 in [2]
0.36 (?)	0.353	–	–	Rβ	plot	Fig. 4 in [2]
0.38	0.337	–	–	6	plot	Fig. 4 in [2]
0.38	0.332	–	–	58480	plot	Fig. 4 in [2]
0.40	0.319	–	–	5	plot	Fig. 4 in [2]
0.43	0.301	–	–	Forster	plot	Fig. 4 in [2]
0.46	0.304	–	–	3	plot	Fig. 4 in [2]
0.47	0.291	–	–	2	plot	Fig. 4 in [2]
0.49	0.290	–	–	1	plot	Fig. 4 in [2]
0.372	0.323 (18)	0.5	10		sXRD	Fig. 1 in [207]
0.55	0.272 (4)	0.453 (5)	11		EDP	Fig. 1a in [50]
0.54	0.274 (4)	0.464 (3)	11		EDP	Fig. 2 in [36]
0.48	0.291 (3)	0.5	11		EDP	Fig. 3 in [36]
0.54	0.274 (10)	0.468 (3)	2		pXRD	Fig. 6 in [47]
0.54	0.27 (3)	0.454 (4)	9		EDP	Fig. 2 in [47]
0.4 (?)	0.32 (2)	0.5	7		EDP	Fig. 13a in [208]
0.25 (?)	0.362 (13)	0.5	5		EDP	Fig. 13b in [208]
0.4 (?)	0.315 (10)	0.5	11	5	sXRD	Fig. 4 in [180]
0.5 (?)	0.292 (11)	0.5	26		EDP	Fig. 6a in [186]
0.4 (?)	0.301 (14)	0.5	11		sXRD	Fig. 4 in [4]
0.83	0.177 (7)	0.471 (4)	11		EDP	Fig. 1.1.15 in [18]
0.83	0.173 (9)	0.472 (4)	11		EDP	Fig. 2d in [51]

Table A.1: Dependence of $\mathbf{q} = (\alpha\,0\,\gamma)$ on the composition as reported in the literature. If the vacancy concentration is marked with a question mark (?) the provided composition is rather considered as an estimate. The fourth column refers to how many satellites were used to determine $\mathbf{q}$. The list is chronologically ordered.
EDP = electron diffraction pattern, sXRD = single crystal X-ray diffraction pattern, pXRD = powder X-ray diffraction pattern

According to the description in the reference the diffraction pattern was obtained with a Debye-Scherrer camera using a ground mullite sample with 82.5 wt% Al_2O_3. The lattice parameters were determined and are given in the reference, but the diffraction angles of the two clearly visible extra reflections as well as the X-ray wavelength were not given. Fortunately a Si standard was mixed to the sample. Diffraction angles 2θ were extracted with DataThief III from Figure 6 in [47]. The Si lines are present at diffraction angles corresponding to a wavelength of 1.94 Å, which is the wavelength of the K_α line of Fe. The extracted 2θ values of two additional reflections are 23.1° and 26.0° corresponding to lattice spacings d of 4.84 Å and 4.31 Å, respectively. A consistent explanation of these lines is possible using the superspace formalism with $\mathbf{q} = (0.2740, 0, 0.4677)$ and an indexation as satellite reflections with indices $101\bar{1}$ and 1001, respectively. Assuming that the uncertainty of the extracted angles is about 0.1°, the components of $\mathbf{q}$ are determined to be $\alpha = 0.274\,(10)$ and $\gamma = 0.468\,(3)$.

A.2 VASP and GULP input parameters

An example INCAR file used for DFT calculations with VASP is shown in the following box. Calculations based on this input file are labelled PBEsol-D.

```
Title:  Push the button.
 IBRION = 1      # Geometric optimisation with quasi-Newton algorithm
 ISIF = 3        # Optimise atom coordinates and cell parameters
 GGA = PS        # Perdew-Burke-Ernzerhof functional optimised for solids
 IVDW = 11       # Dispersion correction, DFT-D3 method of Grimme (2006)
 ENCUT = 520 eV  # energy cut-off of plane wave basis
 LREAL = AUTO    # Non-local parts of pseudopotentials in real space
 ISMEAR = 0      # Gaussian smearing of orbital occupancies
 SIGMA = 0.05    # Parameter for Gaussian smearing
 EDIFF = 1E-4    # Electronic relaxation convergence criterion
 EDIFFG = -0.01  # Ionic relaxation convergence criterion
```

Running the GULP input file shown in the following box geometrically optimises the structure as described in § 2.5.2.

```
# GULP 4.3.5 (85306 ideas to relax)
optim happiness #alternative:  rfo dfp or fbfgs
title
    Sillimanite
end
cell
    7.519278 7.535828 5.769490 90.0 90.0 90.0 1 1 1 0 0 0
fractional
Al1 core 0.000000 0.000000 0.000000 0.0 1.0 0.0 0 0 0
Al2 core 0.137970 0.330297 0.250000 0.0 1.0 0.0 1 1 1
Si1 core 0.652848 0.166073 0.250000 0.0 1.0 0.0 1 1 1
O11 core 0.856987 0.093914 0.250000 0.0 1.0 0.0 1 1 1
O12 core 0.350500 0.421611 0.250000 0.0 1.0 0.0 1 1 1
O2  core 0.624259 0.282287 0.014575 0.0 1.0 0.0 1 1 1
O3  core 0.980951 0.498031 0.250000 0.0 1.0 0.0 1 1 1
space # space group Pbnm
P b n m
species
Al 1.4175
Si 1.8900
O -0.9450
buckingham
Al core Al core 31570400.0 0.068 14.0507 0.0 10.00 1 0 0
Al core Si core 731927000.0 0.057 18.8132 0.0 10.00 1 0 0
Al core O  core 28476.4 0.172 34.5773 0.0 10.00 1 0 0
Si core Si core 79935500000.0 0.046 25.1898 0.0 10.00 1 0 0
Si core O  core 50196.9 0.161 46.2972 0.0 10.00 1 0 0
O  core O  core 6462.56 0.276 85.0910 0.0 10.00 1 0 0
maxcyc opt 200 #42
output cif Sillimanite_gulp.cif
```

A.3 DFT calculations of sillimanite, andalusite and kyanite

Distances in the following tables are given in units of Å.

Functional	a (Å)	b (Å)	c (Å)	V (Å^3)	d(Al^{VI}–O)	d(Al^{IV}–O)	d(Si^{IV}–O)	E (eV)
PBE	7.5718	7.7762	5.8167	342.49	1.933	1.777	1.643	−244.624
PBE-D	7.5428	7.7329	5.8003	338.32	1.924	1.771	1.639	−248.686
PBEsol	7.5164	7.6949	5.7894	334.85	1.915	1.768	1.636	−255.602
PBEsol-D	7.4917	7.6597	5.7755	331.42	1.908	1.764	1.6331	−258.846
Experimental single crystal XRD references:								
0.0001 GPa [187]	7.48388 (17)	7.6726 (3)	5.76807 (13)	331.21 (2)	1.91	1.76	1.62	
25 °C [160]	7.4883 (7)	7.6808 (7)	5.7774 (5)	332.29 (5)	1.912	1.763	1.627	
Antecedent calculations:								
PBE [183]	7.4474	7.6014	5.7469	325.34				
PBE [201]	7.557	7.768	5.811	341.11				−246.026
PBE [166]	7.5678	7. 7694	5.8453	343.69	1.934	1.782	1.651	
PBEsol [166]	7.5061	7.6823	5.8159	335.37	1.916	1.773	1.642	
PBE0 [166]	7.4931	7.6791	5.7910	333.22	1.914	1.765	1.633	

Table A.2: Comparison of calculated and reported structure parameters of sillimanite.

Functional	a (Å)	b (Å)	c (Å)	V (Å^3)	d(Al^{VI}–O)	d(Al^{V}–O)	d(Si^{IV}–O)	E (eV)
PBE	7.8812	7.9817	5.6129	353.08	1.954	1.853	1.648	−244.866
PBE-D	7.8273	7.9459	5.5965	348.08	1.945	1.846	1.644	−248.646
PBEsol	7.8010	7.9205	5.5830	344.96	1.936	1.840	1.642	−256.085
PBEsol-D	7.7578	7.8917	5.5701	341.01	1.928	1.833	1.639	−259.137
Experimental single crystal XRD references:								
0.0001 GPa [187]	7.7930 (3)	7.89734 (17)	5.55583 (14)	341.93 (2)	1.93	1.84	1.63	
25 °C [160]	7.7980 (7)	7.9031 (10)	5.5566 (5)	342.45 (6)	1.935	1.836	1.631	
Antecedent calculations:								
PBE [166]	7.8757	7.9963	5.6311	354.63	1.9547	1.8554	1.6556	
PBEsol [166]	7.798	7.9343	5.599	346.42	1.9367	1.8414	1.6486	
PBE0 [166]	7.7935	7.9098	5.5733	343.57	1.9337	1.8374	1.6386	

Table A.3: Comparison of calculated and reported structure parameters of andalusite

Functional	a (Å)	b (Å)	c (Å)	V (Å^3)	α (°)	β (°)	γ (°)	E (eV)
PBE	7.2035	7.9341	5.6355	303.32	89.90	101.13	106.01	−244.24
PBE-D	7.1695	7.8956	5.6044	298.82	89.96	101.10	105.98	−248.86
PBEsol	7.1438	7.8785	5.5877	296.16	90.00	101.11	106.01	−256.12
PBEsol-D	7.1169	7.8471	5.5636	292.65	90.05	101.08	105.99	−259.86
Experimental single crystal XRD references:								
0.001 kbar [210]	7.124 (2)	7.856 (2)	5.577 (2)	293.3 (3)	89.99 (2)	101.15 (2)	105.95 (2)	
25 °C [160]	7.1262 (12)	7.8520 (10)	5.5724 (10)	293.60 (9)	89.99 (2)	101.11 (2)	106.03 (1)	
Antecedent calculations:								
PBE [166]	7.2092	7.9502	5.6516	305.00	89.95	101.14	106.02	
PBEsol [166]	7.143	7.8881	5.6012	297.17	90.06	101.12	106.01	
PBE0 [166]	7.1279	7.8635	5.5868	294.86	89.99	101.14	106.01	

Table A.4: Comparison of calculated and reported structure parameters of kyanite. Here, α, β and γ are the angles of the lattice parameters.

A.4 Exclusion of tetragonal symmetry

The lattice parameters a and b are of similar length and in the space group *Pbam* along both directions a 2_1 screw axis is perpendicular to a glide plane. It was therefore suspected that the symmetry of mullite samples, for which an equal length of a and b is observed, might be tetragonal [211]. In tetragonal systems the directions a and b are equivalent and therefore reflection pairs $hk0$ and $kh0$ are symmetrically equivalent. In powder diffraction patterns it is easy to see that the corresponding intensities are clearly different. For example in Figure 3.2a the reflection 210 is weaker than 120 observed at 26.0° and 26.2°, respectively. This indicates that the adaptation of the orthorhombic structure to tetragonal symmetry requires a strong deformation and it is not likely that this deformation is induced by changing the composition. The streak pattern of the diffuse scattering is approximately diamond shaped in mullite, but again the intensity distribution is not in agreement with tetragonal symmetry. A four-fold rotation axis requires that for any satellite reflection with indices $hk\ell m$ with $\mathbf{q}_1 = (\alpha\,0\,\gamma)$ there is a satellite reflection $kh\ell m$ with $\mathbf{q}_2 = (0\,\alpha\,\gamma)$. This was never observed experimentally. Due to these observations tetragonal symmetry was not considered for further investigation in this thesis. The crystal structure of 9/1-mullite and other high aluminous mullites also suggest that tetragonal mullite does not exist [53, 143].

A.5 Equivalent settings of $Pbam(\alpha 0\frac{1}{2})0ss$

Different settings allow an equivalent description of the crystal structure of mullite. $\mathbf{q}$ may be defined so that $\alpha' = 1 - \alpha$, a different origin may be chosen or the rational component of $\mathbf{q}$ may be removed by setting $\gamma = 0$ in a supercell description. Depending on these choices there are eight possible superspace groups (Tab. A.5). All of them can be derived from the superspace group $Pcma(0\frac{1}{2}\gamma)000$ which is the superspace group with number 55.1.10.6 in the tables generated by Stokes *et al.* (2011) [212] and number 55.6 in the International Tables Volume C [72]. The superspace group identifier 55.1.10.6 is composed of four numbers. The first refers to the number of the space group (55, *Pbam*), the second defines that there is one additional dimension, the third is the number identifying the tenth (3+1)d Bravais class, which is $Pmmm(0\frac{1}{2}\gamma)$, and the last number refers to the sixth entry in the list of possible superspace groups with the respective Bravais class.

The vast majority of structural investigations on mullite place the octahedral Al1 site at the origin and the other atoms are placed so that the longest axis of the octahedra at the origin is approximately parallel to the direction [120]. Furthermore, the modulation wave vectors was always described with $\alpha < 0.4$. This setting corresponds to $Pbam(\alpha 0\frac{1}{2})0ss$ or $Xbam(\alpha 00)0ss$.

Superspace group	q	origin shift	basic cell size	centring
$Pbam(\alpha0\frac{1}{2})0ss$	$(\alpha \quad 0 \quad \frac{1}{2})$	$(0,0,0,0)$	$1 \times 1 \times 1$	–
$Pbam(\alpha0\frac{1}{2})0s0$	$(\alpha \quad 0 \quad \frac{1}{2})$	$(0,0,\frac{1}{2},0)$	$1 \times 1 \times 1$	–
$Pbam(\alpha0\frac{1}{2})00s$	$(1-\alpha \quad 0 \quad \frac{1}{2})$	$(0,0,0,0)$	$1 \times 1 \times 1$	–
$Pbam(\alpha0\frac{1}{2})000$	$(1-\alpha \quad 0 \quad \frac{1}{2})$	$(0,0,\frac{1}{2},0)$	$1 \times 1 \times 1$	–
$Xbam(\alpha00)0ss$	$(\alpha \quad 0 \quad 0)$	$(0,0,0,\frac{1}{4})$	$1 \times 1 \times 2$	$X = (0,0,\frac{1}{2},\frac{1}{2})$
$Xbam(\alpha00)0s0$	$(\alpha \quad 0 \quad 0)$	$(0,0,\frac{1}{4},0)$	$1 \times 1 \times 2$	$X = (0,0,\frac{1}{2},\frac{1}{2})$
$Xbam(\alpha00)00s$	$(1-\alpha \quad 0 \quad 0)$	$(0,0,0,\frac{1}{4})$	$1 \times 1 \times 2$	$X = (0,0,\frac{1}{2},\frac{1}{2})$
$Xbam(\alpha00)000$	$(1-\alpha \quad 0 \quad 0)$	$(0,0,\frac{1}{4},0)$	$1 \times 1 \times 2$	$X = (0,0,\frac{1}{2},\frac{1}{2})$

Table A.5: Equivalent superspace group settings of $Pbam(\alpha0\frac{1}{2})0ss$. The origin shift is expressed with respect to the basic cell size.
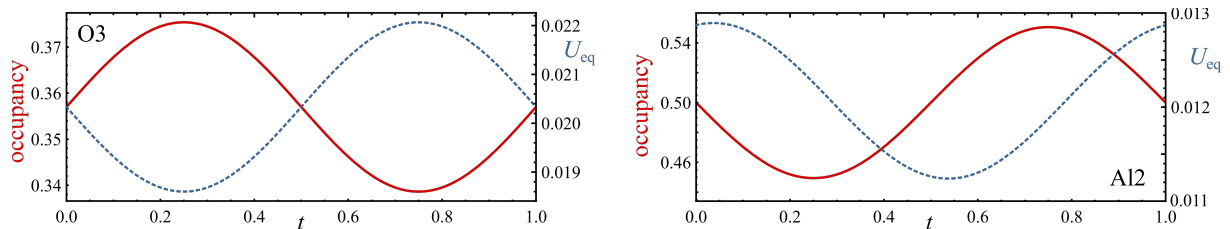
Figure A.1: Occupational modulation and modulation of equivalent isotropic displacement parameter $U_{eq}(t)$ (in units of Å^2) of O3 and Al2 based on the refinement of the disordered SSM (SA1).

A.6 Phase relationship between occupational and ADP modulation

A comparison of the ADP modulation and the occupational modulation of O3 shows a clear antiphase correlation (Fig. A.1). Symmetry restrictions force that the phase shift is either 0 or π. However, these restrictions do not hold for Al3 and O4, for which the same antiphase relationship is observed. Only in the case of Al2 a different phase relationship is observed (Fig. A.1). This was not further analysed in the thesis and is shown here for the interested reader.

A.7 Al/Si ordering of M25 #1 in superspace

The Al/Si ordering of M25 #1 is slightly different from the other ideal Al/Si ordering patterns of M40 and M50 due to the altered orientation of Al-Si diclusters. In superspace six block wave functions are necessary to describe the occupational modulation of Al2 and Si2 (Fig. A.2).
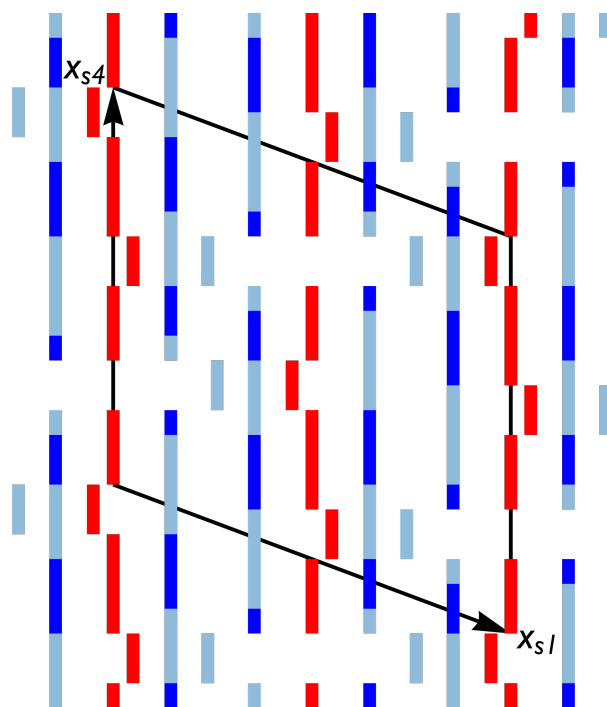
Figure A.2: Section of superspace model that describes the Al/Si ordering of M25 #1.

A.8 Lack of ordered samples

Unfortunately, there were no ordered samples available for this thesis. A personal communication with Dr. Georg Bednorz and Dr. Yuha Ylä-Jääski with respect to their TEM study on ordered mullite [36] allows the conclusion, that samples usually exhibit different degrees of order. Most of their samples did not show high order satellite reflections. The sample, from which the diffraction patterns in Figure 5.5 were obtained, was grown with a floating zone apparatus equipped with a halogen lamp. Dr. Daniel Salazar from 'BCMaterials' in Leioa, Spain, kindly carried out crystal growth experiments with the floating zone technique, but so far ordered samples could not be obtained and their analysis was not included in this thesis. Other approaches to obtain highly ordered samples, or samples that show at least third order satellite reflections, failed. Due to the lack of ordered crystals all experiments in this thesis were based on mainly disordered samples.

A.9 CIF files

CIF files (Crystallographic Information Framework) of the refinements of § 4.2.5 can be found in the 'Supporting information' of the following publication: Paul B. Klar, Iñigo Etxebarria & Gotzon Madariaga (2018). 'Exploiting superspace to clarify vacancy and Al/Si ordering in mullite'. *IUCrJ* **5**, 497–509 (*https://doi.org/10.1107/S2052252518007467*). The online version of the article can be found by searching 'IUCrJ Klar exploiting superspace mullite'.

List of Tables

List of Figures

Publications and Scientific Activities

Articles

- Paul B. Klar, Noelia de la Pinta, Gabriel A. Lopez, Iñigo Etxebarria, Tomasz Breczweski & Gotzon Madariaga (2017).
  'Ordered vacancy distribution in mullite: A superspace model'.
  Acta Crystallographica Section B: Structural Science, Crystal Engineering and Materials **73**, 377–388

- Paul B. Klar, Iñigo Etxebarria & Gotzon Madariaga (2018).
  'Exploiting superspace to clarify vacancy and Al/Si ordering in mullite'.
  IUCrJ **5**, 497–509

- Paul B. Klar, Iñigo Etxebarria & Gotzon Madariaga (2018).
  'Characterizing modulated structures with first-principles calculations: A unified superspace scheme of ordering in mullite'.
  Acta Crystallographica Section A: Advances and Foundations, submitted.

Conferences and meetings

- IV Meeting of the Italian and Spanish Crystallographic Associations (June 2016)
  'Vacancy ordering in Mullite – A superspace model'
  oral presentation (30 minutes) and poster presentation in Puerto de la Cruz, Tenerife, Spain
  Award: Panalytical Poster Prize

- I Jornadas Doctorales de la UPV/EHU (July 2016)
  'Vacancy ordering in Mullite – A superspace model'
  oral presentation (5 minutes) and poster presentation in Bilbao, Spain
  Award: Best Oral Presentation in the Category 'Experimental Sciences'

- 25th Annual Meeting of the German Crystallographic Society (March 2017)
  'Maximum vacancy ordering in mullite'
  oral presentation (5 minutes) and poster presentation in Karlsruhe, Germany
  Proceeding published in *Zeitschrift für Kristallographie / Supplemente* **37**, P98

- 24th Congress and General Assembly of the International Union of Crystallography (August 2017)
  'Mullite – towards a unified superspace model'
  oral presentation (30 minutes) in Hyderabad, India
  Proceeding published in *Acta Crystallographica* A**73**, C1121

- 26th Annual Meeting of the German Crystallographic Society (March 2018)
  'Mullite Al/Si ordering in superspace revealed by DFT'
  oral presentation (15 minutes) in Essen, Germany
  Proceeding published in *Zeitschrift für Kristallographie / Supplemente* **38**, S15-03

- 1st International Electronic Conference on Crystals (May 2018)
  'Exploiting superspace to enable DFT calculations of modulated structures with disordered sites using the example of mullite'
  online poster presentation in the world wide web
  Abstract and poster published by MDPI AG (doi:10.3390/IECC_2018-05253)

- 9th Conference on Aperiodic Crystals (July 2018)
  'DFT of incommensurate, disordered structures: ordering phenomena in mullite'
  oral presentation (20 minutes) and poster presentation in Ames, Iowa, USA
  Proceeding published by Iowa State University Digital Press (*Aperiodic 2018 Abstracts*, 25)
  Award: Young Investigator Award for an Outstanding Presentation

- 31st European Crystallographic Meeting (August 2018)
  'Al/Si ordering in mullite'
  oral presentation (20 minutes) in Oviedo, Spain

Courses and summer schools

- II International NMR Training Course (October 2015)
  Instituto de Cerámica y Vidrio (ICV-CSIC), Madrid, Spain

- IV Jornadas Doctorales G-9 (March 2016)
  Universidad Pública de Navarra, Pamplona, Spain

- HERCULES European School (April 2016)
  Grenoble, France and Hamburg, Germany
  Award: Poster prize

- 3rd International School on Aperiodic Crystals (July 2016)
  University of Antwerp, Belgium

- 51st ERICE International School on Crystallography – Electron Crystallography (June 2018)
  Ettore Majorana Foundation, Erice, Italy
  Award: Poster prize

Curriculum Vitae

Paul Benjamin Klar, born 18th February, 1988, in Munich, Germany, Europe

Personal interests: Ultimate Frisbee, bicycle travelling, crystal growth, astronomy, u.v.m.

Education

2014–2018	Doctoral Program in Physics, University of the Basque Country, Spain
	Thesis title: The Aperiodic Nature of Mullite (Supervisor: Gotzon Madariaga)
2011–2013	Master of Science in Advanced Materials Science, Technische Universität München (TUM), Ludwig-Maximilians-Universität München (LMU), Universität Augsburg
	Thesis title: Structure Determination and Characterization of Physical Properties of Metal Organic Frameworks (Supervisors: Gotzon Madariaga, Wolfgang Schmahl, Tom Nilges)
2008–2011	Bachelor of Science in Geosciences, Ludwig-Maximilians-Universität München (LMU), Technische Universität München (TUM)
	Thesis title: X-Ray Topographic Characterization of AlN single crystals (Supervisor: Peter Gille)
2007	Abitur, Carl-Orff-Gymnasium Unterschleißheim

Research Activities

03/2018	Research stay under the supervision of Reinhard Neder (1 month), 'Chair of Crystallography and Structural Physics', Friedrich-Alexander University, Erlangen, Germany
01/2017–06/2017	Research stay under the supervision of Lukáš Palatinus (5 months), 'Laboratory of Precession Electron Diffraction', Institute of Physics of the Czech Academy of Sciences
03/2017	Beamtime on BM01, ESRF, Grenoble, France
11/2015	Reserach stay under the supervision of Luis Sanchez Muñoz (2 weeks), 'Glass and Ceramics Institute', Spanish National Research Council, Madrid, Spain
04/2011	Beamtime on TOPO beamline at ANKA, Karlsruhe, Germany

References

[1] Schneider, H., Fischer, R. X. & Schreuer, J. Mullite: Crystal Structure and Related Properties. *Journal of the American Ceramic Society* **98**, 2948–2967 (2015).

[2] Cameron, W. E. Mullite; a substituted alumina. *American Mineralogist* **62**, 747–755 (1977).

[3] Welberry, T. & Butler, B. Local structural information of mullite obtained from diffuse X-ray scattering. *Journal of the European Ceramic Society* **16**, 187–193 (1996).

[4] Freimann, S. & Rahman, S. Refinement of the real structures of 2:1 and 3:2 mullite. *Journal of the European Ceramic Society* **21**, 2453–2461 (2001).

[5] Schmücker, M., Schneider, H., MacKenzie, K. J. D., Smith, M. E. & Carroll, D. L. AlO_4/SiO_4 Distribution in Tetrahedral Double Chains of Mullite. *Journal of the American Ceramic Society* **88**, 2935–2937 (2005).

[6] Birkenstock, J., Petříček, V., Pedersen, B., Schneider, H. & Fischer, R. X. The modulated average structure of mullite. *Acta Crystallographica Section B* **71**, 358–68 (2015).

[7] Angel, R. J., McMullan, R. K. & Prewitt, C. T. Substructure and superstructure of mullite by neutron diffraction. *American Mineralogist* **76**, 332–342 (1991).

[8] Pauling, L. The principles determining the structure of complex ionic crystals. *Journal of the American Chemical Society* **51**, 1010–1026 (1929).

[9] Gale, J. D. GULP: A computer program for the symmetry-adapted simulation of solids. *Journal of the Chemical Society, Faraday Transactions* **93**, 629–637 (1997).

[10] Kresse, G. & Furthmüller, J. Efficient iterative schemes for ab initio total-energy calculations using a plane-wave basis set. *Physical Review B* **54**, 11169–11186 (1996).

[11] Kresse, G. & Joubert, D. From ultrasoft pseudopotentials to the projector augmented-wave method. *Physical Review B* **59**, 1758–1775 (1999).

REFERENCES

[12] Pinheiro, C. B. & Abakumov, A. M. Superspace crystallography: a key to the chemistry and properties. *IUCrJ* **2**, 137–154 (2015).

[13] Petříček, V., Dušek, M. & Palatinus, L. Crystallographic computing system JANA2006: General features. *Zeitschrift für Kristallographie* **229**, 345–352 (2014).

[14] Petříček, V., Eigner, V., Dušek, M. & Čejchan, A. Discontinuous modulation functions and their application for analysis of modulated structures with the computing system JANA2006. *Zeitschrift für Kristallographie* **231**, 301–312 (2016).

[15] Mark & Rosbaud. Über die Struktur der Aluminiumsilikate vom Typus Al_2SiO_5 und des Pseudobrookits. *Neues Jahrbuch für Mineralogie, Abteilung A, Beilageband* **54**, 127–169 (1926).

[16] Aksay, I. A., Dabbs, D. M. & Sarikaya, M. Mullite for Structural, Electronic, and Optical Applications. *Journal of the American Ceramic Society* **74**, 2343–2358 (1991).

[17] Schneider, H., Schreuer, J. & Hildmann, B. Structure and properties of mullite – A review. *Journal of the European Ceramic Society* **28**, 329–344 (2008).

[18] Schneider, H. & Komarneni, S. *Mullite* (Wiley, Weinheim, 2005).

[19] Bowen, G. T. Description and Analysis of the Sillimanite, a new mineral. *American Journal of Science and Arts* **8**, 113 (1824).

[20] Oschatz & Wächter. Zur Theorie der Porzellanbildung. *Polytechnisches Journal* **106** (1847).

[21] Vernadsky, M. W. Note sur l'influence de la haute température sur le disthéne. *Bulletin de la Société française de minéralogie* (1889).

[22] Hermite, M. Societies and Academies. *Nature* **42**, 261–264 (1890).

[23] Shepherd, E. S. & Rankin, G. S. The binary systems of alumina with silica, lime, and magnesia. *American Journal of Science* **s4-28**, 293–333 (1909).

[24] Bowen, N. L. & Greig, J. W. The system: $Al_2O_3.SiO_2$. *Journal of the American Ceramic Society* **7**, 238–254 (1924).

[25] Thomas, H. H. On Certain Xenolithic Tertiary Minor Intrusions in the Island of Mull (Argyllshire). *Quarterly Journal of the Geological Society* **78** (1922).

[26] Rees, W. Alumina-Silica Minerals in Glasshouse Pots and Tank blocks. *Journal of the Society of Glass Technology* **IX** (1925).

167

[27] Schwarz, R. & Merck, H. Beitrag zur Konstitution des Porzellans. *Zeitschrift für anorganische und allgemeine Chemie* **156**, 1–16 (1926).

[28] McVay, T. N. The Determination of Mullite in a Porcelain Body. *Journal of the American Ceramic Society* **10**, 62–63 (1927).

[29] Wyckoff, W. G., Greig, J. W. & Bowen, N. L. X-ray diffraction patterns; mullite and sillimanite. *American Journal of Science* **11**, 459–472 (1926).

[30] Taylor, W. H. The structure of sillimanite and mullite. *Zeitschrift für Kristallographie* **68**, 503–521 (1928).

[31] Warren, B. E. The Role of Silicon and Aluminum in Complex Silicates. *Journal of the American Ceramic Society* **16**, 412–417 (1933).

[32] McConnell, J. D. C. & Heine, V. Incommensurate structure and stability of mullite. *Phys. Rev. B* **31**, 6140–6142 (1985).

[33] Padlewski, S., Heine, V. & Price, G. D. A microscopic model for a very stable incommensurate modulated mineral: mullite. *Journal of Physics: Condensed Matter* **5**, 3417 (1993).

[34] Giaccovazzo, C. *et al.* *Fundamentals of Crystallography* (Oxford University Press, 2011), 3rd edn.

[35] Gladysz, G. M. & Chawla, K. K. *Voids in materials : from unavoidable defects to designed cellular materials* (Elsevier, 2015), 1st edn.

[36] Ylä-Jääski, J. & Nissen, H.-U. Investigation of superstructures in mullite by high resolution electron microscopy and electron diffraction. *Physics and Chemistry of Minerals* **10**, 47–54 (1983).

[37] Paulmann, C. Study of oxygen vacancy ordering in mullite at high temperatures. *Phase Transitions* **59**, 77–90 (1996).

[38] Patterson, E. A. *et al.* Temperature-Dependent Deformation and Dislocation Density in $SrTiO_3$ (001) Single Crystals. *Journal of the American Ceramic Society* **99**, 3411–3420 (2016).

[39] Agrell, S. O. & Smith, J. V. Cell Dimensions, Solid Solution, Polymorphism, and Identification of Mullite and Sillimanite. *Journal of the American Ceramic Society* **43**, 69–78 (1960).

[40] Taylor, S. Abundance of chemical elements in the continental crust: a new table. *Geochimica et Cosmochimica Acta* **28**, 1273–1285 (1964).

REFERENCES

[41] Aramaki, S. & Roy, R. Revised Equilibrium Diagram for the System Al_2O_3-SiO_2. *Nature* **184**, 631–632 (1959).

[42] Aramaki, S. & Roy, R. Revised Phase Diagram for the System Al_2O_3-SiO_2. *Journal of the American Ceramic Society* **45**, 229–242 (1962).

[43] Kodentsov, A., Bastin, G. & van Loo, F. The diffusion couple technique in phase diagram determination. *Journal of Alloys and Compounds* **320**, 207–217 (2001).

[44] Aksay, I. A. & Pask, J. A. The silica-alumina system: stable and metastable equilibria at 1.0 atmosphere. *Science* **183**, 69–71 (1974).

[45] Aksay, I. A. & Pask, J. A. Stable and Metastable Equilibria in the System SiO_2-Al_2O_3. *Journal of the American Ceramic Society* **58**, 507–512 (1975).

[46] Klug, F. J., Prochazka, S. & Doremus, R. H. Alumina-Silica Phase Diagram in the Mullite Region. *Journal of the American Ceramic Society* **70**, 750–759 (1987).

[47] Kriven, W. M. & Pask, J. A. Solid Solution Range and Microstructures of Melt-Grown Mullite. *Journal of the American Ceramic Society* **66**, 649–654 (1983).

[48] Guse, W. & Mateika, D. Growth of mullite single crystals ($2Al_2O_3 \cdot SiO_2$) by the Czochralski method. *Journal of Crystal Growth* **22**, 237–240 (1974).

[49] Smith, D. G. W. & McConnell, J. D. C. A Comparative Electron-Diffraction Study of Sillimanite and Some Natural and Artificial Mullites. *Mineralogical Magazine* **35**, 810–814 (1966).

[50] Nakajima, Y. & Ribbe, P. H. Twinning and superstructure of Al-rich mullite. *American Mineralogist* **66**, 142–147 (1981).

[51] Wang, H., Kulkarni, T., Sarin, V. & Basu, S. Ordered and twinned multidomain structure in highly Al-rich mullite. *Journal of Materials Research* **22**, 3210–3217 (2007).

[52] Shannon, R. D. Revised effective ionic radii and systematic studies of interatomic distances in halides and chalcogenides. *Acta Crystallographica Section A* **32**, 751–767 (1976).

[53] Fischer, R. X., Schneider, H. & Schmucker, M. Crystal structure of Al-rich mullite. *American Mineralogist* **79**, 983–990 (1994).

[54] Peterson, R. C. & McMullan, R. K. Neutron diffraction studies of sillimanite. *American Mineralogist* **71**, 742–745 (1986).

[55] King, S. P. *Development of Solid State NMR on Disordered Systems, from Bioactive glasses to Mullites.* Phd thesis, University of Warwick (2014).

[56] Rehak, P. *et al.* Study of the Al coordination in mullites with varying Al:Si ratio by ^{27}Al NMR spectroscopy and X-ray diffraction. *American Mineralogist* **83**, 1266–1276 (1998).

[57] Sadanaga, R., Tokonami, M. & Takéuchi, Y. The structure of mullite, $2Al_2O_3 \cdot SiO_2$, and relationship with the structures of sillimanite and andalusite. *Acta Crystallographica* **15**, 65–68 (1962).

[58] Burnham, C. W. The Crystal Structure of Mullite. *Carnegie Institution of Washington Annual Reports* **62**, 158–165 (1963).

[59] Burnham, C. W. Crystal Structure of Mullite. *Carnegie Institution of Washington Annual Reports* **63**, 223–228 (1964).

[60] Saalfeld, H. The domain structure of 2:1-mullite. *Neues Jahrbuch für Mineralogie, Abhandlungen* **134**, 305–316 (1979).

[61] Balzar, D. & Ledbetter, H. Crystal structure and compressibility of 3:2 mullite. *American Mineralogist* **78**, 1192–1196 (1993).

[62] Angel, R. J. & Prewitt, C. T. Crystal structure of mullite; a re-examination of the average structure. *American Mineralogist* **71**, 1476–1482 (1986).

[63] Kahn-Harari, A. *et al.* Observation of ordering in silicon and germanium mullites. *Journal of Solid State Chemistry* **90**, 234–248 (1991).

[64] Landau, L. D. Theory of phase transformations. I. *Physikalische Zeitschrift der Sowjetunion* **11**, 26 (1937).

[65] Heine, V. & McConnell, J. D. C. Origin of Modulated Incommensurate Phases in Insulators. *Phys. Rev. Lett.* **46**, 1092–1095 (1981).

[66] Angel, R. J. & Prewitt, C. T. The incommensurate structure of mullite by Patterson synthesis. *Acta Crystallographica Section B* **43**, 116–126 (1987).

[67] Welberry, T. R. & Withers, R. L. An optical transform and Monte Carlo study of the diffuse X-ray scattering in mullite, $Al_2Al_{2+2x}Si_{2-2x}O_{10-x}$. *Physics and Chemistry of Minerals* **17**, 117–124 (1990).

[68] van Smaalen, S. *Incommensurate Crystallography* (Oxford University Press, 2007).

[69] Zou, X., Hovmöller, S. & Oleynikov, P. *Electron Crystallography, Electron Microscopy and Electron Diffraction* (Oxford University Press, 2011).

[70] Leach, A. *Molecular Modelling: Principles and Applications* (Pearson, 2001), 2nd edn.

[71] Sholl, D. S. & Steckel, J. A. *Density functional theory : a practical introduction* (Wiley, Hoboken, New Jersey, 2009).

[72] Prince, E. (ed.) *International Tables for Crystallography - Volume C: Mathematical, physical and chemical tables* (International Union of Crystallography, 2004), 3rd edn.

[73] de Broglie, L. A tentative theory of light quanta. *Philosophical Magazine Letters* **47**, 446–458 (1924).

[74] de Broglie, L. Interference and Corpuscular Light. *Nature* **118**, 441–442 (1926).

[75] Einstein, A. Zur Elektrodynamik bewegter Körper. *Annalen der Physik* **322**, 891–921 (1905).

[76] Thomson, J. J. *Conduction of electricity through gases* (Cambridge University Press, 1906).

[77] Thomson, J. J. *The corpuscular theory of matter* (Scribner's Sons, New York, 1907).

[78] Einstein, A. Über einen die Erzeugung und Verwandlung des Lichtes betreffenden heuristischen Gesichtspunkt. *Annalen der Physik* **322**, 132–148 (1905).

[79] Mohr, P. J., Newell, D. B. & Taylor, B. N. CODATA recommended values of the fundamental physical constants: 2014. *Reviews of Modern Physics* **88**, 035009 (2016).

[80] De Bergevin, F. & Brunel, M. Observation of magnetic superlattice peaks by X-ray diffraction on an antiferromagnetic NiO crystal. *Physics Letters A* **39**, 141–142 (1972).

[81] Ohsumi, H. & Arima, T.-h. Novel insight into structural magnetism by polarized synchrotron X-ray scattering. *Advances in Physics: X* **1**, 128–145 (2016).

[82] Fourier, J. B. J. *Théorie analytique de la chaleur* (Firmin Didot, père et fils, Paris, 1822).

[83] Ewald, P. P. VII. Das reziproke Gitter in der Strukturtheorie. *Zeitschrift für Kristallographie* **56**, 129–156 (1921).

[84] Schrödinger, E. An Undulatory Theory of the Mechanics of Atoms and Molecules. *Physical Review* **28**, 1049–1070 (1926).

[85] Born, M. Zur Quantenmechanik der Stoßvorgänge. *Zeitschrift für Physik* **37**, 863–867 (1926).

[86] Friedrich, W., Knipping, P. & Laue, M. Interferenzerscheinungen bei Röntgenstrahlen. *Annalen der Physik* **346**, 971–988 (1913).

[87] Bragg, W. L. The diffraction of short electromagnetic waves by a crystal. *Proceedings of the Cambridge Philosophical Society* **17**, 43–57 (1913).

[88] Welberry, T. & Weber, T. One hundred years of diffuse scattering. *Crystallography Reviews* **22**, 2–78 (2016).

[89] Compton, A. H. A Quantum Theory of the Scattering of X-rays by Light Elements. *Physical Review* **21**, 483–502 (1923).

[90] Debye, P. Interferenz von Röntgenstrahlen und Wärmebewegung. *Annalen der Physik* **348**, 49–92 (1913).

[91] Waller, I. Zur Frage der Einwirkung der Wärmebewegung auf die Interferenz von Röntgenstrahlen. *Zeitschrift für Physik* **17**, 398–408 (1923).

[92] Ewald, P. P. Zur Begründung der Kristalloptik. *Annalen der Physik* **359**, 519–556 (1917).

[93] Palatinus, L. *et al.* Structure refinement using precession electron diffraction tomography and dynamical diffraction: tests on experimental data. *Acta Crystallographica Section B* **71**, 740–751 (2015).

[94] Vincent, R. & Midgley, P. Double conical beam-rocking system for measurement of integrated electron diffraction intensities. *Ultramicroscopy* **53**, 271–282 (1994).

[95] Kolb, U., Gorelik, T., Kübel, C., Otten, M. T. & Hubert, D. Towards automated diffraction tomography: part I–data acquisition. *Ultramicroscopy* **107**, 507–13 (2007).

[96] Mugnaioli, E., Gorelik, T. & Kolb, U. „Ab initio" structure solution from electron diffraction data obtained by a combination of automated diffraction tomography and precession technique. *Ultramicroscopy* **109**, 758–765 (2009).

[97] Palatinus, L., Petříček, V. & Corrêa, C. A. Structure refinement using precession electron diffraction tomography and dynamical diffraction: theory and implementation. *Acta Crystallographica Section A* **71**, 235–44 (2015).

[98] Xie, D., Baerlocher, C. & McCusker, L. B. Combining precession electron diffraction data with X-ray powder diffraction data to facilitate structure solution. *Journal of Applied Crystallography* **41**, 1115–1121 (2008).

REFERENCES

[99] Proffen, T. & Neder, R. B. DISCUS : a program for diffuse scattering and defect-structure simulation. *Journal of Applied Crystallography* **30**, 171–175 (1997).

[100] Schmidt, E. & Neder, R. B. Diffuse single-crystal scattering corrected for molecular form factor effects. *Acta Crystallographica Section A* **73**, 231–237 (2017).

[101] Patterson, A. L. A Fourier Series Method for the Determination of the Components of Interatomic Distances in Crystals. *Physical Review* **46**, 372–376 (1934).

[102] Karle, J. & Hauptman, H. The phases and magnitudes of the structure factors. *Acta Crystallographica* **3**, 181–187 (1950).

[103] Sayre, D. The squaring method: a new method for phase determination. *Acta Crystallographica* **5**, 60–65 (1952).

[104] Hauptman, H. & Karle, J. Solution of the phase problem for space group P-1. *Acta Crystallographica* **7**, 369–374 (1954).

[105] Oszlányi, G. & Sütö, A. Ab initio structure solution by charge flipping. *Acta Crystallographica Section A* **60**, 134–141 (2004).

[106] Palatinus, L. The charge-flipping algorithm in crystallography. *Acta Crystallographica Section B* **69**, 1–16 (2013).

[107] Palatinus, L. & Chapuis, G. SUPERFLIP - A computer program for the solution of crystal structures by charge flipping in arbitrary dimensions. *Journal of Applied Crystallography* **40**, 786–790 (2007).

[108] Müller, P. Practical suggestions for better crystal structures. *Crystallography Reviews* **15**, 57–83 (2009).

[109] Borchardt-Ott, W. *Crystallography: An Introduction* (Springer, 2011), 3rd edn.

[110] Shechtman, D., Blech, I., Gratias, D. & Cahn, J. W. Metallic Phase with Long-Range Orientational Order and No Translational Symmetry. *Physical Review Letters* **53**, 1951–1953 (1984).

[111] Janssen, T. Aperiodic crystals: A contradictio in terminis? *Physics Reports* **168**, 55–113 (1988).

[112] Ritter, K. & Rising, M. Israeli wins chemistry Nobel for quasicrystals (phys.org, 5.10.2011) (2011). URL `https://phys.org/news/2011-10-daniel-shechtman-nobel-chemistry-prize.html`.

[113] Brouns, E., Visser, J. W. & de Wolff, P. M. An anomaly in the crystal structure of Na_2CO_3. *Acta Crystallographica* **17**, 614 (1964).

[114] Dubbledam, G. C. & de Wolff, P. M. The average crystal structure of γ-Na$_2$CO$_3$. *Acta Crystallographica Section B* **25**, 2665–2667 (1969).

[115] de Wolff, P. M. The Pseudo-Symmetry of Modulated Crystal Structures. *Acta Crystallographica Section A* **30**, 777–785 (1974).

[116] de Wolff, P. M. Symmetry operations for displacively modulated structures. *Acta Crystallographica Section A* **33**, 493–497 (1977).

[117] Janner, A. & Janssen, T. Symmetry of periodically distorted crystals. *Physical Review B* **15**, 643–658 (1977).

[118] Janner, A. & Janssen, T. Symmetry of incommensurate crystal phases. I. Commensurate basic structures. *Acta Crystallographica Section A* **36**, 399–408 (1980).

[119] Janner, A. & Janssen, T. Symmetry of incommensurate crystal phases. II. Incommensurate basic structure. *Acta Crystallographica Section A* **36**, 408–415 (1980).

[120] Van Smaalen, S. An elementary introduction to superspace crystallography. *Zeitschrift für Kristallographie* **219**, 681–691 (2004).

[121] Newton, I. *Philosophiæ naturalis principia mathematica* (Innys, London, 1687).

[122] Hamilton, W. R. On a General Method in Dynamics. *Philosophical Transactions of the Royal Society* **124**, 247–308 (1834).

[123] Tuckerman, M. E. & Martyna, G. J. Understanding Modern Molecular Dynamics: Techniques and Applications. *Journal of Physical Chemistry B* **104**, 159–178 (2000).

[124] Buckingham, R. A. The Classical Equation of State of Gaseous Helium, Neon and Argon. *Proceedings of the Royal Society A: Mathematical, Physical and Engineering Sciences* **168**, 264–283 (1938).

[125] Born, M. & Oppenheimer, R. Zur Quantentheorie der Molekeln. *Annalen der Physik* **389**, 457–484 (1927).

[126] Hartree, D. R. The Wave Mechanics of an Atom with a Non-Coulomb Central Field. Part II. Some Results and Discussion. *Mathematical Proceedings of the Cambridge Philosophical Society* **24**, 111 (1928).

[127] Fock, V. Näherungsmethode zur Lösung des quantenmechanischen Mehrkörperproblems. *Zeitschrift für Physik* **61**, 126–148 (1930).

[128] Slater, J. C. Atomic Shielding Constants. *Physical Review* **36**, 57–64 (1930).

REFERENCES

[129] Hohenberg, P. & Kohn, W. Inhomogeneous Electron Gas. *Physical Review* **136**, B864–B871 (1964).

[130] Kohn, W. & Sham, L. J. Self-Consistent Equations Including Exchange and Correlation Effects. *Physical Review* **140**, A1133–A1138 (1965).

[131] Güttinger, P. Das Verhalten von Atomen im magnetischen Drehfeld. *Zeitschrift für Physik* **73**, 169–184 (1932).

[132] Hellmann, H. *Einführung in die Quantenchemie* (Franz Deuticke, Leipzig, 1937).

[133] Mortensen, J. J. *et al.* Bayesian Error Estimation in Density-Functional Theory. *Physical Review Letters* **95**, 216401 (2005).

[134] Hanke, F. Sensitivity analysis and uncertainty calculation for dispersion corrected density functional theory. *Journal of Computational Chemistry* **32**, 1424–1430 (2011).

[135] Bloch, F. Über die Quantenmechanik der Elektronen in Kristallgittern. *Zeitschrift für Physik* **52**, 555–600 (1929).

[136] London, F. The general theory of molecular forces. *Transactions of the Faraday Society* **33**, 8b (1937).

[137] Grimme, S. Semiempirical GGA-type density functional constructed with a long-range dispersion correction. *Journal of Computational Chemistry* **27**, 1787–1799 (2006).

[138] Grimme, S., Antony, J., Ehrlich, S. & Krieg, H. A consistent and accurate ab initio parametrization of density functional dispersion correction (DFT-D) for the 94 elements H-Pu. *The Journal of Chemical Physics* **132**, 154104 (2010).

[139] van de Streek, J. & Neumann, M. A. Validation of molecular crystal structures from powder diffraction data with dispersion-corrected density functional theory (DFT-D). *Acta Crystallographica Section B* **70**, 1020–1032 (2014).

[140] Hay, H., Ferlat, G., Casula, M., Seitsonen, A. P. & Mauri, F. Dispersion effects in SiO_2 polymorphs: An *ab initio* study. *Physical Review B* **92**, 144111 (2015).

[141] Martinón-Torres, M., Rehren, T. & Freestone, I. C. Mullite and the mystery of Hessian wares. *Nature* **444**, 437–438 (2006).

[142] Bauer, W. H., Gordon, I. & Moore, C. H. Flame Fusion Synthesis of Mullite Single Crystals. *Journal of the American Ceramic Society* **33**, 140–143 (1950).

[143] Schneider, H., Fischer, R. X. & Voll, D. Mullite with lattice concstants a > b. *Journal of the American Ceramic Society* **76**, 1879–1881 (1993).

[144] Fischer, R. X., Schneider, H. & Voll, D. Formation of aluminum rich 9:1 mullite and its transformation to low alumina mullite upon heating. *Journal of the European Ceramic Society* **16**, 109–113 (1996).

[145] Sales, M. & Alarcón, J. Synthesis and Phase Transformations of Mullites Obtained from SiO_2-Al_2O_3 Gels. *Journal of the European Ceramic Society* **16**, 781–789 (1996).

[146] de Sola, E. R., Torres, F. J. & Alarcón, J. Thermal evolution and structural study of 2:1 mullite from monophasic gels. *Journal of the European Ceramic Society* **26**, 2279–2284 (2006).

[147] Doppalapudi, D. & Basu, S. Structure of mullite coatings grown by chemical vapor deposition. *Materials Science and Engineering: A* **231**, 48–54 (1997).

[148] Rinne, F. Röntgenographische Diagnostik beim Brennen von Kalkstein, Dolomit, Kaolin und Glimmer. *Zeitschrift für Kristallographie* **61**, 113–124 (1924).

[149] Brindley, G. W. & Nakahira, M. The KaoIinite-Mullite Reaction Series: I, A Survey of Outstanding Problems. *Journal of the American Ceramic Society* **42**, 311–314 (1959).

[150] Holm, J. L. Kaolinites-mullite transformation in different Al_2O_3-SiO_2 systems: Thermo-analytical studies. *Phys. Chem. Chem. Phys.* **3**, 1362–1365 (2001).

[151] Rietveld, H. M. A profile refinement method for nuclear and magnetic structures. *Journal of Applied Crystallography* **2**, 65–71 (1969).

[152] Dyadkin, V., Pattison, P., Dmitriev, V. & Chernyshov, D. A new multipurpose diffractometer PILATUS@SNBL. *Journal of Synchrotron Radiation* **23**, 825–829 (2016).

[153] Rigaku Oxford Diffraction. CrysAlisPro (2017).

[154] Williams, D. B. & Carter, C. B. *Transmission electron microscopy : a textbook for materials science* (Springer, 2009), 2nd edn.

[155] Palatinus, L. PETS. Analysis of Electron Diffraction Data (2011).

[156] Matsui, M. Molecular dynamics study of the structures and bulk moduli of crystals in the system CaO-MgO-Al_2O_3-SiO_2. *Physics and Chemistry of Minerals* **23**, 345–353 (1996).

[157] Lacks, D. J., Hildmann, B. & Schneider, H. Effects of disorder in mullite: Molecular dynamics simulation and energy landscape analysis. *Physical Review B* **72**, 214305 (2005).

[158] Chen, J.-C., Chen, C.-S., Schneider, H., Chou, C.-C. & Wei, W.-C. J. Atomistic calculations of lattice constants of mullite with its compositions. *Journal of the European Ceramic Society* **28**, 345–351 (2008).

[159] Adabifiroozjaei, E., Hart, J. N., Koshy, P., Mitchell, D. R. G. & Sorrell, C. C. Mullite-glass and mullite-mullite interfaces: Analysis by molecular dynamics (MD) simulation and high-resolution TEM. *Journal of the American Ceramic Society* **101**, 428–439 (2018).

[160] Winter, J. K. & Ghose, S. Thermal expansion and high-temperture crystal chemistry of the Al_2SiO_5 polymorphs. *American Mineralogist* **64**, 573–586 (1979).

[161] Perdew, J. P., Burke, K. & Ernzerhof, M. Generalized Gradient Approximation Made Simple. *Physical Review Letters* **77**, 3865–3868 (1996).

[162] Perdew, J. *et al.* Restoring the Density-Gradient Expansion for Exchange in Solids and Surfaces. *Physical Review Letters* **100**, 136406 (2008). `0707.2088`.

[163] Monkhorst, H. J. & Pack, J. D. Special points for Brillouin-zone integrations. *Physical Review B* **13**, 5188–5192 (1976).

[164] Bragg, W. & Gibbs, R. E. The Structure of α and β quartz. *Proceedings of the Royal Society A: Mathematical, Physical and Engineering Sciences* **109**, 405–427 (1925).

[165] Pauling, L. & Hendricks, S. B. The Crystal Structure of Hematite and Corundum. *Journal of the American Chemical Society* **47**, 781–790 (1925).

[166] Demichelis, R., Civalleri, B., D'Arco, P. & Dovesi, R. Performance of 12 DFT functionals in the study of crystal systems: Al_2SiO_5 orthosilicates and Al hydroxides as a case study. *International Journal of Quantum Chemistry* **110**, 2260–2273 (2010).

[167] Cline, J. P. Certificate of Analysis - Standard Reference Material 1878b. Tech. Rep. (2017). URL `https://www-s.nist.gov/srmors/certificates/1878B.pdf`.

[168] O'Connor, B. H. & Raven, M. D. Application of the Rietveld Refinement Procedure in Assaying Powdered Mixtures. *Powder Diffraction* **3**, 2–6 (1988).

[169] Cline, J. P. Certificate of Analysis - Standard Reference Material 676a. Tech. Rep., National Institute of Standards & Technology (2014). URL `https://www-s.nist.gov/srmors/certificates/676A.pdf`.

[170] Tohei, T., Watanabe, Y., Lee, H.-S. & Ikuhara, Y. First principles calculation of thermal expansion coefficients of pure and Cr doped α-alumina crystals. *Journal of Applied Physics* **120**, 142106 (2016).

[171] Perez-Mato, J. M., Zakhour-Nakhl, M., Weill, F. & Darriet, J. Structure of composites $A_{1+x}(A'_xB_{1-x})O_3$ related to the 2H hexagonal perovskite: relation between composition and modulation. *Journal Of Materials Chemistry* **9**, 2795–2808 (1999).

[172] Vegard, L. Die Konstitution der Mischkristalle und die Raumfüllung der Atome. *Zeitschrift für Physik* **5**, 17–26 (1921).

[173] Yang, H., Hazen, R. M., Finger, L. W., Prewitt, C. T. & Downs, R. T. Compressibility and crystal structure of sillimanite, Al_2SiO_5, at high pressure. *Physics and Chemistry of Minerals* **25**, 39–47 (1997).

[174] Petříček, V., van der Lee, A. & Evain, M. On the use of crenel functions for occupationally modulated structures. *Acta Crystallographica Section A* **51**, 529–535 (1995).

[175] Izaola, Z. *et al.* Revision of pyrrhotite structures within a common superspace model. *Acta Crystallographica Section B* **63**, 693–702 (2007).

[176] Madsen, A. Ø., Civalleri, B., Ferrabone, M., Pascale, F. & Erba, A. Anisotropic displacement parameters for molecular crystals from periodic Hartree-Fock and density functional theory calculations. *Acta Crystallographica Section A* **69**, 309–321 (2013).

[177] Schneider, H. & Eberhard, E. Thermal Expansion of Mullite. *Journal of the American Ceramic Society* **73**, 2073–2076 (1990).

[178] Cameron, W. E. Composition and Cell Dimensions of Mullite. *American Ceramic Society Bulletin* **56**, 1003–1011 (1977).

[179] Ban, T. & Okada, K. Structure Refinement of Mullite by the Rietveld Method and a New Method for Estimation of Chemical Composition. *Journal of the American Ceramic Society* **75**, 227–230 (1992).

[180] Butler, B. D. & Welberry, T. R. Analysis of diffuse scattering from the mineral mullite. *Journal of Applied Crystallography* **27**, 742–754 (1994).

[181] McConnell, J. D. C. & Heine, V. An aid to the structure analysis of incommensurate phases. *Acta Crystallographica Section A* **40**, 473–482 (1984).

REFERENCES

[182] Aroyo, M. I., Kirov, A., Capillas, C., Perez-Mato, J. M. & Wondratschek, H. Bilbao Crystallographic Server. II. Representations of crystallographic point groups and space groups. *Acta Crystallographica Section A* **62**, 115–128 (2006).

[183] Aryal, S., Rulis, P., Ouyang, L. & Ching, W. Y. Structure and properties of the low-density phase ι-Al_2O_3 from first principles. *Phys. Rev. B* **84**, 174123 (2011).

[184] Momma, K. & Izumi, F. VESTA 3 for three-dimensional visualization of crystal, volumetric and morphology data. *Journal of Applied Crystallography* **44**, 1272–1276 (2011).

[185] Nakajima, Y., Morimoto, N. & Watanabe, E. Direct Observation of Oxygen Vacancy in Mullite, $1.86Al_2O_3 \cdot SiO_2$ by High Resolution Electron Microscopy. *Proceedings of the Japan Academy* **51**, 173–178 (1975).

[186] Sayir, A. & Farmer, S. C. Directionally Solidified Mullite Fibers. In *MRS Proceedings*, vol. 365 of *MRS Proceedings*, 11–20 (1994). URL `https://doi.org/10.1557/PROC-365-11`.

[187] Burt, J. B., Ross, N. L., Angel, R. J. & Koch, M. Equations of state and structures of andalusite to 9.8 GPa and sillimanite to 8.5 GPa. *American Mineralogist* 319–326 (2006).

[188] Fischer, R. X. *et al.* A new mineral from the Bellerberg, Eifel, Germany, intermediate between mullite and sillimanite. *American Mineralogist* **100**, 1493–1501 (2015).

[189] Schneider, H. & Majdič, A. Kinetics of the thermal decomposition of kyanite. *Ceramurgia International* **6**, 61–66 (1980).

[190] Rahman, S., Feustel, U. & Freimann, S. Structure description of the thermic phase transformation sillimaniteâmullite. *Journal of the European Ceramic Society* **21**, 2471–2478 (2001).

[191] Cameron, W. Exsolution in 'stoichiometric' mullite. *Nature* **264**, 736–738 (1976).

[192] Schmücker, M., Hildmann, B. & Schneider, H. Mechanism of 2/1- to 3/2-mullite transformation at 1650 °C. *American Mineralogist* **87**, 1190–1193 (2002).

[193] Guse, W. Compositional analysis of Czochralski grown mullite single crystals (1974).

[194] Cameron, W. E. A mineral phase intermediate in composition between sillimanite and mullite. *American Mineralogist* **61**, 1025–1026 (1976).

[195] Hariya, Y., Dollase, W. & Kennedy, G. An experimental investigation of the relationship of mullite to sillimanite. *American Mineralogist* **54**, 1419–1441 (1969).

[196] Pyzik, A. J., Todd, C. S. & Han, C. Formation mechanism and microstructure development in acicular mullite ceramics fabricated by controlled decomposition of fluorotopaz. *Journal of the European Ceramic Society* **28**, 383–391 (2008).

[197] Ren, Q. *et al.* Effect of the calcining temperatures of low-grade bauxite on the mechanical property of mullite ceramics. *International Journal of Applied Ceramic Technology* **15**, 554–562 (2018).

[198] Figueiredo, J. M. R. *et al.* Influence of composition and processing variables of clay-based formulations - use in refractory materials. *Cerâmica* **64**, 10–19 (2018).

[199] Lerdprom, W. *et al.* Impact of spark plasma sintering (SPS) on mullite formation in porcelains. *Journal of the American Ceramic Society* **101**, 525–535 (2018).

[200] Ripin, A. *et al.* X-ray shielding behaviour of kaolin derived mullite-barites ceramic. *Radiation Physics and Chemistry* **144**, 63–68 (2018).

[201] Chen, C.-S., Chou, C.-C., Chang, S.-W., Fischer, R. X. & Schneider, H. First-principles study on variation of lattice parameters of mullite $Al_{4+2x}Si_{2-2x}O_{10-x}$ (x = 0.125, 0.250, 0.375). *American Mineralogist* **95**, 1617–1623 (2010).

[202] Zamani, S. M. M. & Behdinan, K. The effect of oxygen vacancy and temperature on the lattice parameters of mullite using a novel bridging cell multiscale method. *Ceramics International* **43**, 12239–12248 (2017).

[203] Aryal, S., Rulis, P. & Ching, W.-Y. Mechanical Properties and Electronic Structure of Mullite Phases Using First-Principles Modeling. *Journal of the American Ceramic Society* **95**, 2075–2088 (2012).

[204] Dowty & E. Stability and calculated vibrational spectra of mullite and other aluminum tetrahedral tricluster structures. *Geological Society of America, Abstracts with Programs* **17** (1985).

[205] Gaines, R. V., Skinner, H. C. W., Foord, E. E., Mason, B. & Rosenzweig, A. *Dana's new mineralogy* (Wiley, 1997), 8th edn.

[206] Strunz, H. & Nickel, E. H. *Strunz mineralogical tables* (Schweizerbart Science Publishers, 2001), 9th edn.

[207] Tokonami, M., Nakajima, Y. & Morimoto, N. The diffraction aspect and a structural model of mullite, $Al(Al_{1+2x}Si_{1-2x})O_{5-x}$. *Acta Crystallographica Section A* **36**, 270–276 (1980).

REFERENCES

[208] Rahman, S. H. & Weichert, H.-T. Interpretation of HREM images of mullite. *Acta Crystallographica Section B* **46**, 139–149 (1990).

[209] Tummers, B. DataThief III (2006). URL `https://datathief.org/`.

[210] Comodi, P., Zanazzi, P. F., Poli, S. & Schmidt, M. W. High-pressure behavior of kyanite; compressibility and structural deformations. *American Mineralogist* **82**, 452–459 (1997).

[211] Cameron, W. E. Nonstoichiometry in sillimanite: Mullite compositions with sillimanite-type superstructures. *Physics and Chemistry of Minerals* **1**, 265–272 (1977).

[212] Stokes, H. T., Campbell, B. J. & Van Smaalen, S. Generation of (3 + d)-dimensional superspace groups for describing the symmetry of modulated crystalline structures. *Acta Crystallographica Section A* **67**, 45–55 (2011).